Title
The Formation and Evolution of Giant Molecular Clouds

Author
Imara, Nia

Publication Date
2010

Peer reviewed|Thesis/dissertation

The Formation and Evolution of Giant Molecular Clouds

by

Nia Imara

A dissertation submitted in partial satisfaction of the
requirements for the degree of
Doctor of Philosophy

in

Astrophysics

in the

Graduate Division
of the
University of California, Berkeley

Committee in charge:
Professor Leo Blitz, Chair
Professor Christopher McKee
Professor Steven Stahler
Professor Richard Muller

Fall 2010

The Formation and Evolution of Giant Molecular Clouds

Abstract

The Formation and Evolution of Giant Molecular Clouds

by

Nia Imara
Doctor of Philosophy in Astrophysics

University of California, Berkeley

Professor Leo Blitz, Chair

To adequately address topics such as stellar and galactic evolution, it is necessary to address the question of giant molecular cloud (GMC) formation and evolution, topics that continue to be actively debated in astrophysics. In this thesis, I present new studies on the kinematic properties of individual molecular clouds in the Galaxy and M33 and on their global properties in low-metallicity environments. My primary aim in analyzing the kinematic features of GMCs is to determine the extent to which they are explained by current formation theories. Clues pointing to the origins of GMCs are revealed by comparing the large-scale linear velocity gradients, which they are frequently observed to possess, with the gradients in the high-density atomic hydrogen (HI) from which they are expected to form. Using high-resolution ^{13}CO observations of five Milky Way GMCs, I create intensity-weighted velocity maps from which I measure the maximum gradient magnitudes and directions of the clouds. I use data from the Leiden/Argentine/Bonn Galactic HI survey to identify and measure the properties of regions of atomic gas associated with the GMCs. If the molecular cloud gradients—ranging from 0.04 to 0.20 km s^{-1} pc^{-1}—are due to rotation, their angular momentum is always less than that in the surrounding HI. Though this result is consistent with the the hypothesis that GMCs form from large-scale instabilities, one must necessarily introduce some mechanism capable of reducing the angular momentum in order to explain the discrepancies in the molecular and atomic gas. The second key result is that—with the exception of the Orion A molecular cloud—there are large differences in the gradient directions of the molecular and atomic gas. A continuation of this study is given for a much larger sample of GMCs in M33. The results are consistent with those in the Milky Way; in particular, the gradient directions of the GMCs are uncorrelated with the HI gradient directions. Additional findings include the observation that the local surface density of atomic gas slowly increases with GMC mass as $\Sigma_{\rm HI} \propto M_{\rm GMC}^{0.27\pm0.06}$. Also, the properties of high-density atomic hydrogen in which GMCs have not been observed generally has smaller gradients (~ 0.03 km s^{-1} pc^{-1}) than does the HI associated with GMCs (~ 0.05 km s^{-1} pc^{-1}). This suggests that high shear in atomic gas is either a prerequisite for or consequence of GMC formation. Studying the properties of GMCs in different environments is another avenue for enhancing our understanding of their evolution. An extinction map of the low-metallicity

Large Magellanic Cloud (LMC) is presented, using near-infrared photometry from the Two Micron All Sky Survey. A mean visual extinction of 0.38 mag is found, and an extended distribution of molecular gas is observed across the face of the galaxy that was previously undetected by CO observations. The CO-to-H_2 conversion factor in the LMC, $9.3 \pm 0.4 \times 10^{20}$ cm^{-2} (K km s^{-1})$^{-1}$, is nearly 5 times greater than the average value in the Milky Way. My work demonstrates that CO is not a good tracer of H_2, and caution must be applied in using the Galactic X-factor in low-metallicity environments.

For S. L. Perkins and C. A. Lee.

Contents

List of Figures

List of Tables

Acknowledgments

I thank all those who have supported and encouraged me along the way.

Chapter 1

Introduction

Beyond our little planet, space is filled with an assortment of fascinating and mysterious objects: planets, rocks, dust, stars, plasmas, molecular clouds, hydrogen clouds, black holes, dark matter, dark energy.... As humans, stars, of course, are very important to us for a number of reasons. Perhaps the foremost reason is that we want to know where we come from, and the story of our origins—as a Solar System, as a planet, as societies and individuals—often begins with stars. But where do stars come from? Decades of research have enabled us to create a picture of stellar nurseries: An enormous cloud more than 100,000 times larger than our solar system and a million times more massive than our Sun is racing through space at 16,000 miles per hour. The cloud, composed of molecules and dust particles, is incredibly cold—below $-400°$ Fahrenheit. Compared to its surroundings, it is also very dense. A magnetic field pervades the cloud, on the inside of which are thousands of highly compact clumps of gas flying around and smashing into each other every several million years or so. And within these clumps—inside even more compact, rapidly spinning cores of gas—are where the initial, practically invisible stages of star formation occur....

Thousands of these *giant molecular clouds* (GMCs), in which all star formation is observed, exist in the Milky Way and contain most of the molecular mass in the Galaxy (e.g., Scoville & Solomon 1975). Molecular cloud and stellar evolution are closely interconnected. For instance, the fraction of gas in the interstellar medium (ISM) in the molecular phase determines the efficiency with which a given galaxy forms stars. On the other hand, the number of extant stars influences the molecular fraction in a galaxy. Once molecular material gathers into GMCs, the way in which these structures evolve determines the star formation rate. Via highly energetic winds and supernova events, high-mass stars formed in GMCs eventually expel heavy elements into the ISM, thus altering the chemical composition of the material which will yield new generations of molecular clouds. Stellar winds and supernovae are also believed to be the main mechanism responsible for the destruction of GMCs (e.g., Blitz & Shu 1980; Williams & McKee 1997). We see, therefore, how the balance between GMC formation and destruction is intimately connected to the evolution of baryonic matter in galaxies.

In this thesis, I address questions regarding the origin and evolution of molecular clouds.

Since the first surveys of molecular clouds over thirty years ago (Scoville & Solomon 1975; Gordon & Burton 1976; Cohen & Thaddeus 1977), a number of pertinent questions—questions indispensable to our understanding of stellar and galactic evolution—remain unresolved: *What is the dominant mechanism that forms GMCs*? *Does their formation and evolution depend more on global or local properties of a galaxy*? *How do their chemical, physical, and kinematic properties impact stellar evolution*? *What is the source of energy that keeps these massive structures from collapsing*? *How old are GMCs, and do they have observable stages of evolution*? This thesis focuses on issues raised by the first two of these interrelated questions.

In the remaining sections of this chapter, background material is given that will help to further clarify and formulate the central themes addressed in my thesis: the kinematics of individual GMCs and their global properties in low-metallicity environments. In the first two parts of §1.1, I summarize the physical and kinematic properties that most GMCs in the Milky Way and other galaxies are observed to share. I dedicate the last part of this section, §1.1.3, to describing how astronomers observe GMCs and the techniques they use to measure their properties. Though astronomers have not been able to pin down the ages of individual GMCs, a variety of methods have been used to estimate upper limits of their lifetimes. I summarize these methods and the inferred GMC ages in §1.2. Theories of GMC formation are discussed in §1.3. As we will see, the conclusions astronomers draw about the origin of GMCs depend not only on how accurately GMC properties are measured, but on how these properties are interpreted. At the end of this chapter, in §1.4, I outline the goals of my thesis and the contributions it makes towards our understanding of GMC formation and evolution.

1.1 Structure of Molecular Clouds

1.1.1 Physical Structure

Giant molecular clouds are enormous clouds of mostly molecular gas. The most common molecule in GMCs is molecular hydrogen (H_2); they also contain helium ($\sim 36\%$ by mass) and dust ($\sim 1\%$). In the Milky Way and other galaxies, these gravitationally bound, discrete structures with masses on the order of 10^4 to 10^6 $M_\odot$ (e.g., Blitz & Thaddeus 1980; Fukui et al. 1999; Engargiola et al. 2003). The mass distribution of GMCs is observed to follow a power-law of the form $\mathrm{d}N/\mathrm{d}M \propto (M/M_0)^\alpha$, where N is the number of clouds and M_0 is the upper mass limit, which is about $3 - 6 \times 10^6$ $M_\odot$ in the Galaxy (Williams & McKee 1997; Rosolowsky 2005). The index α may be depend on the galactic environment. In the Galaxy, $\alpha = -1.6 \pm 0.1$ (e.g., Williams & McKee 1997; Rosolowsky 2005; Blitz et al. 2007). In the Large Magellanic Cloud (LMC), $\alpha \approx -1.7$ and in M33, $\alpha \approx -2.5$ (Blitz et al. 2007). Integrating over these mass distributions shows that most of a galaxy's GMC mass is contained in the biggest GMCs.

The dimensions of GMCs range from 20 pc to 100 pc. Though the morphology of

GMCs is often filamentary—as is the case with the Orion A and Perseus molecular clouds, for instance (see Figure 1.1)—they are often approximated as spheres when measuring their effective radii and other properties. As we will see later on in Chapter 4, measuring the sizes of GMCs in this way can contribute to sources of error elsewhere. The mean particle density in GMCs, $n_{\mathrm{H_2}} \approx 50 - 100$ cm^{-3}, is about two orders of magnitude higher than the mean density in the ISM, $n_{\mathrm{H}} \approx 1$. Most of the mass in GMCs is contained in overdense *clumps*, which may be considered the basic building blocks of molecular clouds. Williams et al. (1995) found that in the Rosette molecular cloud, high-mass star formation seems to occur only in the few, gravitationally bound clumps. Observations of OB associations in the Milky Way show that most of these stars are embedded or have recently been embedded in GMCs (e.g., Blitz 1978, 1979).[1] In the Solar neighborhood, a number of molecular clouds contain high-mass stars, including Orion, Perseus, and Lupus.

Surrounding GMCs are envelopes of atomic hydrogen (HI) with column densities of around $N(\mathrm{HI}) \approx 2 \times 10^{20}$ cm^{-2} (McKee & Ostriker 2007). Such envelopes are inevitable since ambient ultraviolet radiation dissociates H_2 at the surface of molecular clouds. But GMCs are often associated with much more atomic hydrogen having large column densities on the order of 1.4×10^{21} cm^{-2}, corresponding to a surface density of 10 $M_\odot$ pc^{-2}. This is the saturation level of HI observed in the Milky Way and other spiral galaxies, above which most of the gas turns molecular (Martin & Kennicutt 2001; Wong & Blitz 2002; Bigiel et al. 2008). Engargiola et al. (2003) observed that GMCs in M33 are nearly always located on high-density HI filaments, though high-density HI does not always contain GMCs. This suggests that dense atomic gas is necessary but not sufficient for GMC formation.

1.1.2 Kinematic Structure

Molecular clouds generally share a set of three interrelated properties. As first pointed out by Larson (1981):

(1) The internal motions of GMCs are chaotic, or turbulent, with their internal velocity dispersions systematically increasing with cloud size. Various surveys have found that the line-sizewidth relationship for Galactic GMCs is

$$\Delta v \propto R^{0.5 \pm 0.1}, \tag{1.1}$$

where Δv is the velocity dispersion and R is the effective radius of a molecular cloud (e.g., Sanders et al. 1985; Dame et al. 1986; Solomon et al. 1987). This relationship exists on wide range of size scales in the ISM and seems to have no preferred length-scale, which is a signature of "turbulent" motion.

(2) GMCs are in approximate virial equilibrium; in other words, the gravitational potential energy of GMCs is roughly in balance with twice the total kinetic energy,

$$\frac{GM^2}{R} \approx M \Delta v^2, \tag{1.2}$$

[1] OB associations are groups of young, massive stars. They are named after O stars and B stars, which, because of their high masses, burn out their store of hydrogen faster than low-mass stars.

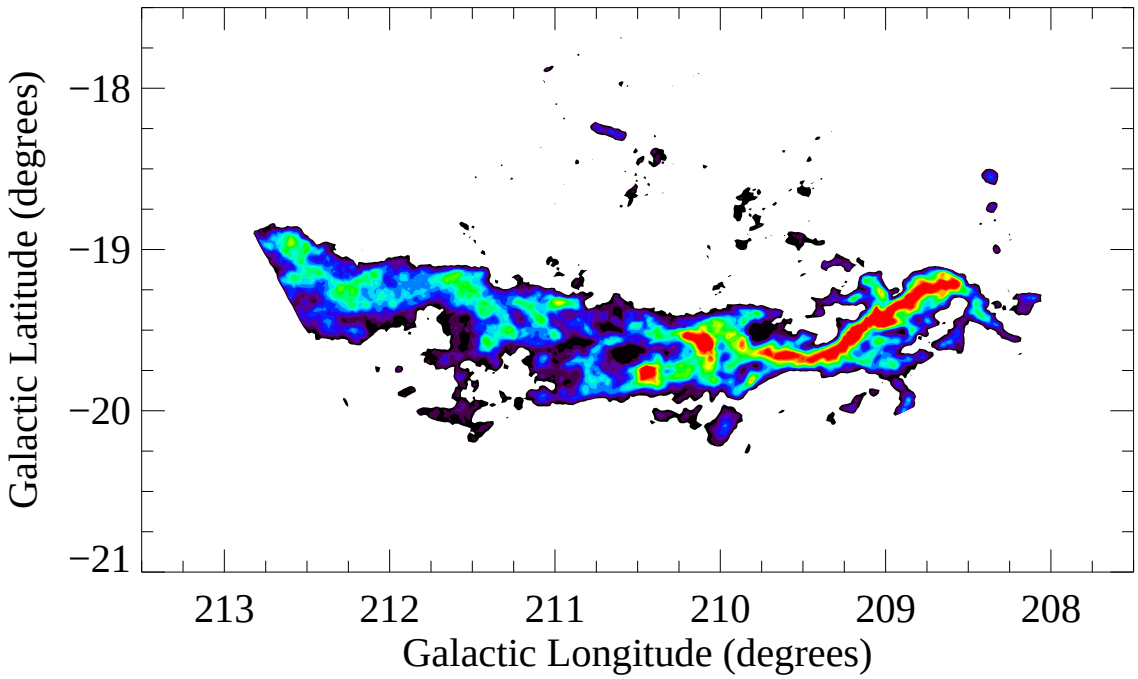

Figure 1.1: The Orion A molecular cloud mapped in ^{13}CO emission. The scale ranges from 10 K km s^{-1} (dark blue) to 100 K km s^{-1} (red).

where G is the gravitational constant and M is the cloud mass. This observation, that molecular clouds tend to have masses that are much larger than their Jeans masses, has traditionally been interpreted to mean that at least parts of GMCs are gravitationally bound (e.g., Larson 1981; Blitz 1993). We will see later on in §1.3, however, that this is not a unique interpretation. Moreover, this second "law" is not airtight in its own right; low-mass clouds ($< 10^3$ $M_\odot$) have been observed to be non-self-gravitating (e.g., Maloney 1990; Heyer et al. 2001). Heyer et al. (2001) concluded that clouds having masses less than $\sim 10^3$ $M_\odot$ in the outer Galaxy are not gravitationally bound. Furthermore, determining whether a GMC is virialized requires assumptions about its size, R, as well as the morphology of the cloud that may not always be accurate.

(3) Molecular clouds have roughly constant column densities. This result follows from the first two laws: $M \sim R^2$. In the Galaxy, GMCs have surface densities around 100 $M_\odot$ pc^{-2} (e.g., Blitz 1993). Rosolowsky et al. (2003) found that molecular clouds in M33 have a surface density of roughly 120 $M_\odot$ pc^{-2}.

An important implication of Larson's laws is that because GMCs having comparable masses share the same large-scale properties, Δv, R, and $N(\mathrm{H_2})$, they may be formed by a common mechanism that is coupled primarily to their mass. Also significant is that Larson's laws are observed to hold in other Local Group galaxies, including the LMC (Mizuno et al. 2001) and M33 (Rosolowsky et al. 2003).

In addition to their internal chaotic motions, GMCs appear to have systematic, ordered motions. Molecular line observations (see §1.1.3 below) have shown that the velocity fields of GMCs are sometimes characterized by large-scale linear gradients. Since solid-body rotation is characterized by $v \propto R$, many authors have argued that the gradients in Galactic molecular clouds may be caused by large-scale cloud rotation (e.g., Kutner et al. 1977; Blitz 1993; Phillips 1999). For instance, the Orion A molecular cloud, which lies parallel to the the Galactic plane, has a velocity gradient that decreases from about 12 km s^{-1} to 3 km s^{-1} with increasing Galactic latitude (e.g., Kutner et al. 1977; Bally et al. 1987). The magnitude of the gradient, ~ 0.2 km s^{-1} pc^{-1} (Imara & Blitz 2010), corresponds to a rotation period of about 30 Myr. The typical gradient observed in most other Galactic GMCs is much smaller, ~ 0.05 km s^{-1} pc^{-1} (e.g., Blitz 1993; Phillips 1999; Imara & Blitz 2010), corresponding to a rotation period of 130 Myr. It is not expected that rotation will have a large impact on GMC evolution since, as we will see in §1.2, the typical rotation period is much longer than the expected lifetimes of GMCs, about 20 – 40 Myr. Moreover, the rotational energy of GMCs (if they are rotating) is just a small fraction of their gravitational energy and turbulent energy. Therefore, cloud rotation is not able to inhibit GMCs from undergoing self-gravitational collapse, for instance.

Although the energetics and dynamics of observed GMCs are not dominated by their large-scale coherent motions, the velocity gradients in GMCs can reveal a great deal about their evolution: understanding the origins of the gradients can give us insight into the origin of GMCs themselves and/or about how star formation proceeds. If rotation is inherited during the formation of GMCs, then Galactic differential rotation is one likely source of angular momentum initially imparted to a cloud. But if gradients arise *after* GMCs are formed, this

could have different implications for GMC and stellar evolution. For instance, gradients may be produced by whatever mechanism causes star formation in molecular clouds. Kutner et al. (1977) discussed how a large-scale disturbance, such as a density wave passing through a GMC, might both produce a velocity gradient in the GMC and trigger star formation. Alternatively, star formation activity itself may generate gradients. Bally et al. (1987) proposed that the gradient in Orion A is the result of an expanding superbubble driven by the Orion A OB association.

When I first discovered for myself the possibility that the gradients observed in GMCs are due to rotation—that rotation may have been present since they formed—this interested me because I thought conservation of angular momentum could be used to extrapolate to the initial conditions required for GMC formation. I soon ran into the "angular momentum problem," however, a phenomenon that has challenged astronomers in many areas of astrophysics. The problem is this: if GMCs inherit their rotation from the interstellar medium during formation, they have *much less* angular momentum than is implied by Galactic rotation. Therefore, the reasoning goes, a mechanism must exist which can "shed" or redistribute angular momentum from GMCs into the surrounding ISM as they form (e.g., Mouschovias & Paleologou; Mestel & Paris 1984; Blitz 1993; Rosolowsky et al. 2003).

The angular momentum problem also exists outside of the Milky Way. Rosolowsky et al. (2003) did the first study of the angular momentum distribution of extragalactic GMCs in M33 and found that they have linear velocity gradients consistent with rotation and having magnitudes comparable to those of Milky Way GMCs. Rosolowsky et al. also found that roughly 40% of the 45 GMCs in their catalog have gradients that differ from the direction of galactic rotation by more than 90° (Figure 1.2). If the gradients are due to rotation, this implies that 40% of the molecular clouds are counterrotating with respect to M33. This phenomenon has also been observed in the Milky Way—in Orion A, for instance (Kutner et al. 1977; Bally et al. 1987)—and will have to be explained by any reasonable theory of GMC formation.

Magnetic braking is the mechanism that some astronomers have invoked as a solution to the angular momentum problem. Given that that the ISM in general and molecular clouds in particular are observed to be magnetized (e.g., Crutcher 1999; Heiles & Troland 2005), astronomers have long been trying to understand the influence of magnetic fields in the various stages of GMC and stellar evolution. Mestel & Spitzer (1956) first suggested magnetic braking as a viable way of slowing down cloud rotation. In this picture, the rotating cloud is coupled to the ISM by a frozen-in magnetic field. The field lines twist as the cloud rotates, and angular momentum is transported away from the cloud along the field lines.

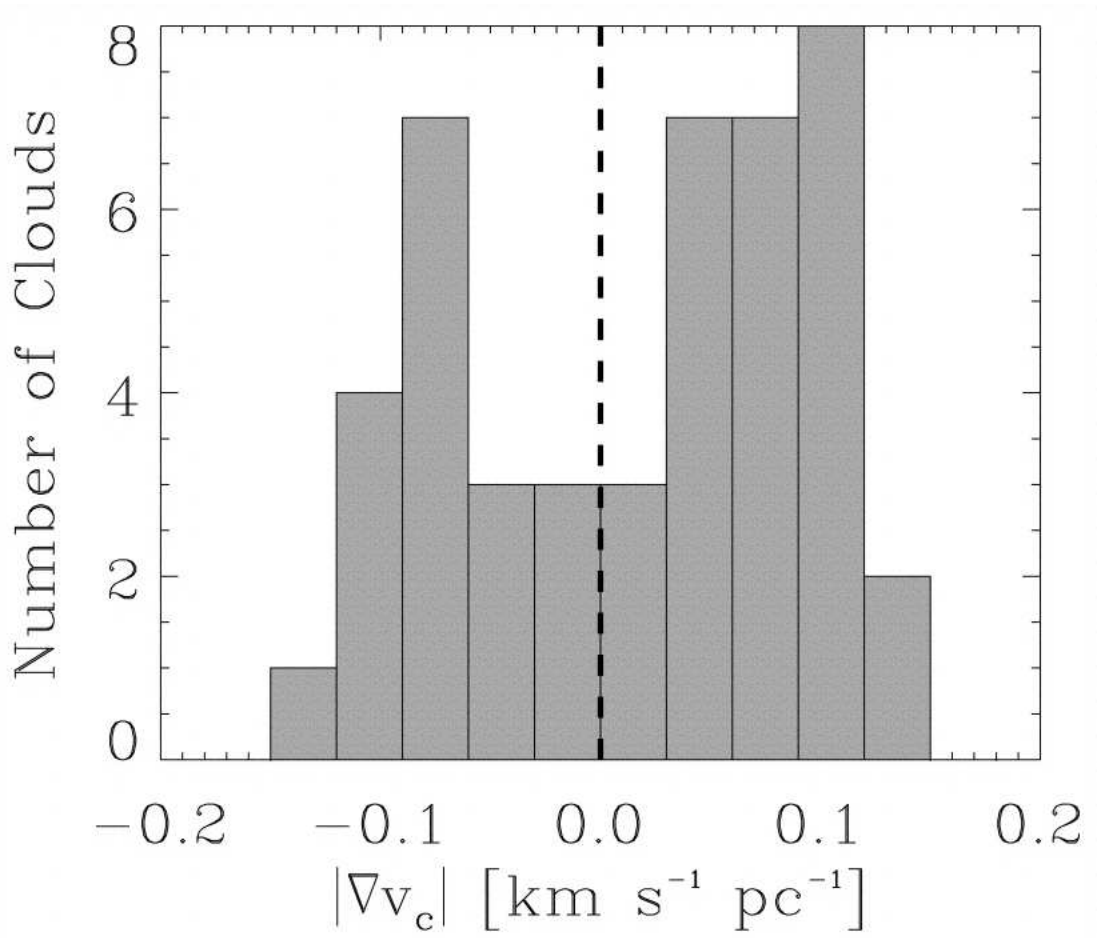

Figure 1.2: Gradient magnitudes of giant molecular clouds in M33. Gradients of GMCs with gradient position angles differing from the galactic kinematic position angle by more than 90° are given negative values. If the gradients are due to rotation, then $\sim 40\%$ of GMCs are counterrotating with respect to the galaxy. *Image credit: Rosolowsky et al. (2003).*

Upon finding out about magnetic braking, I began researching the possible observational consequences...and I soon became dissatisfied with what I found. Mouschovias & Paleologou (1979) provided some of the only concrete expectations of magnetic braking that I found in the literature. They predicted that (i) magnetic braking is efficient in that it may be able to slow cloud rotation by at least an order of magnitude within a few million years; (ii) magnetic braking should bring the surrounding ISM into corotation with a contracting, rotating molecular cloud; and (iii) the energy released during magnetic braking may produce high energy cosmic rays. I realized I could test the second of these predictions observationally but that even this would not definitively rule in or rule out the existence of magnetic braking. It turns out that the braking efficiency depends on a number of factors that are difficult to confirm observationally; for instance, the magnetic field must be oriented at a large angle with respect to the spin axis of the rotating cloud. I also learned that it may be very difficult to determine if there exists an excess of cosmic rays toward molecular clouds that can be attributed solely to braking. This is partly because most of the directional information that could be used to determine the origin of cosmic rays is lost, since they travel along magnetic field lines, and since they are affected by the solar magnetosphere.

1.1.3 Measuring GMC Properties

Most of what we know about molecular cloud properties has been deduced from radio observations of their molecular emission. Since the dominant constituent of GMCs, molecular hydrogen, is undetectable at the low temperatures ($\sim$ 10 K) of molecular clouds, other *tracers* must be used to infer the quantity and distribution of molecular gas in GMCs.[2] The most common molecular tracers are carbon monoxide (CO) and its isotopes. Though there is only one CO molecule for every $\sim 12,500$ H_2 molecules in a GMC, its strong emission at a wavelength of 2.6-mm makes it easy to detect. Spectral line observations of CO provide spatial and kinematic information from which we can infer fundamental properties of molecular clouds, including column density, mass, area, and velocity. The rarer isotopes (e.g., ^{13}CO and ^{12}C^{18}O), because they are optically thin, are often used to observe the detailed structure and internal dynamics of GMCs.

The X-Factor

To determine the amount of molecular gas from CO emission, an empirical scaling from the CO integrated intensity, $I_{\rm CO}$, to the H_2 column density is needed. This is the definition of the X-factor:

[2]Molecules can make transitions into different energy states in three different ways: electronic, vibrational, and rotational transitions. The temperatures of molecular clouds correspond to line radiation in the cm and mm wavelength range of the electromagnetic spectrum; at these wavelengths (i.e., energies) only rotational transitions are possible. However, rotational transitions only occur for molecules that have a permanent dipole moment, which H_2, a homonuclear diatomic molecule, does not.

$$X \equiv \frac{N(\mathrm{H_2})/\mathrm{cm^{-2}}}{I_{\mathrm{CO}}/\mathrm{K\ km\ s^{-1}}}. \tag{1.3}$$

One technique used to determine X is to assume a GMC is virialized and then infer the H_2 column density from its virial mass, M_{vir}, and projected surface area. Solomon et al. (1987) demonstrated that M_{vir} is proportional to L_{CO}, the CO luminosity over a cloud's surface. Once M_{vir} is calculated from L_{CO}, it is possible to derive $N(\mathrm{H_2})$, which is proportional to the mass integrated over the area of the cloud. This technique has its drawbacks, however. First of all, it assumes that X is independent of metallicity. It also assumes that virialization applies, though, as we have seen, only the more massive GMCs are virialized. For low-mass molecular clouds, which may be pressure-bound but not virialized, M_{vir} overestimates the clouds' actual masses, leading to an overestimate of X. Furthermore, astronomers have often approximated GMCs as spheres in order to estimate R, whereas observations show that these structures are often filamentary.

In spite of these disadvantages, the method of assuming GMCs are virialized to infer X is given some justification by the fact that most molecular mass in the Galaxy is locked up in the most massive GMCs. Also, in the Milky Way, different techniques used to infer $N(\mathrm{H_2})$ have consistently given $X_{\mathrm{MW}} \approx 2 - 3 \times 10^{20}$ cm^{-2} (K km s^{-1})$^{-1}$ (e.g., Strong & Mattox 1996; Dame et al. 2001; Blitz et. al 2007).[3] Nevertheless, determining molecular cloud masses independently of CO observations is desirable, especially in other galaxies where X is expected to vary depending on the environment. Comparing the oxygen abundance to the X-factor in five Local Group galaxies, Wilson (1995) found that X increases with average metallicity of the galaxy.[4] These observations are in keeping with expectation. The consequences of lower metallicity for GMCs are (1) less CO and (2) less dust, relative to higher metallicity environments. Thus, in systems having low metallicity relative to the Galaxy, the less abundant CO is expected to be more susceptible to photo-dissociation by UV radiation (e.g., McKee 1989), which can penetrate more deeply into the less-dusty molecular clouds. In such environments, molecular material will go untraced by CO observations in locations—such as the boundaries of molecular clouds—where there is H_2 but little CO.

We can see, therefore, why X in the Milky Way is not expected to be applicable to low-metallicity dwarf galaxies like the Large and Small Magellanic Clouds. As we will see in Chapter 4, these galaxies offer excellent opportunities to test how X varies with galactic

[3]Two techniques that I will not detail here include the following: Observations of γ-rays, which are produced from collisions between cosmic rays and atomic nuclei, can be used to determine the total column density of hydrogen toward a molecular cloud. Subtracting the contribution due to atomic hydrogen yields $N(\mathrm{H_2})$, which can then be compared to I_{CO} in the same molecular cloud to measure X. Observations of far-infrared dust emission, which is also proportional to the total gas column density, have also been used to determine X.

[4]The metallicity of a galaxy refers to the amount of heavy elements (i.e., elements heavier than helium) comprising its interstellar medium. Each generation of star formation is expected to increase the metallicity of the ISM, since it is the high mass stars that expel most of the heavy elements (e.g., carbon, oxygen, nickel, iron) into the ISM towards the end of their lifetimes on the main sequence. Metallicity, therefore, is also an indicator of a galaxy's evolutionary stage.

environment, with the main goal being to measure GMC properties as accurately as possible and learn how their properties may vary from environment to environment.

Extinction mapping is an alternative method for inferring the distribution of molecular gas that exploits the fact that GMCs are dusty. GMCs are always associated with dust because dust grains are catalysts for H_2 formation. This is because H_2 formation on the surface of dust grains is far more efficient than other types of three-body collisions that occur in GMCs.[5] Also, dust associated with a GMC protects the molecules from the ambient UV radiation field, which is capable of destroying molecules by photo-dissociation.

As starlight travels to us through a molecular cloud, it is dimmed (i.e., extincted) and reddened by intervening dust. This phenomenon is wavelength-dependent; light having longer wavelengths undergoes less extinction than does light having shorter wavelengths. Figure 1.3 shows images taken at different wavelengths of the Bok globule Barnard 68 in Ophiuchus.[6] At 0.44 μm, (between violet and blue light), we see a dark patch because practically all the light at this wavelength is extinguished by the dust in the globule. More and more background light makes it through the globule at progressively longer wavelengths. The last three images on the bottom, from left to right, are taken in the J, H, and K near-infrared bands. In the Galaxy, light in the K-band undergoes about ten times less extinction than does visible light.

Infrared detectors, such as the those used in the Two Micron All-Sky Survey (2MASS), allow simultaneous observations of hundreds of sources in multiple wavelength bands. They are ideal for probing deep into the structure of molecular clouds, since molecular clouds are nearly transparent to infrared light.

A star's color is the difference between its magnitudes at two different wavelengths. Consider a star, situated behind a molecular cloud, with a known intrinsic color, which is determined primarily by its temperature. By comparing its intrinsic color to the color observed through the molecular cloud, one can measure the extinction that has occurred along a line-of-sight toward the molecular cloud. This can be done for many lines-of-sight through the cloud to create a map of the dust distribution, which is proportional to the total hydrogen column density $N(\mathrm{H})$ (see Figure 1.4). The gas-to-dust ratio in the Milky Way is

$$\frac{N(\mathrm{H})}{A_\mathrm{V}} = 1.87 \times 10^{21}\ \mathrm{mag}^{-1}\ \mathrm{cm}^{-2}, \tag{1.4}$$

where A_V is the amount of extinction in visible light (Bohlin et al. 1978). This ratio is found to be roughly constant in the Milky Way, though A_V does depend on the properties of dust grains in clouds. The H_2 column density is finally determined by subtracting the contribution due to atomic hydrogen from the total:

$$N(\mathrm{H}) = N(\mathrm{HI}) + 2N(\mathrm{H_2}). \tag{1.5}$$

[5] At the cold temperatures ($\sim$ 10 K) of GMCs, molecular hydrogen cannot form by two-body collisions.

[6] Bok globules are dense regions of gas and dust not embedded in molecular clouds.

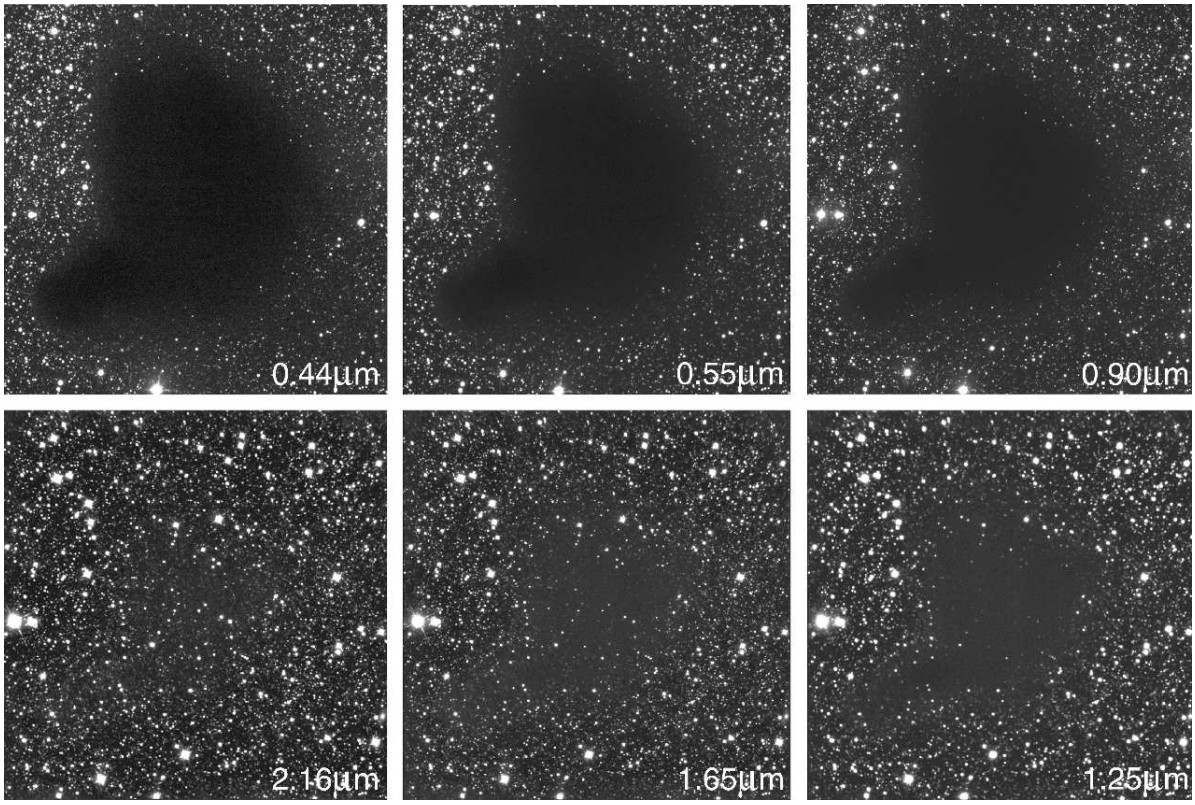

Figure 1.3: The Bok globule Barnard 68 imaged in optical (BVI) and near-infrared (JHK_s) photometry obtained with the European Southern Observatory's Very Large Telescope and New Technology Telescope. The images demonstrate how dust becomes increasingly transparent with increasing wavelength. *Image credit: Alves et al. (2001).*

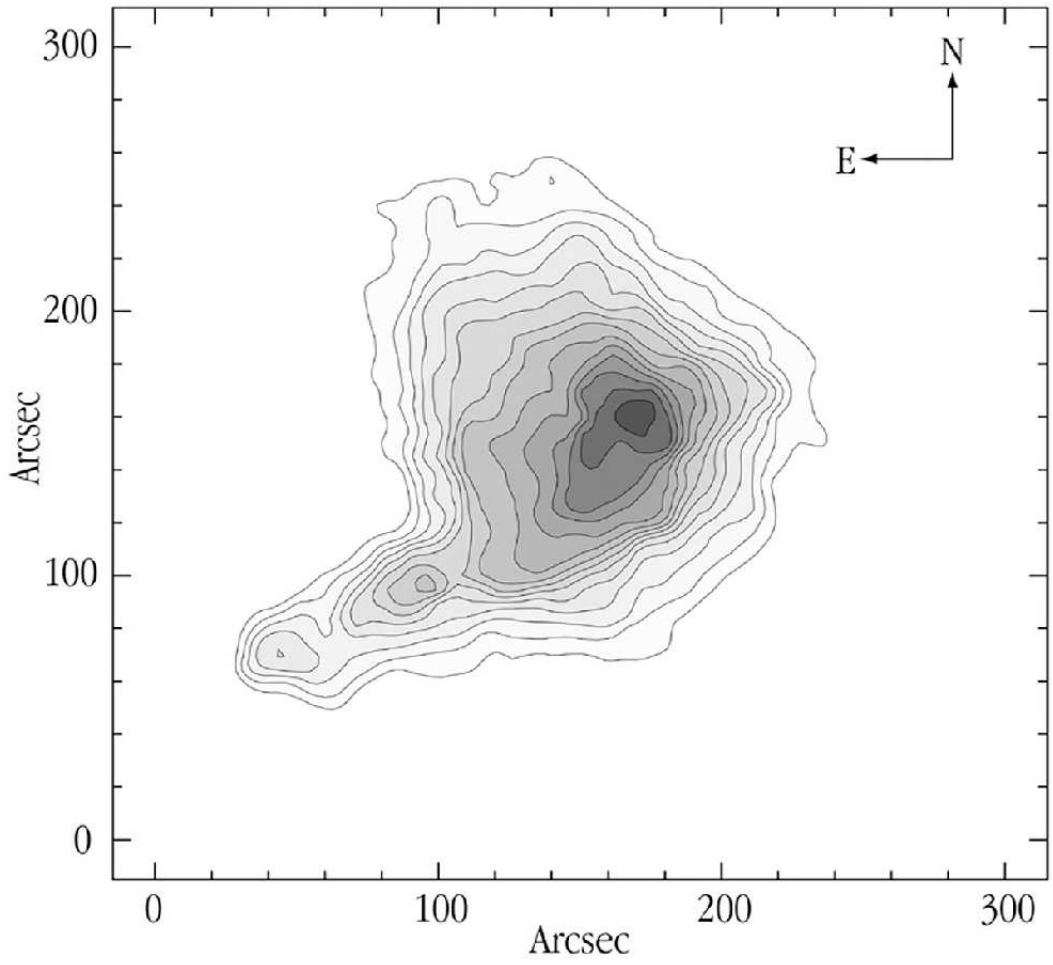

Figure 1.4: Barnard 68: Distribution of extinction due to dust as determined from near-infrared measurements. The distribution of H_2 can be derived from this map since extinction is proportional to the total hydrogen column density and there is little associated atomic gas. *Image credit: Lada et al. (2007).*

The advantage of using extinction mapping to determine the quantity of H_2 is that no assumptions need to be made regarding the virialization or the shapes of molecular clouds—direct comparisons of $N(H_2)$ and I_{CO} can be made along each line-of-sight. More importantly, extinction mapping is capable of detecting H_2 in regions where CO is undetectable, either because CO does not exist or because CO observations are not sensitive enough. One of the main drawbacks of this method is that a constant gas-to-dust ratio must be assumed, although A_V depends on the properties of interstellar dust grains. In Chapter 4 of my thesis, I will describe this technique in further detail and describe the challenges I had to overcome when applying it to an extragalactic system.

1.2 Ages of Giant Molecular Clouds

As I got deeper into my research, I was eventually led to the question: is there a way to determine the ages of molecular clouds? I wanted to know if GMCs have any observable markers indicating their evolutionary stage. Does a GMC's age manifest itself in terms of the level of star formation activity? Is age manifest in its morphology, its chemical composition, or its dynamical state? These questions are very closely connected to the question of how GMCs originate. Understanding how GMCs form and evolve is also fundamental to our understanding of star formation.

I soon learned that astronomers have been tackling the issue of GMC ages for decades. Early on, certain groups argued that GMCs are long-lived ($> 10^8$ years; Scoville & Hersh 1979; Solomon & Sanders 1979). This argument was mainly based on the *seemingly* high ratio of molecular to atomic gas in the molecular ring of the Galaxy. However, Blitz & Shu (1980), using a revised and lowered estimate of the X-factor to determine the H_2 mass, demonstrated that the H_2-to-HI ratio is much lower than previously estimated. Since the seventies, much of the evidence that has built up seems to indicate that GMCs are relatively short-lived structures:

- Blitz (1978, 1979) found that most OB stars are associated with GMCs. Processes associated with massive star formation—such as stellar winds, the expansion of HII regions, and supernova explosions—are are energetic enough to destroy GMCs. Blitz & Shu (1980) estimated that HII regions could disperse a GMC in < 30 Myr. They noted that if GMCs were long-lived, we might expect to observe them just as frequently between spiral arms *without* high-mass stars, which we do not. GMCs are generally distributed along the spiral arms and their positions are highly correlated with HII regions.

- Bash et al. (1977) observed that Galactic GMCs are usually found in the vicinity of stellar clusters having ages no greater than 30 Myr. At the time, GMCs without star formation had not been observed. So it was reasoned that GMCs must have ages at least as old as the stars which formed from them.

- In an update of the Bash et al. (1977) study, Leisawitz et al. (1989) found that GMC masses tend to decreases as the ages of open clusters with which they are associated

increases. The maximum age of associated clusters, $\sim$ 50 Myr, sets another upper limit on GMC ages.

- The dense clumps in which most of a GMC's mass is concentrated move at speeds of several km s^{-1}, faster than the sound speed within clumps (e.g., Blitz 1978; Williams et al. 1994). This means that clumps will tend to merge as they undergo inelastic collisions. Blitz & Shu (1980) deduced that the average timescale for collision between clumps, $\sim$ 10 Myr, and argued that GMCs could not maintain their clumpy structure for more than a few collision times.

- For the LMC, Blitz et al. (2007) compared the locations of GMCs to clusters and HII regions to estimate a typical GMC lifetime of roughly 27 Myr, with a phase devoid of star formation lasting about 1/4 of their age. Applying the same method in M33, Blitz et al. (2007) found that GMCs have an average age of 20 Myr, with a quiescent phase lasting $\sim$ 1/3 of their age.

1.3 Formation Theories

Giant molecular clouds may form by a "bottom-up" mechanism or from a large-scale "top-down" instability. In the first case, it has been proposed that GMCs are built up by the random coalescence of smaller clouds (e.g., Kwan 1979; Scoville & Hersh 1979; Norman & Silk 1980). However, as shown by Blitz & Shu (1980), the 200 Myr or longer it would take for GMCs to grow to their observed masses in this scenario is much longer than the time it would take for GMCs to be dispersed by star formation activity. This is not to say that agglomeration does not play a role in GMC formation, but that *random* agglomeration is unlikely to be the principal way that a GMC accumulates mass. In the spiral arms of the Galaxy, density waves may increase the collision rate of small clouds behind shocks (Bally 2001).

A number of formation mechanisms fall under the "top-down" category, in which atomic or molecular gas collapses or condenses from a large region. The Parker instability has been advanced as one such possible mechanism for GMC formation (e.g., Mouschovias et al. 1974; Blitz & Shu 1980; Shibata & Matsumoto 1991). The instability arises when magnetic field lines, unstable to long-wavelength perturbations, in an external gravitational field "buckle." Interstellar gas frozen to the field lines slides down the field lines into the valleys, accumulating until sufficiently high densities are attained for the formation of molecular clouds. This magnetohydrodynamic (MHD) instability is attractive because is has time scales comparable to the estimates of GMC lifetimes, and it also seems to explain the excess of atomic hydrogen with which molecular clouds are associated (e.g., Shu & Blitz 1980).

However, Rosolowsky et al. (2003) found that the Parker instability overestimates the magnitudes of GMC velocity gradients (Figure 1.5). Furthermore, MHD simulations have shown that the Parker instability is stabilized at moderate densities by magnetic tension forces (e.g., Kim et al. 1998; Santillán et al. 2000; Kim et al. 2002). Kim et al. (2002)

point out that self-gravitating instabilities (i.e., Jeans instabilities) progress more rapidly than other mechanisms and that the growth rates increase with surface density. They rule out the Parker instability as the dominant mechanism responsible for GMC formation, in favor of a magneto-Jeans instability (MJI).

Large-scale colliding flows have also been proposed as a way of forming GMCs (e.g., Chernin et al. 1995; Vazquez-Semadeni et al. 1995; Ballesteros-Paredes et al. 1999; Heitsch et al. 2005). In this case, converging flows of atomic gas supersonically collide, and the resulting shock waves isothermally compress the ISM into regions that become sufficiently dense for molecular clouds to form. This model is motivated by interpretations of GMC properties that differ from some of the traditionally held views. In particular, in this scheme, GMCs are transient and are not necessarily in equilibrium. The observation that GMCs have pressures in excess of the pressure of the surrounding ISM has traditionally been interpreted to mean that GMCs must be self-gravitating (e.g., Blitz 1993). However, proponents of GMC formation by converging flows argue that this excess pressure arises naturally at the interface where the colliding material compresses (Vazquez-Semadeni et al. 1995; Ballesteros-Paredes et al. 1999). One of the main shortcomings of this model is that the timescale for H_2 formation is somewhat long, $\sim$ 30 Myr, compared to the upper limits of GMC ages (Ballesteros-Paredes et al. 1999). Furthermore, though this scenario offers an explanation for how turbulence is initiated in GMCs, it does not explain how turbulence is sustained over the lifetimes of GMCs, and it tends to underestimate the surface densities typically observed in Galactic GMCs (McKee & Ostriker 2007).

It has also been proposed that GMCs can be produced in the gravitational instabilities that arise in supershells driven by OB associations (McCray & Kafatos; Elmegreen 1994; Bally 2001). Yet another possibility is that GMCs condense out of the turbulent ISM. Wada et al. (2000) investigated the the development of non-linear perturbations in LMC-like conditions and found that turbulence could produce the filamentary structures similar to those observed in the LMC.

The reality may be that a number of processes conspire to produce molecular clouds and that different processes dominate depending on the galaxy and the environment. Yet, there may be one factor, common to many galaxies, that regulates the amount of gas in the molecular form. Many authors have argued that pressure is the main parameter that determines the molecular fraction in galaxies (e.g., Spergel & Blitz 1992, Elmegreen 1993; Wong & Blitz 2002). For seven molecule-rich galaxies, Wong & Blitz (2002) showed that the molecular fraction and midplane hydrostatic pressure follow a power-law relationship ($\Sigma_{H_2}/\Sigma_{HI} \propto P^{0.8}$). Following this work, Blitz & Rosolowsky (2004) investigated the molecular fraction-pressure relationship in 28 additional galaxies and found that pressure appears to be the most important parameter regulating the ratio of molecular to atomic gas at a given location. Later, for 14 galaxies, including one low-metallicity dwarf, Blitz & Rosolowsky (2006) found that $\Sigma_{H_2}/\Sigma_{HI} \propto P^{0.92}$ for over two orders of magnitude in pressure. The significance of these studies is that they enable us to determine global star formation rates—which depend on the rates of GMC formation and destruction—in galaxies without knowing the specifics of how gas is collected into GMCs.

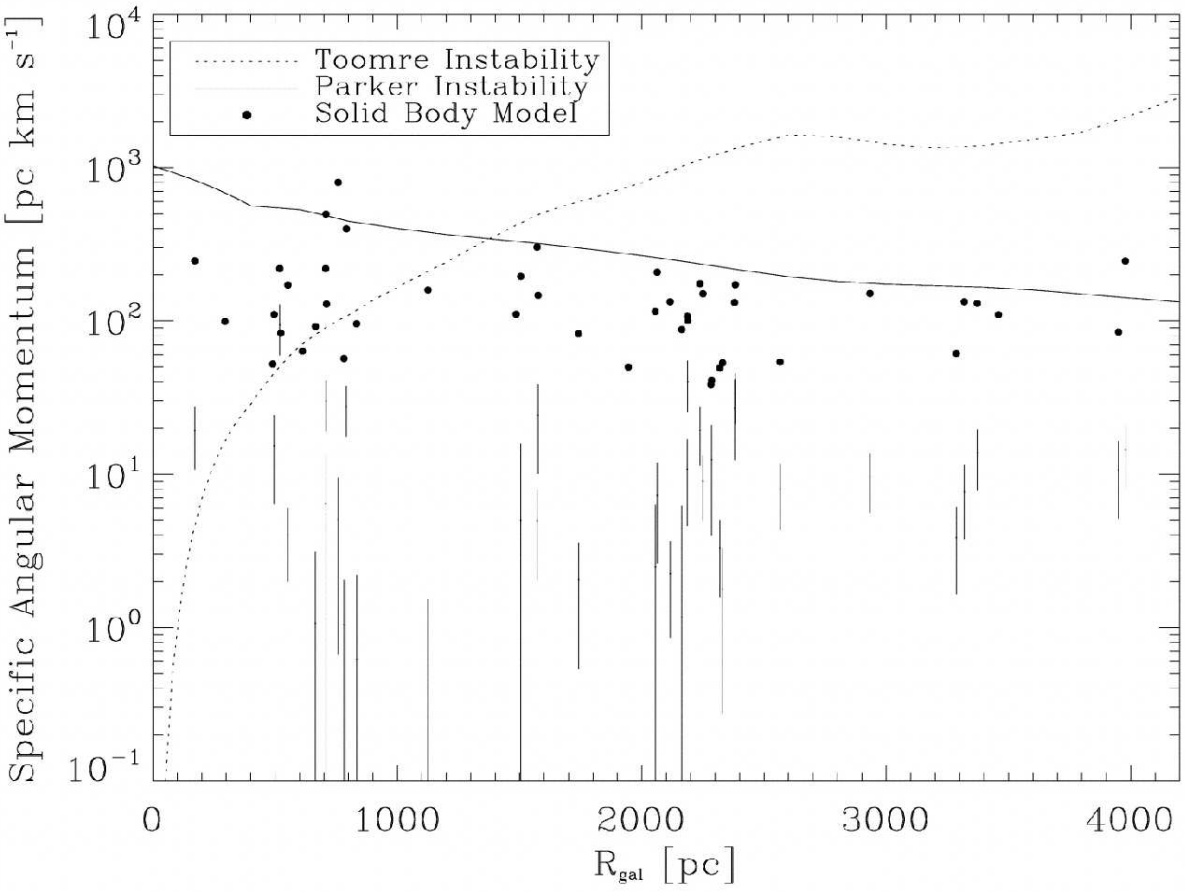

Figure 1.5: The specific angular momentum (j) as a function of galactic radius in M33. The measurements of the GMCs are indicated by ± 1-σ error bars. The dotted and solid lines indicate j initially imparted to GMCs as predicted by the Toomre and Parker instabilities. The circles indicate j initially imparted in a model which includes projection effects and assumes that GMCs are solid-body rotators. In each of these simple "top-down" formation theories, the initial j is systematically larger than that observed in GMCs. *Image credit: Rosolowsky et al. (2003).*

1.4 This Thesis

My research for the past several years has focused on the kinematic properties of GMCs and on their characteristics in low-metallicity environments. When I encountered the angular momentum problem discussed in §1.1.2, I saw this as an opening toward developing our understanding of GMC evolution. As I researched this subject, I came to the idea that perhaps we should make sure we have accounted for all of the angular momentum before we invoke mechanisms to explain away the discrepancy between the predicted and observed angular momenta in molecular clouds. I began to ask: *How does the large-scale rotation of GMCs compare with the motion of the atomic hydrogen with which they are associated and from which they presumably form? How does GMC rotation compare to the motion of the hundreds of clumps inside of them?* And as I reviewed the literature to find out if and how others had addressed these questions, I learned that a systematic study of the angular momentum distribution amongst Galactic GMCs had never been done (Blitz 1993). These were the main factors that led to the work I present in the next two chapters of this thesis.

In Chapter 2, I present a detailed analysis of the kinematic properties of Galactic molecular clouds and the atomic gas with which they are associated.[7] The primary aim of this study is to test whether the kinematic features observed in GMCs are in agreement with current formation theories. Using high-resolution ^{13}CO observations of five molecular clouds in the Milky Way, I created intensity-weighted velocity maps from which I then measured gradient properties of the GMCs. Most previous studies estimated gradients in molecular clouds by taking a single slice through the data cube and measuring the slope of a plot of velocity versus distance in the map from the axis of constant velocity (e.g., Kutner et al. 1977; Bally et al. 1987; Williams et al. 1995). In my work, I applied the method of Goodman et al. (1993), which enables one to evaluate all of the points in a data cube simultaneously to determine a best fit to the gradient magnitude and direction.[8] For each GMC, I fit a planar function to the velocity field using least-squares to solve for the coefficients, which define the maximum gradient magnitude and direction of the cloud.

I used the same method to measure the kinematic properties of atomic gas associated with the molecular clouds. I created the HI velocity maps using data from the Leiden/Argentine/Bonn (LAB) Galactic HI survey (Kalberla et al. 2005) whose high sensitivity is presently unsurpassed. In order to select the HI associated with the GMCs, I developed a set of criteria based on the spatial and kinematic correspondence of the atomic and molecular gas. The first chief result of this chapter is that if GMCs are rotating, their angular momentum is always less than that in the local atomic gas. By itself, this result is consistent with the picture of top-down formation, but one must necessarily introduce some mechanism capable of redistributing angular momentum in order to explain the discrepancies in the atomic and molecular gas. The second key result is that—with one exception—I observed large differences in the gradient directions of the molecular and atomic gas. If the gradients

[7] Chapter 2 has been submitted for publication as Imara & Blitz 2010.

[8] Goodman et al. (1993) applied this technique to the cores within molecular clouds.

are due to rotation, this suggests that the kinematic properties presently observed in GMCs are not characteristic of those in the atomic gas from which they presumably formed. These two results are difficult to explain in the framework in which GMCs form by a top-down instability.

In Chapter 3, I present a continuation of the angular momentum study on a much larger sample of GMCs in M33 cataloged by Rosolowsky et al. (2003).[9] Because M33 has a moderate inclination ($\sim 51°$; Corbelli & Salucci 2001), I was able to bypass the problem of source confusion, a problem and source of error that arises when making observations through the Galactic disk. The HI observations in this case came from the VLA archives (Thilker et al. 2002). A main contribution of this study, as with the Milky Way study, is that the comparisons between the velocity fields of the molecular and atomic gas were made directly from observation. In previous analyses (e.g., Blitz 1993; Rosolowsky 2003), the gradients and angular momenta of the molecular clouds were compared to the local values inferred from the galactic rotation curve. Actual measured values typically have larger gradient magnitudes than inferred from the rotation curve. The results of this chapter are consistent with those in the Milky Way. Additional findings include the observation that the local surface density of atomic gas slowly increases with GMC mass. Also, I measured the properties of a population of overdense atomic hydrogen in which GMCs have *not* been observed and found that this group generally has smaller gradients (~ 0.03 km s^{-1} pc^{-1}) than does the HI associated with molecular clouds (~ 0.05 km s^{-1} pc^{-1}).

Chapter 4 investigates how GMC properties are influenced by their environment.[10] The Large Magellanic Cloud, one of the closest dwarf galaxies to us, has a low-metallicity environment with respect to the Milky Way in that it has a lower fraction of heavy elements and a higher gas-to-dust ratio. Thus, it provides an excellent laboratory for exploring how GMC evolution may have taken place in the early Universe. The quantity and distribution of H_2 are properties of fundamental importance for our understanding of star formation, and the integrity of the conclusions we draw obviously depends on the accuracy of our measurements. Cohen et al. (1988) completed the first complete survey of the LMC in ^{12}CO and, more recently, Mizuno et al. (2001) created the first complete catalog of extragalactic GMCs in their high-resolution (~ 40 pc) CO survey of the same galaxy. Both groups estimated the X-factor: Cohen et al., by comparing the luminosity of LMC molecular clouds with the luminosity of Milky Way clouds; and Mizuno et al., by assuming that LMC GMCs are virialized.

The research presented in Chapter 4 is motivated by the expectation that CO observations of GMCs in low-metallicity environments may not account for all the molecular emission, and assuming GMCs are virialized to calculate the X-factor may not be appropriate. Near-infrared photometry is used to create an extinction map of the LMC and to infer the X-factor independent of assumptions about virialization. This map was the first published extinction map of an extragalactic system created using the near-infrared color excess

[9] Chapter 3 has been submitted for publication as Imara, Bigiel & Blitz 2010.

[10] Chapter 4 has been publishedas Imara & Blitz 2007.

method. Two of the biggest challenges of this work were foreground contamination and the low signal-to-noise of individual measurements. I had to find creative ways of dealing with a large foreground population of point sources—a problem which is not as much of an issue when this method is applied to nearby Galactic sources. I found that the LMC has a mean visual extinction of 0.38 mag and an X-factor that is nearly 5 times the Milky Way value. I also observed extended H_2 emission across the face of the galaxy that was not detected by CO observations.

Chapter 5 provides a summary of my thesis. I make some concluding remarks and provide suggestions for future work that may advance our understanding of GMC formation and evolution.

Chapter 2

Angular Momentum in Local Giant Molecular Clouds

Abstract

We present a detailed analysis comparing the velocity fields in molecular clouds *and* the atomic gas that surrounds them in order to address the origin of the gradients. To that end, we present first-moment intensity-weighted velocity maps of the molecular clouds and surrounding atomic gas. The maps are made from high-resolution ^{13}CO observations and 21-cm observations from the Leiden/Argentine/Bonn Galactic HI Survey. We find that (i) the atomic gas associated with each molecular cloud has a substantial velocity gradient—ranging within 0.02 to 0.07 km s^{-1} pc^{-1}—whether or not the molecular cloud itself has a substantial linear gradient. (ii) If the gradients in the molecular and atomic gas were due to rotation, this would imply that the molecular clouds have less specific angular momentum than the surrounding HI by a factor of 1 – 6. (iii) Most importantly, the velocity gradient position angles in the molecular and atomic gas are generally widely separated—by as much as 130° in the case of the Rosette Molecular Cloud. This result argues against the hypothesis that molecular clouds formed by simple top-down collapse from atomic gas.

2.1 Introduction

Giant molecular clouds, both Galactic and extragalactic, are observed to have velocity gradients that many authors have interpreted as being caused by rotation (e.g., Kutner et al. 1977, Phillips 1999; Rosolowsky et al. 2003). If we start with the premise that these clouds are rotating because they have inherited the angular momentum of the rotating galactic disk out of which they formed, conservation of angular momentum should provide clues that give us insight to the origin of their formation. However, simple formation theories that assume giant molecular clouds (GMCs) form by condensing out of the Galactic disk are at

odds with some of the observations. For instance, they do not adequately explain why the directions of GMC velocity gradients are not typically aligned with the direction of Galactic rotation, counter to the expectation of conservation of angular momentum. Furthermore, simple formation scenarios tend to overpredict the observed specific angular momentum of GMCs (e.g., Blitz 1990; Rosolowsky et al. 2003). This is the so-called "angular momentum problem."

Provided there is no transfer of angular momentum, the angular momentum of a GMC should be equal to that of the gas out of which it formed. But Blitz (1990), working under the assumption that the velocity gradients in molecular clouds are due to rotation, showed that the angular momentum due to Galactic differential rotation in the solar neighborhood interstellar medium is consistently greater than that contained within molecular clouds. Even molecular clouds with the largest observed velocity gradients—such as the Rosette and Orion A molecular clouds—have less specific angular momentum compared to the ISM from which they presumably formed. Blitz (1990) also pointed out that because the molecular clouds in his sample are rotating in a sense *opposite* to that of Galactic rotation, they could not have conserved angular momentum from the initial states he calculated, unless the local Galactic rotation curve is falling, or unless the clouds always collapsed azimuthally.

The angular momentum problem also extends to extragalactic molecular clouds. Rosolowsky et al. (2003) showed that simple GMC formation theories consistently overestimate the magnitude of the observed angular momentum of molecular clouds in the galaxy M33. On average, they found that simple theory overpredicts the observed magnitudes of specific angular momentum by more than a factor of 5. Furthermore, they found that 40% of the GMCs in M33 are counterrotating with respect to the galactic plane.

In this paper, we shed light on the angular momentum problem by doing a detailed analysis of the kinematics in GMCs *and* the surrounding ISM. Whereas previous studies estimated the initial angular momentum imparted to GMCs from the Galactic rotation curve (e.g., Blitz 1990; Blitz 1993), we compare the velocity fields of GMCs to those of the ISM with which they are associated directly from observation. In light of the observation that GMCs have a spatial and kinematic correlation with high-surface density atomic gas (§2.3), we pose the question: Does the rotation of the large-scale HI associated with GMCs mirror that of the GMCs themselves? Our primary goal is to determine whether or not rotation is the cause of the velocity gradients in GMCs. To that end, we create first-moment maps of the molecular clouds in our sample and of the atomic gas surrounding them are for comparison. In the following section, we describe the ^{13}CO and 21-cm data used to conduct this study. In §3, we create intensity-weighted first moment ^{13}CO and HI maps of five Galactic clouds: Perseus, Orion A, NGC 2264, Monoceros R2 (MonR2), and the Rosette. The results from these measurements are given in §4, and a summary is provided in §5.

2.2 Data

To measure velocity gradients and other properties across the molecular clouds, we use high-resolution, high-sensitivity published ^{13}CO observations. Because ^{13}CO emission is nearly always optically thin in Galactic GMCs, we have the advantage of getting a detailed view of the kinematic structure of the molecular clouds in our sample. And because ^{13}CO has narrower line widths than the optically thick ^{12}CO, the former permits finer separation of velocity components than the latter. Nevertheless, the large scale velocity gradient of a GMC measured using ^{13}CO is generally consistent with that measured using ^{12}CO, since the gradient is being measured across several parsecs and small scale variations in the velocity field tend to get averaged out.

The data for Perseus, Orion A, NGC 2264, and the MonR2 molecular clouds were generously provided by J. Bally (see Bally et al. 1987). Observations of these clouds were taken at the AT&T Bell Laboratories 7 m telescope and have a beam size of 100″. Perseus, Orion A, and NGC 2264 data were resampled onto 60″ grids. The MonR2 data were resampled onto a 30″ grid. The spectral resolution of 128 channels at 100 kHz corresponds to a velocity resolution of 0.27 km s^{-1}. On the T_A^* scale, the cubes have rms noise levels of 0.17 K (Perseus), 0.32 K (Orion A), 0.42 (NGC 2264) and 0.29 K (MonR2).

J. Williams and M. Heyer graciously provided the FCRAO data of the Rosette Molecular Cloud (see Heyer, Williams, & Brunt 2006). The beam size is 47″ and the data were interpolated onto a 20″ grid. The spectral resolution is 59 kHz per channel, and the velocity resolution is 0.133 km s^{-1}. The data have an rms noise of 0.21 K in T_A^*, similar to that of the Bell Labs data.

The HI data are obtained from the Leiden/Argentine/Bonn (LAB) Galactic HI Survey (Kalberla et al. 2005), which spans velocities from -400 km s^{-1} to $+400$ km s^{-1}. (The LSR velocities of the molecular clouds in our sample range from 6 to 14 km s^{-1} with velocity dispersions of a few km s^{-1}.) The survey has a half power beam width of 0.6°, velocity resolution of 1.3 km s^{-1}, and an rms noise level of 0.07 K. The high sensitivity and resolution of the LAB data set enables a detailed study of the atomic gas from which the GMCs formed.

2.3 Analysis

Observations in the Milky Way indicate the molecular clouds are typically associated with high-density atomic gas with column densities around $N(\mathrm{HI}) \sim 2 \times 10^{21}\mathrm{cm}^{-2}$ (e.g., McKee & Ostriker 2007). The Rosette Molecular Cloud is a prototypical example: Williams et al. (1995) measured the mean column of the HI associated with the GMC to be $1.3 \times 10^{21}\mathrm{cm}^{-2}$. Furthermore, in external galaxies, GMCs are often observed to be located on or near bright HI peaks. In the Large Magellanic Cloud, Mizuno et al. (2001) observed that most GMCs are associated with HI having column densities greater than 10^{21} cm^{-2}. Rosolowsky et al. (2003) found that every GMC they identified in M33 lies on an over-dense HI filament, though every over-dense HI region does not contain a GMC. This seems to imply

that high column density atomic gas is necessary but not sufficient for GMC formation.

It is our goal to do a detailed comparison of the velocity fields in the GMCs and local atomic gas. To that end, we first describe how the physical properties—including column densities, masses, and velocity gradients—in both the atomic and molecular gas are determined. We then provide our criteria for choosing spatial and kinematic regions of atomic gas associated with the molecular clouds. Lastly, in this section, we discuss how we estimate the specific angular momentum. These parameters are summarized in Tables 1 and 2.

2.3.1 Cloud Properties

The HI column density, $N(\mathrm{HI})$, is calculated along each line of sight by integrating the atomic hydrogen emission above a certain background value and over the selected velocity range, (see §3.1 and Table 1),

$$N(\mathrm{HI}) = 1.82 \times 10^{18} \int_{v_{\rm min}}^{v_{\rm max}} \frac{T_{\rm b,HI}}{\mathrm{K\ km\ s^{-1}}}\ \mathrm{d}v\ \mathrm{cm^{-2}}, \tag{2.1}$$

where $T_{\rm b,HI}$ is the brightness temperature of the HI observations and $\mathrm{d}v$ is the channel velocity width. Assuming that the HI is optically thin, Equation **??** provides a lower limit to measured column density, which we convert into units of surface density in Figures 2.1 – 2.5.

The total HI mass is then determined by summing over all pixels in the map where emission is detected, that is, where the emission is at least three times the root-mean-square (rms) noise level:

$$M_{\rm HI} = \sum_{\rm pixels} \mu \cdot m_{\rm H} \cdot N(\mathrm{HI})_{\rm pixel} \cdot (d^2 \Delta\alpha \Delta\delta), \tag{2.2}$$

where $\mu = 1.36$ is the correction for helium, d is the distance to a given molecular cloud, and $d^2\Delta\alpha\Delta\delta$ is the area of one pixel, which corresponds to one resolution element.

The ^{13}CO column density, $N(^{13}\mathrm{CO})$, is derived assuming that the ^{13}CO emission is optically thin and in local thermodynamic equilibrium. Following Frerking et al. (1982),

$$N(^{13}\mathrm{CO}) = 2.13 \times 10^{14}\ [1 - \mathrm{e}^{-5.287/T_{\rm ex}}]^{-1} \times \int_{v_{\rm min}}^{v_{\rm max}} \frac{T_{\rm b,CO}\ \mathrm{d}v}{\mathrm{K\ km\ s^{-1}}}\ \mathrm{cm^{-2}}, \tag{2.3}$$

where $\int T_{\rm b,CO}\ \mathrm{d}v$ is the integrated ^{13}CO intensity and $T_{\rm ex}$ is the excitation temperature. Normally, $T_{\rm ex}$ is determined by measuring the ^{12}CO radiation temperature toward ^{13}CO peaks. Since we lack ^{12}CO observations at the same resolution as the ^{13}CO data, we use a constant excitation temperature in the calculation of $N(^{13}\mathrm{CO})$ for each of the five GMCs. Based on the following arguments, we adopt a value of 20 K for each of the GMCs. If the actual excitation temperature in a given region is between 10 and 30 K, the derived ^{13}CO column density will be in error by less than a factor of 2.

Castets et al. (1990) showed that the ^{13}CO emission in Orion A mainly arises from regions where $T_{\rm ex} \approx 20 - 25$ K, and dense cloud cores have temperatures of $T_{\rm ex} \approx 15 - 20$ K. Nagahama et al. (1998) showed that, with the exception of two peaks at $l \sim 209^\circ$ and $l \sim 212.5^\circ$ associated with embedded young stellar groups, $T_{\rm ex}$ rises slowly and monotonically in Galactic longitude, with an average ranging from $13 - 20$ K. In his study of molecular clouds, including Perseus, Orion A, and MonR2, Carpenter (2000) adopts a constant value of $T_{\rm ex} = 10$ K, though the coefficient in his formula for $N(^{13}{\rm CO})$ yields slightly higher values than ours in Equation 2.3. Thus, for Orion A, Perseus, NGC 2264, and Monoceros R2, we use $T_{\rm ex} = 20$ K in our calculation of $N(^{13}{\rm CO})$.

Williams et al. (1995) showed that $T_{\rm ex}$ in the Rosette decreases slowly with increasing distance from the Rosette Nebula (centered at $l = 206.2^\circ,\ b = -2.1^\circ$) from ~ 20 to 5 K. In our analysis, we adopt a uniform value of $T_{\rm ex} = 20$ K for the Rosette. Our estimate of the cloud's mass using this value is slightly lower than that estimated by Williams et al. (1995), who measured the mass over a larger surface area (see below).

Next, the H_2 column density is evaluated assuming a ratio of $N({\rm H_2})/N(^{13}{\rm CO}) = 7 \times 10^5$ (Frerking et al. 1982). Pixels having values at least three times the rms noise level are counted as detected. Finally, the molecular mass M_{13} is calculated over the areas where emission is detected (that is, higher than the 3-$\sigma_{\rm rms}$ level) using

$$M_{13} = \sum_{\rm pixels} \mu \cdot m_{\rm H_2} \cdot N({\rm H_2})_{\rm pixel} \cdot (d^2 \Delta\alpha \Delta\delta), \tag{2.4}$$

where $m_{\rm H_2}$ is the mass of an H_2 molecule. We note that the areas over which emission is detected and, subsequently, the masses we calculate will be smaller than cited in previous studies in which these quantities were measured using ^{12}CO emission. This is because the stronger ^{12}CO line is observed over larger areas in GMCs than the ^{13}CO line. In the Rosette, for instance, we measure a projected area of 1500 pc^2 and a mass of $6.0 \times 10^4\ M_\odot$, while Williams et al. (1995) measure 2200 pc^2 and $7.7 \times 10^4\ M_\odot$. In Table 1, both the ^{13}CO masses and previously measured ^{12}CO masses are listed for the GMCs.

2.3.2 Velocity Gradients

Velocity gradients are measured from first moment maps of the atomic and molecular gas. First, the intensity-weighted average velocity along each line of sight is determined using

$$v_{\rm lsr} = \frac{\sum_i v_i T_i}{\sum_i T_i}, \tag{2.5}$$

where v_i and T_i are the velocity and temperature at location i. Following Goodman et al. (1993), the uncertainty of a given measurement is

$$\sigma_{\rm lsr} = 1.2 \left(\frac{T_{\rm rms}}{T_{\rm peak}} \right) ({\rm d}v\ \Delta v_{\rm FWHM})^{1/2}, \tag{2.6}$$

where $T_{\rm rms}$ is the spectrum noise, $T_{\rm peak}$ is the maximum temperature along the line of sight, and $\Delta v_{\rm FWHM}$ is the FWHM linewidth of the spectrum along the line of sight.

A plane is then fitted to the first moment map of velocity centroids, as in Goodman et al. (1993), assuming a linear velocity gradient:

$$v_{\rm lsr} = v_0 + a(x - x_0) + b(y - y_0), \tag{2.7}$$

where v_0 is the mean cloud velocity, and (x_0, y_0) is an arbitrary reference position, which we take to be the center of our maps, and the coefficients are

$$a = \frac{\partial v}{\partial x}, \quad b = \frac{\partial v}{\partial y}. \tag{2.8}$$

The gradient magnitude and direction, Ω and θ, are derived from the coefficients to the fit,

$$\Omega \equiv |\nabla v_{\rm lsr}| = \frac{(a^2 + b^2)^{1/2}}{d}, \tag{2.9}$$

$$\theta = \tan^{-1} \frac{b}{a}, \tag{2.10}$$

where θ, measured in degrees East from North, points in the direction of increasing velocity. Note that since we have no information regarding the inclination of a given cloud, i, to our line of sight, gradient measurements are underestimates of the actual values, $\Omega_{\rm true} = \Omega / \sin i$.

The uncertainties in these values are calculated by propagating the errors in the coefficients. To check whether planes are good fits to the velocity centroid maps, we make plots of the central velocity at a given location in the cloud versus the perpendicular offset from the cloud's rotation axis. This is done by taking the average velocity along lines parallel to the rotation axis at various distances. In most cases, as will be discussed in §4.3, these plots show that planes are good fits to the velocity centroid maps.

2.3.3 Selecting HI Regions

We select HI regions in the position-velocity LAB data cube that are centered, spatially and kinematically, on the five GMCs in our sample. We do not know *a priori* the kinematic or spatial extent of the HI regions that are associated with each GMC nor the extent of the HI velocity gradients. Molecular clouds have well-defined boundaries at which the molecules are dissociated by UV radiation and where there is a distinct transition from primarily molecular to primarily atomic gas (e.g. Savage et al. 1977; Blitz & Thaddeus 1980). The atomic gas associated with GMCs does not have such distinct boundaries, however, making it difficult to distinguish HI that may be related to GMCs from background emission. Thus, we begin by examining regions in position-velocity space that are far from the center of the GMC. While we want to capture the full extent of any linear velocity gradient we may measure in a given region of atomic gas, we do not want to make our aperture so large

that we end up including in our measurements too much atomic gas that is unrelated to the molecular clouds.

We start by varying the size of the region (that is, the subcube extracted from the LAB data) and examine how the velocity gradient magnitude and direction change. We fix the velocity range (see below) and vary the spatial size of the region centered on the GMC from about 10 to several tens of parsecs, in increments of 10 pc. We find that the gradient direction remains roughly constant until the radius of the region over which it is measured reaches 40 ± 10 pc, independent of the size of the GMC. Beyond this, the measurements start to fluctuate, as the gradient in the vicinity of the molecular cloud becomes washed out by unrelated features.

Thus for each cloud, we end by selecting a spatial boundary of atomic gas which extends roughly 30 – 50 pc from the center of the CO emission. Because the peaks of the HI regions are included in the maps we generate, varying the size of the region within 40 ± 10 pc does not change the gradient direction by more than a few degrees. The 1-σ uncertainty level of θ ranges from 3 to 6 degrees for the clouds in our sample. Our criterion is supported by previous studies such as that of Andersson et al. (1991) who found that the spatial extent of high-intensity HI halos, measured from the edge of the molecular cloud, ranges 5 – 10 pc (see also §2.5). Figures 2.1 through 2.5 show the HI surface density maps derived from the zeroth-moment intensity maps, with the outline of the molecular clouds overlaid. Also overplotted in each figure is a dashed circle indicating the HI region selected for the analysis. Keep in mind, we are showing the ^{13}CO emission of the molecular clouds, and so the maps in Figures 2.1 – 2.5 do not show the full extent of the molecular emission in the GMCs.

To choose relevant velocities of the atomic gas associated each GMC, we begin by examining the HI emission in the velocity range ± 20 km s^{-1} centered about the mean LSR velocity of the ^{13}CO emission. Again, this is because we want to be sure that our measurements include as much as possible of the associated atomic gas. In the direction of the Rosette, for instance, the HI has been observed to extend several km s^{-1} beyond the CO emission (Williams et al. 1995). Studies of both Milky Way molecular clouds (e.g., Wannier et al. 1983, Williams et al. 1995) and extragalactic clouds (e.g. Engargiola et al. 2003) have shown that the HI emission line profile tends to peak in the direction of GMCs. In effect, we are using the HI velocity as a proxy for distance in order to associate the atomic gas with the GMCs. As Figures 2.1 – 2.5 show, although the HI emission line is broader than the CO line, the velocity difference between the peaks in the respective lines never exceeds $\sigma_{\rm HI}$, where $\sigma_{\rm HI}$ is the velocity dispersion of the HI profile.

The bottom panel in Figures 2.1 through 2.5 show the average ^{13}CO spectrum through each GMC with the HI spectrum in the same direction (within the dashed circle) overplotted. Because the ^{13}CO–HI peaks are nearly coincident in each case, this indicates that most of the HI in the direction of a given cloud is associated with that cloud within the selected velocity range. In the cases of Perseus, Orion A, and MonR2, the HI emission drops abruptly beyond ± 15 km s^{-1} of the ^{13}CO emission. NGC 2264 and the Rosette have more complicated HI spectra, each showing double peaks that may be indicative expansion or of a blended, possibly unrelated component. The latter explanation would not be surprising since, of the

five clouds in the sample, NGC 2246 and the Rosette are located closest to the Galactic plane where line-of-sight blending is more of a problem.

Based on Figures 2.1 – 2.5, we determine the boundaries of the HI emission we will use for the subsequent analysis. For Perseus, Orion A, and MonR2, the HI line profiles are approximated as Gaussians and we assume that HI emission having velocities within $\pm 2\sigma_{\rm HI}$ is associated with a given molecular cloud. Since both NGC 2264 and the Rosette each have a second peak in their HI temperature profiles ($T_{\rm b,HI}$) at higher velocities and because we want to be careful to exclude as much unrelated emission as possible, we set a slightly more stringent criterion on the velocities we select. For each cloud, a maximum velocity is identified at the local minimum in $T_{\rm b,HI}$ where the Gaussians overlap. In the NGC 2264 spectrum, for instance, $T_{\rm b,HI}$ drops to 29 K at 15 km s^{-1} and then peaks again at around 20 km s^{-1} (see Figure 2.3). Thus, we eliminate all emission having velocities above 15 km s^{-1}, the location of the local minimum. All of these selections are listed in the third to last column of Table 1.

2.3.4 Specific Angular Momentum

Once the magnitudes of the velocity gradients in the molecular clouds and the surrounding HI are measured, we may calculate and compare their specific angular momenta, under the assumption that the linear gradients are due to solid body rotation. The specific angular momentum, j, is simply the total angular momentum of a body divided by its mass,

$$j = \beta \Omega R^2, \tag{2.11}$$

where R is the radius of the region, and the constant β takes into account the moment of inertia of a rotating body. For roughly spherical GMCs having constant surface mass density distributions, $\beta = 2/5$. Unless otherwise stated, we take the size of a given molecular cloud to be its effective radius, as defined by its projected area: $R_{\rm eff} = \sqrt{A/\pi}$.

We would like to estimate the expected specific angular momentum initially imparted to a GMC by the ISM from which it forms. This depends on the process of GMC formation, and we assume here that GMCs form via a "top-down" formation mechanism. For instance, it has been suggested that molecular cloud formation occurs when an instability triggers collapse or condensation from the Galactic disk (e.g., Mouschovias et al. 1974; Blitz & Shu 1980; Elmegreen 1982; Kim et al. 1998). Blitz & Shu (1980) show that "bottom-up" formation of GMCs via the random agglomeration of pre-existing low-mass clouds is unlikely because of the long timescales for this process. Gravitational instabilities and magneto-gravitational instabilities, however, tend to proceed more quickly.

If the HI surrounding the GMCs is reflective of the ISM out of which the GMCs initially formed, the quantity $(1/2)\Omega R^2$ provides an estimate of the initial specific angular momentum of the GMCs, assuming they are rotating. Henceforth, we will often refer to this as the *expected* specific angular momentum. Note that this disregards the possible effects of magnetic fields; that is, we are assuming that the magnetic field strength of the forming cloud

is 0. The initial angular velocity imparted to a given GMC is the local value of Ω, which we calculate from the first-moment maps of the HI using Equation 2.9. In principle, the size of the region from which a forming cloud gathers material, the "accumulation radius" R_A, could have a range of values because it depends on details of the formation mechanism, as well as on assumptions regarding the initial surface density and geometry of the gas from which a GMC formed. Nevertheless, we can set an effective lower limit on R_A by calculating the size of the region from which a GMC must contract to obtain its present mass, $M_{\rm GMC}$.

Following Blitz (1993), let us assume that the initial geometry of the collapsing region is a cylinder with a diameter equal to its height. The size of the cylinder is determined by requiring that the mass contained within it is equal to the present mass of the GMC:

$$2\pi\rho_{\rm HI}R_A^3 = M_{\rm GMC}, \tag{2.12}$$

where $\rho_{\rm HI}$ is the mean volume density of the atomic gas from which the GMC formed. Blitz (1993) estimated R_A using the mean value of $\Sigma_{\rm HI}$ in the Galactic plane near the Sun, 5 $M_\odot$ pc^{-2} (Henderson et al. 1982). This corresponds to a mass density of $\rho_{\rm HI}$ = 0.0125 $M_\odot$ pc^{-3} (or a number density of 0.5 cm^{-3}), using an effective scale height of atomic gas of 200 pc in the solar vicinity (Falgarone & Lequeux 1973). However, using larger values of $\Sigma_{\rm HI}$ (leading to lower estimates of R_A) might be more appropriate, given the observation that GMCs tend to form in regions of HI with densities higher than global galactic values (e.g., Engargiola et al. 2003; Imara et al. 2010). We estimate the accumulation radii using $\Sigma_{\rm HI}$ = 10 $M_\odot$ pc^{-2}, a value more in keeping observations of the atomic gas associated with GMCs. For instance, around the Rosette, Williams et al. (1995) measure an HI column density of 1.3×10^{21} cm^{-2}, which corresponds to a $\Sigma_{\rm HI} \approx 10$ $M_\odot$ pc^{-2}, twice the mean Galactic value. From the Sancisi (1974) study of atomic gas near Perseus, the inferred surface density is 11 $M_\odot$ pc^{-2}. Our estimates of R_A are listed in Table 2, as well as the effective radii of the GMCs.

Finally, we note that the predicted specific angular momentum in the atomic gas has a marked dependence on the GMC mass. Substituting $R_A \sim (M_{\rm GMC}/\rho_{\rm HI})^{1/3}$ from Equation 2.12 for the radius in Equation 2.11 yields $j_{\rm HI} \sim M_{\rm GMC}^{2/3}$. The masses we calculate using the ^{13}CO observations underestimate the total molecular mass of the GMCs. For this reason, we use the larger GMC masses, as previously measured using ^{12}CO observations, to predict the initial specific angular momentum imparted to forming molecular clouds. Typically, $R_A \sim 3R_{\rm GMC}$.

2.4 Results

Figures 2.6 through 2.11 show the HI velocity maps (grayscale) overlaid with velocity maps of ^{13}CO (color) for each GMC. Overplotted on these maps are axes of rotation: the lines perpendicular to the gradient directions, $\theta_{\rm GMC}$ and $\theta_{\rm HI}$, as calculated from Equation 2.10. These lines are the position angles of the rotation axes, ψ, (where $\psi = \theta + 90°$), of the molecular and atomic gas *if* the gradients are in fact due to rotation.

In order to check whether planes are good fits to the first-moment velocity maps, we make position-velocity cuts parallel to the maximum gradient directions and plot the results (bottom panels of Figures 2.6 – 2.11). We are essentially plotting the central velocity at a given location in the cloud versus displacement along the gradient on a pixel by pixel basis. Figures 2.6, 2.10, and 2.11 show that planes are good fits to the first-moment maps of HI surrounding Orion A, MonR2, and the Rosette because there is a clear linear trend in the gradient in the atomic hydrogen. The velocity fields of the HI associated with Perseus and NGC 2264 appear to have more complex structure. In the case of the NGC 2264 and MonR2 molecular clouds (Figures 2.9 and 2.10), however, the position-velocity plots do not have monotonically increasing or decreasing slopes, indicating a more complex velocity structure in the *molecular* gas (red points). In these two cases, we nevertheless overplot the lines perpendicular to the gradient direction calculated from Equation 2.10.

The specific angular momenta in the atomic and molecular gas, listed in Table 3, are compared in Figure 2.12. There appears to be a reasonable correlation—$j_{\rm HI}$ and $j_{\rm GMC}$ increasing together as $j_{\rm HI} \propto j_{\rm GMC}^{0.66\pm0.20}$—although small number statistics prevent us from making a firm conclusion. In each case, the initially expected specific angular momentum, $j_{\rm HI}$, is always greater than $j_{\rm GMC}$. These measurements alone are consistent with a picture whereby GMCs form via some top-down mechanism, such as a gravitational instability, and somehow shed angular momentum in the process. But since angular momentum is a vector quantity, this scenario is difficult to reconcile with the observation that the gradient position angles in the molecular and atomic gas differ and appear to be uncorrelated (Figure 2.13).

The key finding of our analysis is that the regions of atomic gas associated with molecular clouds have linear velocity gradients, yet the directions of these gradients are—with one exception—unaligned with the direction of the gradients in the associated GMCs. Under the hypothesis that the gradients are caused by solid body rotation, this would imply that GMCs are *not* corotating with the surrounding ISM. The second key result is that the magnitudes of the velocity gradients in the GMCs are larger than the gradient magnitudes in the atomic gas. Thirdly, if the gradients in the molecular and atomic gas are from rotation, the angular momenta in the molecular clouds is less than predicted from calculations of the angular momenta in the associated atomic gas.

Below, we describe the results in detail for each GMC. The gradient directions, magnitudes, and specific angular momenta of both the molecular and atomic gas are given in Table 3.

Orion A

Figure 2.6 shows that the Orion A molecular cloud has a large-scale gradient whose velocity decreases from about 12 km s^{-1} to 3 km s^{-1} with increasing Galactic longitude. Of the GMCs in this study, observations of the kinematics and morphology of the Orion A molecular cloud seem to make the best case for a top-down picture of GMC formation. The direction of the gradient and the long axis of Orion A are parallel to each other and to the Galactic plane. If the gradient were due to rotation, this would imply that Orion A is rotating

in a sense nearly opposite to that of the Galactic disk. This result is in agreement with previous studies (e.g., Kutner et al. 1977, Blitz 1993). The velocity gradient of the HI in the immediate surroundings of Orion A points in nearly the same direction as that in the molecular cloud. Figure 2.6 shows that the gradient in the atomic hydrogen, integrated over the velocity range from about -7 to 22 km s^{-1}, differs from the gradient in the molecular cloud by only 9°.

The origin of the velocity gradient in Orion A has been debated; it has previously been explained by cloud rotation (Kutner et al. 1977), expansion driven by the Orion OB association (Bally et al. 1987), and expansion driven by stellar winds from newborn stars (Heyer et al. 1992). If due to rotation, the 0.22 km s^{-1} pc^{-1} gradient in the molecular cloud implies a specific angular momentum of 42.2 pc km s^{-1}. However, considering that Orion A is filamentary and much more closely resembles a cylinder rotating about its minor axis than a sphere, this estimate of j is likely to be low limit, since the configuration of the former has a higher moment of inertia than the latter. For a cylinder rotating about its minor axis, $j_{\rm cyl} = 1/12\Omega(3R^2 + L^2)$, where R is the radius of the cylinder and L is the length. The cylindrical radius and length of Orion A are approximately 1.5° and 9°, corresponding to 11 pc and 65 pc. Consequently, $j_{\rm cyl} = 84$ pc km s^{-1}, much closer to, but still a bit less than the estimated angular momentum of the associated atomic gas (107 pc km s^{-1}).

These two results—that the gradients of the molecular and local atomic gas are in near alignment, and the magnitudes of the specific angular momenta are within range of each other—suggest that Orion A may be a case in which the molecular cloud and surrounding HI are corotating and in which conservation of angular momentum is demonstrated. As we will see below, it appears to be an exceptional case.

Perseus

Figure 2.7 shows that a strong linear gradient exists in the Perseus molecular cloud. The velocities in the GMC range from about 1 to 11 km s^{-1} with increasing Galactic latitude. The gradient direction is tilted about 20° to the North-West. Of the molecular clouds in the sample, Perseus has the largest velocity gradient at 0.23 km s^{-1} pc^{-1}. If the gradient is caused by rotation, from Equation 3.3, the specific angular momentum in Perseus is 24.2 pc km s^{-1}, as indicated in Table 3.

Examination of the black points in the position velocity-plot shown in Figure 2.7 indicates that the velocity gradient of the HI region centered on Perseus is not linear. As with each cloud in this study, we take the center of the HI field to be located at the position centroid of the GMC in Galactic coordinates, (l_0, b_0). This affects the appearance of the position-velocity plot, which shows the velocity of points in the field as a function of distance from the gradient judged from l_0, b_0. The HI surface density map in Figure 2.2 shows a high-surface density ($\sim 16\ M_\odot$) HI filament extending vertically near a Galactic longitude of 157.5°. Whereas the other GMCs in this sample have some portion of their molecular material laying directly on top of an HI peak, this is not strictly the case with Perseus, which is tilted toward the East from the bright HI filament. Thus, we generate

another first-moment map of the HI centered on the filament at $l_0, b_0 = 157.5, -18$, as well as another position-velocity plot centered here. Figure 2.8 shows that a linear fit is a much more suitable fit to the gradient in the HI when we shift the reference point. When measured this way, the magnitude of the gradient measured using Equation 2.9 shifts from 0.038 to 0.067 km s^{-1} pc^{-1}, the value we cite in Table 3. The gradient direction is nearly 100°, very close to the sense of Galactic rotation, in which velocities increase from West to East. But the directions of the gradients in the molecular cloud and the atomic gas surrounding the GMC differ by nearly 120°.

Of the clouds in this analysis, Perseus has the largest velocity gradients in the molecular gas. The magnitude of the gradient in the molecular gas (0.23 km s^{-1} pc^{-1}) is 3.4 times that in the HI (0.067 km s^{-1} pc^{-1}). The estimated specific angular momentum in the atomic gas is $j_{\rm HI} = 60$ pc km s^{-1}, 2.5 times j measured in the molecular cloud. Although this is consistent with a scenario in which the Perseus molecular cloud formed by collapsing out of the atomic gas, its angular momentum being redistributed somehow in the process, based on the observation that there is such a large difference between the gradient directions in the molecular and atomic gas, it is difficult to see how the GMC could have formed in such a simple way.

NGC 2264

The first-moment maps and position-velocity plot in Figure 2.9 show that the NGC 2264 molecular cloud and surrounding HI both have complex kinematic features. Though there is no significant linear gradient across the entire GMC, there is a weak gradient in the atomic gas. The gradient in the atomic gas is stronger to the South of the rotation axis, where the velocity decreases from about 8 to 5 km s^{-1} as the Galactic latitude increases from $\sim -1.8°$ to $+1.5°$. As seen in Figure 2.3, the NGC 2264 molecular cloud is composed of two main structures. The structure in the North has a larger range of velocities, with $v = 2$ – 10 km s^{-1}, than does the structure in the South, which averages around 6 km s^{-1}, close to the mean velocity of the molecular cloud as a whole. This is also the average velocity of the HI peak located at near $l = 201.5°$, $b = 0.5°$ (Figure 2.3), which is associated with the southern segment of the GMC.

The magnitude of the gradient in the atomic gas near NGC 2264 is 0.019 km s^{-1} pc^{-1}, which is less than $\Omega(= 0.025$ km s^{-1} pc$^{-1})$ in the solar vicinity assuming a flat rotation curve. The magnitude of the gradient fitted across the entire GMC, using Equation 2.9, is 0.046 km s^{-1} pc^{-1}. But the northern segment of the cloud in isolation has a gradient closer to 0.08 km s^{-1} pc^{-1}.

It seems unlikely that rotation is the origin of the velocity field in the NGC 2264 molecular cloud. Table 3 records the velocity magnitude and direction calculated by fitting a plane to the field, even though the gradient is not linear. Using these values, the specific angular momentum of the GMC, 4 pc km s^{-1}, is smaller than the expected value by at least a factor of 6. The gradient direction in the GMC, pointing nearly 50° East from North, differs from $\theta_{\rm HI}$ by 140°. An alternative explanation of the velocity field in NGC 2264 may be, at least in

part, the internal stellar activity. It is noteworthy that the HII region associated with NGC 2264 (the Cone Nebula) is located in the north, near the part of the GMC that has a larger velocity dispersion than the southern part. The nebula, at $l = 202.95$, $b = 2.20$ (Kharchenko et al. 2005) is located between two high velocity regions of the GMC that are receding at speeds near 10 km s^{-1}. This morphology is suggestive of an expanding ring seen from an edge-on perspective. Taken all together, it appears that these features could be causally connected: an HII region causes the high-speed expansion of the surrounding molecular gas, which subsequently sweeps up atomic gas into a high-density ridge. It is perhaps significant that we see a similar pattern in the Rosette.

Yet another explanation of the kinematics of NGC 2264 is put forth by Furész et al. (2006), based on their finding that the stars and ^{13}CO emission in NGC 2264 are well-correlated in position-velocity space. They suggest that the velocity field of the GMC is explained by the models of Burkert & Hartmann (2004), in which molecular clouds form from supersonic collisions of gas. This argument seems to be corroborated by the overall pattern of the cloud's velocity structure: higher velocities at the outskirts of the cloud and lower velocities proceeding toward the center of the cloud. This pattern could be explained by gravitationally driven infall at the interface of the colliding flows. In this scenario, star formation occurs preferentially in the condensations that develop during the collapse of the molecular cloud, thus explaining the position-velocity correlation observed between stars and high-density molecular gas.

The colliding flows hypothesis may also explain the velocity structure of the atomic gas. Figure 2.9 shows that the HI has slightly higher velocities at positions in the field far from the gradient axis and lower velocities close to the axis—again, suggestive of infall accelerated by gravity. If other molecular clouds form by this mechanism, however, it is unclear why we do not see this pattern in the atomic gas surrounding the rest of the GMCs in our sample. Possibly, the NGC 2264 system still retains signs of its early formation history due to the relatively young age of the GMC (~ 1 – 3 Myr; Flaccomio et al. 2000; Ramírez et al. 2004). It is difficult to make a definitive conclusion since we are observing HI so close to the Galactic plane where the problem of line-of-sight blending is exacerbated.

MonR2

Figures 2.4 and 2.10 show that the MonR2 molecular cloud sits right on top of a high-density cloud of HI that has a strong linear velocity gradient. The gradient, which extends for over 80 pc, has a magnitude of 0.035 km s^{-1} and increases from about 7 km s^{-1} to 12 km s^{-1} from South to North-West. If the gradient is due to rotation, $j = 47$ – 180 pc km s^{-1}, depending on the size of the region considered. From conservation of angular momentum, one might expect MonR2 to have a gradient somewhere between $\Omega = 0.38$ – 0.84 km s^{-1} pc^{-1}, pointed about 11° West of North like the gradient in the atomic gas. This is not what we see in Figure 2.10, however.

The velocity field of the MonR2 molecular cloud has a much more complex structure than does the atomic gas. The outer northern, western, and southern edges of the cloud

reach velocities up to 12 – 13 km s^{-1}. The inner portion of the cloud is moving at slower speeds around 9 – 11 km s^{-1}, which is also the velocity range at which the HI peak located at $l = 213.5°$, $b = -12.5°$ dominates. Considering the apparently random nature of the velocity field, it is unlikely that the GMC is undergoing large-scale, coherent rotation. The position-velocity plot for the molecular cloud in Figure 2.10 (red points) has a zero slope, as does NGC 2264, indicating that it has no significant linear gradient. It is difficult to say whether or not the present velocity field originated during the cloud's formation or during some later stage in its evolution. If the GMC originally had a more organized velocity field and did *not* inherent its present field during formation, perhaps a series of interactions with external forces or internal events—such as turbulence and star formation activity—have washed out any signature of a systematic velocity gradient which was previously present in the molecular cloud.

The Rosette

The separation between the gradient directions in the Rosette molecular cloud and the surrounding atomic gas is approximately 130°. Figure 2.11 shows that in the velocities of the molecular cloud tend to increase from roughly 7 – 14 km s^{-1} in the North-East to as high as $\sim$ 17 km s^{-1} in the South and South-West. The gradient in the HI is directed perpendicular to the Galactic plane. We note that, of the clouds in our sample, the HI maps near the Rosette probably suffer the greatest degree of line-of-sight blending. The cloud is very close to the Galactic plane, and at the distance of the Rosette, 1600 pc, we have the lowest spatial resolution ($\sim$ 17 pc) in the atomic gas. Therefore the surface density and velocity maps displayed in Figures 2.5 and 2.11 almost certainly fail to capture many of the local, small-scale variations in the structure of the atomic gas.

We measure a gradient in the molecular cloud of 0.09 km s^{-1} pc^{-1}, consistent with the 0.08 km s^{-1} pc^{-1} measured by Williams et al. (1995). If the gradient is due to rotation, the specific angular momentum of the cloud is approximately 26 pc km s^{-1}. Based on the estimate of the minimum value of the accumulation radius, the specific angular momentum in the surrounding ISM is nearly 3 times larger.

Figure 2.5 shows the outline of the molecular cloud overlaid on a surface density map of the atomic gas, which is integrated over the range v = 4 – 27 km s^{-1}. A "shell" of HI containing two high-density peaks is associated with the molecular cloud. The brightest peak of the shell sits at the southern edge of the molecular cloud near a latitude of $b = -3°$, and another peak in the surface density occurs near $b = -1.5°$. The southern portion of the HI shell appears to mimic the ring-like structure in the molecular cloud sitting just to the north of it. When the location of the structures in both the molecular and atomic gas are compared with the first-moment map in Figure 2.11, we see that the southern portion of the HI shell is moving near the same velocity, $\sim$ 13 - 14 km s^{-1}, as the south-east segment of the ring in the GMC. The western half of the ring in the GMC is moving at higher velocities. Also note how the HI peak located near $b = -1.5°$ is moving slightly faster ($\sim$ 14 km s^{-1}) than the molecular gas in that region ($\sim$ 13 km s^{-1}). All of this suggests that both the

HI shell and the ring-like structure in the GMC are expanding. Kuchar & Bania (1993) demonstrated that the HII region NGC 2244 (the Rosette Nebula) could have given rise to the expansion in the atomic gas. And Williams et al. (1995) found that certain properties of clumps within the GMC vary with distance from the nebula, centered at $l = 206.25°$, $b = -2.11$ (Celnik 1983).

Taken all together, the evidence leads us to suggest that the gradient in the Rosette molecular cloud is *not* caused by rotation, but by the high-luminosity HII region, NGC 2244. High-energy winds of stars in NGC 2244 may have excavated a hole in the GMC, causing HI to be swept up into a high-density ridge by the expanding molecular gas (e.g., Kuchar et al. 1991, Kuchar & Bania 1993). In this picture, because the nebula has had less of an impact on distant regions of the cloud, these distant regions are moving at lower velocities compared to molecular gas near the HII region.

2.5 Implications for GMC Formation

Our key findings are that the angular momentum in the GMCs is less than that in the surrounding atomic gas, and the velocity gradient position angles in the molecular and atomic gas are widely divergent—with Orion A being the one exception. This leads us to suggest that rotation may *not* be the best explanation of the velocity fields observed in the GMCs.

Traditionally, at least three possible solutions have been invoked to resolve the angular momentum problem:

1. One or more of the assumptions in the theory are inappropriate. For instance, if the average surface density of the precursor atomic gas is underestimated, this will lead to an overestimate in the accumulation radius and, consequently, an overestimate of the angular momentum initially imparted to a GMC. In our analysis, we used 10 $M_\odot$ pc^{-2} for the mean surface density of the precursor gas, twice the average value in the Solar vicinity. Assuming that the initial gas had an even higher density, say 20 $M_\odot$ pc^{-2}, this would not change the main result, namely that $j_{\rm HI}$ is consistently greater than $j_{\rm GMC}$. This is because the accumulation radius depends weakly on the initial surface density of the gas ($R_A \propto \Sigma_{\rm HI}^{-1/3}$). On the other hand, if collapsing molecular clouds do not gather material far from the Galactic plane, using larger values of R_A might be appropriate. Yet this would only exacerbate the discrepancy between the predicted and observed angular momenta. It might also be argued that using the effective radius of a GMC leads to underestimates in $j_{\rm CO}$ if the GMC is filamentary. In the previous section we took this into consideration with Orion A and recalculated $j_{\rm CO}$ assuming a cylindrical morphology. This raised $j_{\rm CO}$, which, nevertheless, remained less than $j_{\rm HI}$. Moreover, varying the size of the GMC or the region from which it gathers material does not solve the problem of the gradient directions in the molecular and atomic gas being unaligned.

2. An alternative explanation of the angular momentum problem is that though the assumptions regarding the initial conditions may be valid, there may be some kind of external

braking force which rapidly reduces the angular momentum of a GMC during its initial condensation. Magnetic braking is often evoked as an angular momentum shedding mechanism (e.g., Mouschovias 1977; Fleck & Clark 1981; Mestel & Paris 1984; Rosolowsky et al. 2003). Zeeman splitting of the OH 18-cm line and the 21-cm line of neutral hydrogen have been used to measure the magnetic field strengths of GMCs. Since GMCs are magnetized and MHD effects are expected to play a significant role in their evolution, magnetic braking—in which magnetic field lines anchoring a GMC to the ambient ISM provide the tension necessary to slow down rotation—is a possible solution to the angular momentum problem. Heiles & Troland (2005) measured the mean magnetic field strength in the cold neutral medium of the Milky Way to be $B_0 = 6 \pm 1.8$ μG. The braking time is set by the time it takes for Alfvén waves to travel across a region of gas having a moment of inertia comparable to the GMC (Mestel & Paris 1984). In order for magnetic braking to be efficient at slowing down cloud rotation, it would have to occur on timescales no greater than the timescale for cloud collapse. For gas having an initial density of 1 cm^{-3} (=0.025 $M_\odot$ pc^{-3}), the Alfvén speed is $B_0(4\pi\rho)^{-1/2} \approx 9.5$ km s^{-1}. In a region having an accumulation radius of 70 pc, this corresponds to a braking time of roughly 7.4 Myr. By comparison, the timescale for self-gravitational cloud formation in a region having the same density, assuming that this process occurs on a timescale close to the dynamical free-fall time (Mouschovias & Paleologou 1979; Mestel & Paris 1984; Elmegreen 2007), is $(3\pi/4G\rho)^{1/2} \approx 44$ Myr.

However, the effectiveness of magnetic braking largely depends on how the mass of the forming cloud compares to its magnetic critical mass. Mestel & Paris (1984) argue that braking will efficiently slow down rotation only if the mass, M, of the forming cloud is much less than its magnetic critical mass, M_C. Using Crutcher's (1999) magnetic field strength measurements of molecular clouds, McKee & Ostriker (2007) infer that GMCs have approximately $M > 2M_C$, that is, they are magnetically supercritical. Elmegreen (2007) argues that the ISM out of which GMCs form has a magnetic field that is "near-critical," i.e., $M \sim M_C$. Furthermore, magnetic braking slows rotation most efficiently when the cloud's angular momentum vector is perpendicular to the magnetic field (Mouschovias & Paleologou 1979). Due to the complexity of making precise measurements of the magnetic field in the ISM, it is not established whether or not this is the case. Clearly, more observations are needed in order to determine the importance of magnetic fields in GMC evolution.

3. Finally, perhaps GMCs are not rotating after all, and the "problem" is unfounded. As some authors have pointed out, the interpretation that velocity gradients indicate rotation is not unique. Expansion and shear, for instance, also produce velocity gradients. The numerical simulations of Hennebelle et al. (2008) suggest that the converging flows of atomic gas could produce GMCs. If shearing occurs at the interface of colliding flows, might this result in an excess of shear, that is, values of Ω that are higher than the shear arising from the local Galactic rotation curve? Assuming a flat rotation curve, the local value of Ω in the solar neighborhood is 0.025 km s^{-1} pc^{-1}. This is slightly less than, but basically comparable to the gradient magnitudes we measure in Perseus, Orion A, and MonR2 (Table 3). As discussed previously, we are underestimating Ω in every case, since we have no information regarding the inclination of clouds. Also, since blending of emission along the line-of-sight

is most extreme in the cases of NGC 2264 and the Rosette, which are situated close to the Galactic plane, it is likely that $\Omega_{\rm HI}$ is underestimated to an even greater degree in these cases. Nevertheless, we cannot conclude whether or not shear is the cause of the velocity gradients based on these observations. It is an issue we would like to further investigate with a larger sample of clouds.

Burhert & Bodenheimer (2000) show that turbulence may also cause linear velocity gradients. They demonstrated that the gradient magnitude of turbulent cores scales with size as $\Omega \propto R^{-0.5}$. Figure 2.14 shows Ω as a function of R for both the molecular clouds and HI. Neither the GMCs nor the HI appear to follow the $\Omega \propto R^{-0.5}$ relationship, though we do not have enough data points to make a definite conslusion.

Studying the properties of GMC kinematics in other galaxies will also help to develop our picture of GMC formation. In their analysis of 45 GMCs in M33, Rosolowsky et al. (2003) did the first systematic, extragalactic study of GMC angular momentum properties. They showed that simple GMC formation theories consistently overestimate the magnitude of the observed angular momentum. They measured the velocity gradients from high-resolution ^{12}CO($J = 0 \rightarrow 1$) data, finding that the gradients of M33 clouds are similar in magnitude to Galactic clouds. They then tested several formation models by calculating the accumulation radii of the cataloged clouds which are predicted by the various models, including the Toomre and Parker instabilities. On average, the theories, which do not include the effects of magnetic fields on rotation, overpredict observed magnitudes of velocity gradients by more than a factor of 5. And 40% of the GMCs in M33 are counterrotating with respect to the sense of galactic rotation.

We extend this study by performing the analysis established here on a much larger sample of GMCs in M33 cataloged by Rosolowsky et al. (2003). Since M33 has a relatively low inclination of $\sim 51^\circ$ (Corbelli & Salucci 2000), such a study has the advantage of bypassing the problem of source confusion along lines of sight that arises when doing comparable surveys of molecular clouds in the Milky Way.

2.6 Summary and Conclusions

We have presented a detailed comparison between the kinematics of five Galactic molecular clouds and the atomic gas that surrounds them. We developed a method for selecting regions of HI that are associated with the GMCs and found that each GMC was nearby high-density HI which peaked above the mean Galactic value. First-moment maps were created using the ^{13}CO emission of the GMCs and the HI 21-cm emission, and then a plane was fit to each map of velocity centroids. We determined the magnitudes and directions of the velocity gradients from the coefficients to the fits. From these observations and measurements, we arrived at the following conclusions:

1. Orion A, Perseus, and the Rosette each have a significant linear velocity gradient across the face of the molecular clouds, while NGC 2264 and MonR2 have complex, non-linear velocity fields. The Perseus molecular cloud has the strongest linear gradient in the

sample, with a magnitude of 0.23 km s^{-1} pc^{-1}.

2. The atomic gas associated with Orion A, MonR2 and the Rosette has significant linear velocity gradients, regardless of whether the molecular cloud has one. The HI gradients range from 0.019 to 0.067 km s^{-1} pc^{-1}, or 0.76 to 2.7 times the shear in the solar vicinity as measured by the Galactic rotation curve.

3. If the gradients in the molecular and atomic gas were due to rotation, the specific angular momentum in the GMCs is less than that predicted by the formation scenario in which a GMC preserves angular momentum while undergoing top-down collapse from the surrounding ISM by a factor of 1 to 6. The discrepancy can be narrowed if different assumptions are made regarding the initial density and geometry of the gas. But the direction of the trend—that the observed angular momentum is less than the predicted—remains the same.

4. We observe large differences between the velocity gradient directions in the GMCs and the atomic gas, with Orion A being the one exception. At more than 130°, two of the most extreme angle separations can be seen in the MonR2 and the Rosette systems (Figure 2.10 and 2.11). Furthermore, the gradient directions in neither the molecular nor the atomic gas are in alignment with the overall direction of Galactic rotation. If the gradients were due to rotation, this indicates that some GMCs are counterrotating with respect to the Galaxy.

5. That the velocity gradient position angles in the atomic and molecular gas are divergent indicates that the GMCs in our sample probably did not inherit their present velocity fields from the atomic gas from which they formed. Finally, in at least two cases, NGC 2264 and the Rosette, a good explanation of the morphology and kinematics observed in the gas is that they are caused by stellar winds from O stars in the HII regions located in the GMCs, not rotation.

Table 2.1: **GMC Properties**

	Coordinates		Distance	M_{13}	$M_{\rm GMC}$	Projected Area	$v_{\rm LSR}(^{13}{\rm CO})$	v(HI)	References	
Cloud	l_0	b_0	[pc]	[10^4 $M_\odot$]	[10^4 $M_\odot$]	[pc^2]	[km s^{-1}]	[km s^{-1}]	Distance	^{12}CO
Perseus.....	159	-20	320	1.4	1.2	825	7.5	$-8, 14$	1	6
Orion A.....	210	-19	414	2.4	6.9	1510	9.6	$-7, 22$	2	7
NGC 2264...	202	1	800	2.5	2.2	674	6.6	$-7, 15$	3	8
MonR2.....	213	-13	830	3.0	9.0	2940	10.8	$-5, 23$	4	9
Rosette.....	207	-2	1600	4.0	7.7	2200	13.1	$4, 27$	5	10

Properties are determined using the methods outlined in §2.3 of the text. Masses calculated using ^{13}CO observations are listed under M_{13}. The GMC masses calculated by previous authors are listed under $M_{\rm GMC}$.

References.–(1) de Zeeuw et al. 1999; (2) Genzel et al. 1981; (3) Sagar & Joshi ; (4) Racine 1968; (5) Blitz & Stark 1986; (6) Sargent 1979; (7) Menten et al. 2007; (8) Blitz 1978; (9) Maddalena et al. 1986; (10) Williams et al. 1995.

Table 2.2: **Accumulation Radii**

Cloud	$R_{\rm GMC}$	R_A
Perseus.....	16.2	42.4
Orion A.....	21.9	76.0
NGC 2264...	14.6	51.9
MonR2.....	30.6	83.6
Rosette.....	26.5	78.8

The effective GMC radii, $R_{\rm GMC}$, and the accumulation radii, R_A, are listed in units of pc. Lower limits of R_A are estimated using Equation 3.2, assuming that the GMCs initially formed from HIhaving an average surface density of 10 $M_\odot$ pc^{-2}.

Table 2.3: **GMC Properties: Dynamics**

Cloud	$\Omega_{\rm GMC}$ [0.01 km s^{-1} pc^{-1}]	$\Omega_{\rm HI}$ [0.01 km s^{-1} pc^{-1}]	$\theta_{\rm GMC}$ [deg]	$\theta_{\rm HI}$ [deg]	$j_{\rm GMC}$ [pc km s^{-1}]	$j_{\rm HI}$ [pc km s^{-1}]
Perseus.....	23.1	6.70	-20.2	99.4	24.2	60.3
Orion A.....	22.0	3.71	-111	-102	42.2 [84.1]	107
NGC 2264...	4.60	1.87	47.8	-173	3.92	25.2
MonR2.....	6.68	3.48	-72.4	-11.2	25.5	120
Rosette.....	9.18	2.36	-132	1.12	25.8	73.4

The magnitude of the velocity gradient, Ω, and the direction of rotation θ measured in degrees East of North are determined using the methods outlined in the text. The specific angular momentum, j, is calculated for each GMC and HIregion assuming that the gradients are due to rotation. Listed in brackets is j for Orion A, assuming that the GMC has the morphology of a cylinder with a rotation axis perpendicular to its long axis. Typical errors are $\delta\Omega = 0.001 - 0.005$, $\delta\theta({\rm CO}) = 0.5 - 2^\circ$, $\delta\theta({\rm HI}) = 5 - 10^\circ$, and $\delta j = 0.5 - 2$ pc km s^{-1}.

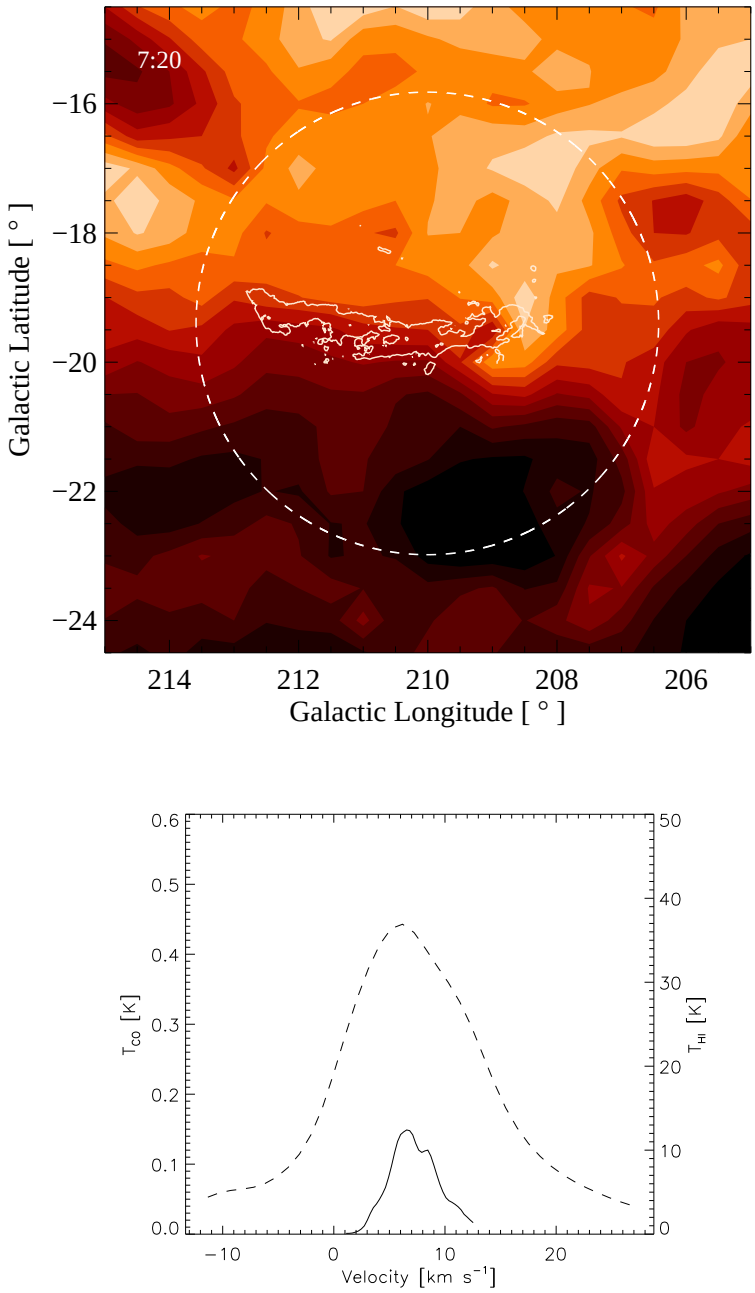

Figure 2.1: Orion A. The bottom figure plots the average spectra of the ^{13}CO emission (solid line) in the GMC and of the HI emission (dashed line) in the region of atomic gas. The top figure shows a surface density map of HI overlaid with an outline of the molecular cloud. The range of HI surface density, in units of $M_\odot$ pc^{-2}, is marked in the top left-hand corner, and the contour spacing is 1 $M_\odot$ pc^{-2}. Atomic gas within the dashed line is used for the subsequent analysis described in the text.

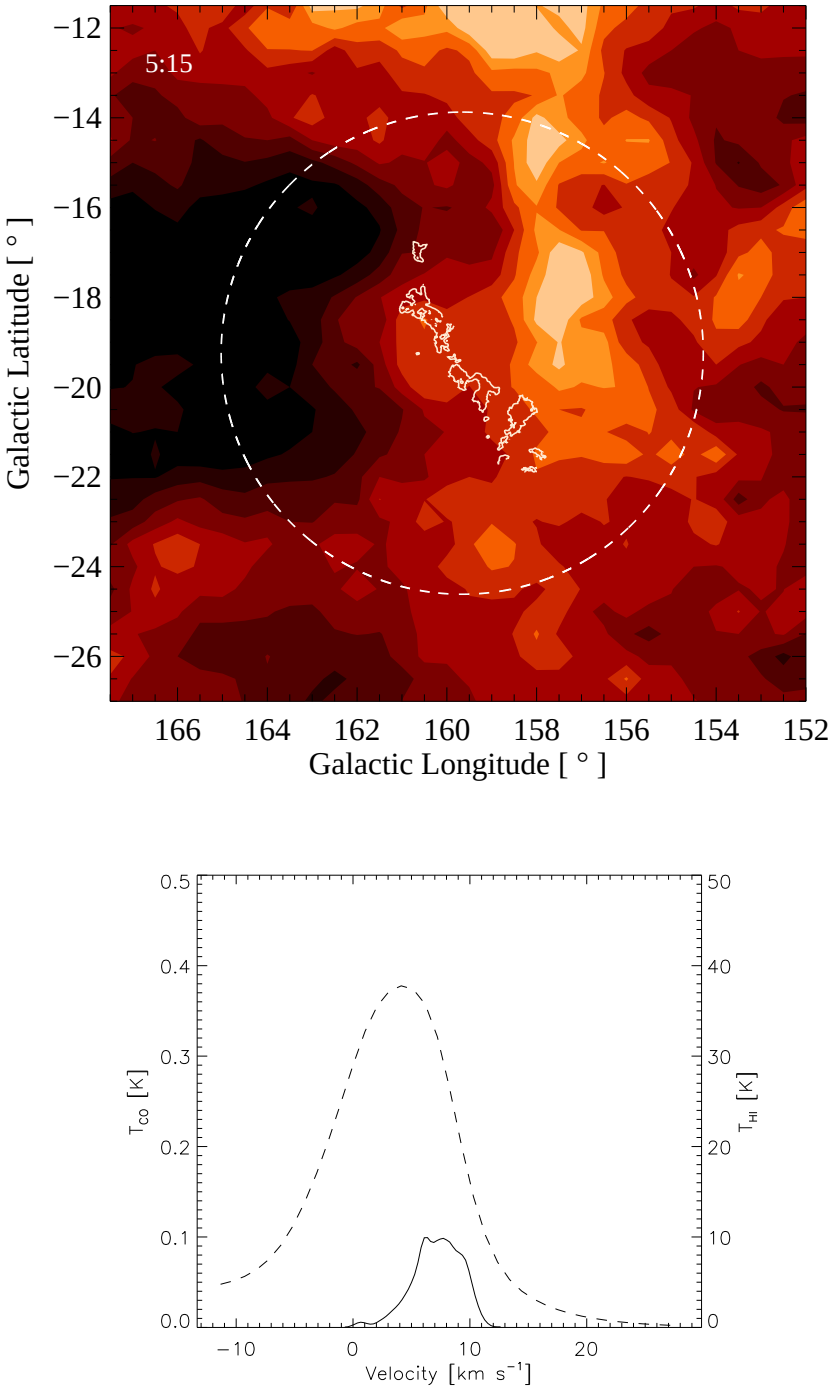

Figure 2.2: Perseus. Same as Figure 2.1.

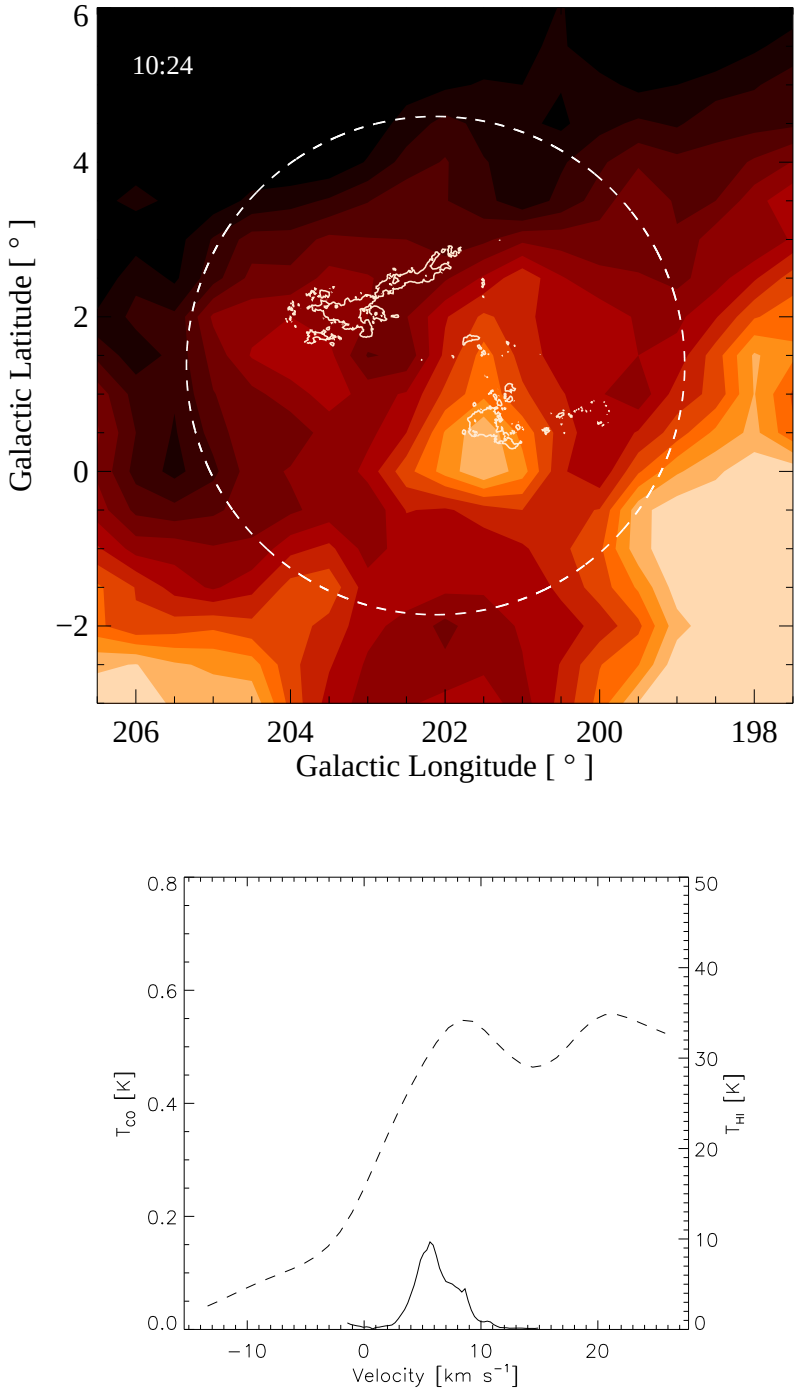

Figure 2.3: NGC 2264. Same as Figure 2.1.

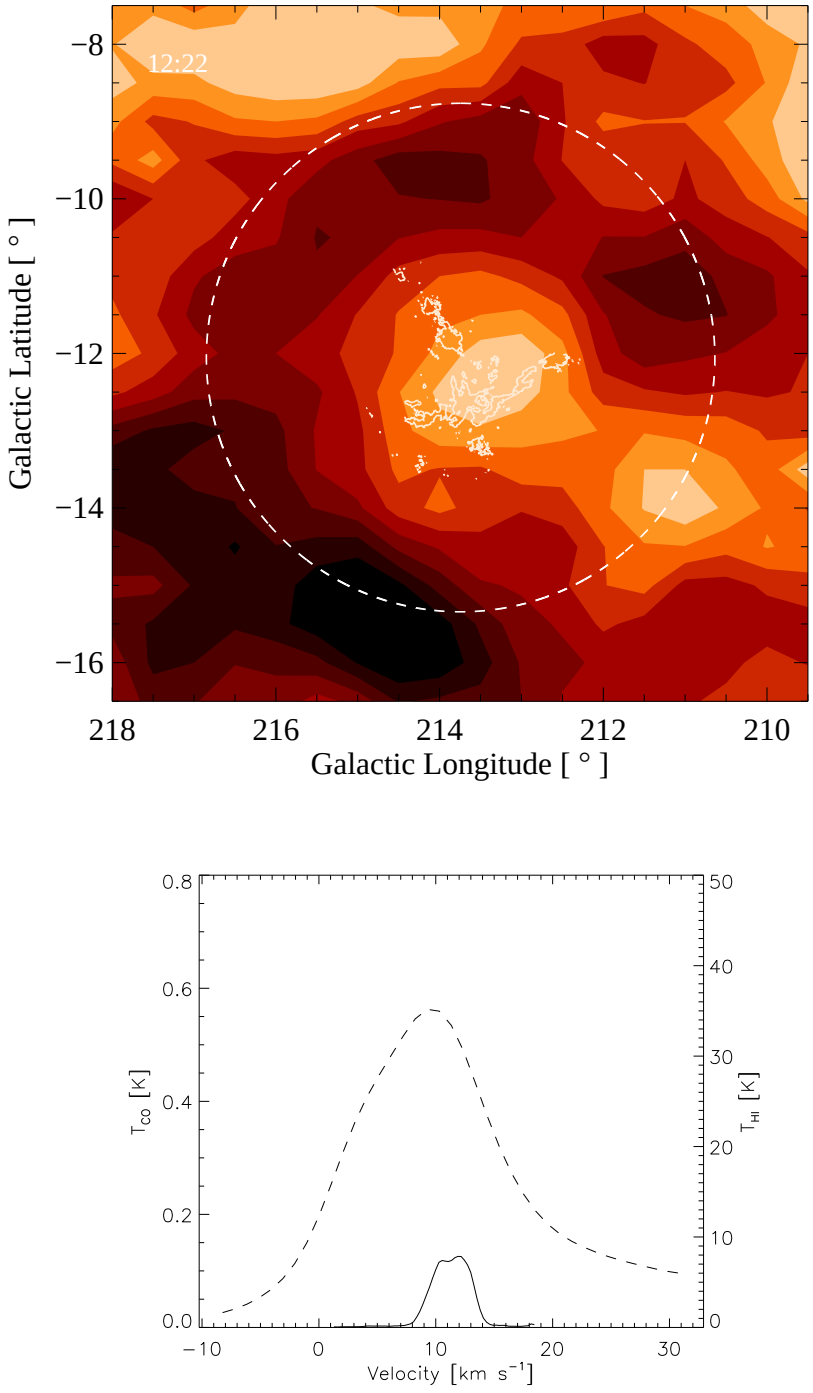

Figure 2.4: MonR2. Same as Figure 2.1.

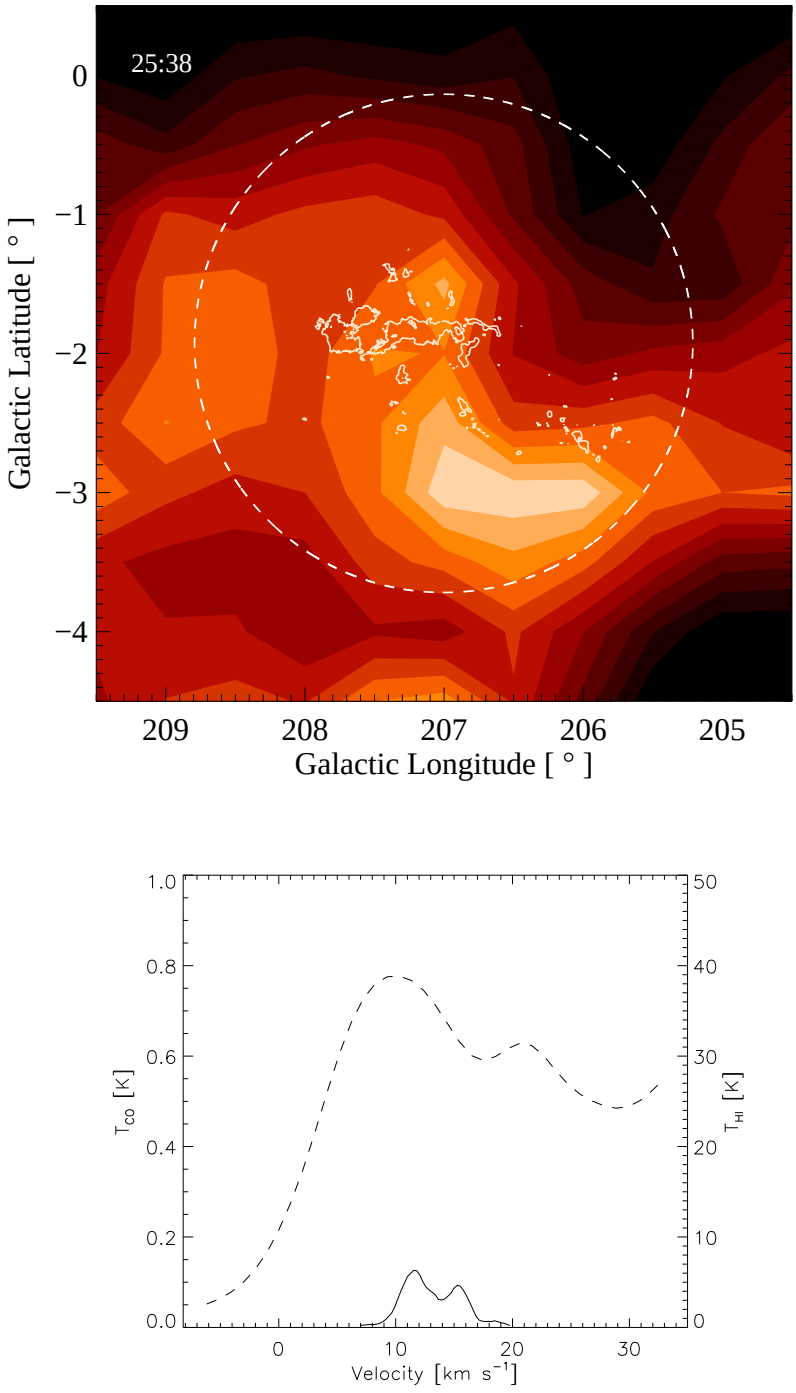

Figure 2.5: The Rosette. Same as Figure 2.1.

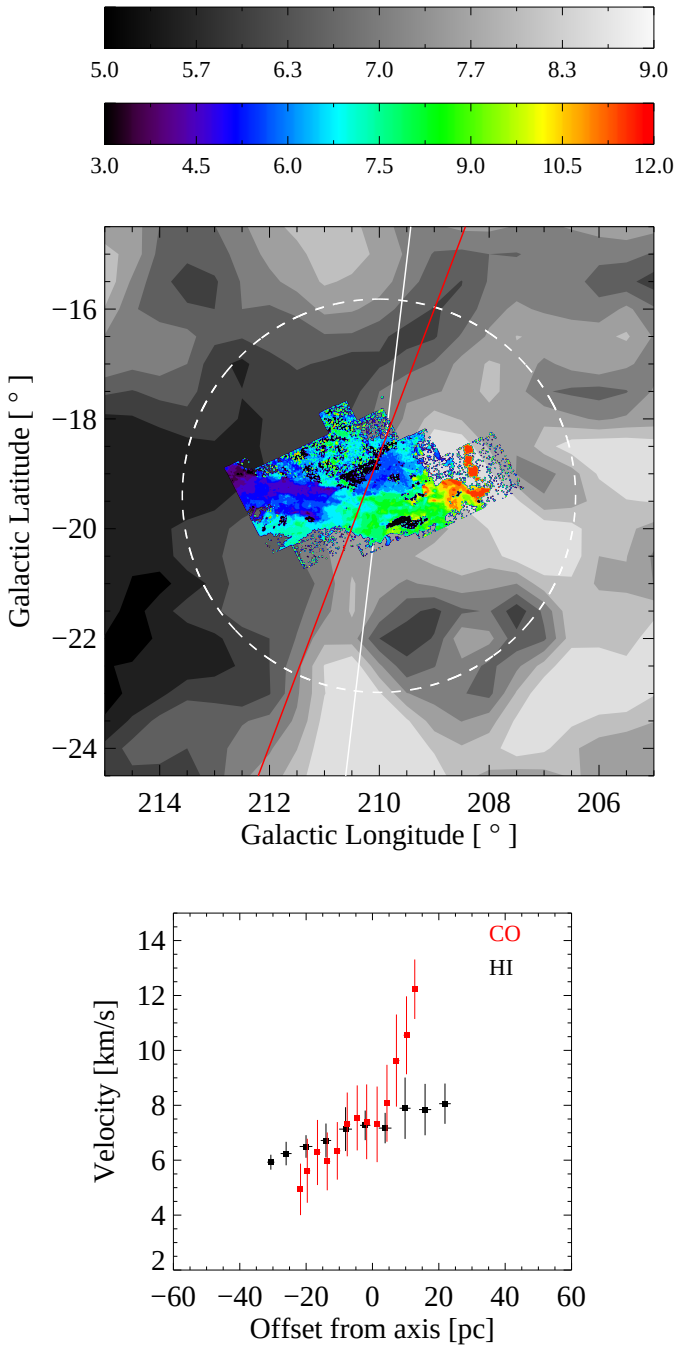

Figure 2.6: Orion A. The top figure shows the intensity-weighted first moment maps of HI (grayscale) overlaid with ^{13}CO (color). Both maps have contour spacings of 0.5 km s^{-1}, and the velocity ranges of the maps are indicated by the color bars. The bottom figure plots the central velocity versus perpendicular offset from the rotation axis for pixels in the above map located within the dashed line. The ^{13}CO data are binned every 3 pc and the HI data, every 6 pc. The error bars indicate the dispersion within the bins.

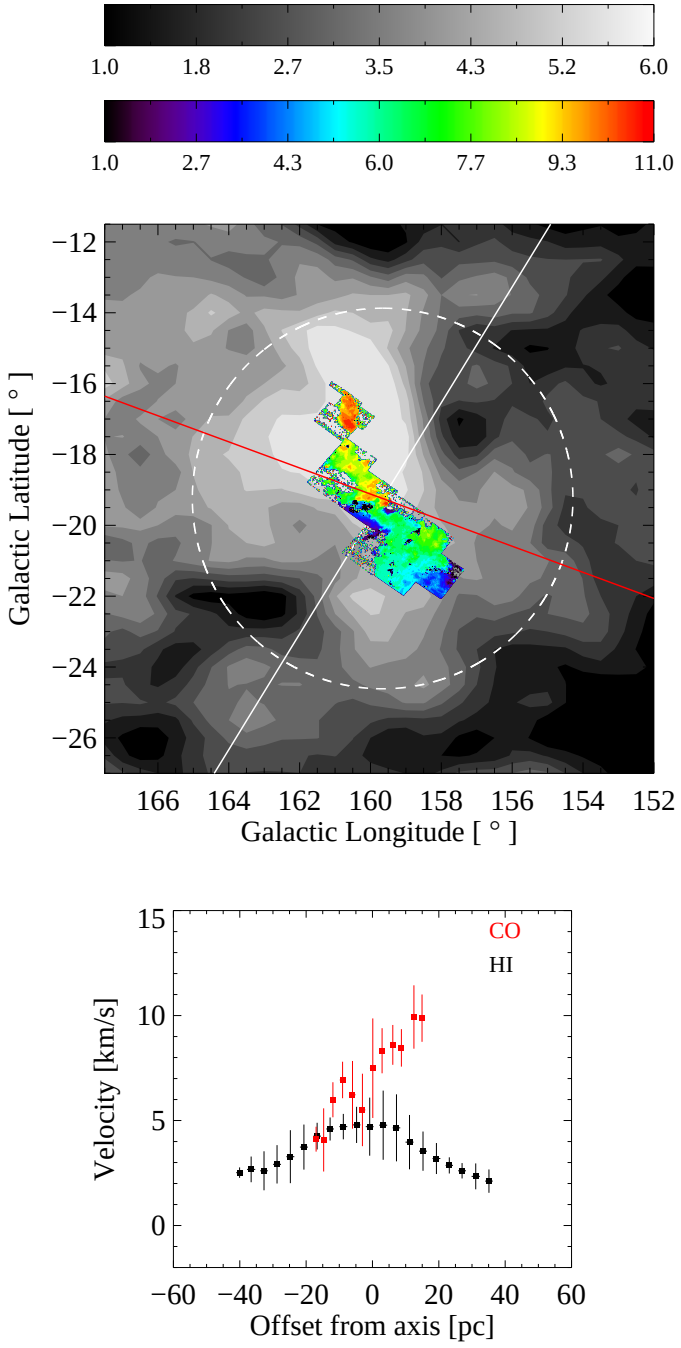

Figure 2.7: Perseus. Same as Figure 2.6, except the HI data in the position-velocity plot are binned every 4 pc. The non-linearity of the HI position-velocity plot indicates that there is not a linear velocity gradient over the entire region within the dashed circle. In the following figure, we see that by changing the reference position, there is a significant linear gradient in the atomic gas.

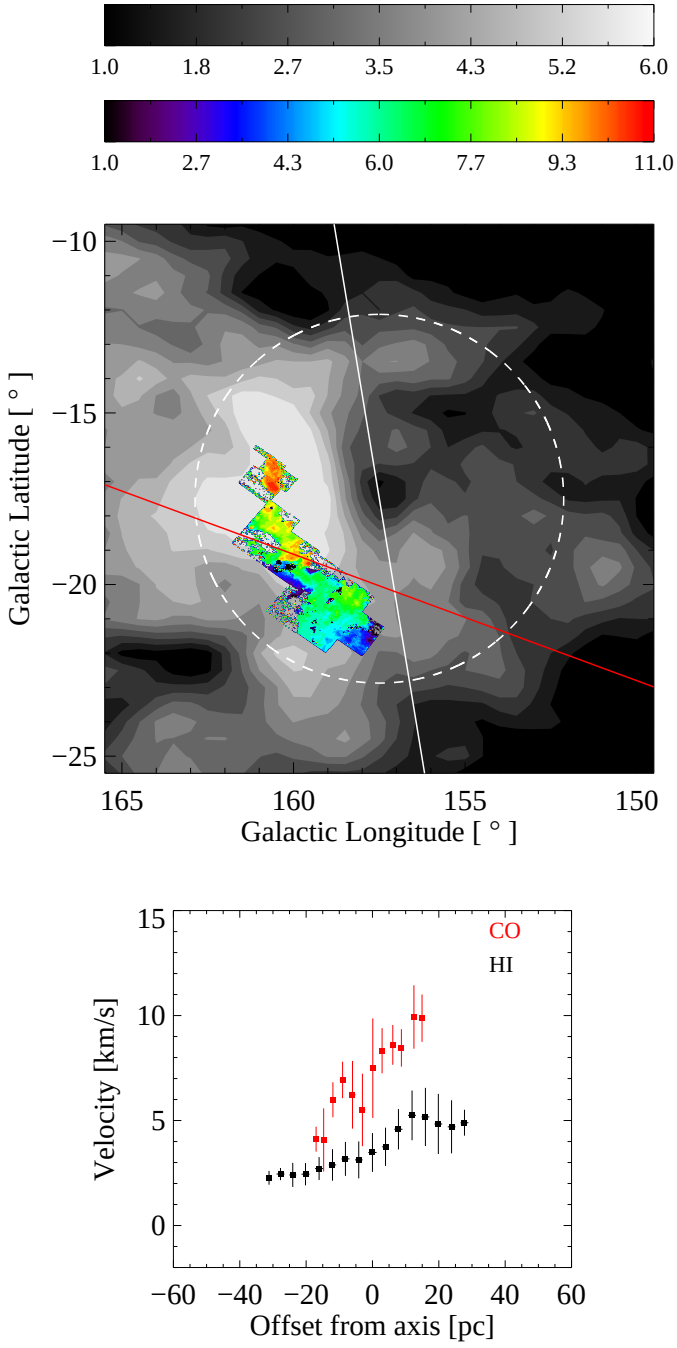

Figure 2.8: Perseus. Same as Figure 2.6, accept the HIdata in the position-velocity plot are binned every 4 pc. The surface density map in Figure 2.2 shows that a high-density HIpeak is located to the West of the molecular cloud. By changing the reference position to $l_0, b_0 = 157.5, -18$, near the center of the peak, we find that there is a significant linear gradient across the field centered on the peak.

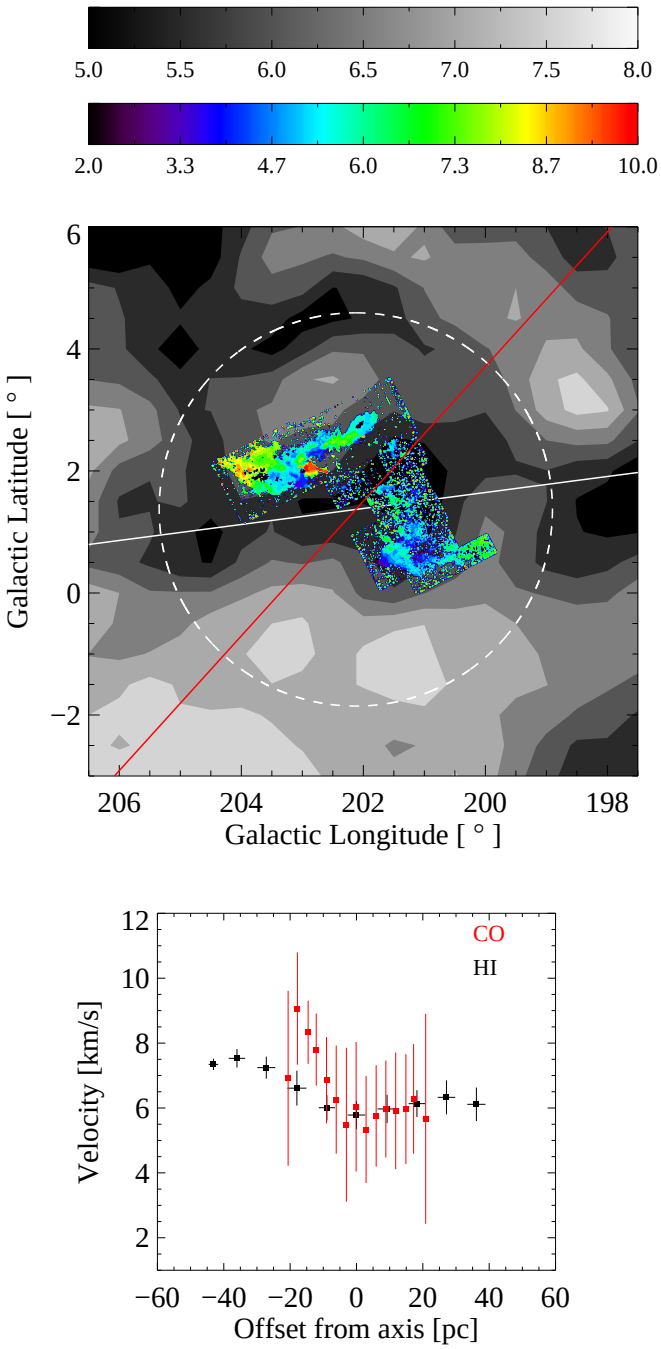

Figure 2.9: NGC 2264. Same as Figure 2.6, except the HI data in the position-velocity plot are binned every 9 pc. Although there is no significant linear gradient across the face of the GMC, we plot the "rotation axis" (red line) measured using Equation 2.10 as if there was.

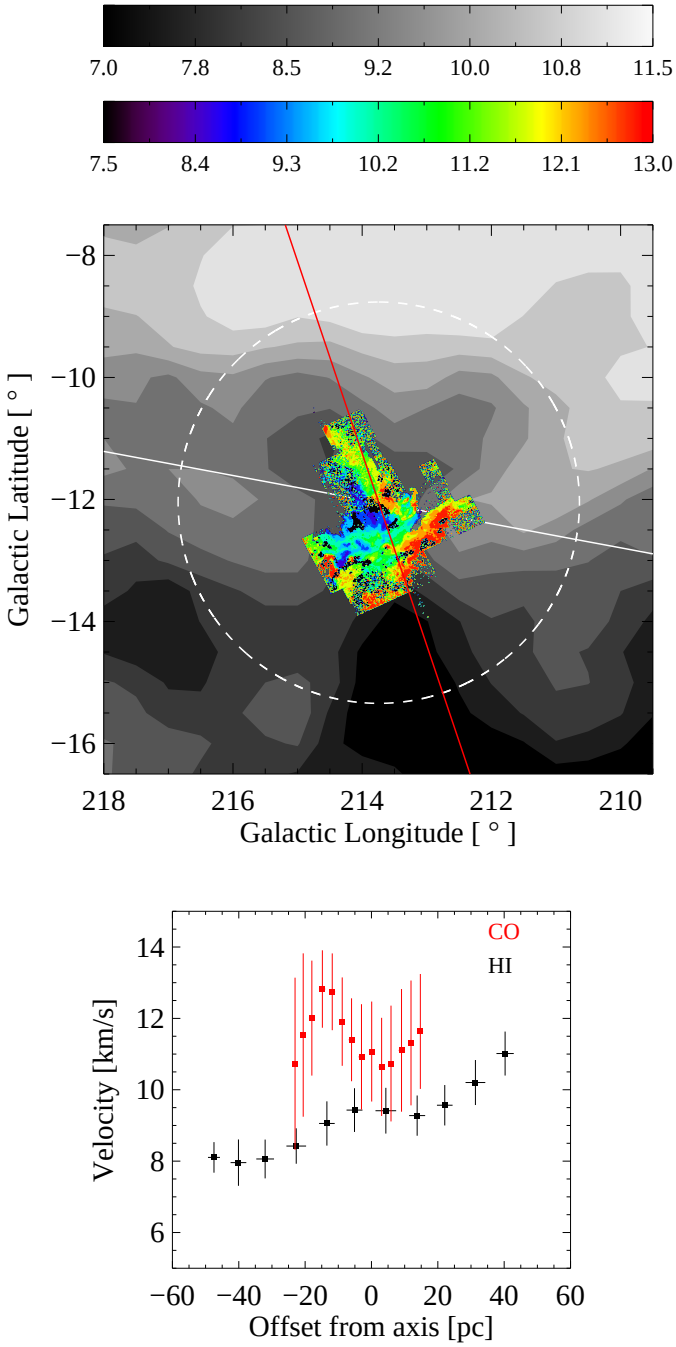

Figure 2.10: MonR2. Same as Figure 2.6, except the HI data in the position-velocity plot are binned every 9 pc. Although there is no significant linear gradient across the face of the GMC, we plot the "rotation axis" (red line) measured using Equation 2.10 as if there was.

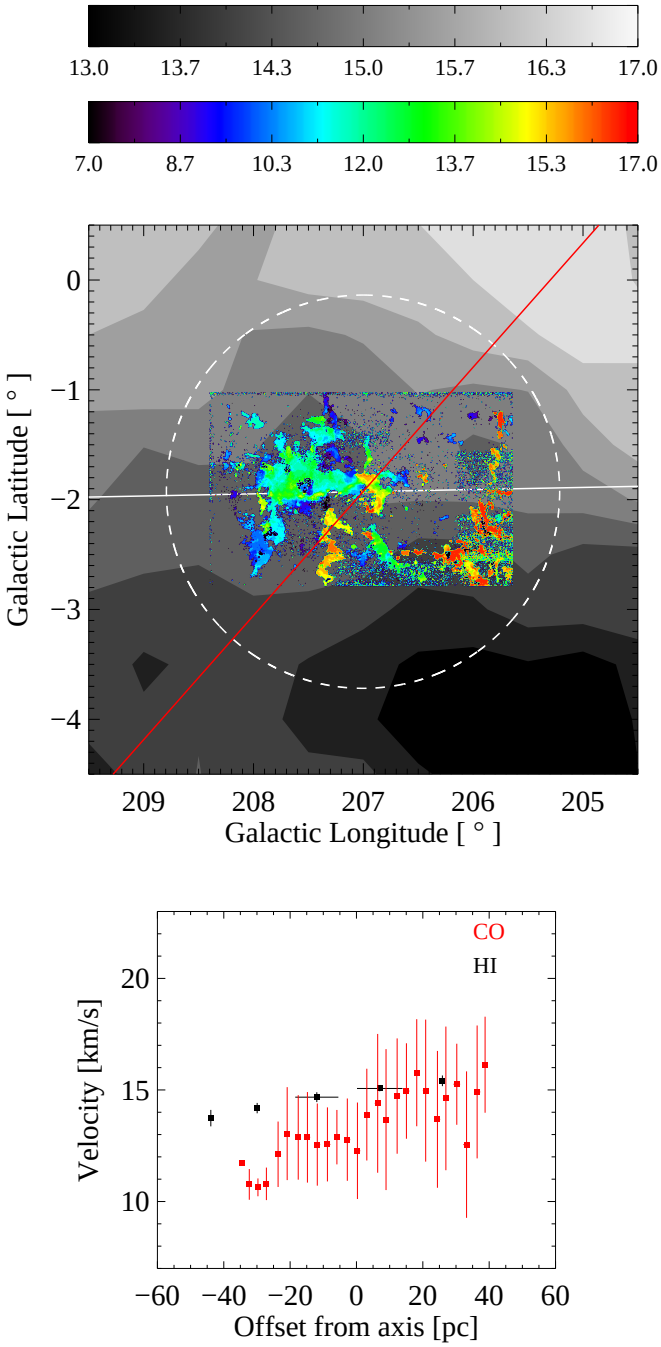

Figure 2.11: Rosette. Same as Figure 2.6, except the HI data in the position-velocity plot are binned every 17 pc.

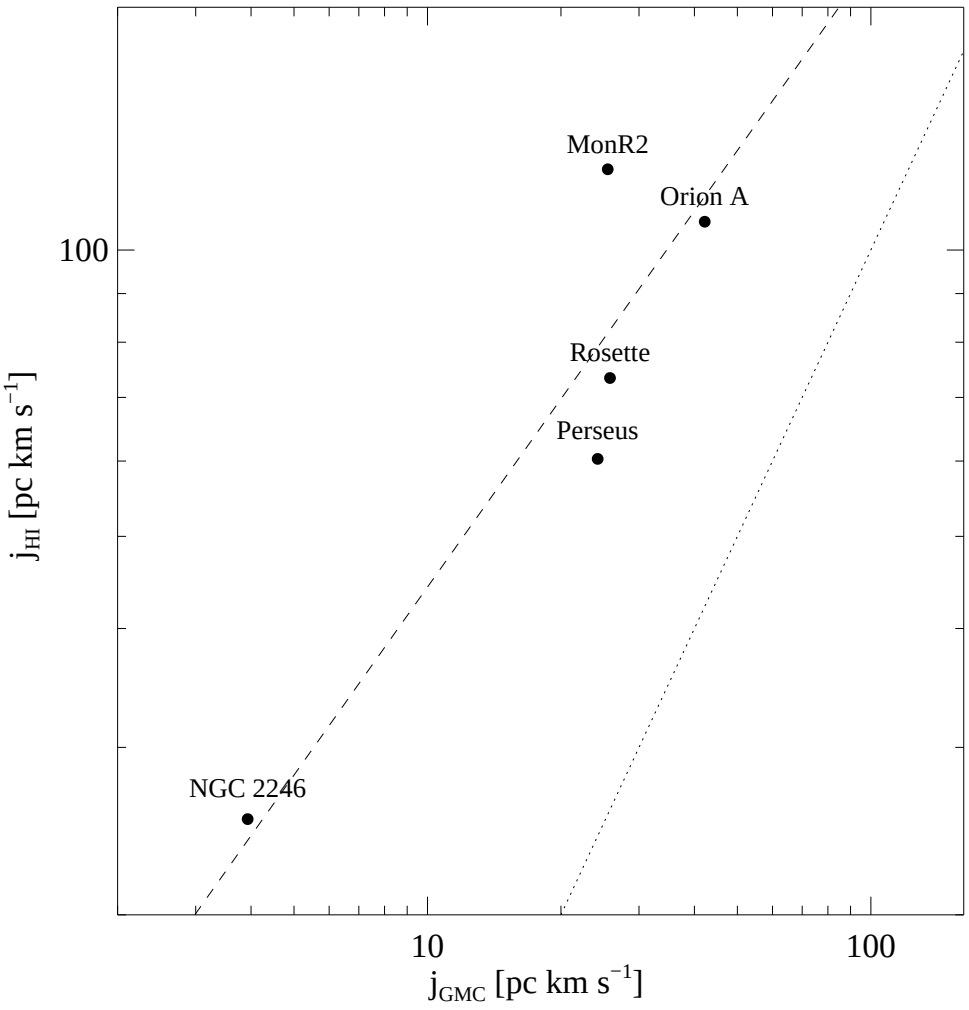

Figure 2.12: Specific angular momentum of the atomic hydrogen, $j_{\rm HI}$, versus GMC specific angular momentum, $j_{\rm GMC}$. The dashed line is a least-squares fit to the data: $j_{\rm HI} \propto j_{\rm GMC}^{0.66\pm0.20}$. Note that all of the data points lay above the hypothetical case in which $j_{\rm HI} = j_{\rm GMC}$ (dotted line).

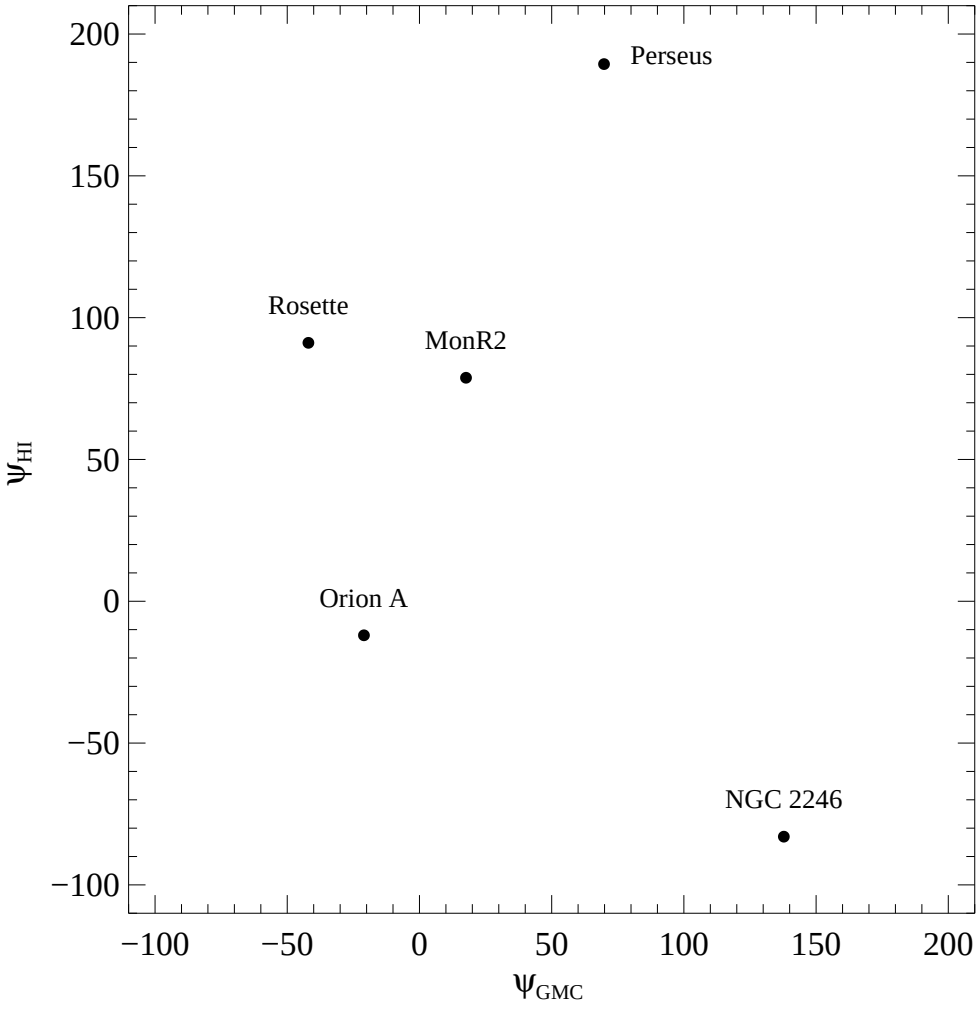

Figure 2.13: The gradient position angles of the atomic hydrogen, $\psi_{\rm HI}$, versus position angles of the GMCs, $\psi_{\rm GMC}$ appear to be uncorrelated.

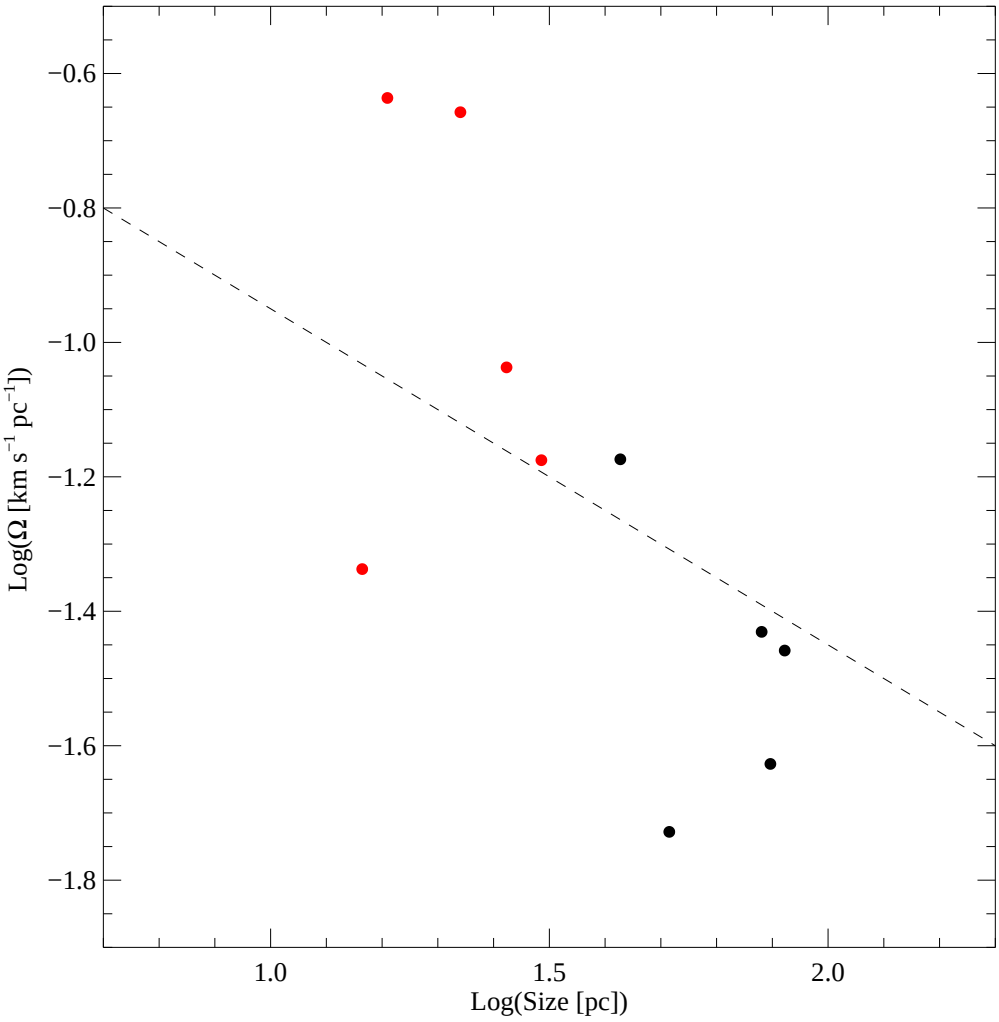

Figure 2.14: The gradient magnitude versus size for HI and GMCs (red points). Overplotted is the proportionality $\Omega \propto R^{-0.5}$ that Burkert & Bodenheimer (2000) found for turbulent cores.

Chapter 3

Angular Momentum in the Molecular and Atomic Gas of M33

Abstract

We present an analysis comparing the properties of 45 giant molecular clouds (GMCs) in M33 and the atomic hydrogen (HI) with which they are associated. High-resolution VLA observations are used to measure the properties of HI in the vicinity of GMCs and in regions where GMCs have not been detected. The majority of molecular clouds coincide with a local peak in the surface density of atomic gas, though 7% of GMCs in the sample are not associated with high-surface density atomic gas. The mean HI surface density in the vicinity of GMCs is 10 $M_\odot$ pc^{-2} and tends to increase with GMC mass as $\Sigma_{\rm HI} \propto M_{\rm GMC}^{0.27}$. Thirty-nine of the 45 HI regions surrounding GMCs have linear velocity gradients of ~ 0.05 km s^{-1} pc^{-1}. If the linear gradients previously observed in the GMCs result from rotation, 53% are counterrotating with respect to the local HI. And if the linear gradients in these local HI regions are also from rotation, 62% are counterrotating with respect to the galaxy. If magnetic braking reduced the angular momentum of GMCs early in their evolution, the angular velocity of GMCs would be roughly one order of magnitude *lower* than what is observed. Based on our observations, we consider the possibility that GMCs may not be rotating. Atomic gas not associated with GMCs has gradients closer to 0.03 km s^{-1} pc^{-1}, suggesting that events occur during the course of GMC evolution that may increase the shear in the atomic gas.

3.1 Introduction

Observations of molecular clouds at millimeter wavelengths show that they often have systematic velocity gradients. If, as many authors have argued, these velocity gradients are indicative of cloud rotation (e.g., Kutner et al. 1977; Blitz 1993; Rosolowsky et al.

2003), then angular momentum conservation should contribute to our understanding of the formation and evolution of molecular clouds. Significant progress was made in this direction when Rosolowsky et al. (2003) studied the angular momentum properties of giant molecular clouds (GMCs) in M33. Their measurements, based on high-resolution ^{12}CO($J = 0 \rightarrow 1$) observations, showed that M33 molecular clouds have velocity gradient magnitudes that are comparable to Milky Way GMCs (~ 0.1 km s^{-1} pc^{-1}). They found that typical gradients of the GMCs are 5 to 10 times smaller than would be expected from simple formation theories. Furthermore, just as Galactic GMCs are sometimes observed with gradients that are not parallel to the sense of Galactic rotation (e.g., Blitz 1993; Phillips 1999; Imara & Blitz 2010), Rosolowsky et al. (2003) found that the gradient directions of M33 GMCs are often not in alignment with the galaxy rotation. This is the so-called "angular momentum problem" of GMC formation.

It is our goal in this paper to address the question of the origin of velocity gradients in GMCs by doing a detailed analysis of the gradients in the atomic gas associated with the M33 molecular clouds catalogued by Rosolowsky et al. (2003). This paper is an extension of our study in the Milky Way in which we compared the velocity fields of GMCs to those of the local atomic gas surrounding them. Our study is prompted, in part, by observations in external galaxies showing that high-density HI appears to be a necesssary but not sufficient condition of GMC formation (e.g., Mizuno et al. 2001; Engargiola et al. 2003). Furthermore, it has been suggested that the discrepancy between observations and theoretical expectations in GMC angular momentum arises because angular momentum has been redistributed or "shed" during the course of GMC evolution (Mouschovias & Paleologou 1979; Mestel & Paris 1984; Rosolowsky et al. 2003, Kim et al. 2003). It seems reasonable, then, to look for evidence of this redistribution in the immediate environs of GMCs. And thus, we are motivated to search for clues to the angular momentum problem by comparing the velocity fields in GMCs to those of the atomic gas with which they are associated. Whereas Rosolowsky et al. (2003) make inferences about the HI velocity field from the M33 rotation curve, in this study, we take measurements of the gradients in the atomic gas associated with the GMCs directly from observations.

In the next section, we describe the observations used to perform this analysis. In §3.3, we provide the methodology and discuss the properties of atomic gas surrounding molecular clouds in M33. Implications for GMC formation and evolution are discussed in §3.4, and the results are summarized in §3.5.

3.2 Data

The data for the M33 molecular clouds are obtained from the Rosolowsky et al. (2003) catalog. Their work was a high-resolution continuation to the Engargiola et al. (2003) survey of 148 GMCs. Rosolowsky et al. observed 17 fields of the highest-mass clouds from their previous study in ^{12}CO($J = 0 \rightarrow 1$) using the C configuration of the BIMA array (Welch et al. 1996) in the fall of 2000 and spring of 2001. The $\sim 6''$ resolution of the observations,

corresponding to a linear resolution of 20 pc, was sufficiently high to resolve most GMCs and measure their sizes, which was done using the prescription of Rosolowsky & Leroy (2006). The high spatial resolution, in combination with the velocity resolution of 2 km s^{-1}, also allowed them to determine velocity gradients as small as ~ 0.01 km s^{-1} pc^{-1} in the GMCs. The magnitudes and directions of the gradients measured by Rosolowsky et al. are listed in Table 1.

Observations of the 21-cm line in M33 were taken from VLA archives and reduced by Schruba (A. Schruba & A. LeRoy, priv. comm.). The data, taken by Thilker et al. in 1997, were first described by Thilker et al. (2002). We converted the data cube from units of flux density (S_ν) to brightness temperature (T_b) via the Rayleigh-Jeans relation,

$$T_b = 1360 \frac{S_\nu \lambda^2}{b_{maj} \times b_{min}} \text{ K} = 6.055 \times 10^5 \frac{S_\nu}{b_{maj} \times b_{min}} \ K, \tag{3.1}$$

where S_ν is in Jy, $\lambda = 21.1$ cm is the observing wavelength, and $b_{maj} \times b_{min} = 8.3'' \times 7.5''$ is the synthesized beam size in arcseconds. The final map has $2''$ pixels. The LSR velocity range covered was -321 to -65 km s^{-1} with 1.3 km s^{-1} channel spacing, which was sufficient to include all of the gas in the disk of M33.

3.3 HI Properties

In order to compare the velocity gradients of molecular clouds with the gradients of the material from which they formed, we develop a set of criteria for selecting regions of atomic gas that are associated with the GMCs in our sample. The challenge is to determine *physically meaningful* boundaries of atomic gas surrounding a given molecular cloud. Thus, for each GMC, we begin by isolating subcubes in the VLA 21-cm data set that coincide with the GMCs kinematically and spatially. Properties of the molecular clouds and the regions surrounding them are listed in Table 1. We use a distance to M33 of 850 kpc for this analysis (Kennicutt 1998).

3.3.1 Selecting HI

Molecular clouds have well-defined boundaries at which a phase transition occurs between the molecular and atomic gas and, thus, they generally have well-defined dimensions and masses (e.g., Kutner et al. 1977; Blitz & Thaddeus 1980; Blitz 1993). The neutral gas associated with GMCs, however, does not have such distinct edges but rather has slower, more gradual transitions from high- to low-surface density material. In trying to determine appropriate boundaries for HI associated with GMCs, therefore, our challenge is to define regions that are large enough so that most of the HI belonging to a given system is included, and yet the regions must be centered close enough to the GMCs so that the associations are physically meaningful and we do not include too much unrelated material.

There are a number of properties of HI and GMCs observed both in the Milky Way and M33 that help us develop our selection criteria. First, an HI peak is typically found to have a velocity distribution which may be approximated by a Gaussian and whose line center falls near the CO line center of the affiliated molecular cloud (Andersson et al. 1991; Engargiola et al. 2003). We assume that atomic gas whose emission peaks near the line center of a given GMC is associated with that GMC. Since the velocity dispersion of the HI gas is several times larger than that of the CO, we select velocities falling within ± 25 km s^{-1} of the CO line center, so that we include as much emission as possible from the atomic gas associated with a given GMC. We decide to select from a wider range of velocities than the previous study (i.e., Chapter 2) because the work of Engargiola et al. (2003) shows that the HI associated with GMCs in M33 has emission extending as much as ± 35 km s^{-1} from the line center of the CO emission. And because M33 has a moderate inclination ($\sim 51°$; Corbelli & Salucci), the problem of source confusion is minimized, allowing us to select a more generous range of velocities. Changing the range of velocities by a 5 – 10 km s^{-1} does not significantly change the results. This is because the velocity maps we create are weighted by the intensity (see §3.3.3), so low-level emission occurring near the wings of the spectra does not make significant contributions to the velocity maps nor, therefore, to the measurement of the velocity gradients.

Identifying appropriate spatial boundaries is less clear-cut. Figure 3.1 shows that in M33, there is a spatial correspondence between GMCs and over-dense HI filaments. The radial accumulation length, R_A, can give us an idea of the extent of the atomic gas associated with GMCs. The size of an area which collapses to form a molecular cloud, R_A, can be estimated by requiring that the total HI mass in the region be equal to the observed mass of the cloud. The minimum value of R_A is determined by assuming that the initial configuration of atomic gas is a cylinder stretching to infinity in the direction perpendicular to the galactic disk:

$$\pi R_A^2 \Sigma_{\rm HI} = M_{\rm GMC}, \tag{3.2}$$

where $\Sigma_{\rm HI}$ is the average local surface density of atomic hydrogen, measured from the 21-cm data. We estimate $\Sigma_{\rm HI}$ for different sized regions centered on the GMCs. The mean value of $\Sigma_{\rm HI}$ spans a narrow range of values for regions having a size of ≤ 200 pc. Within 150 pc of molecular clouds, $\Sigma_{\rm HI}$ is 8.8 $M_\odot$ pc^{-2}; within 50 pc the average surface density is 11.5 $M_\odot$ pc^{-2}. Figure 3.2 plots the mean HI surface density within 70 pc of GMCs versus GMC mass. The figure shows that as GMC mass increases, the surface density of associated HI (and therefore HI mass) slowly increases as $\Sigma_{\rm HI} \propto M_{\rm GMC}^{0.27}$. We find that the average HI surface density in the vicinity of GMCs is roughly 10 $M_\odot$ pc^{-2}. This is the saturation level of atomic gas, observed in other spiral galaxies including the Milky Way, above which gas becomes primarily molecular (Martin & Kennicutt 2001; Wong & Blitz 2002; Bigiel et al. 2008). We calculate R_A for the slightly different estimates of $\Sigma_{\rm HI}$ and find a mean value of ~ 70 pc. Thus, we define HI regions in the 21-cm data cube as 140 pc $\times$ 140 pc $\times$ 50 km s^{-1} connected regions that are centered on the locations of GMCs in position and velocity space. Note that the area defined by the accumulation radius of a GMC contains

gas which has filled in the space previously occupied by that which formed the GMC.

The top-right panels of Figures 3.3 – 3.8 show surface density maps of the HI surrounding six of the 45 GMCs in this study. The bottom-right plot displays the average ^{13}CO and HI spectra toward the clouds. (The left-hand panels are described in §3.3.3.) Based on the spatial and kinematic proximity of GMCs to local maxima in the atomic gas, we observe three rough "classes" of clouds. Most GMCs in the catalog are spatially and kinematically coincident with local HI maxima. Clouds 1, 4, 39, and 45 are representative examples—at least 1/3 of the area of the molecular cloud coincides with a local peak in the atomic gas. Twenty-nine out of 45 the GMCs, 64%, fall into this class. The average GMC mass in this class is 2×10^5 $M_\odot$, with a dispersion of 80%. Another group of clouds is kinematically but not quite spatially coincident with HI maxima. GMCs in this class, including Clouds 16, 24 (Figure 3.6), 35, and 44 are located near the edge of a bright HI peak or sit on a filament between two peaks. The thirteen (29%) molecular clouds belonging to this class tend to have their mean LSR velocities offset from the mean HI velocity by a few km s^{-1}. The typical GMC mass in this second class is nearly 3 times smaller than in the first: 7×10^4 $M_\odot$, with a dispersion of 30%.

At least two GMCs in the catalog, Clouds 13 (Figure 3.5) and 38, are not associated with any local HI maximum. For both of these clouds, the center of the GMC is roughly 60 pc from the nearest peak in HI surface density, and the central velocity of the molecular and atomic clouds differ by at least 10 km s^{-1}. At 1.0×10^5 $M_\odot$, the total mass (molecular and atomic) in the region surrounding Cloud 13 is among the lowest in this study; only four other regions have less total mass, including Clouds 7, 8, 9, and 43. Cloud 38 does not appear to have any other characteristics, such as mass or size, that distinguishes it from others in the catalog. The one other case in which the there are no HI peaks in the vicinity of the molecular cloud may be Cloud 43. It has the lowest mass of the sample, and it is one of three GMCs farthest from the galactic center. However, because of its anomalously high LSR velocity of -74 km s^{-1}, compared to a mean galactic value of -111 km s^{-1} at that location, this molecular cloud—which was not observed in the original Engargiola et al. (2003) catalog—may be a false detection.

3.3.2 HI Without GMCs

Since over-dense regions of atomic hydrogen appear to be necessary but not sufficient for molecular cloud formation, we would like to know what the distinguishing features are between atomic gas harboring GMCs and regions of dense HI in which GMCs have not been detected. One way to address this issue is to search for velocity gradients along "non-GMC" HI filaments in M33 and then compare the properties to regions of HI containing GMCs. We would like to know, for example, if we can find regions of HI having low angular momentum—that is, angular momentum comparable to that which is observed in GMCs?

We select a random population of 45 over-dense HI regions—corresponding to the number of GMCs in the Rosolowsky et al. (2003) catalog—in the M33 map in which GMCs have not been observed. The regions, displayed in Figure 3.9, must have a mean surface density

of at least 10 $M_\odot$ pc^{-2} within 140 pc × 140 pc, the same size as the regions of HI associated with GMCs. Examples of the non-GMC surface density maps and HI spectra are shown in the right-hand panels of Figures 3.10 – 3.12.

To choose a relevant range of velocities at each location, we begin by estimating the mean velocity at which the emission peaks. The mean HI velocity, v_0, at a given location is derived from the intensity-weighted first moment of the entire velocity distribution. For the HI associated with GMCs, we select velocities falling within ±25 km s^{-1} of the CO line center. For the non-GMC HI, the surface density and velocity maps are created by integrating over velocities within ±25 km s^{-1} of v_0. Table 2 lists the coordinates, central velocities, and other properties of the non-GMC HI regions.

3.3.3 Velocity Gradients

We create intensity-weighted first moment maps both of the 140 pc × 140 pc × 50 km s^{-1} HI regions surrounding the molecular clouds and of the atomic gas not observed to contain molecular clouds. Following Imara & Blitz (2010), we fit planes to the resulting velocity maps and solve for the coefficients of the fit, which define the velocity gradient, $\Omega_{\rm HI}$, and the gradient direction, $\theta_{\rm HI}$. The maps of regions containing GMCs are shown in the upper-left panels of Figures 3.3 – 3.8 and, of non-GMC regions, in Figures 3.10 – 3.12. The results of the fits are given in Tables 1 and 2.

We find that (1) approximately 41 out of 45 of the HI patches harboring GMCs have significant linear velocity gradients; the mean for this group is 0.050±0.004 km s^{-1} pc^{-1} (Figure 3.13); (2) the mean of the gradients in the non-GMC HI, 0.033 ± 0.003 km s^{-1} pc^{-1}, are generally smaller than those measured in atomic gas observed to contain GMCs; (3) the position angles of the GMC rotation axes are generally *not* aligned with the axes of the surrounding atomic gas, as seen in Figure 3.15; and (4) about 62% of the HI regions associated with GMCs have position angles that differ from the axis of the galaxy by more than 90°; 42% of the non-GMC HI regions have positon angles that differ from the galaxy at least 90° (Figure 3.16).

Gradient Magnitudes

The upper-left panels of Figures 3.3 – 3.8 show the first moment maps of the atomic gas within 140 pc × 140 pc of six of the GMCs in this study.[1] The position-velocity plots on the bottom-left indicate whether planes are good fits to the first moment maps. These plots show the mean velocity at a given location in the velocity map as a function of perpendicular offset from the rotation axis. When a position-velocity plot can be fitted with a non-zero slope, m, this indicates that a plane is good fit to the first-moment map and that the velocity gradient can be assumed to be linear. The slope of the position-velocity plot, m, and the uncertainty in the least-squares fit of the slope, σ_m, are calculated for each gradient individually and are indicated in the figures; the ratio of these parameters is listed in Tables 1 and 2.

[1]See the Appendix for figures of the remaining HI regions.

Based on examination of the first moment maps and the position-velocity plots, we set the following criteria for degree of linearity in the gradients. Regions of HI having position-velocity plots $< 2\ \sigma_m$ have non-linear, random velocity fields. Regions with $m \approx 2$–$3\ \sigma_m$ have "marginally" linear velocity gradients; Figure 3.7 is an example of such a borderline case. Regions with $m \geq 3\ \sigma_m$ have unambiguously linear gradients. We find that 39 out of 45 HI regions associated with GMCs fall into this last category. Applying the same criteria to the non-GMC atomic gas, 43 regions have $m \geq 3\ \sigma_m$. Examples of the velocity fields in these regions are displayed in Figures 3.10 – 3.12. We do not observe a significant correlation between the gradient magnitudes of molecular and atomic gas (Figure 3.14). Tables 1 and 2 list the minimum linear extent of the gradients, as well as their magnitudes and directions.

Figure 3.13 displays the distribution of gradient magnitudes in the molecular and atomic gas. The mean of the magnitudes in the atomic gas surrounding GMCs, 0.050 ± 0.004 km s^{-1} pc^{-1}, are comparable to those measured in clouds in the Milky Way (Imara & Blitz 2010). On average, the magnitudes in the HI around GMCs are less than the typical 0.07 km s^{-1} pc^{-1} observed in GMCs. The average gradient observed in non-GMC HI is 0.033 ± 0.003 km s^{-1} pc^{-1}.

Gradient Directions

Many authors have argued that the linear velocity gradients observed in molecular clouds are caused by rotation (e.g., Kutner et al. 1977; Blitz 1993; Phillips 1999). If this is the case, the velocity gradient magnitude of a cloud is a measure of its angular speed and the gradient direction, θ, is perpendicular to its spin axis. Figure 3.15 demonstrates that 53% of GMCs have position angles that differ from the those measured in the surrounding atomic gas by more than 90°. Thus, if the molecular clouds are rotating, slightly more than half of the clouds are counter-rotating with respect to the atomic gas with which they are surrounded.

Rosolowsky et al. (2003) show that with respect to galactic position angle, $\phi_{\rm gal}$ (they use a value of 21°), GMCs are preferentially aligned with the galaxy and approximately 40° are retrograde rotators. We find that localized regions of HI—both with GMCs and not observed to contain GMCs—have gradient directions that are generally *unaligned* with respect to the galactic axis. Figure 3.16 shows that 62% of the HI regions with GMCs have gradient position angles that differ by more than 90° from the sense of galactic rotation. The median difference between HI position angles, $\phi_{\rm HI}$, and $\phi_{\rm gal}$ is $-90°$ for HI containing GMCs and $-60°$ for non-GMC HI.

Rosolowsky et al. (2003) demonstrate that GMCs lying close together tend to have their gradients aligned. Similarly, we find that neighboring regions of HI containing GMCs have comparable gradient directions, within 1° to 15° of each other. This is not surprising, since for neigboring GMCs we are taking measurements in overlapping regions of atomic gas. In fact, sixteen of the molecular clouds in this sample have accumulation radii which overlap by at least $(1/2)R_A$, raising the question of whether the distribution of $\phi_{\rm HI} - \phi_{\rm gal}$, shown in Figure 3.16, is biased due to over-counting. We consider this by taking the average $\phi_{\rm HI}$ for regions with accumulation radii overlapping by at least 1/2. We count such regions once

and find that the distribution of $\phi_{\rm HI} - \phi_{\rm gal}$ is not significantly altered. The median difference between between $\phi_{\rm HI}$ and $\phi_{\rm gal}$, in this case, is still $-90°$.

Figure 3.17 displays the velocity vector field of both groups of atomic gas. The arrows point in the direction of increasing velocity and have sizes proportional to the gradient magnitudes. Along the HI filament in the the North-East of M33, the non-GMC HI regions tend to have gradient directions pointing toward the South and South-West. And a string of non-GMC HI regions along the prominent filament in the South-West—Clouds 23A, 21A, 19A, 13A, 12A, 17A, and 15A—all have gradients pointing within 40° of due South. Gradient alignment is not always observed along filaments, however. The non-GMC HI regions in the nearly vertical filament at a right ascension of of $\sim 01^{\rm h}33^{\rm m}30^{\rm s}$ have a seemingly random distribution of gradient position angles. We also observe adjacent regions of HI associated with GMCs having large differences in gradient directions—for instance, Clouds 20 and 23 located near $\sim 01^{\rm h}34^{\rm m}$, 30°39 have gradients pointing in nearly opposite directions. Overall, neither population of HI appears to have a global, systematic pattern.

3.4 Implications for GMC Evolution

Assuming that molecular clouds are rotating, measurements of their angular momentum may reveal information about their past. The angular momentum per unit mass, j, is a useful quantity for comparing the angular momenta in different regions having comparable mass. For a rotating body with a power-law density profile, the specific angular momentum is

$$j = \beta \Omega R^2, \tag{3.3}$$

where β is a constant determined by the mass distribution, and R is the cloud radius. The constant β ranges from 0.33 for oblong bodies to 0.5 for disks having a constant mass distribution. We adopt the intermediate value, $\beta = 0.4$ (used for spherical structures having constant surface density), for GMCs. Note that because we do not know the inclination, i, of a given cloud along our line of sight, our measurement of Ω underestimates the true value, $\Omega / \sin i$ and, hence, our measurement of j is also underestimated. The position angle of the gradient is the direction of the total angular momentum vector.

Equation 3.3 may also be used to estimate the specific angular momentum initially imparted to a GMC by the ISM from which it forms. This depends on the process of GMC formation, and here, following Rosolowsky et al. (2003) and Imara & Blitz (2010)[2], we assume that GMCs collapse or condense from the surrounding atomic gas via a "top-down" mechanism, such as a large-scale gravitational instability. In this case, Ω is the velocity gradient in measured in the galactic disk at the location of the GMC, the accumulation radius R_A (Equation 3.2) is the size of the region that collapsed to form the GMC, and $\beta = 0.5$.[3]

[2] I.e., Chapter 2

[3] See Chapter § 2.3.4 for a more detailed discussion on the *expected* specific angular momentum initially imparted to a GMC.

Figure 3.18 displays the distribution of specific angular momenta for GMCs and the predicted j for the two populations of HI regions. The histograms show that, if the gradients observed in the molecular clouds are due to rotation, and assuming simple top-down formation, *the specific angular momentum of the molecular clouds is less than that of the atomic material from which they presumably formed.* Rosolowsky et al. (2003) found that the angular momentum expected from simple formation theories, including the Toomre and Parker instabilities, was higher than the observed value by an average factor of 5 and by as much as an order of magnitude. We measure an average factor of 27, with a ratio of more than an order of magnitude for 11 clouds. Figure 3.19 shows that $j_{\rm HI} > j_{\rm GMC}$ is always the case for the 36 resolved GMCs in the Rosolowsky et al. (2003) catalog. The reason that we are measuring larger ratios between the expected and observed j is because we have taken direct measurements of the HI velocity gradients, $\Omega_{\rm HI}$, whereas Rosolowsky et al. used a galactic rotation curve (Corbelli & Schneider 1997) to estimate $\Omega_{\rm HI}$. In other words, we have measured higher velocity gradients in the atomic gas surrounding GMCs than those determined from the galactic rotation curve. Overplotted in Figure 3.19 are data points from our study of five molecular clouds in the Milky Way (Imara & Blitz 2010). The Galactic GMCs, including Perseus, Orion A, NGC 2264, MonR2, and the Rosette, follow the trend of the M33 clouds in that the ratio of the specific angular momenta, $j_{\rm HI}/j_{\rm GMC}$, is always greater than unity and decreases with increasing $j_{\rm GMC}$ as $(j_{\rm HI}/j_{\rm GMC}) \propto j_{\rm GMC}^{-1.17\pm0.05}$. This proportionality is driven by the equality between $j_{\rm GMC}$ and its inverse, as we do not observe a significant correlation between $j_{\rm HI}$ and $j_{\rm GMC}$.

If GMCs inherit their rotation from the ambient HI from which they condense, one might expect their gradients to be much larger than observed. By conservation of angular momentum, in the absence of external forces, the ratio of the velocity gradient magnitudes before and after contraction is proportional to the radii of the rotating bodies: $\Omega_{\rm after}/\Omega_{\rm before} = (R_{\rm before}/R_{\rm after})^2$. Thus, to conserve angular momentum, a cloud that contracts from an accumulation length of 70 pc to a typical GMC radius of 25 pc would have to spin up by a factor of ~ 8. Figures 3.13(a), 3.13(b), and 3.14 show, however, that the magnitudes of GMC gradients are rarely much greater than those of the HI with which they are associated. From Figure 3.14 and Table 1 we see that the average value of $\Omega_{\rm GMC}/\Omega_{\rm HI}$ is 1.8 and reaches a maximum of 4.6. From conservation of angular momentum, we might also expect to find molecular clouds rotating in the same sense as the surrounding ISM from which they formed. As previously shown in Figure 3.15, however, the position angles in the GMCs and associated HI differ by at least 90° in over half of the regions.

These key results may imply one of the following: (1) Since GMCs formed, external torques, such as magnetic fields, may have caused the redistribution of angular momentum in the molecular clouds; (2) the HI with which GMCs are presently associated is unrelated to and unrepresentative of the atomic gas which originally formed the molecular clouds; or (3) the HI and GMCs are to some extent associated, but the origin of the GMC velocity gradients is not rotation. We consider each of these in turn below.

1. First, given that the interstellar media of galaxies are magnetized—the mean field strength of M33 is $\sim 6 \pm 2$ μG (Beck 2000)—magnetic fields potentially play dominant roles

in the formation and evolution of GMCs. For instance, many authors have advanced the Parker instability as a mechanism for GMC formation (e.g., Mouschovias et al. 1974; Blitz & Shu 1980; Shibata & Matsumoto 1991). Parker (1966) showed that in a gravitational field, a vertically layered gas coupled to a magnetic field is unstable to long-wavelength perturbations. The attractiveness of this magnetohydrodynamic (MHD) instability is that it has time and length scales that are comparable to the estimates of GMC lifetimes and to the distance observed between GMCs. Thus, if MHD effects play a significant role in the formation of GMCs, presumably they might also be responsible for redistributing angular momentum during later stages of GMC evolution.

While Rosolowsky et al. (2003) ruled out the Parker instability as the dominant mechanism for GMC formation because it over-predicts the amount of angular momentum observed in GMCs, they suggested that magnetic braking *could* slow down the rotation of GMCs, since the Alfvén speed in the ISM of M33 ($\sim$ 6 km s^{-1}) is comparable to the timescales of certain instabilities they evaluated. Yet because only 10% of the GMCs in their catalog have values of j approaching values expected from j(HI), they propose that magnetic braking must occur early on in the lifetime of GMCs or else occurs in the atomic gas surrounding GMCs. Mouschovias & Paleologou (1979) predicted a set of observational consequences for a rotating cloud collapsing out of an ISM threaded by a magnetic field that is initially perpendicular to the cloud's axis of symmetry. As the cloud collapses, one expectation is that the surrounding medium in the vicinity of the cloud will be set into corotation with cloud, a phenomenon that we do not observe in our results. Mouschovias & Paleologou also predicted that magnetic braking is highly efficient at slowing down rotation. According to their simulations, a rotating cloud with mass 10^3 $M_\odot$ and density 10^3 cm^{-3} will have its angular momentum reduced by at least 99% within 1 Myr, and the efficiency of magnetic braking will increase as the cloud contracts and as the density contrast between it and the surrounding medium increases. It would be worthwhile to find out what updated models predict for the rate of angular momentum loss in clouds having the masses and densities observed in GMCs.

2. If the atomic gas presently surrounding GMCs is unrelated to the past formation history of GMCs, the comparisons we are making may be invalid. In order to resolve this issue we need some sort of control field with which to compare the HI currently harboring GMCs. It is for precisely this reason that we performed the analysis, outlined in §3.3.2, on "non-GMC" HI regions. We found that the two populations of HI have distinctly different distributions of gradient magnitudes and position angles. The atomic gas associated with GMCs has a typical Ω of 0.05 km s^{-1} pc^{-1} and the non-GMC HI has a typical value of 0.03 km s^{-1} pc^{-1}. Also, the median difference between the position angle of the HI and that of the galaxy is $-90°$ for the former population and $-60°$ for the latter. These differences in Ω and ϕ between the two groups indicate that something unique has occurred in atomic gas associated with GMCs—presumably, something that has either *caused* the formation of the GMCs or has *resulted from* their formation.

We have already seen that the mean gradient magnitude in atomic gas associated with GMCs is greater than the typical gradient in non-GMC HI (§3.3.3). This implies that

HI containing GMCs has *higher* angular momentum (and/or shear) than non-GMC HI. We can evaluate how significant the difference is between the two populations by investigating the parameter $\beta_{\rm rot}$, the ratio of a cloud's rotational energy to its self-gravitational energy (Goodman et al. 1993):

$$\beta_{\rm rot} \equiv \frac{1}{3}\frac{\Omega^2 R^2}{GM/R}. \tag{3.4}$$

Figure 3.20 shows that non-GMC HI has a narrower distribution of $\beta_{\rm rot}$ and a lower mean, $\beta_{\rm rot} = 0.10 \pm 0.02$, than does atomic gas containing GMCs. Thirty-two of 45 of the non-GMC HI regions have $\beta_{\rm rot} < 0.1$, whereas only 14 of the HI regions containing GMCs have values of $\beta_{\rm rot} < 0.1$. Note that for HI regions containing GMCs, we calculate $\beta_{\rm rot}$ excluding the gravitational potential energy due to the GMCs within them (Figure 3.20 [a]). This group has an average $\beta_{\rm rot}$ of 0.39 ± 0.09, with 4 clouds having $\beta_{\rm rot} > 1$ (Clouds 1, 2, 17, and 43), implying that these regions may have a considerable amount of rotational energy. Note that for HI regions containing GMCs, we calculate $\beta_{\rm rot}$ excluding the gravitational potential energy due to the GMC within it (Figure 3.20 [a]). If we calculate $\beta_{\rm rot}$ including *all* of the gas within a given region, the average for HI containing GMCs goes down to 0.24 ± 0.04. The regions listed above still appear to have a considerable amount of rotational energy in comparison to their gravitational energy: $\beta_{\rm rot} = 0.90$, 0.75, 0.88, and 1.1 for clouds 1, 2, 17, and 43, respectively. Clouds having large values of $\beta_{\rm rot}$ can potentially become stable against gravitational instabilities. It is difficult to see how GMCs could have formed under such conditions. These observations suggest that between the time prior to the onset of GMC formation to the time after formation, processes occur that increase Ω observed in the HI associated with GMCs. An alternative is that GMCs preferentially form from gas having high Ω, possibly in regions that are unstable to gravitational collapse.

It is also worth pointing out that HI regions falling into Classes 2 and 3 (see §3.3.1)—regions where the GMCs are not quite spatially coincident with local HI maxima—tend to have lower gradient magnitudes ($\Omega \sim 0.04$ km s^{-1} pc^{-1} with a dispersion of 40%) than regions in Class 1 (0.06 km s^{-1} pc^{-1} with a dispersion of 50%). We apply a t-test and find that the difference between the two classes is significant to the 95% confidence level. However, molecular clouds belonging to either class do not appear to have different distributions of Ω; that is GMCs in both Class 1 and Class 2 have the same average gradient ($\sim$ 0.07 km s^{-1} pc^{-1}). This suggests that activity within the GMCs may have more of an impact on the surroundings than the surrounding environment has on the velocity fields of the GMCs.

3. Given that the gradient directions of the GMCs and associated atomic gas are generally not aligned, this raises the possibility that the linear velocity gradients observed in molecular clouds may not be caused by rotation. Burkert & Bodenheimer (2000) demonstrated that turbulent velocity fields can also cause linear gradients. They found that the gradient magnitude of turbulent cores scales with size as $\Omega \propto R^{-0.5}$. As shown in Figure 3.21, fitting a power-law relationship to the gradients observed in the HI surrounding GMCs as a function of the accumulation radius, we find $\Omega_{\rm HI} \propto R_A^{-0.7\pm0.2}$. The relationship between $\Omega_{\rm GMC}$ and size for the 36 resolved GMCs is $\Omega_{\rm GMC} \propto R^{-0.3\pm0.2}$. Figure 3.21 also displays

a combined fit for atomic gas and GMCs, which is in good agreement with the Burkert & Bodenheimer (2000) result.

In a previous study, (Imara & Blitz 2010)[4], we found that star formation activity provides a reasonable explanation of the gradients observed in a small sample of Milky Way molecular clouds. In at least three out of five cases, including Orion A, NGC 2264, and the Rosette, the velocity fields may have been produced by expansion driven by highly energetic stellar winds. The location of HII regions corresponds to the highest velocities of the molecular material in these clouds. Though the sample was too small to make a firm conclusion, it appears that the HII regions within these molecular clouds may also be influencing the morphology of the associated atomic gas. In NGC 2264 and the Rosette, for instance, there are local peaks of HI that appear to have been swept up by expanding molecular gas. Following up this study of M33 with an analysis comparing the locations of HII regions to the kinematic properties of GMCs could provide useful insight to how the velocity fields of the latter evolve.

3.5 Summary

We have presented a detailed comparison of the velocity fields in 45 GMCs detected in M33 by Rosolowsky et al. (2003) using BIMA observations and the atomic hydrogen with which they are associated. Using high-resolution VLA 21-cm observations to create surface density and intensity-weighted first-moment maps of the HI, we also compared the properties of atomic gas containing molecular clouds with atomic gas in which molecular clouds have not been detected. Based on our measurements, including the velocity gradient magnitudes and directions of these regions, we make the following conclusions:

1. The average surface density of atomic hydrogen associated with the GMCs is ~ 10 $M_\odot$ pc^{-2}, similar to the saturation level of HI above which gas becomes primarily molecular in other galaxies, including the Milky Way (Martin & Kennicutt 2001; Wong & Blitz 2002; Bigiel et al. 2008). A power-law relationship exists between the HI surface density and GMC mass: $\Sigma_{\rm HI} \propto M_{\rm GMC}^{0.27\pm0.06}$.

2. We observe three categories of GMCs, based on their proximity to local peaks in the atomic gas. The majority of GMCs (64%) coincide spatially and kinematically with local HI peaks. Twenty-nine percent of GMCs are located near the edge of an HI peak, or sit between two peaks. Clouds in this category tend to have their mean LSR velocities offset from the mean HI velocity by a few km s^{-1}. The remaining three clouds (7%) are not associated with HI maxima and the mean velocities of the molecular cloud and atomic gas are offset by ~ 10 km s^{-1}.

3. Thirty-nine out of 45 of the HI regions in the vicinity of GMCs have linear velocity gradients of around 0.050 km s^{-1} pc^{-1} and spanning 0.013 to 0.13 km s^{-1} pc^{-1}. If GMCs are rotating and initially inherited their angular velocity from the surrounding HI, conservation of angular momentum would require that the angular speed of a typical GMC ($R \approx 25$ pc)

[4]I.e., Chapter 2.

speed up by a factor of 8. The average value of $\Omega_{\rm GMC}/\Omega_{\rm HI}$, however, is only 1.8. Magnetic braking has been used by some authors to explain how the slowing of GMC rotation may have occurred.

4. Fifty-three percent of the molecular clouds have gradients whose directions differ from the gradient direction in the local HI by more than 90°. If the gradients in the GMCs were caused by rotation, this implies that over half of them are counter-rotating with respect to the atomic gas with which they are surrounded. This measurement is difficult to reconcile with the notion that gradients are due to rotation and that GMCs form in a simple top-down matter.

5. Gradients in the atomic gas associated with GMCs generally have larger magnitudes than expected from galactic differential rotation alone. Also, 62% of these regions have gradient position angles that differ from the sense of galactic rotation by more than 90°.

6. We examined the properties of high-density HI regions in which molecular clouds have not been detected and found that they have a lower range of velocity gradients, $\sim$ 0.03 km s^{-1} pc^{-1}, than regions where GMCs are observed. This suggests that something occurs during the course of GMC evolution that may increase the shear of the atomic gas. Neither population of atomic gas has gradient directions that are preferentially aligned with the kinematic position angle of the galaxy, nor did we find a correlation between gradient magnitude and direction in either population.

7. A power-law relationship exists between gradient magnitude and size in both the molecular clouds and the HI surrounding them. For GMCs, $\Omega_{\rm GMC} \propto R^{-0.3\pm0.2}$; for HI, $\Omega_{\rm HI} \propto R_A^{-0.7\pm0.2}$, where R_A is the accumulation length. The combined relationship is $\Omega \propto R^{-0.5\pm0.1}$, consistent with what Burkert & Bodenheimer (2000) found for the velocity fields of turbulent molecular cores.

8. Our analysis raises considerable doubt to the hypothesis that the origin of GMC velocity gradients is rotation. Alternative explanations worth exploring include turbulence, shear, and star formation activity.

Table 3.1: **Cloud Properties in M33**

Cloud	R.A.	Dec.	$\Omega_{\rm GMC}$	$\Omega_{\rm HI}$	$\theta_{\rm HI}$	$\theta_{\rm HI}-\theta_{\rm GMC}$	Extent	$M_{\rm HI}$	$\lvert m\rvert/\sigma_m$
	[J200]		[0.01 km s^{-1} pc^{-1}]		[deg]	[deg]	[pc]	[10^5 $M_\odot$]	
1	1 33 52	30 39.3	8.38	12.51	-175	6	140	1.8	11.20
2	1 33 53	30 39.0	2.29	8.66	-178	-114	140	1.9	5.08
3	1 33 44	30 38.9	9.58	7.14	-159	-77	160	2.8	10.51
4	1 33 56	30 41.3	10.10	6.07	-134	-90	120	2.1	6.61
5	1 33 55	30 41.6	13.60	7.18	-166	-106	160	2.3	9.33
6	1 33 57	30 41.1	11.90	7.13	-151	-170	180	2.0	10.80
7	1 33 50	30 37.5	8.36	2.83	-133	83	170	1.1	3.45
8	1 33 52	30 37.7	3.49	7.24	177	-149	140	1.4	5.63
9	1 33 52	30 37.5	2.20	6.02	168	177	130	1.5	5.38
10	1 33 59	30 41.5	1.90	2.50	108	124	160	1.7	3.06
11	1 34 00	30 40.8	9.53	3.63	170	146	120	3.0	3.55
12	1 33 54	30 37.7	10.60	[3.66]	[-103]	[-135]	[...]	1.4	1.50
13	1 33 59	30 41.8	3.29	[1.31]	[121]	[167]	[...]	1.0	0.92
14	1 33 52	30 37.0	7.70	5.41	-108	-17	170	1.7	5.91
15	1 33 40	30 39.2	9.57	4.65	-151	-84	120	2.4	5.60
16	1 33 40	30 38.7	1.25	[3.88]	[-93]	[147]	[...]	1.5	2.57
17	1 34 02	30 38.6	14.00	13.10	-171	-167	160	3.8	19.09
18	1 34 10	30 42.0	4.70	8.31	149	-34	120	2.3	11.37
19	1 33 50	30 33.9	0.69	6.19	-169	138	160	2.9	16.25
20	1 34 08	30 39.2	8.74	5.81	-157	-140	170	2.5	17.93
21	1 33 43	30 33.2	4.40	[1.28]	[-96]	[126]	[...]	3.1	0.46
22	1 34 13	30 42.0	6.75	4.29	116	23	140	2.3	4.59
23	1 34 13	30 39.1	7.77	2.98	-63	59	180	3.1	9.78
24	1 34 07	30 47.8	4.05	4.25	-128	-123	180	3.7	11.49
25	1 34 06	30 47.9	7.24	3.65	-137	-28	110	3.6	5.84
26	1 33 40	30 45.6	11.90	2.61	150	-69	60	3.2	3.52
27	1 33 40	30 45.9	1.54	5.21	135	23	130	3.8	6.09
28	1 34 10	30 36.3	3.49	2.22	-57	-33	150	3.1	4.54
29	1 34 16	30 39.3	8.91	3.08	146	-43	180	4.2	8.28
30	1 33 40	30 46.2	9.44	6.91	121	-81	190	3.7	21.49
31	1 33 58	30 48.7	3.58	[1.64]	[67]	[153]	[...]	2.7	2.17
32	1 34 01	30 48.9	4.76	[1.72]	[174]	[111]	[...]	2.1	0.94
33	1 34 11	30 48.4	5.35	4.35	-10	44	100	4.2	7.42
34	1 34 07	30 49.0	13.80	4.58	43	-25	110	2.9	3.80
35	1 33 57	30 49.0	9.35	2.45	128	-96	170	2.7	8.03
36	1 33 59	30 49.3	3.96	2.02	156	-149	110	2.7	6.89
37	1 34 09	30 49.1	7.37	2.28	-6	-30	130	4.9	3.75
38	1 34 07	30 50.0	9.67	5.17	-111	132	160	1.7	5.02
39	1 34 13	30 33.7	7.47	8.72	-165	-55	150	4.8	14.86
40	1 34 33	30 46.5	7.93	5.82	150	-65	140	4.8	6.94
41	1 34 33	30 46.8	6.97	6.11	90	-84	120	4.8	5.87
42	1 34 34	30 46.3	8.22	4.37	100	-129	90	4.1	4.67
43	1 33 22	30 25.9	9.95	5.33	-109	-5	150	0.2	5.87
44	1 34 38	30 40.4	10.80	4.07	115	145	170	4.2	5.91
45	1 34 39	30 40.7	8.56	4.48	133	101	140	5.0	7.09

The cloud numbers correspond to those in the Rosolowsky et al. (2003) catalog. The gradient magnitudes and directions are Ω and θ, respectively. The difference between the HI and GMC gradient directions is $\theta_{\rm HI}-\theta_{\rm GMC}$. The extent of the gradient is listed for HI regions having linear gradients. The gradient measurements of clouds in which linear gradients have not been detected ($|m|/\sigma_m < 3$) are listed in brackets.

Table 3.2: **Properties of Non-GMC HI in M33**

Cloud	R.A. [J2000]	Dec. [J2000]	Ω_{HI} [0.01 km s^{-1} pc^{-1}]	θ_{HI} [deg]	M_{HI} [10^5 $M_\odot$]	v_0 [km s^{-1}]	m/σ_m
1A	1 35 05	30 45.1	[0.62]	[-78]	3.5	-211	3.98
2A	1 35 06	30 50.2	1.76	-172	4.6	-231	13.82
3A	1 35 05	30 51.9	3.30	-96	4.0	-233	16.50
4A	1 34 52	30 54.1	3.21	-173	4.1	-246	27.62
5A	1 34 39	30 55.9	2.41	-148	4.0	-260	26.35
6A	1 34 31	30 57.2	2.32	144	3.7	-267	17.39
7A	1 34 24	30 56.8	1.25	-147	3.8	-267	20.41
8A	1 34 16	30 52.2	1.11	84	3.1	-263	8.01
9A	1 34 04	30 54.7	3.14	-82	3.3	-258	22.09
10A	1 33 16	30 31.4	0.67	168	4.0	-119	8.54
11A	1 33 17	30 33.5	9.54	-127	3.4	-133	41.02
12A	1 32 58	30 31.0	3.67	-178	5.2	-128	22.84
13A	1 32 51	30 31.6	2.46	147	4.2	-135	21.41
14A	1 32 35	30 30.6	2.01	133	5.0	-126	25.62
15A	1 32 57	30 27.6	2.61	-151	3.1	-116	31.86
16A	1 32 55	30 26.1	0.91	-43	2.6	-109	14.65
17A	1 32 49	30 28.6	2.08	-148	3.2	-118	19.45
18A	1 32 29	30 27.3	1.21	120	3.8	-115	6.07
19A	1 32 50	30 33.2	1.70	171	4.8	-140	13.11
20A	1 32 31	30 35.4	0.83	31	6.1	-140	8.85
21A	1 32 44	30 35.1	3.49	140	5.3	-147	29.62
22A	1 32 41	30 36.0	3.06	-93	4.9	-150	12.16
23A	1 32 50	30 35.2	7.96	-170	4.3	-147	61.35
24A	1 33 50	30 44.4	4.44	-178	4.0	-219	24.53
25A	1 33 11	30 48.4	6.11	-68	5.9	-201	49.19
26A	1 33 12	30 49.6	5.22	-113	6.2	-202	39.74
27A	1 33 13	30 50.7	3.19	78	5.4	-206	22.55
28A	1 33 19	30 51.8	2.82	-146	3.9	-216	18.78
29A	1 33 14	30 53.2	1.79	0	5.4	-213	6.82
30A	1 33 17	30 55.2	[0.82]	[-101]	3.9	-212	2.24
31A	1 33 17	30 56.4	[0.35]	[55]	5.1	-214	1.65
32A	1 33 26	30 48.4	5.07	-117	4.0	-206	45.15
33A	1 33 36	30 49.1	6.26	-169	3.5	-224	67.19
34A	1 34 40	30 30.4	3.58	-84	3.6	-162	23.48
35A	1 34 14	30 25.8	6.03	-176	3.8	-126	34.44
36A	1 33 46	30 20.9	1.58	-1	3.5	-109	15.13
37A	1 33 01	30 24.0	5.15	8	3.6	-106	30.46
38A	1 32 48	30 23.6	2.67	9	3.4	-104	14.41
39A	1 32 40	30 25.6	1.26	-127	3.0	-115	15.00
40A	1 34 34	30 44.7	8.61	-144	4.1	-220	81.84
41A	1 34 36	30 38.3	4.25	-122	4.3	-189	51.84
42A	1 34 25	30 39.3	3.42	139	2.3	-202	25.70
43A	1 34 08	30 31.7	6.90	-111	2.5	-148	43.44
44A	1 34 14	30 46.6	3.56	70	4.0	-243	46.75
45A	1 33 13	30 44.9	3.55	179	4.1	-187	19.76

Properties of HI regions in which GMCs have not been detected.

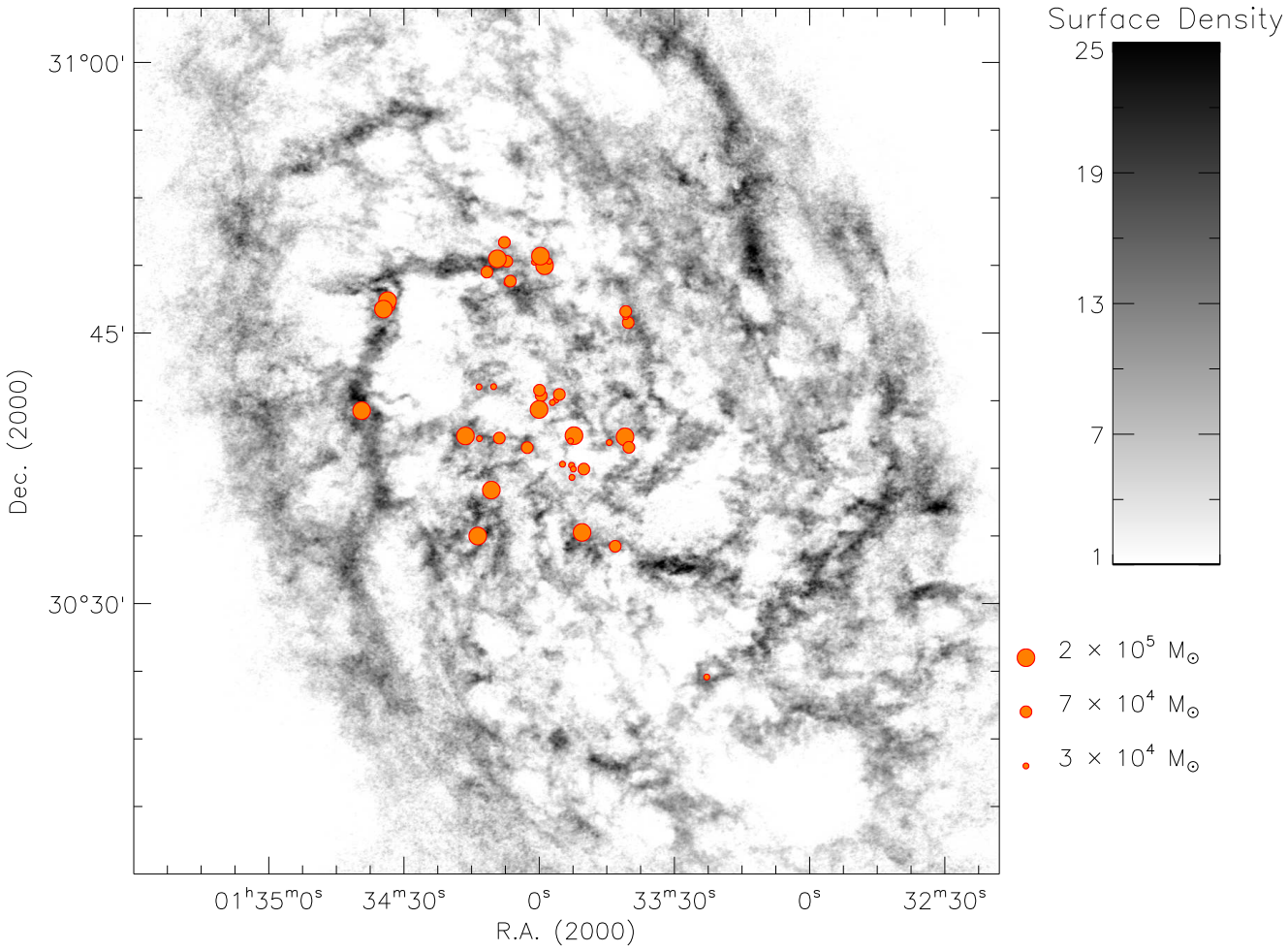

Figure 3.1: M33: Grayscale image in units of $M_\odot$ pc^{-2} of the 21-cm emission of the central $45' \times 45'$ field. Molecular clouds are overlaid with area scaled to mass. All GMCs lay in regions of high-density HI. The galactic mean of $\Sigma_{\rm HI}$ is roughly 4 $M_\odot$ pc^{-2}, while the mean value in the vicinity of GMCs is 10 $M_\odot$ pc^{-2}.

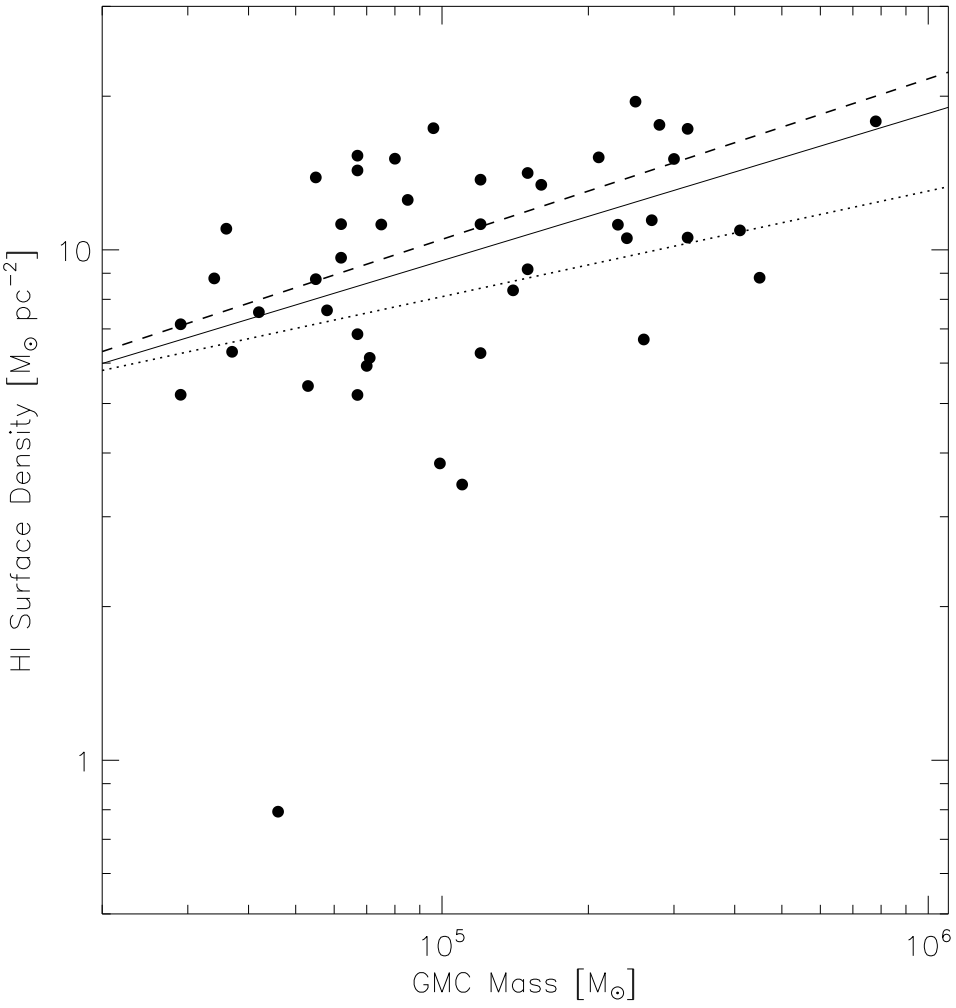

Figure 3.2: Mean local $\Sigma_{\rm HI}$ versus GMC mass. The solid line is the least-squares fit for the plotted points, which show the mean HI surface density within 70 pc of GMCs. The dotted and dashed lines are the least-squares fits for $\Sigma_{\rm HI}$ within $R < 150$ pc and $\Sigma_{\rm HI}$ within $R < 50$ pc, respectively. The average surface density of atomic gas surrounding GMCs is $10.2 \pm 0.4\ M_\odot\ {\rm pc}^{-2}$. The HI surface density increases slowly with increasing GMC mass as $\Sigma_{\rm HI} \propto M_{\rm GMC}^{0.27\pm0.06}$, where the power-law is the mean of the three least-squares fits and the uncertainty is the 1-σ spread.

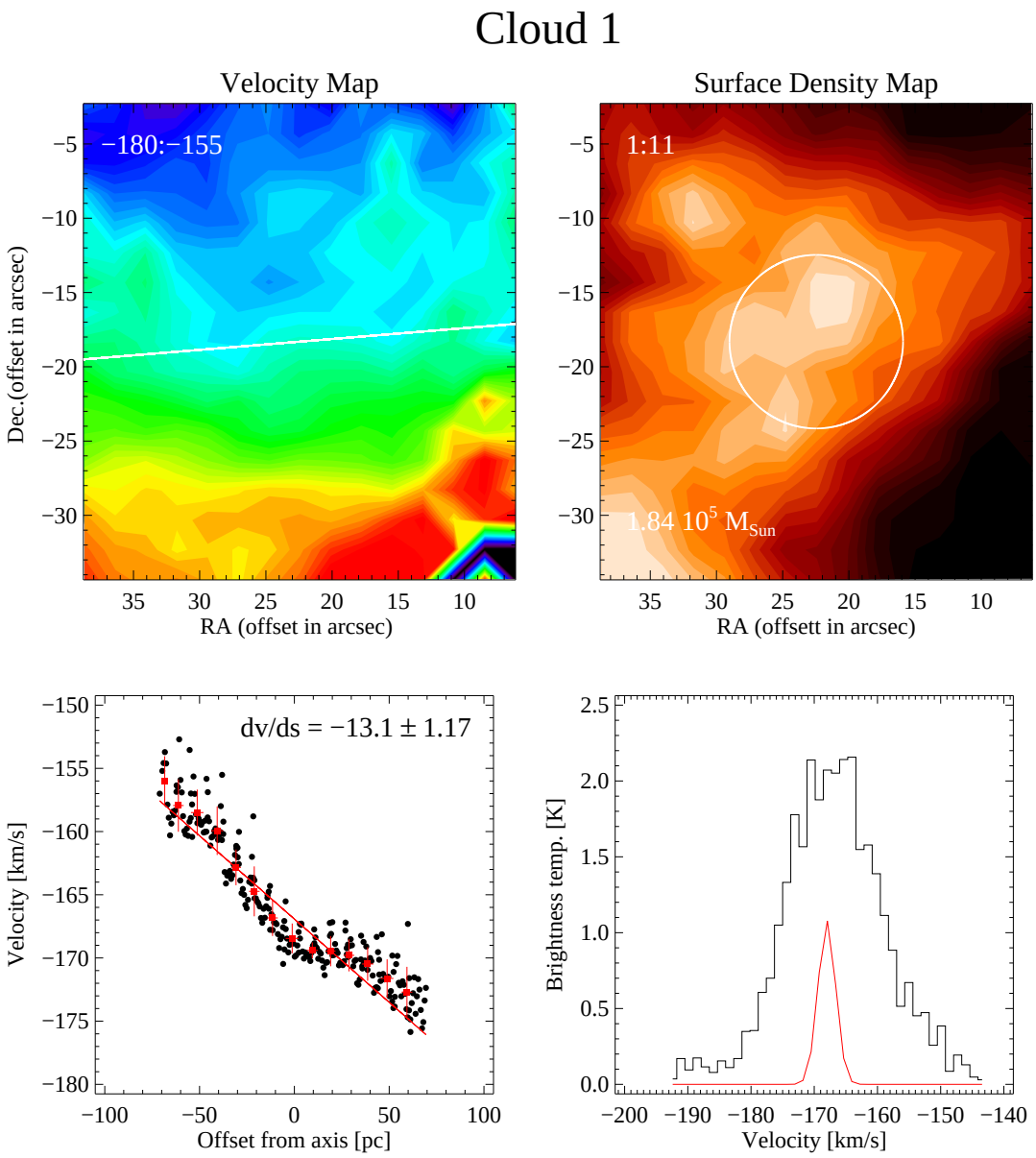

Figure 3.3: Cloud 1: The top left figure shows the intensity-weighted first moment map of the HI with the gradient axis overlaid. The velocity range of the map is indicated in the top left corner in units of km s^{-1}; red represents the maximum speed. Below this figure is a plot of the central velocity at a given location in the first-moment map versus perpendicular offset from the gradient axis; the linearity of the plot indicates that a plane is a good fit to the first-moment map. The top right figure is a surface density map of the HI overlaid with a circle proportional to the size of the associated GMC. The range of HI surface densities displayed in the map are in the top right corner in units of $M_\odot$ pc^{-2}, and the total HI mass in the region is written in the bottom left corner. Below is a plot of the average spectra of HI emission (black) and CO emission (red) toward the region.

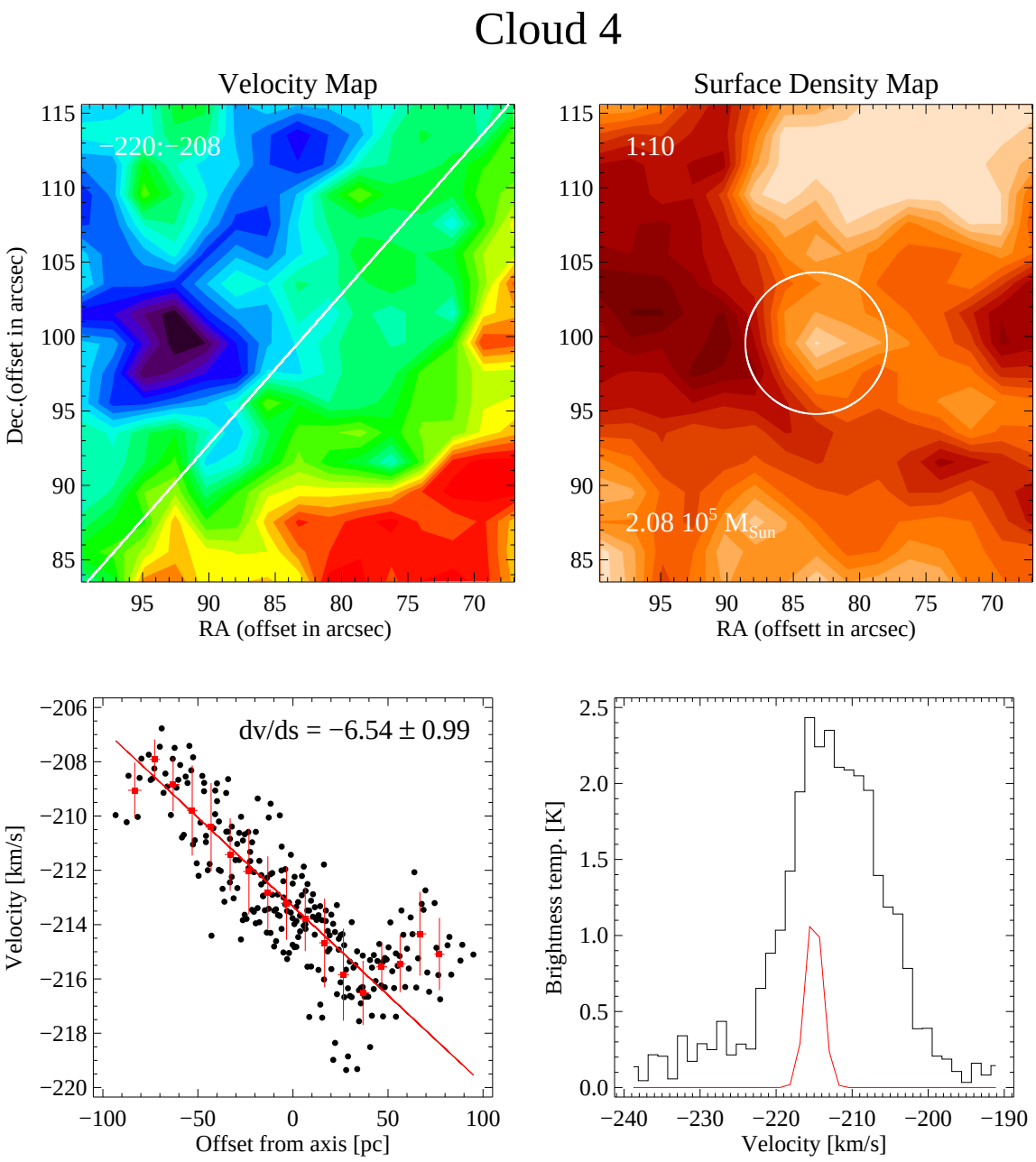

Figure 3.4: Cloud 4: Same as Figure 3.3.

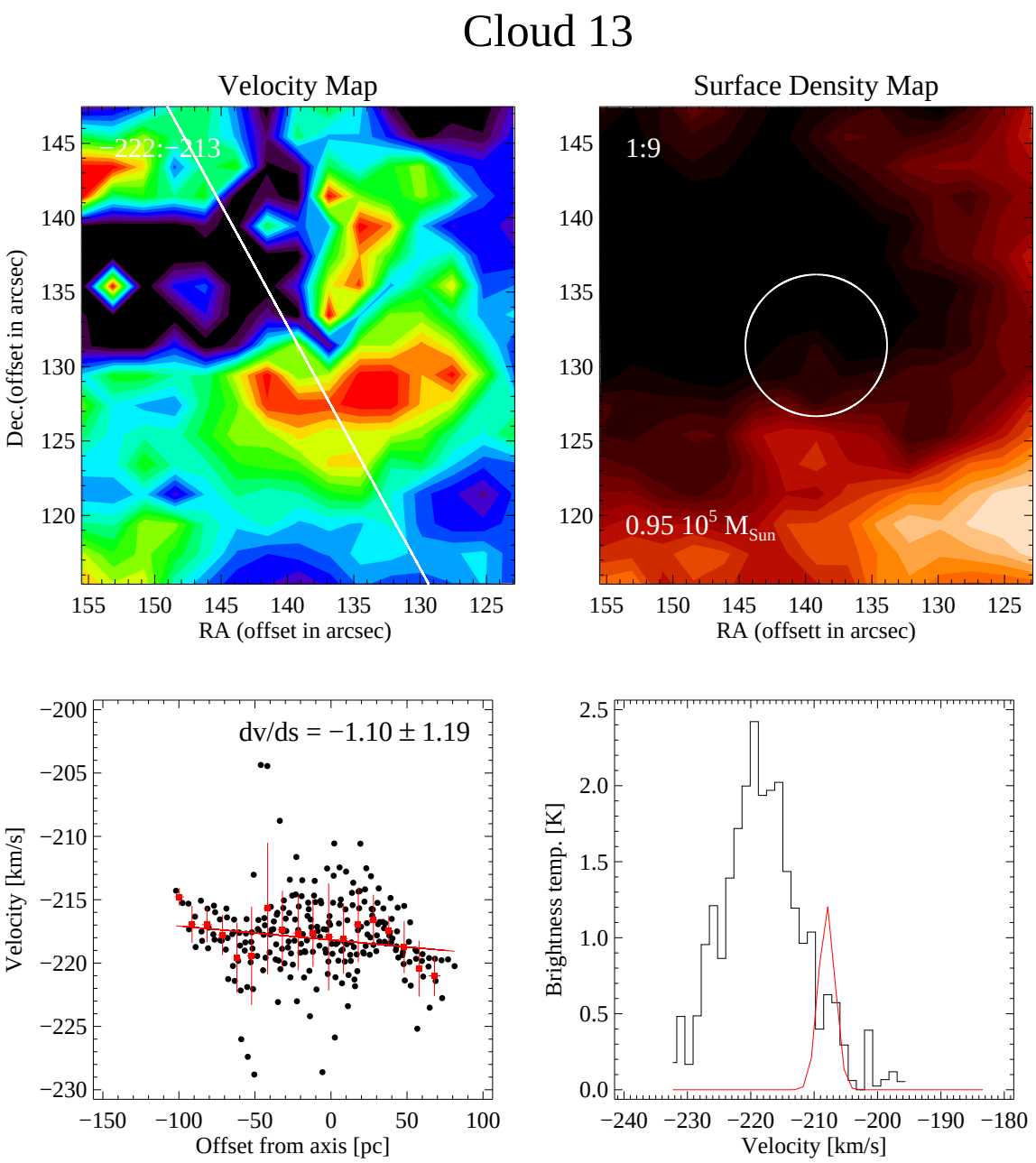

Figure 3.5: Cloud 13: Same as Figure 3.3, accept that the slope of the position-velocity plot is close to zero, indicating that a plane is not a good fit to the first-moment map. Cloud 13 is an example of a region that does not exhibit a linear gradient and in which the GMC does not coincide with a local maximum in the HI.

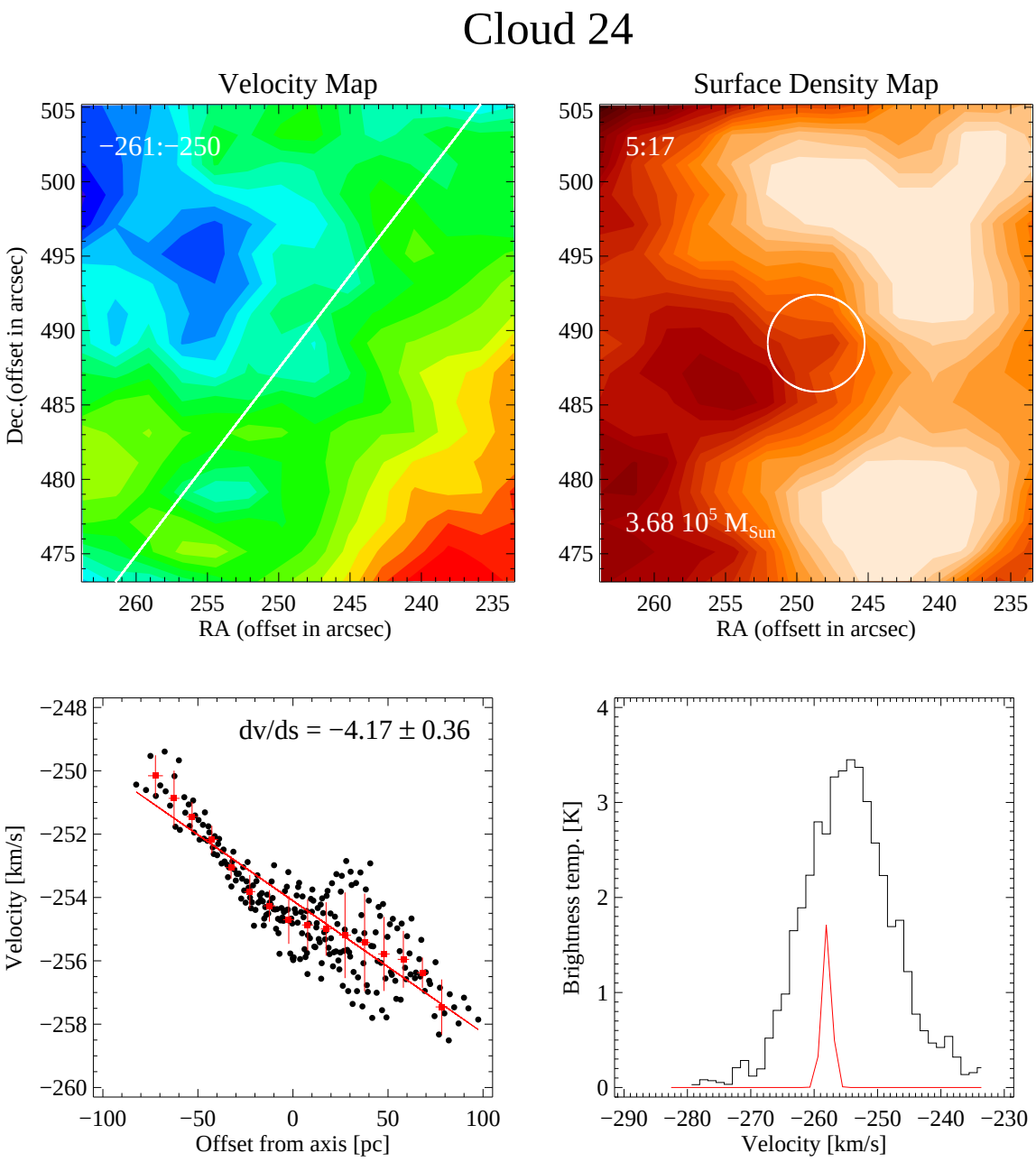

Figure 3.6: Cloud 24: Same as Figure 3.3.

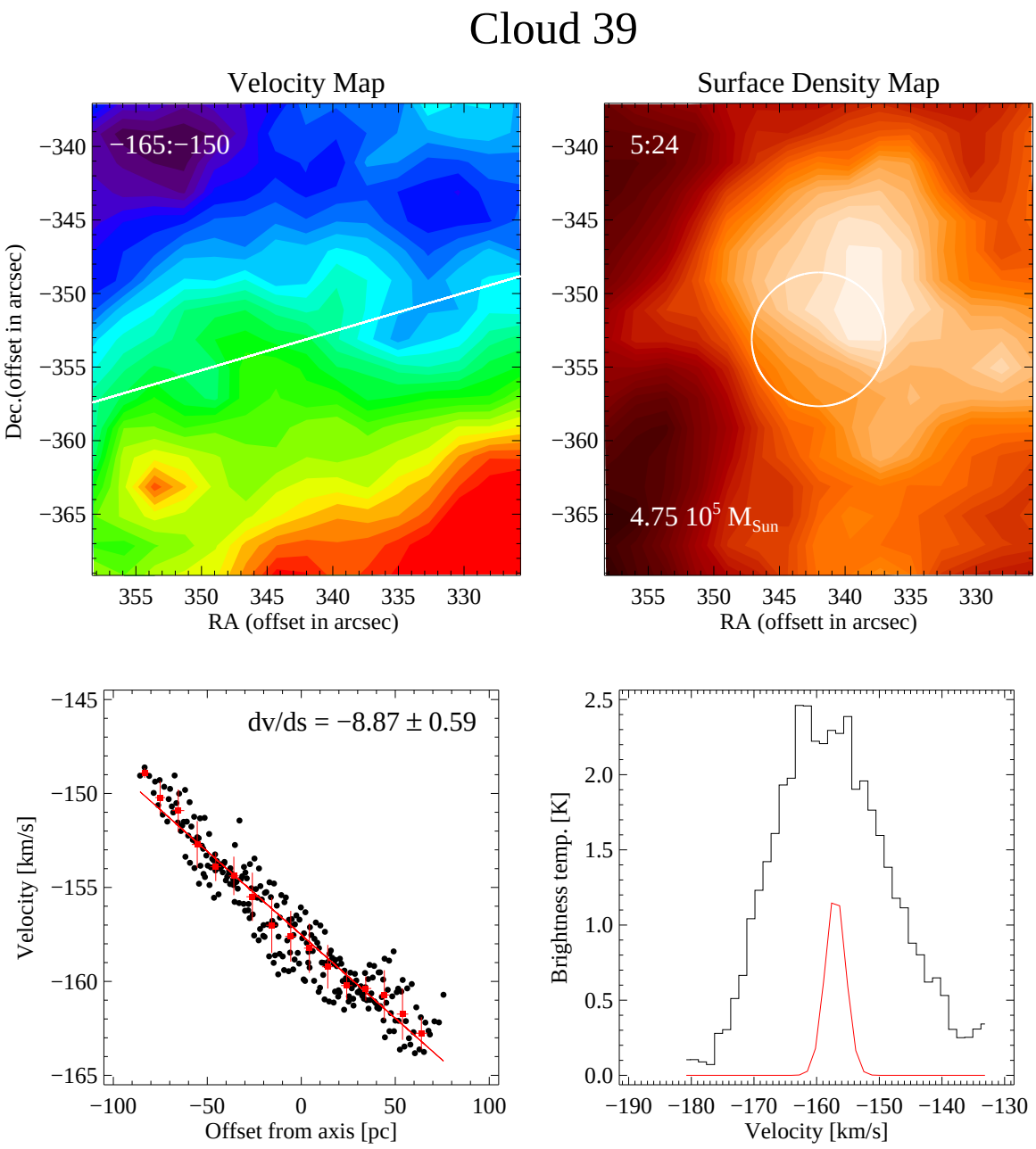

Figure 3.7: Cloud 39: Same as Figure 3.3.

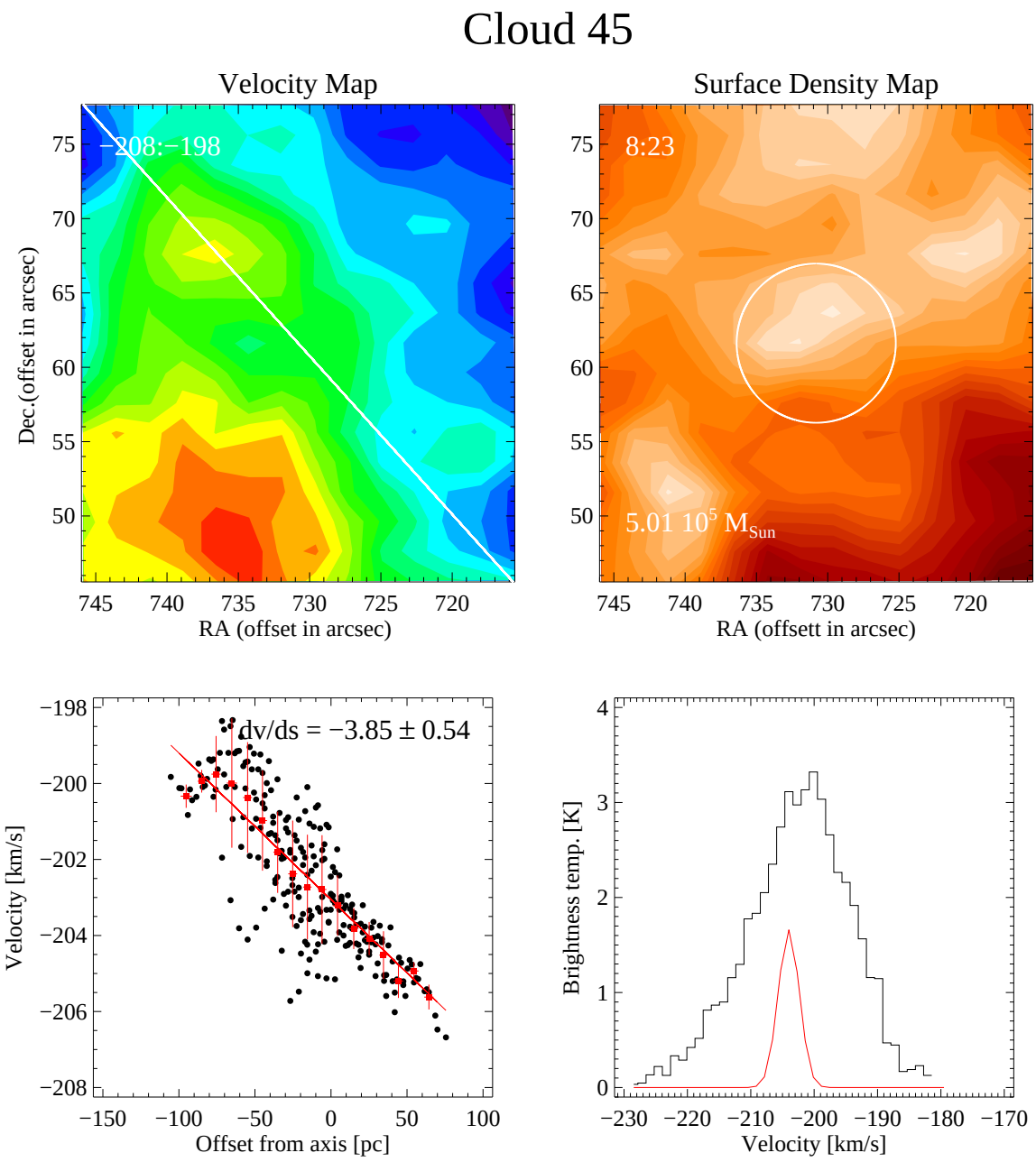

Figure 3.8: Cloud 45: Same as Figure 3.3.

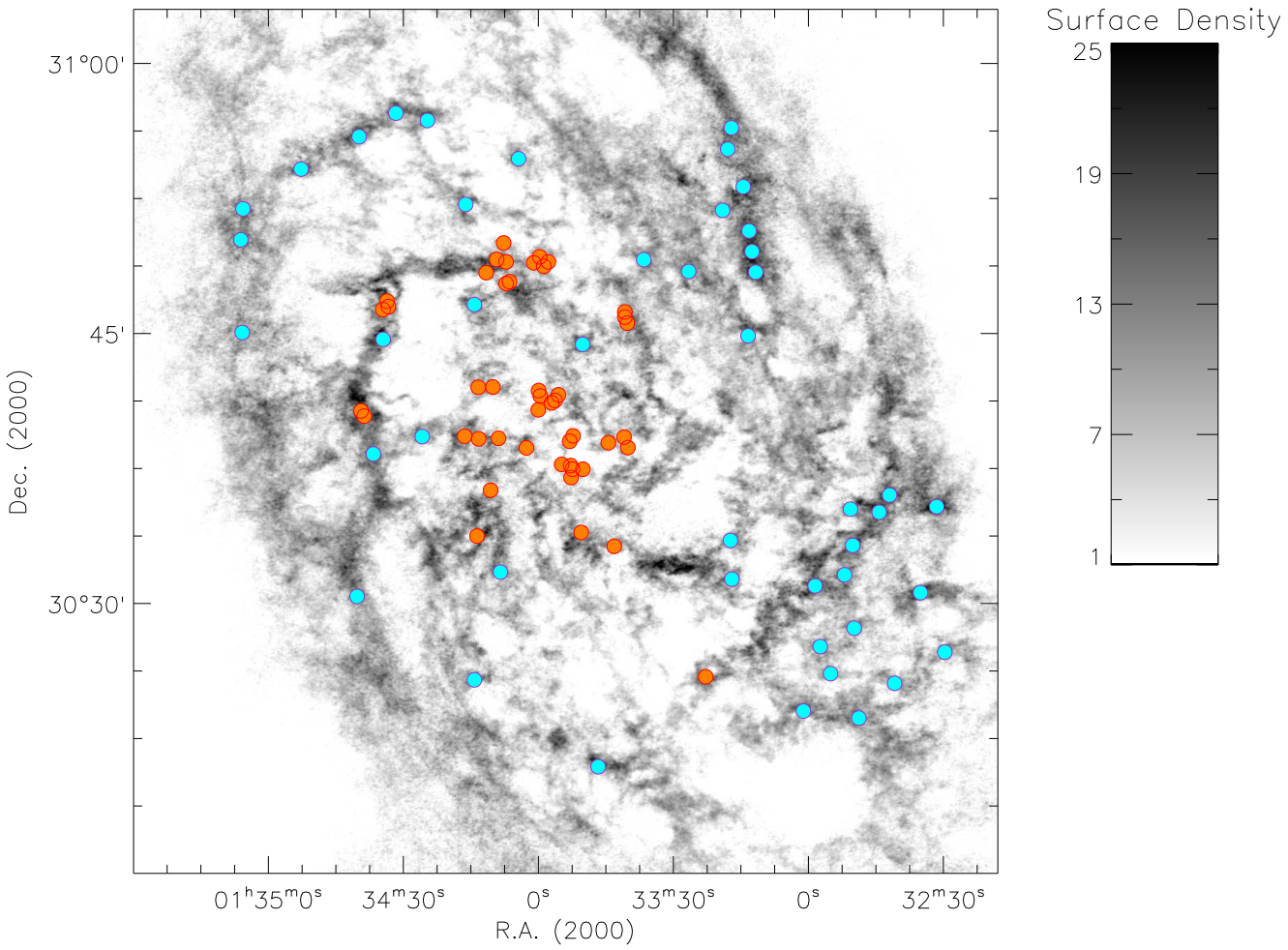

Figure 3.9: M33: Grayscale image in units of $M_\odot$ pc^{-2} of the 21-cm emission of the central $45' \times 45'$ field. The locations of HI regions containing molecular clouds are overlaid in orange, and the locations of HI regions without observed molecular clouds are overlaid in blue.

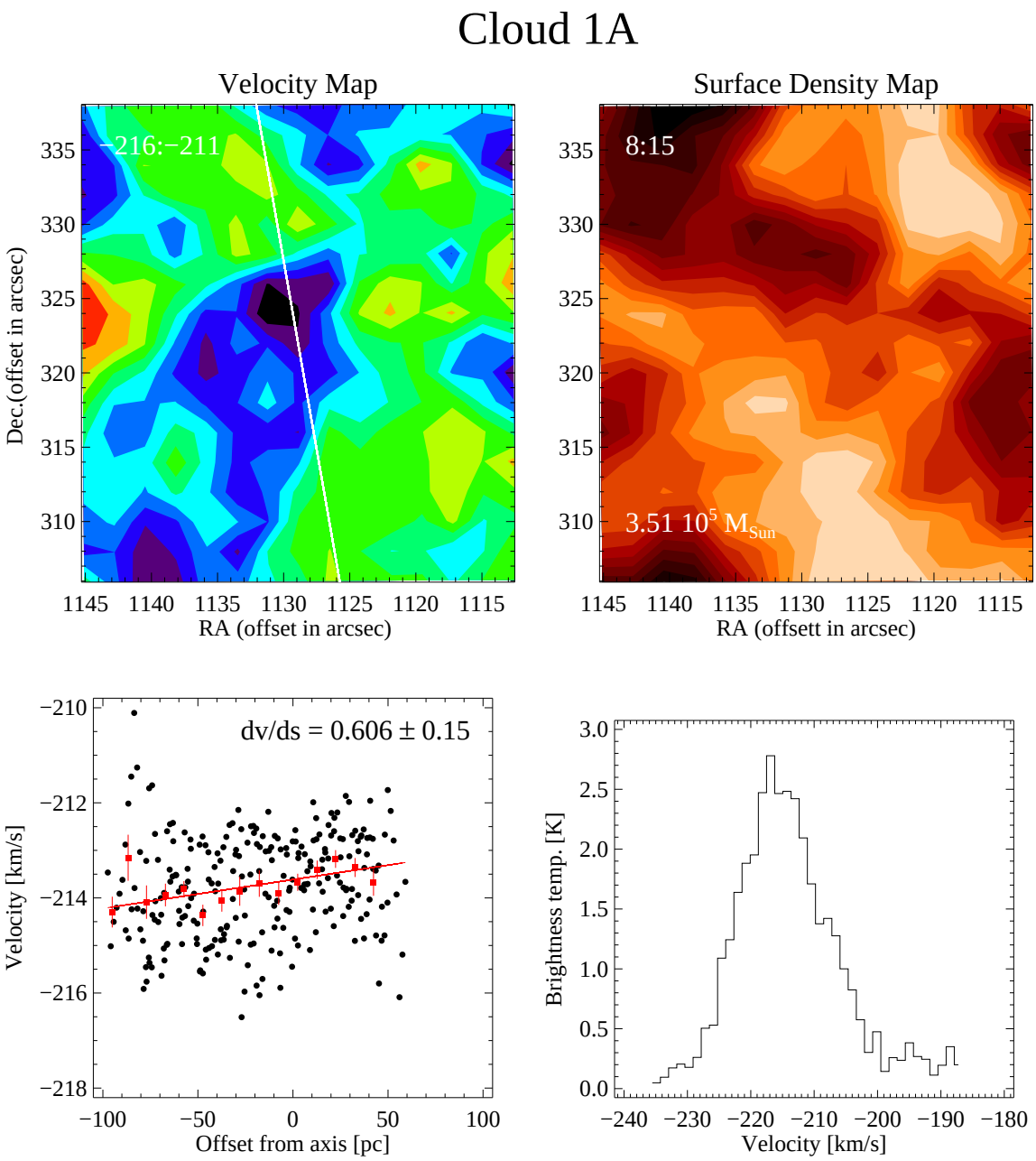

Figure 3.10: Cloud 1A: Same as Figure 3.3, accept for a region in which GMCs have not been observed.

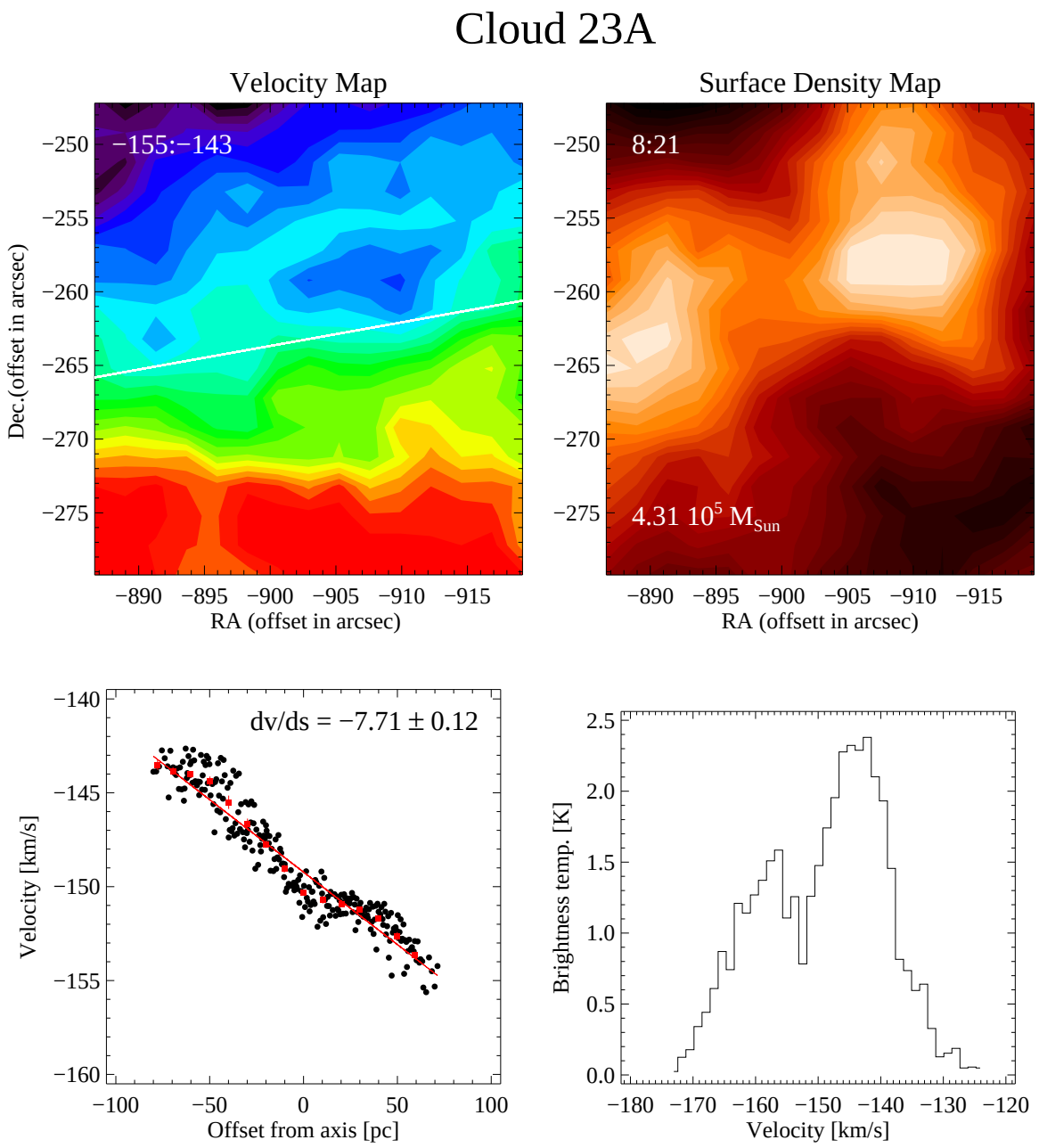

Figure 3.11: Cloud 23A: Same as Figure 3.10

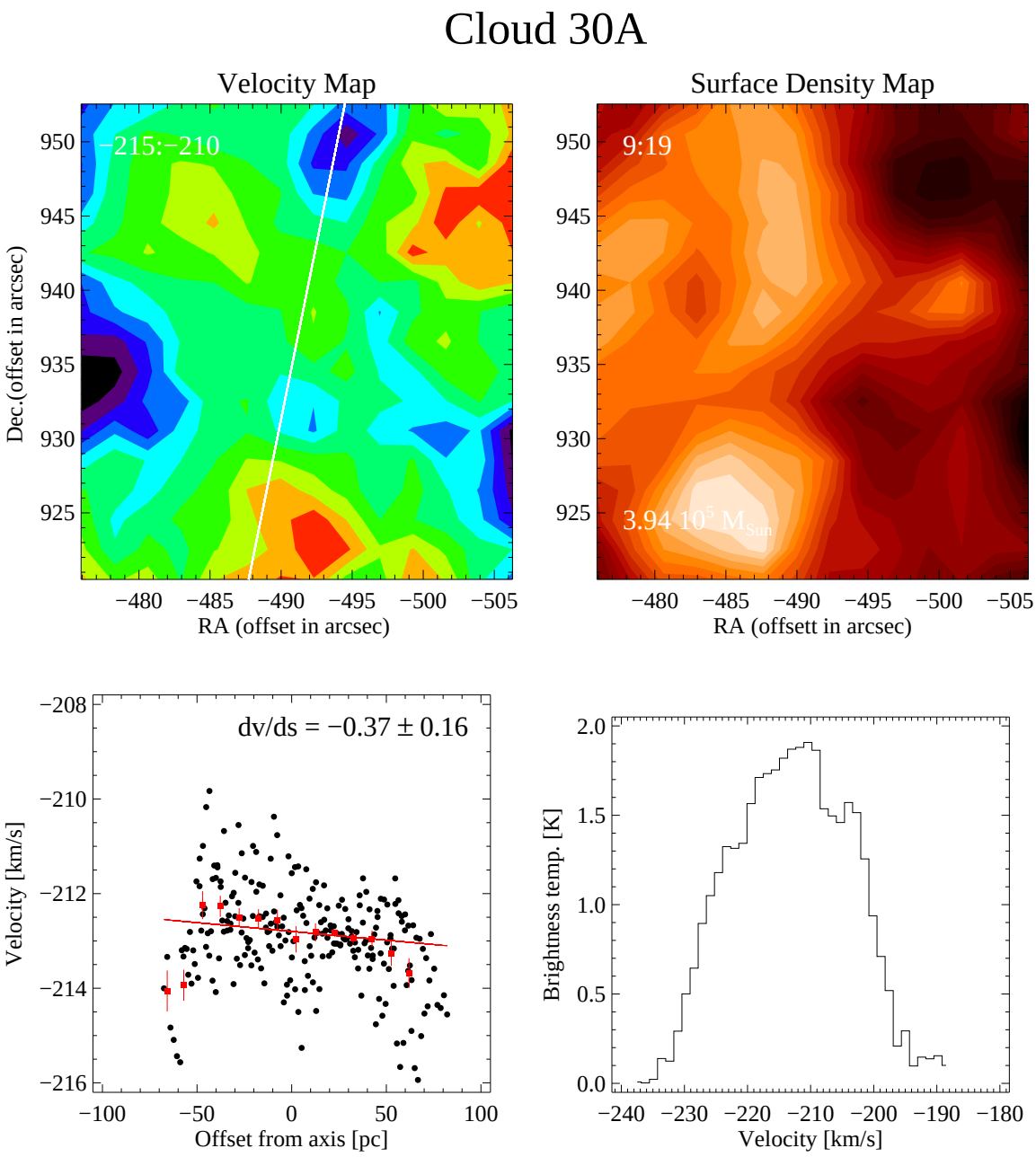

Figure 3.12: Cloud 30A: Same as Figure 3.10

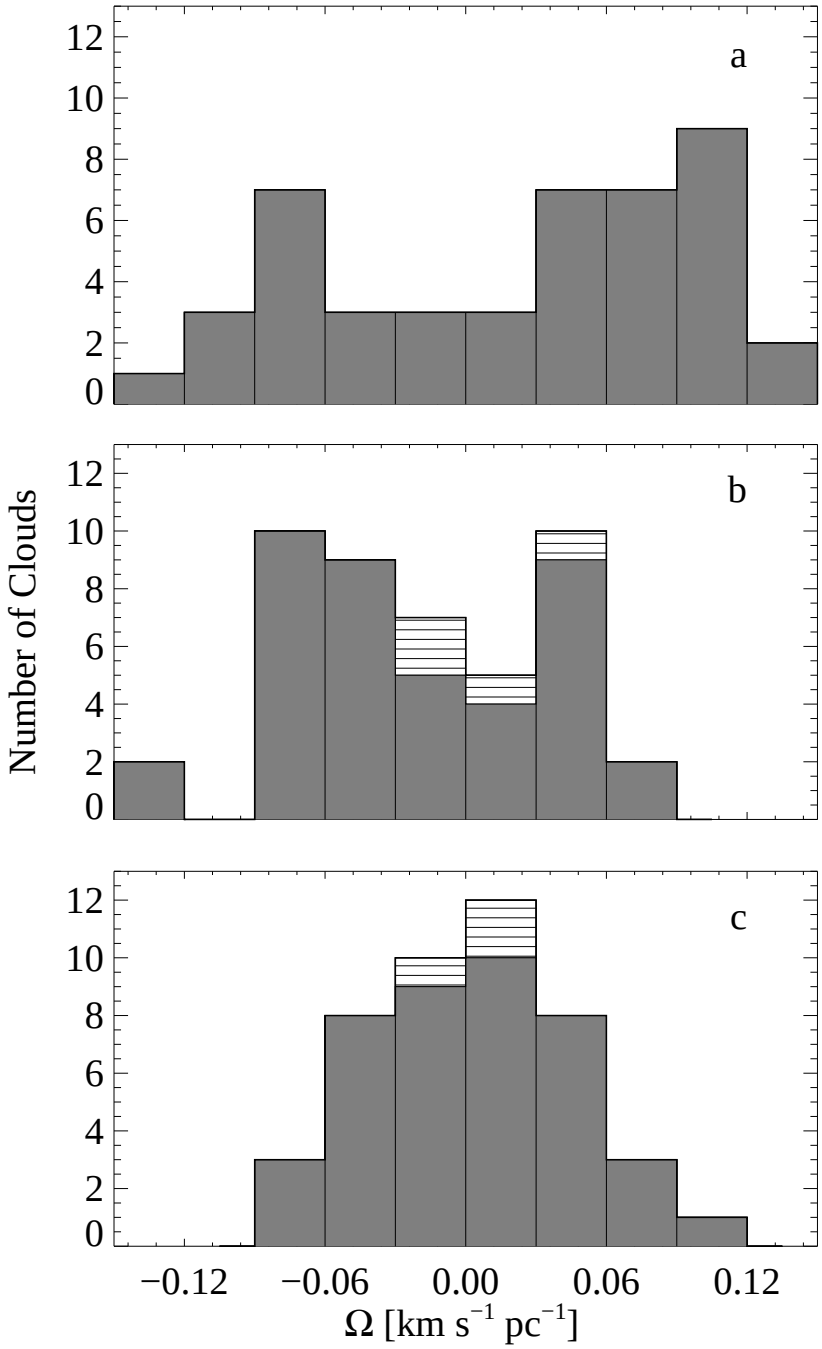

Figure 3.13: Gradient magnitudes for (a) GMCs, (b) HI clouds containing GMCs, and (c) HI clouds without observed GMCs in M33. Clouds having a position angle differing from the galaxy by more than 90° are given negative values. The hatched portions of the histograms in (b) and (c) represent regions having non-linear linear gradients.

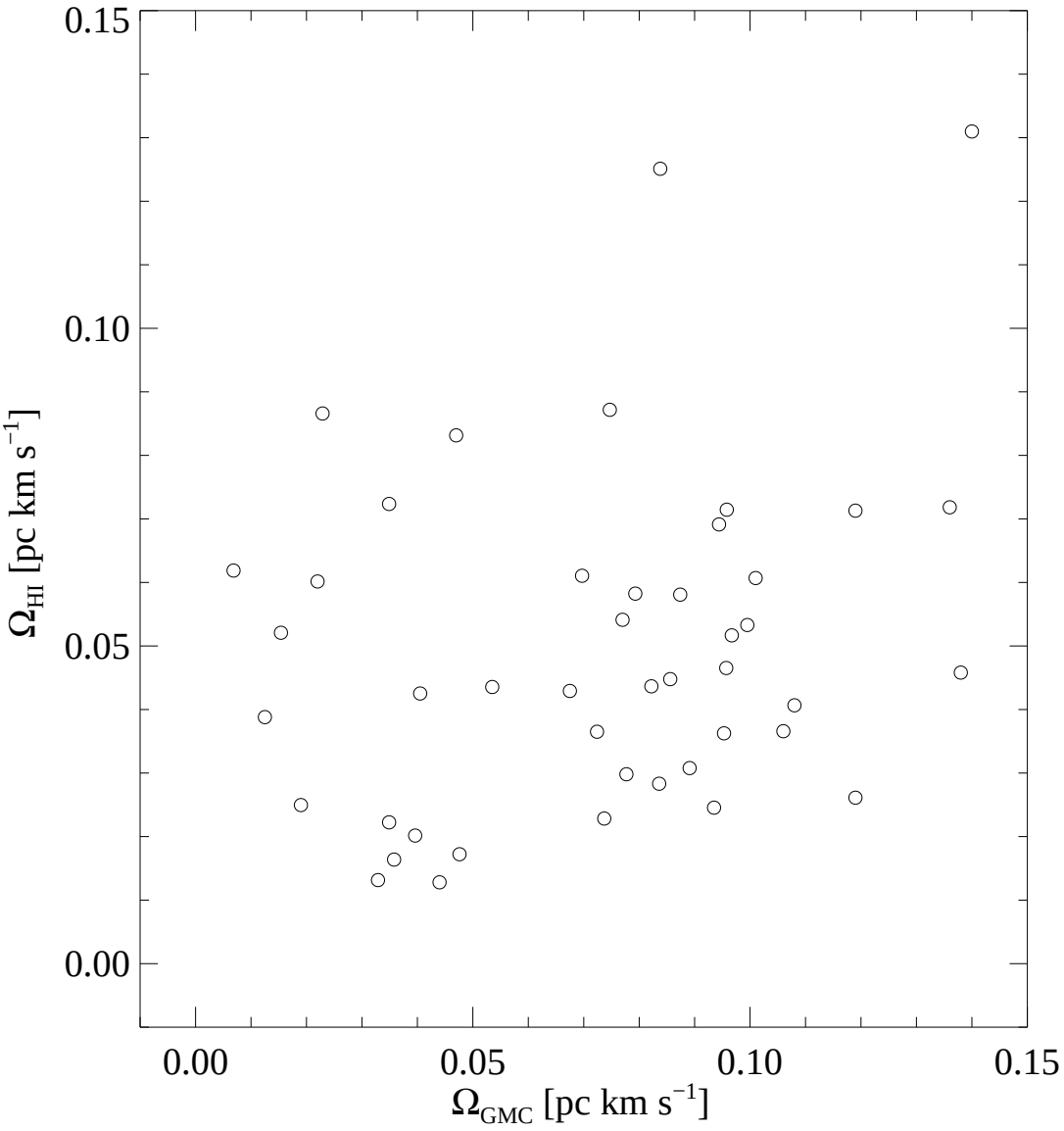

Figure 3.14: Gradient magnitudes in the atomic gas versus GMC gradient magnitudes. There is no significant correlation between $\Omega_{\rm HI}$ and $\Omega_{\rm GMC}$.

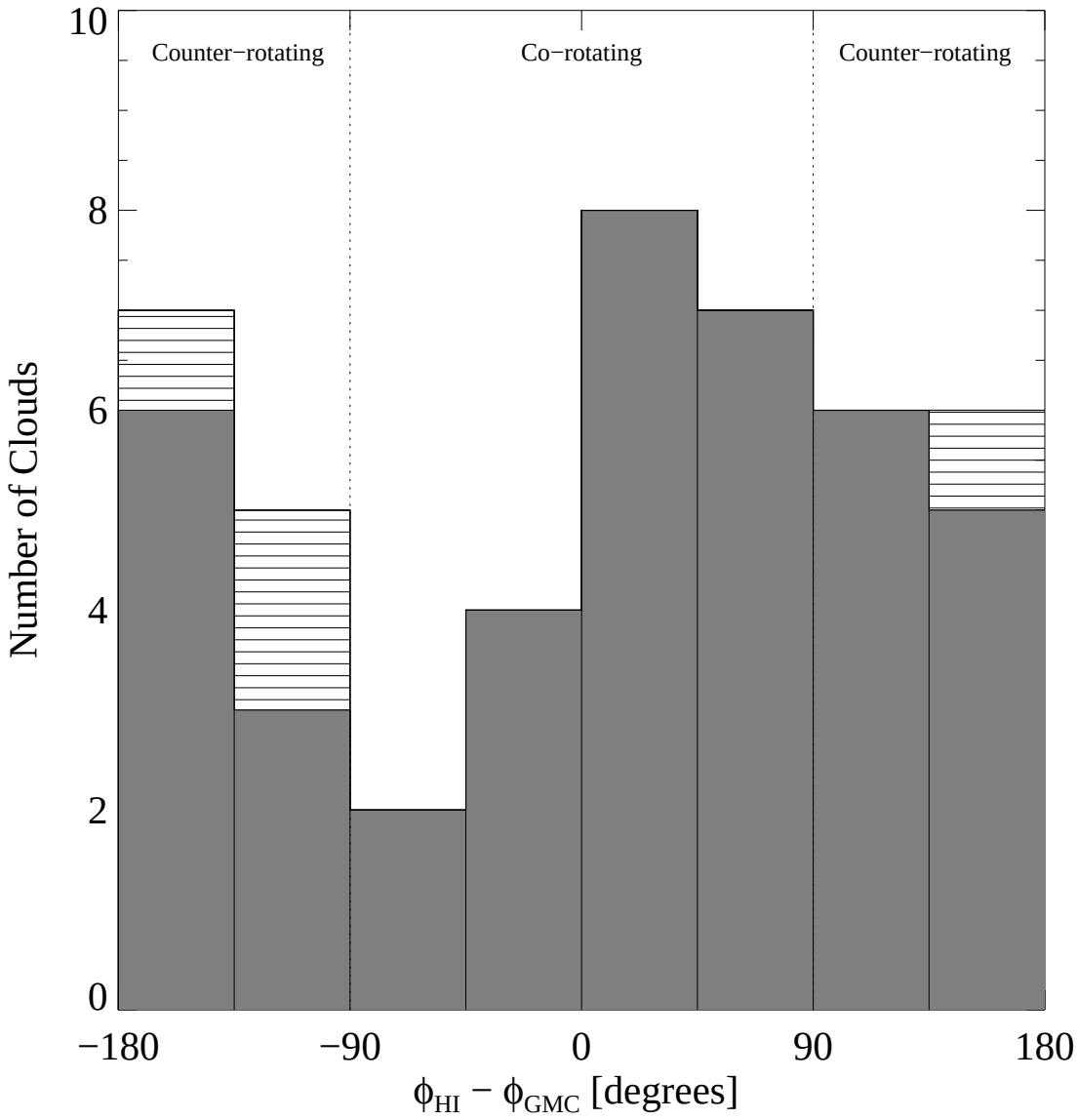

Figure 3.15: Comparison of HI and GMC position angles. *If* the velocity gradients indicate rotation, then most GMCs ($\sim 53\%$) are not rotating in the same sense as the associated HI. The hatched portions of the histograms in (b) and (c) represent regions having non-linear gradients.

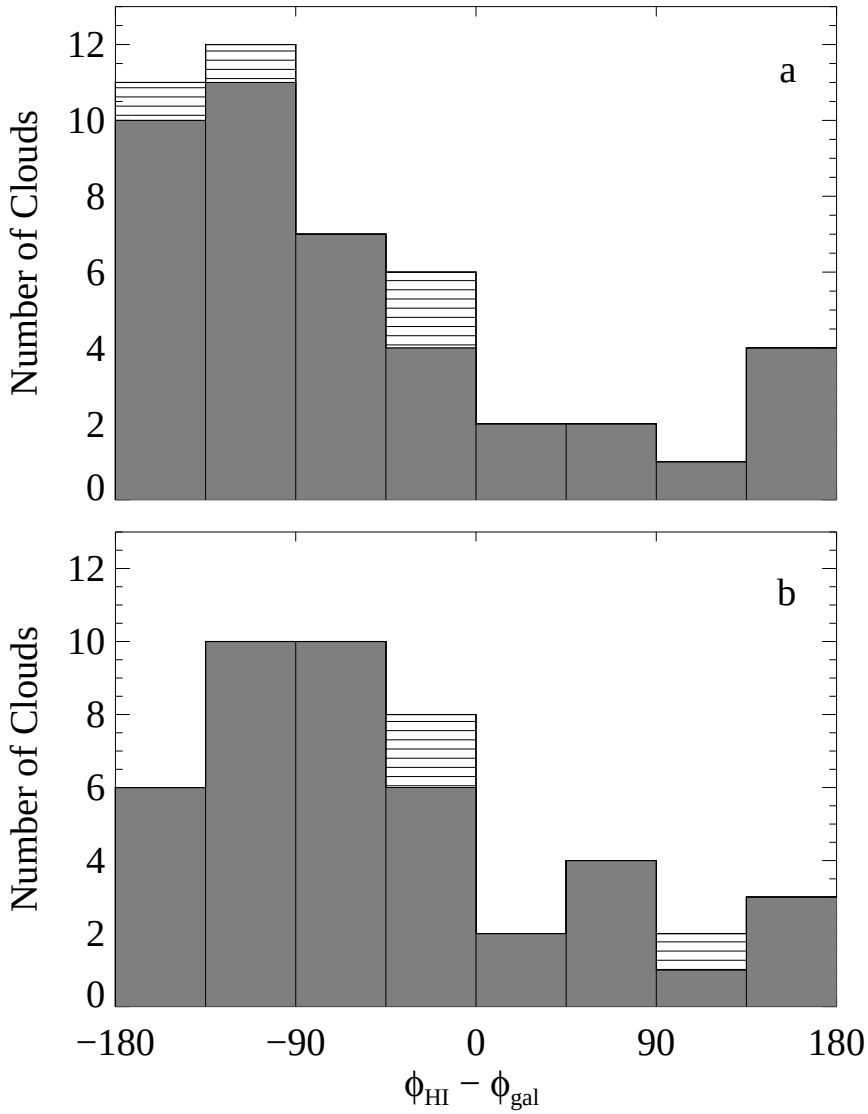

Figure 3.16: Position angles of (a) GMC-harboring HI and (b) non-GMC HI, with respect to that of M33. The hatched portions of the histograms in (b) and (c) represent regions having non-linear gradients.

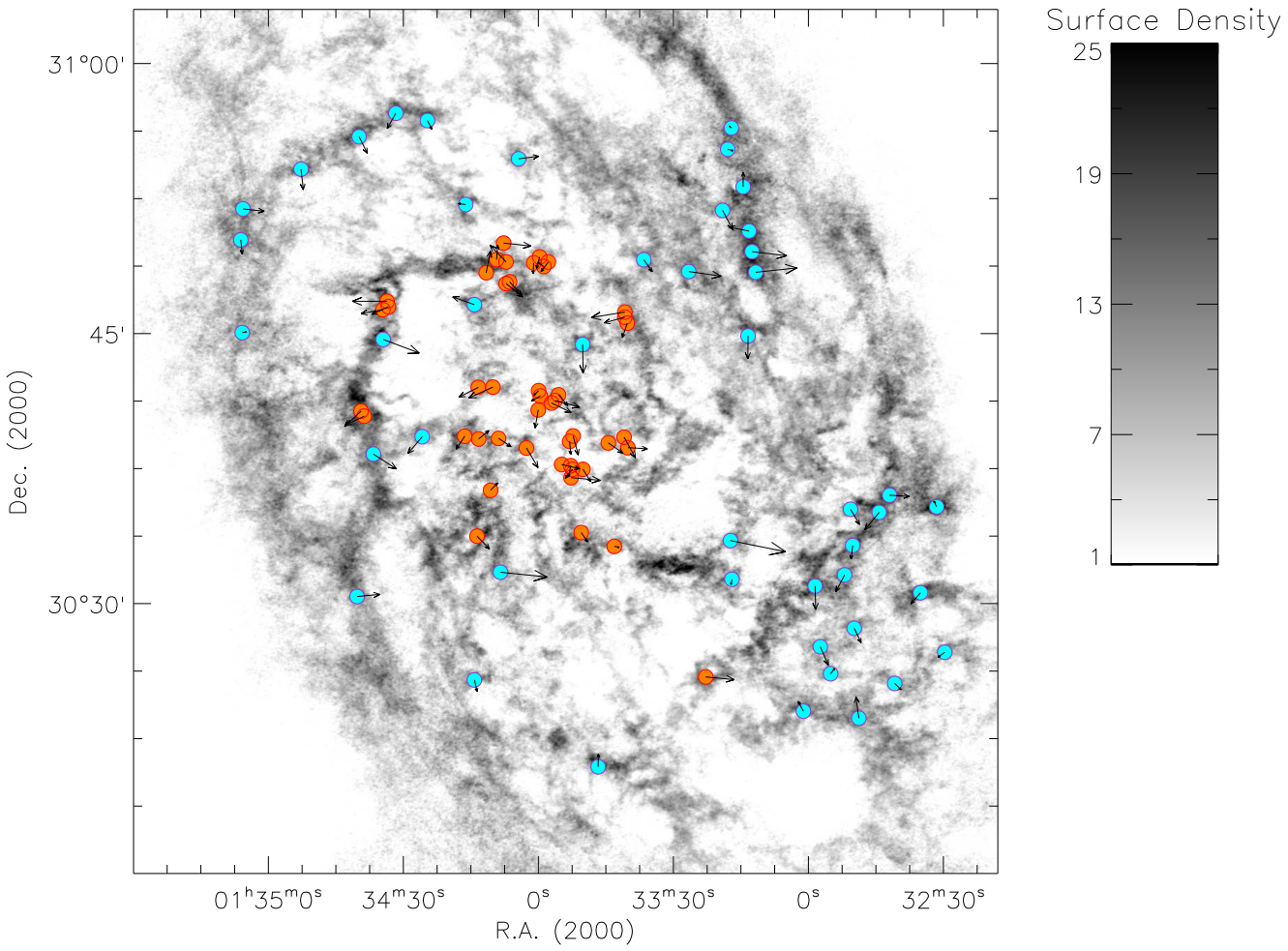

Figure 3.17: M33: The directions of the gradients in the atomic gas are plotted for HI regions containing molecular clouds (orange) and for HI regions without observed molecular clouds (blue). The arrows point in the direction of increasing velocity and have lengths proportional to the gradient magnitude. The gradient directions of the individual velocity fields where GMCs are observed (or, where GMCs may potentially be in the process of forming) do not appear to make up a large-scale, systematic pattern.

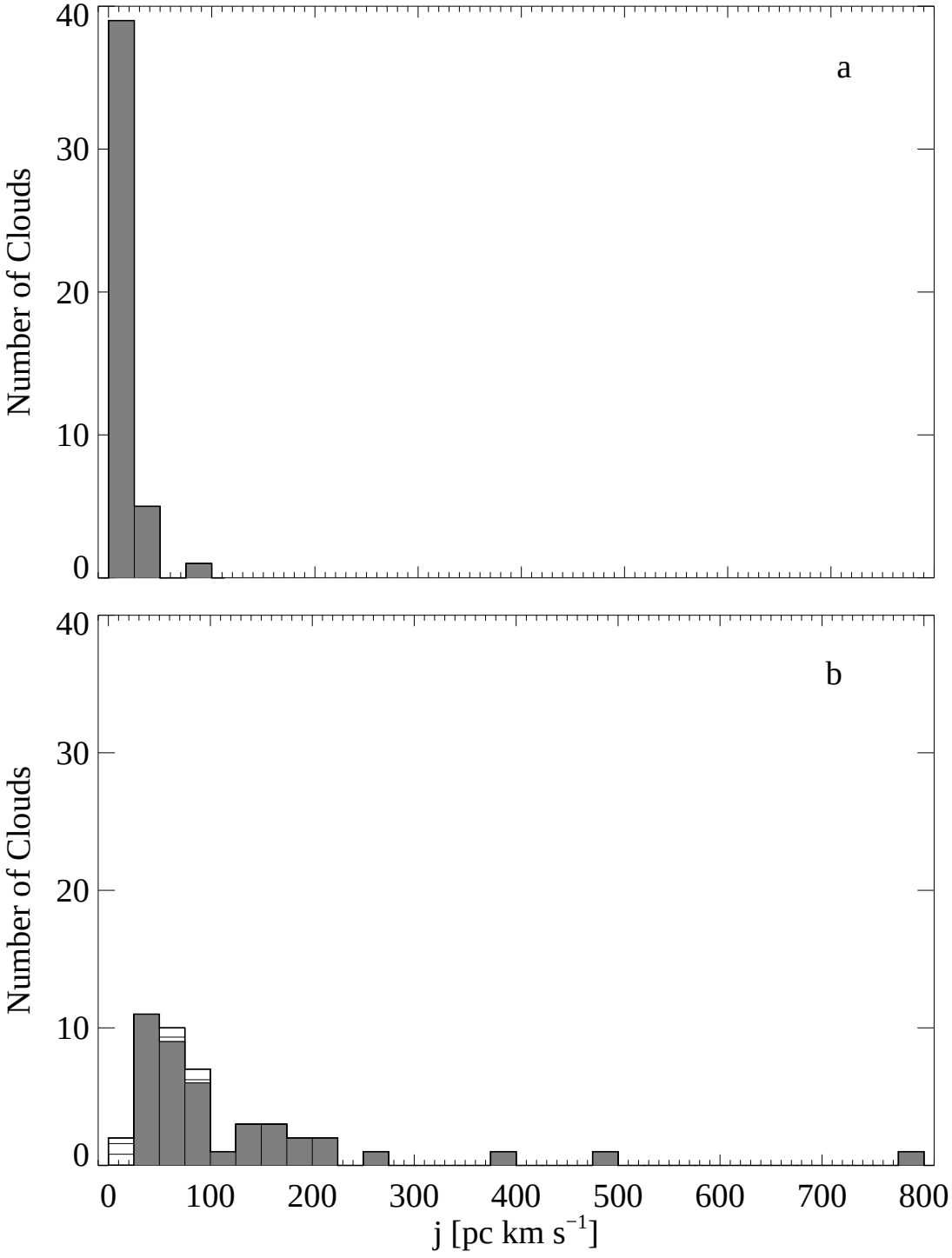

Figure 3.18: Distribution of specific angular momentum for (a) GMCs and for (b) HI clouds containing GMCs.

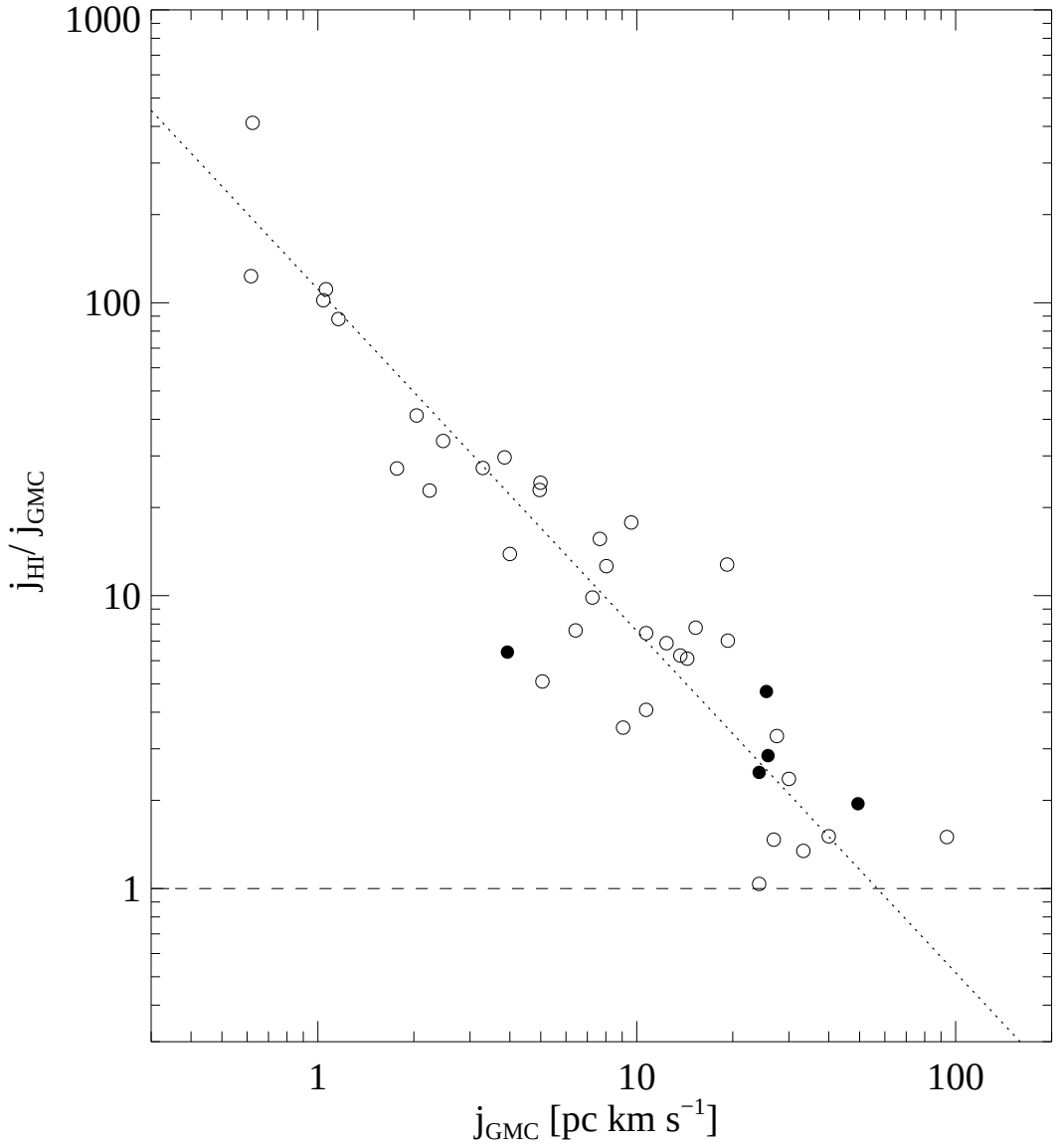

Figure 3.19: Ratio of specific angular momenta in atomic gas and GMCs, $j_{\rm HI}/j_{\rm GMC}$, versus specific angular momentum in the 36 resolved GMCs. This plot shows that $j_{\rm HI} > j_{\rm GMC}$ is always the case. The dotted line shows the least-squares fit to the data: $(j_{\rm HI}/j_{\rm GMC}) \propto j_{\rm GMC}^{-1.17\pm0.05}$. Data points for Milky Way GMCs are overplotted in filled circles (but are not included in the fit).

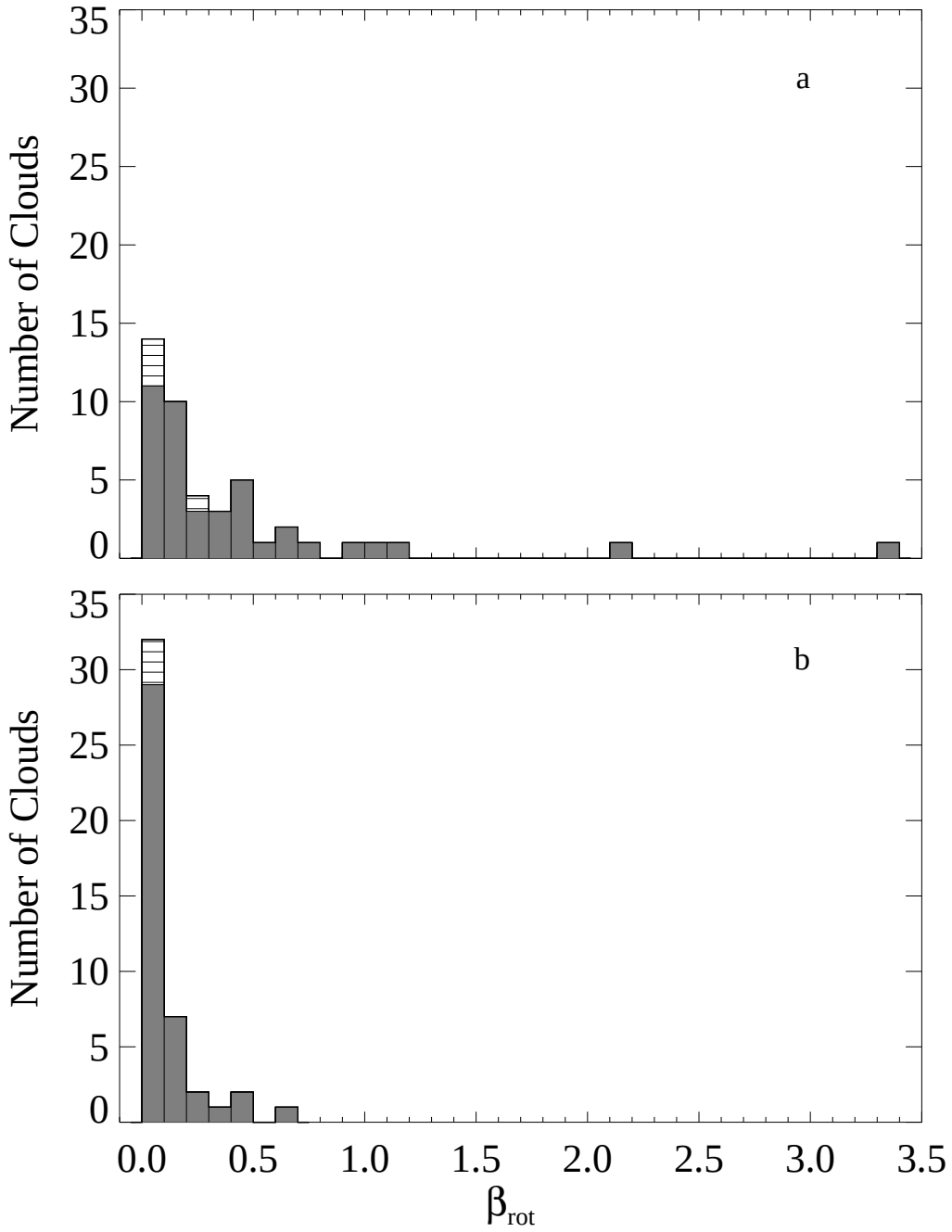

Figure 3.20: Distribution of the $\beta_{\rm rot}$ parameter for (a) HI containing GMCs and (b) non-GMC HI.

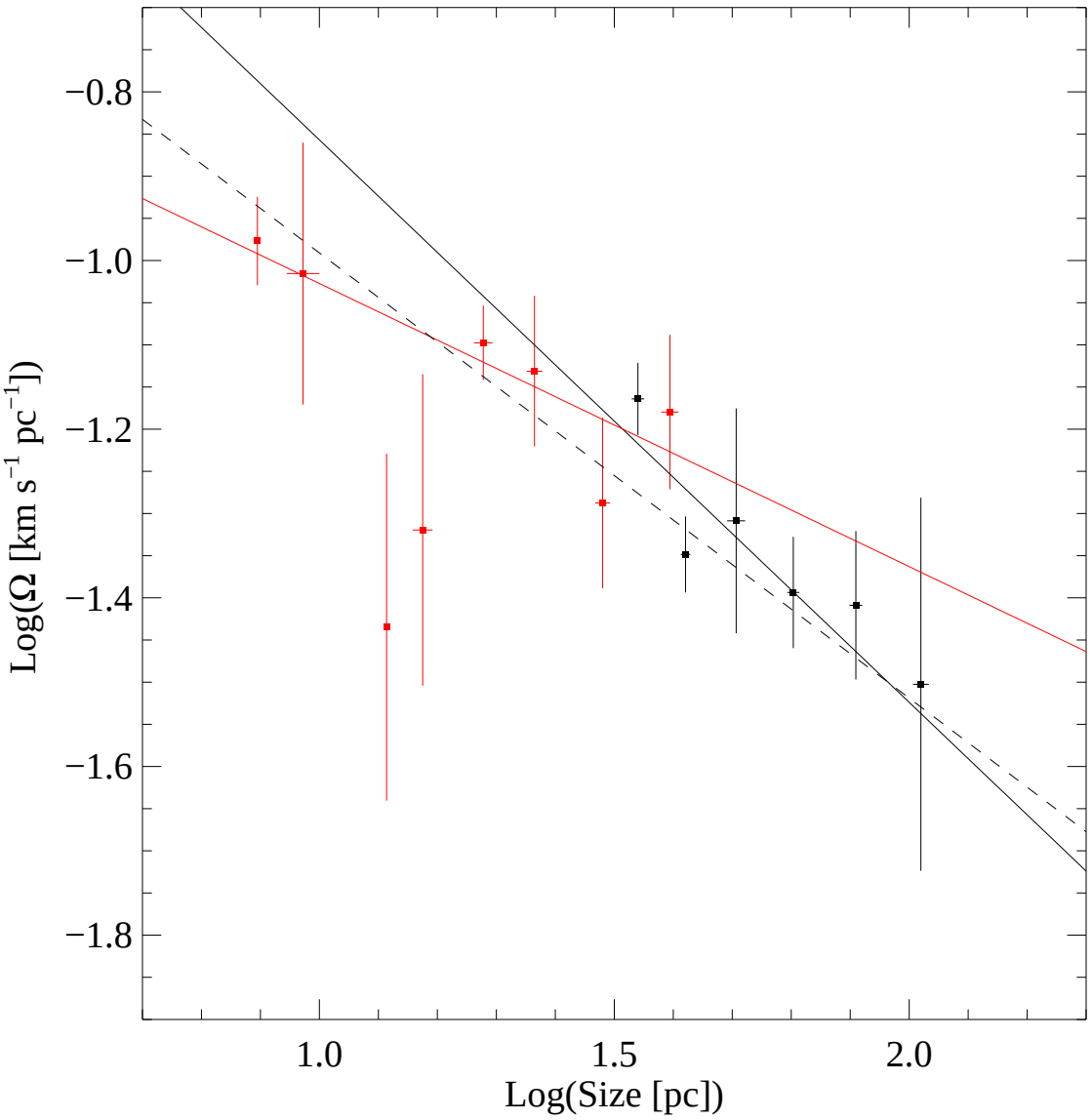

Figure 3.21: Gradient magnitudes observed in GMCs (red) and associated atomic gas (black) as a function of size. The data are averaged in bin sizes of $\Delta R = 0.1$ dex. The lines indicate least-squares, power-law fits to the data. For GMCs, $\Omega_{\rm GMC} \propto R^{-0.3\pm0.2}$, and for HI,$\Omega_{\rm HI} \propto R_A^{-0.7\pm0.2}$, where R_A is the accumulation radius. For GMCs and HI combined is $\Omega \propto R^{-0.5\pm0.1}$, which is the relationship found by Burkert & Bodenheimer (2000) for turbulent molecular cores.

Chapter 4

Extinction in the Large Magellanic Cloud

This chapter has been published in the Astrophysical Journal. It appeared in v. 662 (June 2007) p. 969.

Abstract

We present an extinction map of the Large Magellanic Cloud (LMC), using 204,502 stars from the Two Micron All Sky Survey point source catalog. We first use the NICE method to determine the reddening distribution, $E(H-K)$ and $E(J-H)$, which we compare to the HI distribution to find a near-infrared reddening law of $E(J-H)/E(H-K) = 1.20 \pm 0.04$. A visual extinction map ($\sim 6^\circ \times 6^\circ$) of the LMC is created using the NICER method; at 4 arcmin resolution, a mean value of $A_V = 0.38$ mag is found. We derive the LMC CO-to-H_2 conversion factor, $X_{\rm LMC}$, independent of assumptions about the virialization of giant molecular clouds, by comparing the NICER extinction map with NANTEN ^{12}CO observations. In regions where $A_V > 1$ mag and ^{12}CO emission is ≥ 2 K km s^{-1}, we measure $X_{\rm LMC} = 9.3 \pm 0.4 \times 10^{20}$ cm^{-2} (K km s^{-1})$^{-1}$. In the same regions, the LMC contains a total molecular mass of $(4.5 \pm 0.2) \times 10^7$ $M_\odot$.

4.1 Introduction

Studying the properties of giant molecular clouds (GMCs), the sites of most star formation, in a variety of extragalactic environments provides insight into stellar evolution as a whole. The Large Magellanic Cloud (LMC) is a good laboratory for this type of study because of its proximity ($D \sim 50$ kpc) and its nearly face-on orientation in the sky.

Determining the amount and distribution of molecular hydrogen (H_2), the dominant molecule ($\sim 99.99\%$ by number) in GMCs, is useful for the study of the initial conditions of star formation. Yet due to the lack of a permanent electric dipole moment, H_2 is undetectable

at the low temperatures ($\sim$ 10 K) of molecular clouds, and so a variety of other tracers have been used to identify them and to study their density distribution. Two common methods are star counts and color excess, which trace molecular gas by measuring the dust distribution of GMCs. The spatial location of gas and dust are highly correlated, as the well-known gas-to-dust relationship attests, because H_2 forms most efficiently in dense gas where dust grains provide surfaces onto which HI can collide and be converted into molecular form. The star counts method measures extinction by comparing the number of stars seen behind a dark cloud along a given light of sight with the number in a control field off the clouds and assumed to be dust-free. The color excess method measures reddening by exploiting the decrease in the extinction with increasing wavelength.

Since the 1960s, a number of authors have used the color excess method to map the reddening and inferred dust distribution of the LMC, (e.g., Feast et al. 1960; Isserstedt 1975; Grieve & Madore 1986). But a combination of questionable assumptions—for instance, assuming Galactic intrinsic colors, small data sets, limited spatial coverage, and not accounting for the Galactic foreground contribution to reddening—resulted in significant uncertainties.

Advances in recent years have made it possible to possible to bypass most of these problems. Namely, the advent of infrared (IR) array detectors, such as those used in the Two Micron All-Sky Survey (2MASS), have made possible the simultaneous observations of hundreds of sources in multiple wavelength bands. These detectors have the further advantage that IR light suffers much less extinction than the visible and ultraviolet, so molecular clouds can be probed more deeply. In the Galaxy, for instance, $A_{\rm K} \approx 0.1 A_{\rm V}$. The Near Infrared Color Excess (NICE) technique developed by Lada et al. (91) exploits the advantages offered by these large-scale arrays and has proved to be a powerful way of mapping extinction through molecular clouds. In this method, infrared color excess measurements are made by inferring the intrinsic color, typically $(H-K)$, of target stars from an unreddened control field. The NICER (NICE Revised) method of Lombardi & Alves (2001) generalizes the former by using information from all available independent colors—for instance, $(J-H)$ and $(H-K)$—to map extinction.

Radio observations of interstellar carbon monoxide (CO) have also been used to trace H_2. Cohen et al. (1988) were the first to fully survey the LMC in the $J = 1 \rightarrow 0$ rotational transition of CO. Yet, at their limited resolution ($8.'8$), they were able to resolve only the largest cloud complexes ($\sim$ 140 pc). More recently, Mizuno et al. (2001) completed a comprehensive high-resolution ($\sim$ 40 pc) CO survey using the 4 m NANTEN telescope. Both groups of authors made calculations of the CO-to-H_2 conversion factor, or the "X-factor," of the LMC.

An outstanding question concerning GMCs is how metallicity affects the X-factor. This quantity is of particular interest in the LMC since the galaxy has a lower metallicity ($\sim 1/4$; Dufour 1984) and a higher gas-to-dust ratio ($\sim$ 1.7; Gordon et al. 2003) than the MW. It is conjectured that the relatively less-abundant CO in the LMC is more susceptible to photo-dissociation by UV radiation, which can penetrate more deeply into the less-dusty clouds (e.g., McKee 1989). This argues for $X_{\rm LMC} > X_{\rm MW}$.

Yet there are a number of problems with determining the X-factor solely from CO

observations. Potentially unrealistic assumptions regarding the physical properties of the molecular clouds—for instance, that they are virialized—must be made, since there is not an independent measure of $N(H_2)$.

It is the main goal of this paper to provide such an independent measure of the molecular content in the LMC, one that makes no assumption about the structure, dynamics, or virialization of GMCs. We do this by first creating an extinction map from 2MASS data, in one of the first applications of the NICE(R) techniques to an extragalactic system. A number of other useful results are obtained in the process, including the NIR extinction law, the extinction distribution, and the X-factor of the LMC. In § 2 we describe data selection and the other considerations that go into determining extragalactic reddening. The results, including the extinction map and X-factor, are presented in § 3. Conclusions are presented in § 4.

4.2 Data Selection

4.2.1 2MASS Data

Our reddening maps of the LMC are derived using JHK near-IR photometry obtained from the 2MASS Point Source Catalog.[1] For unconfused sources with Galactic latitude $|b| > 10°$, the limiting magnitudes of the 2MASS catalog at the 10-σ level are 15.8, 15.1, and 14.3 mag in J (1.24 μm), H (1.66 μm), and K_S (2.16 μm), respectively. Possible contaminants, such as image artifacts caused by bright stars, confused sources, solar system objects, and other artifacts are eliminated. [2] Only data having photometric uncertainty ≤ 0.10 mag, corresponding to $S/N \geq 10$, are selected. Our data cover the central $6° \times 6°$ region of the LMC, centered on $(\alpha, \delta) = (5^h20^m, -69°)$. This choice of range was based on an examination of the Mizuno et al. (2001) CO map and the Staveley-Smith et al. (2003) HI map, which reveals the extent of molecular and HI emission, respectively. This initial sample contains 329,702 sources.

The 2MASS resolution, $2''$, corresponds to a physical size of ≈ 0.5 pc at 50 kpc, and so individual LMC stars should be well-resolved. Nikolaev & Weinberg (2000), treating a similar set of LMC data drawn from 2MASS, show that confusion is not a problem at this resolution.

Our preliminary data set contains not only LMC field stars but Galactic foreground point sources. In order to get a quantitative estimate of the MW foreground stellar number density, we obtain 2MASS data for a reference field in the same range of Galactic latitude as the LMC field but removed in Galactic longitude by $-30°$. The angular number densities of the LMC field (prior to data reduction) and MW field are 4.65×10^3 deg^{-2} and 1.68×10^3 deg^{-2}, respectively. Not accounting for the foreground would dilute the measured extinction

[1] http://irsa.ipac.caltech.edu/applications/Gator/

[2] Explanatory Supplement to the 2MASS All-Sky Data Release at http://www.ipac.caltech.edu/2mass/releases/allsky/doc/explsup.html

(A_V) and increase the uncertainty, especially in regions of high A_V. In what follows we use the color-color diagram, in conjunction with Nikolaev & Weinberg's (2000) analysis of the LMC color-magnitude diagram, to correct for this.

4.2.2 Data Reduction

To derive the LMC gas-to-dust ratio (see § 4.3.1) and X-factor (§ 4.3.5), we generate color excess and visual extinction maps for comparison with the galaxy's N(HI) and CO distributions, respectively. We use Lada et al.'s (1994) NICE method to generate the color excess maps, $E(J-H)$ and $E(H-K)$. For the extinction maps, we use the NICER method of Lombardi & Alves (2001), which generalizes Lada's formulation for multi-band observations. In these techniques, the intrinsic color of all stars observed toward a target clouds is taken to be the mean color of a nearby, unreddened control field. An extinction map is generated by averaging the irregularly sampled data into pixels, across each of which the extinction is assumed to be uniform. Application of these techniques, originally applied to Galactic clouds, assumes that all stars observed toward the cloud (i.e., the field stars) are background stars; and the field and control stars are homogeneous (i.e., drawn from the same parent population). Extending these techniques to extragalactic sources raises special concerns as to how well these conditions can be fulfilled.

Before creating the extinction map, a number of reductions and corrections are performed on the raw data, with particular care taken to address those assumptions just mentioned.

Completeness

The observed completeness limits toward the LMC are brighter than the nominal completeness limits stated in the 2MASS catalog (Figure 4.1). Towards regions of higher extinction, intrinsically fainter stars will escape detection before intrinsically brighter stars, so the overall extinction would be underestimated if all stars were included in the measurements (Oestreicher & Schmidt-Kaler 1996). Because only the minimally extincted faint stars would be able to be measured, including them in our sample would drive down the overall mean extinction. However, in dealing with apparent, not absolute, magnitudes, the relative faintness of a given star may be due to extinction or its intrinsic brightness. But statistically, we do not expect a particular population (intrinsically faint *or* bright) to be more likely to lie behind molecular clouds. With our large data set, then, it is reasonable to assume that most observed faint stars (i.e., those below the observed completeness limit) would bias measurements to lower values of extinction if included. Thus, based on our completeness estimates, we used only stars with brightness greater than $J < 15.0$, $H < 14.4$, and $K < 14.3$ mag for subsequent analaysis. This and the following data selections are summarized in Table 4.1.

We tested these assumptions in several ways. First, we confirmed that the use of a constant magnitude limit in each band is appropriate, i.e., that it does not depend on column density. We calculated the limits for different reddening intervals and found that the

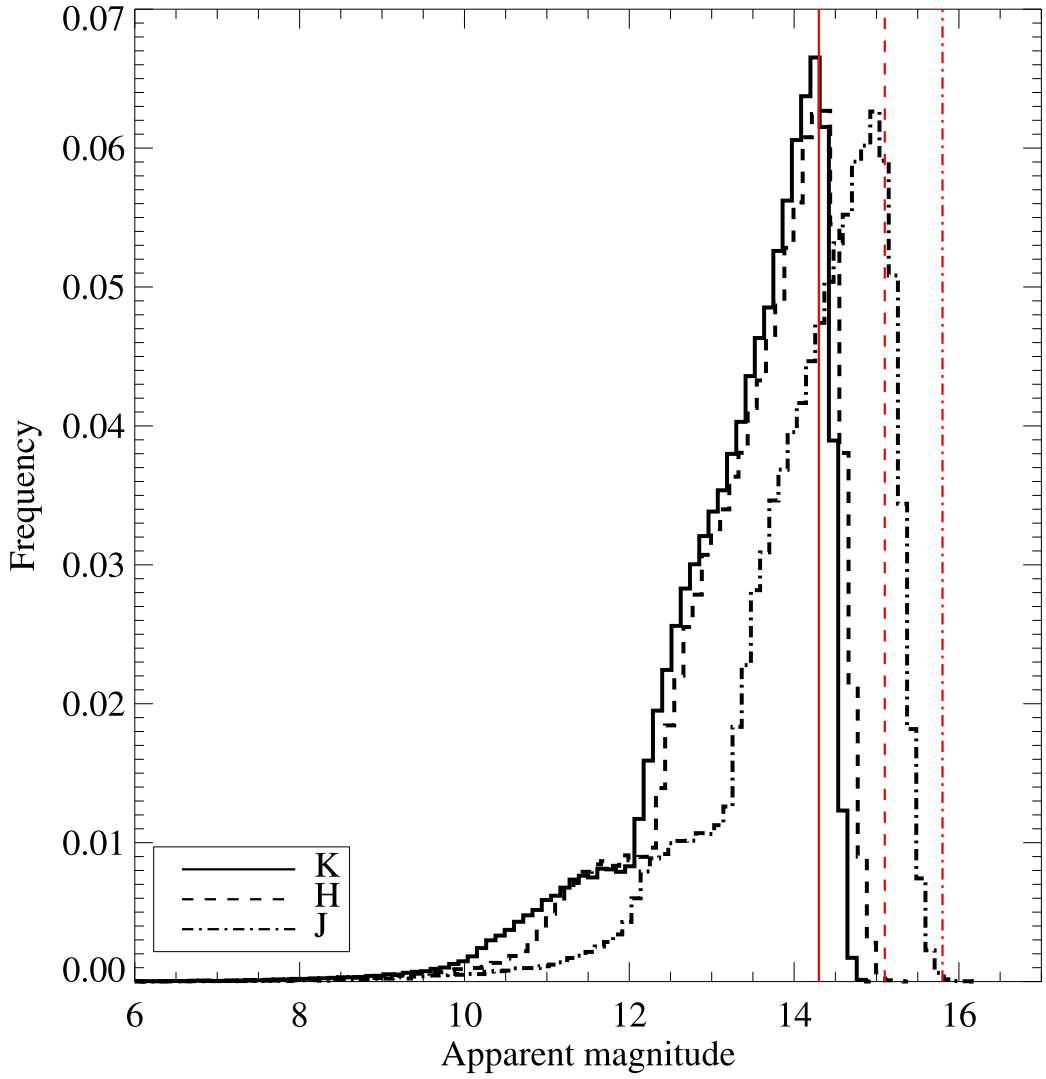

Figure 4.1: Luminosity functions of our sample. The observed completeness limits for J, H, and K, were estimated 15.0, 14.4, and 14.3 mag, respectively. The 2MASS completeness limits (15.8, 15.1, and 14.3 mag) are indicated with vertical lines.

Table 4.1: **2MASS Data Selection Summary**

Criteria	Number of remaining stars
2MASS selection	329,702
Completeness cutoff [a]	258,621
Eliminate MW foreground [b]	204,502

[a] Completeness limits (see Figure 4.1): $J < 15.0$, $H < 14.4$, $K < 14.3$ mag.
[b] Based on Nikolaev & Weinberg (2000) regions.

values stated above remained the same. Second, we measured the extinction for those stars falling outside our stated limits (i.e., those fainter than $J > 15.0$, $H > 14.4$, and $K > 14.3$ mag). Their measured mean reddening of -0.44 mag is unphysical and their distribution is consistant with an error population. Indeed, when we went ahead and created a map including these stars, (i.e., without having imposed a completeness limit), the global mean extinction was lowered significantly (by nearly a factor of 2). Finally, after having created the extinction map only using stars brighter than the completeness estimates, we found that the remaining fainter stars have overall lower reddenings consistant with an error population (i.e., a noise population with a Gaussian distribution centered around zero).

Foreground and non-interstellar reddening

The Galactic foreground contaminates the 2MASS LMC field in two ways: with HI gas and point sources. Within the LMC itself there is foreground contamination, as well as reddening of non-interstellar origin, including that caused by protostars and obscured aymptotic giant branch (AGB) stars.

Galactic HI foreground extinction is not negligible but previous authors, usually for lack of data, adopted uniform foreground reddening in their derivation of LMC extinction maps. In the Parkes multibeam HI survey of the LMC, Staveley-Smith et al. (2003) found a mean Galactic reddening of $\langle E(B-V)\rangle = 0.06$ mag over the LMC disk, varying from 0.01 to 0.14 mag. Staveley-Smith generously provided us with their HI data, which we used to correct for Galactic reddening for stars in the LMC field. For every 2MASS source, foreground extinction in each band was calculated at that position using the MW extinction law of Schlegel et al. (1998; $A_{\rm J}/A_{\rm V} = 0.276$, $A_{\rm H}/A_{\rm V} = 0.176$, $A_{\rm K}/A_{\rm V} = 0.112$), and the MW gas-to-dust ratio of Bohlin et al. (1978; $\beta \equiv N({\rm HI})/A_{\rm V} = 1.87 \times 10^{21}$ mag^{-1} cm^{-2}). These values were then subtracted from the observed 2MASS magnitudes:

$$J_{\rm corrected} = J_{\rm observed} - \frac{0.276}{\beta} N({\rm HI})_{\rm foreground}, \tag{4.1}$$

$$H_{\rm corrected} = H_{\rm observed} - \frac{0.176}{\beta} N({\rm HI})_{\rm foreground}, \tag{4.2}$$

$$K_{\rm corrected} = K_{\rm observed} - \frac{0.112}{\beta} N({\rm HI})_{\rm foreground}. \tag{4.3}$$

While Galactic HI is easily identified given its distinct velocity compared to LMC gas, the correction for Galactic point source contamination is more complicated. Furthermore, we wish to eliminate from our sample objects in the LMC whose reddening is circumstellar in origin. The color-magnitude diagram (CMD) is a useful tool to correct for both effects. Analysis of the CMD allows us to eliminate sources, on a *probabilistic* basis, that are unlikely to have undergone reddening from LMC interstellar dust.

One can use the CMD (K vs. $J-K$) to identify distinct stellar populations (Figure 4.2). This is the main focus of Nikolaev & Weinberg (2000) who, by matching features of the 2MASS CMD to colors of known populations from the literature, discuss which populations are the greatest contributors to the different regions. We use their regions E, F, G, H, J, K, L, and part of D, to create the reddening maps. These areas correspond to LMC populations, primarily of the giant branch, with insignificant Galactic foreground contamination. We eliminate regions A, B, C, and I, which contain roughly 15, 80, 80, and 55 percent foreground, respectively. Region K, which is free of foreground contamination, but consists of dusty asymptotic giant branch stars whose large $J-K$ colors are due to circumstellar reddening, is also eliminated. We confirmed that these highly reddened stars are not preferentially located in regions of high molecular gas by plotting their spatial locations. We also performed the reverse operation. That is, based on the CO map of Mizuno et al. (2001), we located points on the color-color diagram and CMD that fall within the contours of known molecular clouds. In all, there are only 74 stars in the extended "finger" of the color-color diagram corresponding to molecular clouds in the Mizuno et al. (2001) map (see Figure 4.3). After these selections, we are left with 204,502 sources, corresponding to an average number density of 4.76×10^3 deg^{-2}. Figures 4.3 and 4.4 show the color-color diagrams of the LMC field before and after the data reductions presented in this section.

A difficult problem is correcting for foreground contamination within the LMC. The color excess method assumes that stars observed in the line-of-sight to a cloud are background stars. Extinction measurements will be diluted wherever foreground stars are included in the calculations. In addition, as discussed and modeled by Lada et al. (1994), the decrease in measured extinctions due to foreground stars will have a particularly large impact in regions of high extinction, resulting in an increase in dispersion with $A_{\rm V}$. We tried to minimize the effect of foreground in the extinction map by sigma-clipping—that is, by removing sources in a given pixel with anomalous values of $A_{\rm V}$. This was one of the motivations behind the creation of the NICER technique (Lombardi & Alves 2001). Described comprehensively by these authors, the sigma-clipping solution is justifiable when the scatter of intrinsic stellar

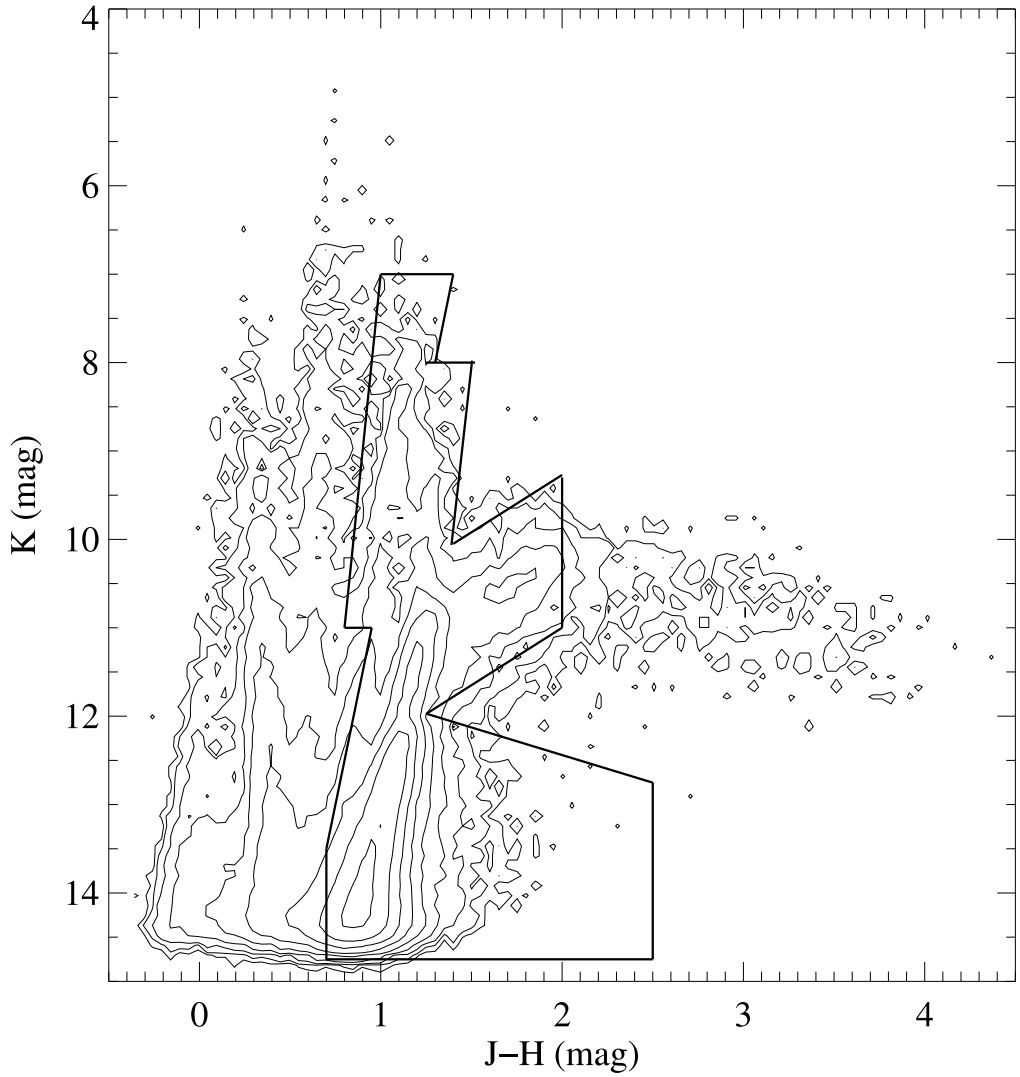

Figure 4.2: Color-magnitude diagram of the LMC field. The contours are logarithmically spaced, from 2 to 3.4, by 0.4. We selected data for the extinction maps from the enclosed region, which corresponds to regions E, F, G, H, J, L and part of D of Nikolaev & Weinberg (2000).

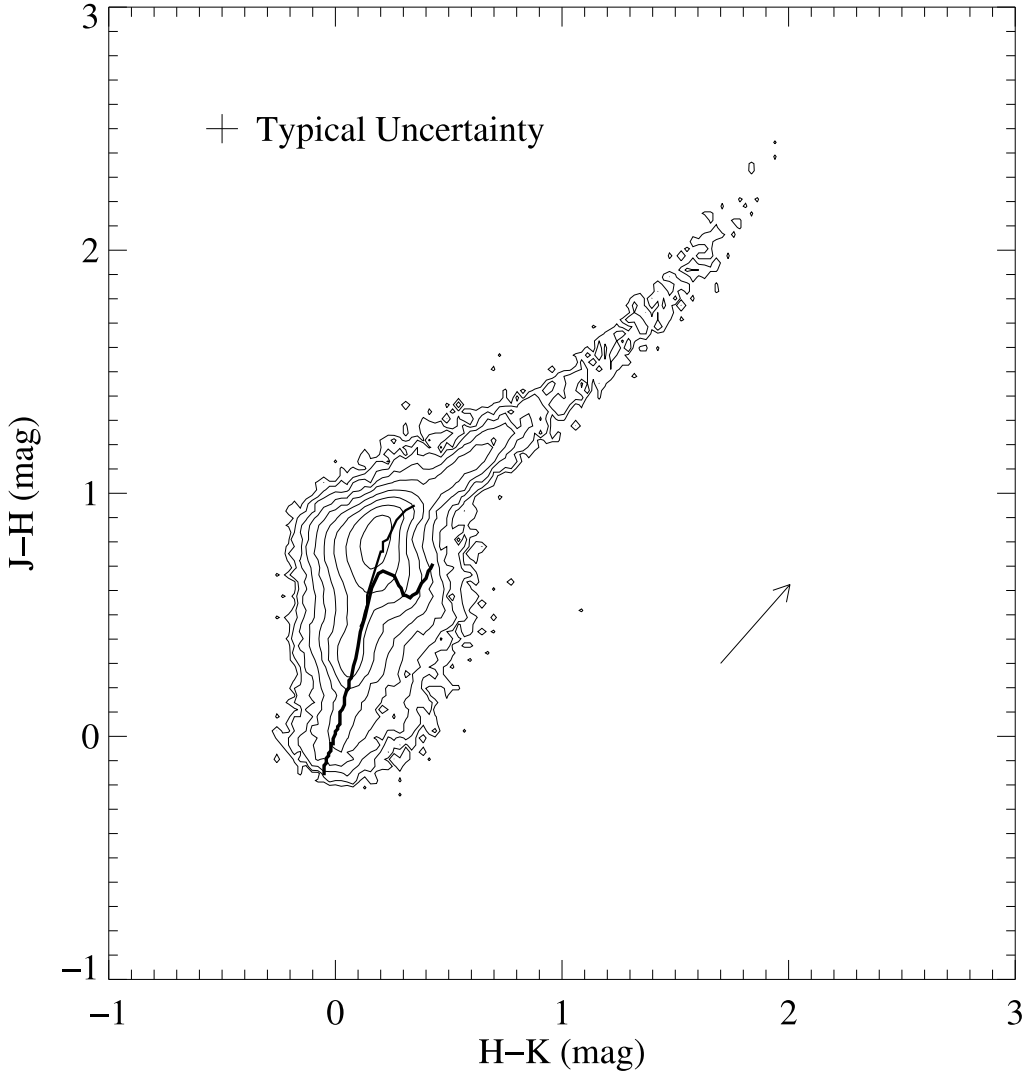

Figure 4.3: Color-color diagram of the LMC field before data reduction. The contours are logarithmically spaced, from 2 to 3.8, by 0.4. Overplotted are the color sequences for Galactic dwarfs and giants from Koornneef (1983). The reddening vector, based on relations from Koornneef (1982), is drawn for $E(B-V) = 1.0$ mag.

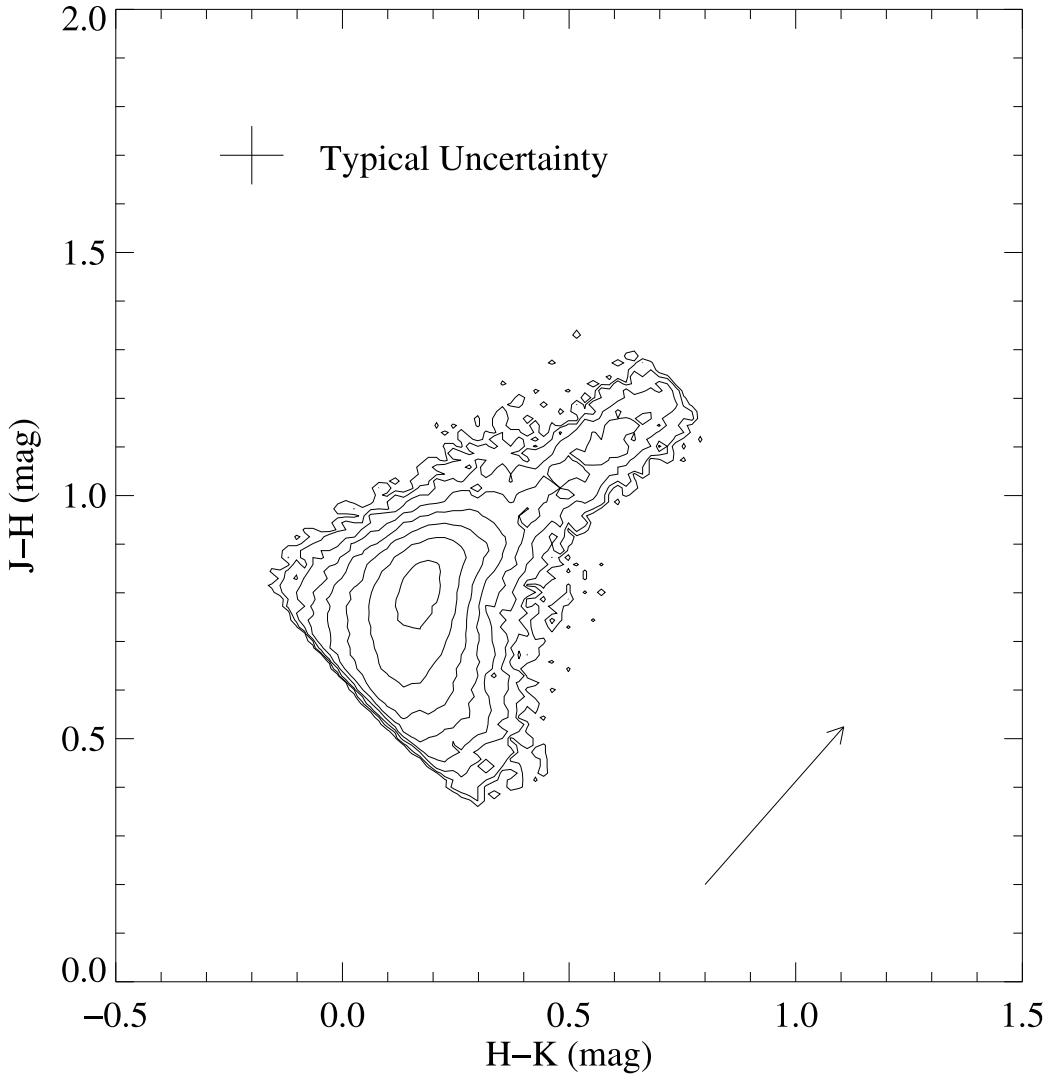

Figure 4.4: Color-color diagram of the 204,502 stars in the LMC field after data reduction. The contours and reddening vector are as in Figure 4.3.

colors is small or when the column density of the GMCs in question is sufficiently high. As we show in the following subsection, the first condition is not met in our case. Neither do we have any *a priori* reason to sigma-clip based on the latter condition.

In any case, to explore the effects of this method on our data set, we did generate a number of sigma-clipped maps. Ultimately, we found no advantages in doing so and used a simple weighted mean for our final maps.

Homogeneity of control and field stars

Success with the NICE(R) technique relies on the mean color of the control group being characteristic of the intrinsic color of the field stars. Recall, the reddening of a given star is the difference between the observed color and the intrinsic color *of a particular spectral type*. Thus, extending the NICE(R) method to an entire extragalactic field raises another concern as to whether the fraction of stars of a particular spectral type varies significantly across the field. In other words, we are concerned with the homogeneity of the field, especially the control group. Based on the selection criteria in the previous section, we are confident that our field consists primarily of giant branch stars, though a variety of stages in evolution are represented (e.g., helium and hydrogen shell burning phases, oxygen- and carbon-rich phases; Nikolaev & Weinberg 2000). As for the control group, we would like the dispersion around the mean control color to be significantly less than the observed range of field star colors, since the dispersion determines the 1-σ confidence level for extinction measurements (Alves et al. 1998).

We examined the HI and CO maps of the LMC for minimally reddened regions and inspected control groups in each of the four "corners" of the galaxy image (Figure 4.5). Not surprisingly, the regions do not have narrow color distributions. The control groups are well-behaved in that they are statistically equivalent—the $(H-K)$ colors to two significant figures and the $(J-H)$ colors to one significant figure. Yet, as Figure 4.6 shows, the width of the control distributions relative to that of the field stars forecasts low signal-to-noise in extinction measurements. The nature of the uncertainties is explored in detail in § 4.3.2 where we derive the extinction maps. We are somewhat consoled, though, since the large number of stars in our data set will act to minimize this problem and because our main interests here are in global properties of the galaxy. We proceed by taking the average of the mean control group colors as the intrinsic colors of the field:

$$\begin{aligned} (H-K)_{\rm intrinsic} &\equiv \langle (H-K) \rangle_{\rm control} \\ &= 0.16 \pm 0.09 \text{ mag}, \qquad (4.4) \\ (J-H)_{\rm intrinsic} &\equiv \langle (J-H) \rangle_{\rm control} \\ &= 0.74 \pm 0.11 \text{ mag}. \qquad (4.5) \end{aligned}$$

By comparison, the mean colors of the entire data set are $(H-K) = 0.175 \pm 0.0946$ and $(J-H) = 0.772 \pm 0.110$ mag (see Figure 4.6). Again, this and the previous selection criteria are summarized in Table 4.1.

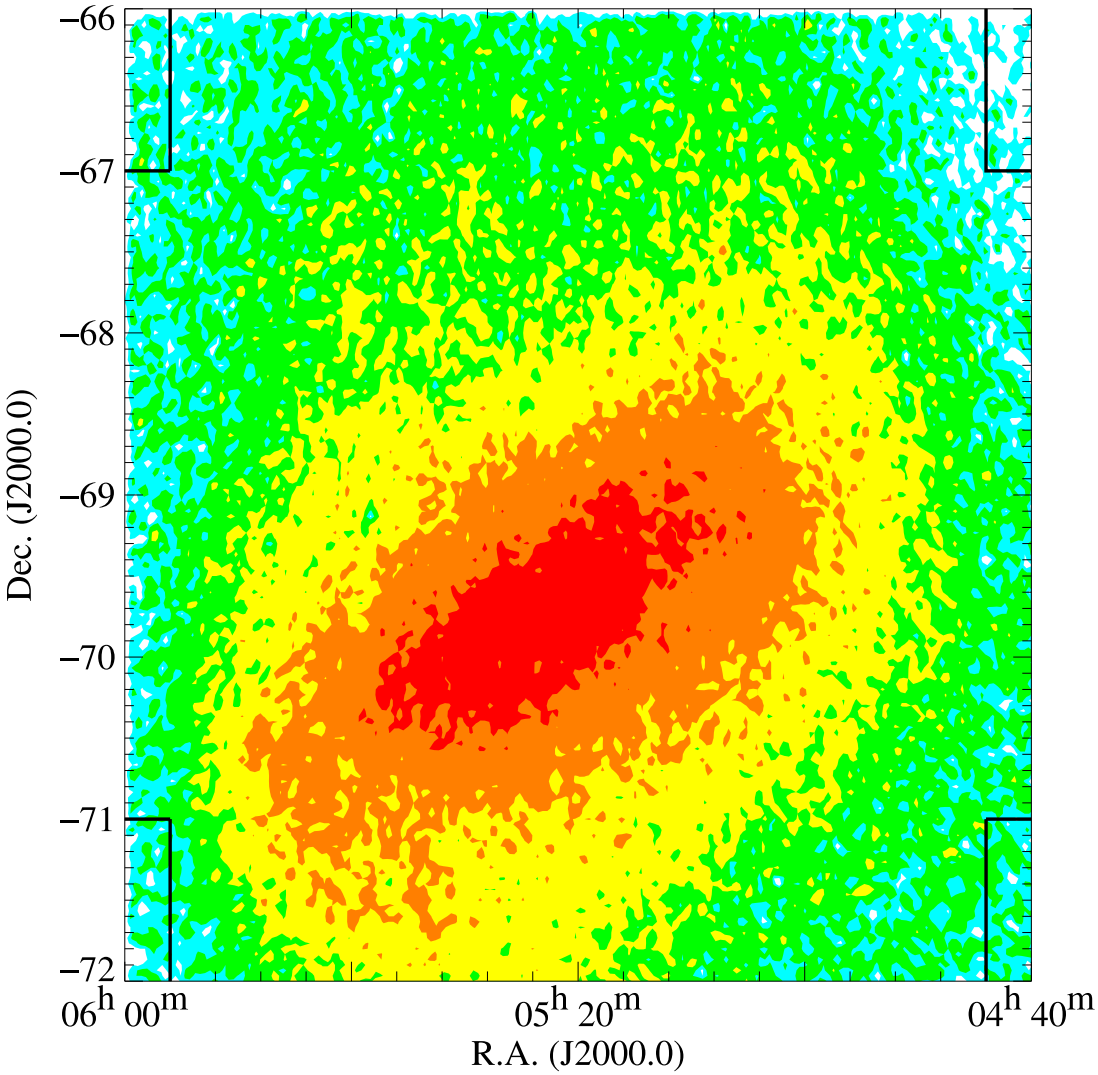

Figure 4.5: Spatial distribution of the selected sources, in pixels of $4' \times 4'$, with average surface density of $\Sigma_{\rm LMC} = 4.76 \times 10^3$ stars deg^{-2}. Counterclockwise starting from the northeast, the outlined control regions have an average of $\Sigma_{\rm cont.} = 1.48$, 1.57, 1.98, and 1.02×10^3 stars deg^{-2}. The color levels cyan, green, yellow, orange, and red correspond to 0.90, 1.80, 3.60, 7.20, and 14.40 $\times 10^3$ stars deg^{-2}, respectively.

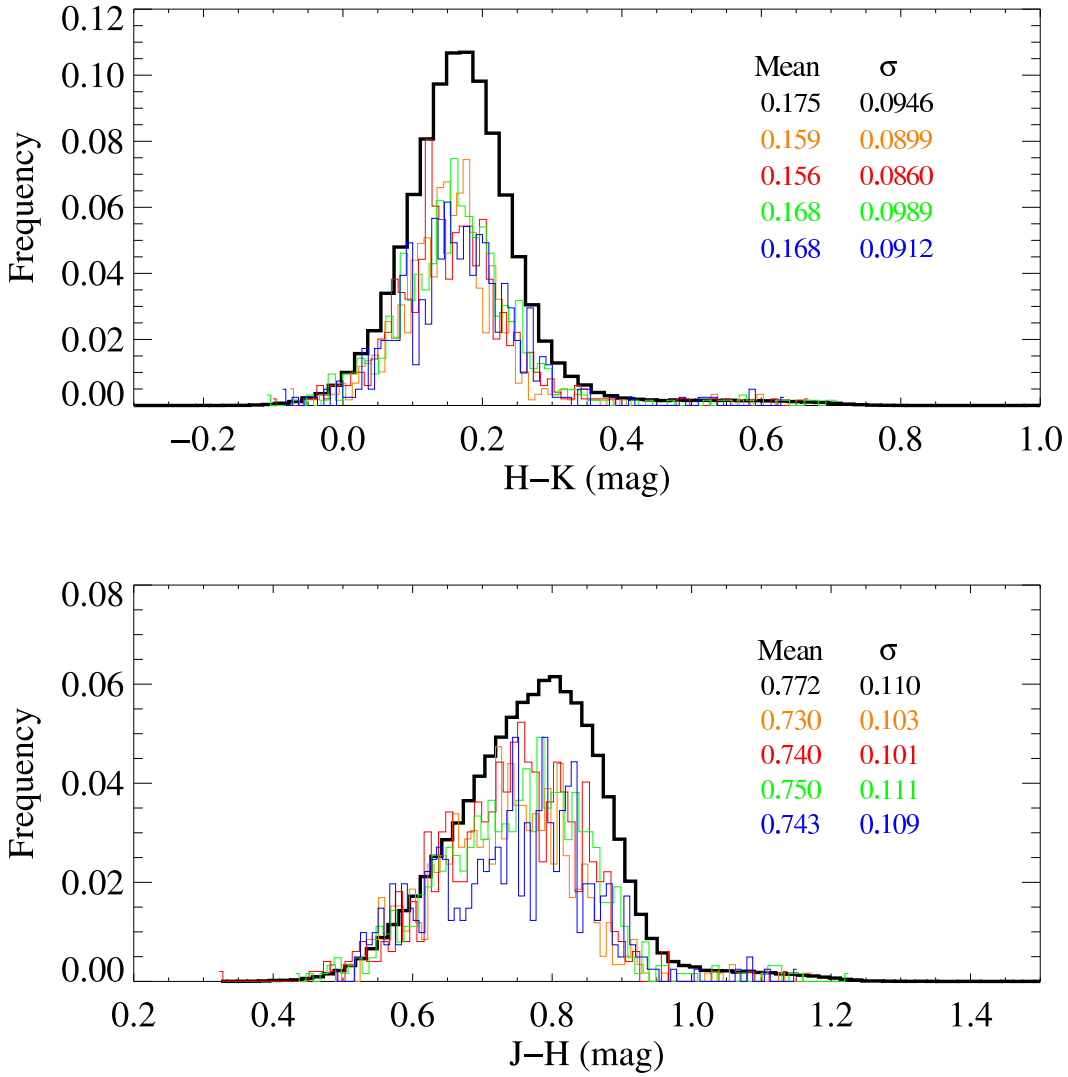

Figure 4.6: The reddening distributions of the LMC field (heavy black line) and control (colored lines) groups. The orange, red, green, and blue lines correspond to data from the northeast, southeast, southwest, and northwest corners of the LMC, as shown in Figure 4.5.

4.3 Results

4.3.1 NIR Extinction Law

The NICE(R) methods require knowledge of the NIR extinction law and assume that this relationship is linear. The extinction law may be described by extinction coefficients, $k_i = A_V/E(m_{\lambda_1} - m_{\lambda_2})$, which relate the extinction to the color excess. Knowing k_i enables us to convert color excess to A_V, which is proportional to $N(H_{total})$ and, hence, to $N(H_2)$. To determine the scaling we must assume a value of the LMC gas-to-dust ratio. Thus, we plot $E(m_{\lambda_1} - m_{\lambda_2})$ versus N(HI), and compare this relationship with the LMC gas-to-dust ratio estimated by Gordon et al. (2003) (Figure 4.7). Their value of $N(\mathrm{HI})/A_V = (3.25 \pm 0.28) \times 10^{21}$ mag^{-1} cm^{-2} is a weighted average of all 24 archival gas-to-dust ratio measurements.

$E(H-K)$ and $E(J-H)$ for individual stars were determined by subtracting the intrinsic colors (Equations 4.4 and 4.5, respectively) from the observed 2MASS colors. Color excess maps were generated by binning the data into $4'$ pixel grids with $2'$ spacing. The color excess at a given location was then given by the average, weighted by the uncertainties, of stars within that pixel. Next, these maps were compared to the N(HI) map on a pixel-by-pixel basis.

In Figure 4.7, the data are averaged in bins of equal N(HI) and fitted for the linear relation

$$E(m_{\lambda_1} - m_{\lambda_2}) = m_i A_V(\mathrm{HI}) + b, \tag{4.6}$$

where $m_i = k_i^{-1}$ and $A_V(\mathrm{HI}) = N(\mathrm{HI})/(2 \times 3.25 \times 10^{21}$ mag^{-1} cm$^{-2})$ is the extinction due to HI. The HI column is divided by 2 since, on average, extinction along a given line-of-sight is caused by half the dust layer. In other words, only half the total column, on average, contributes to the measured reddening. The data are plotted in bins of $\Delta A_V(\mathrm{HI}) = 0.05$ mag, and weighted least-squared fits were done over the range $A_V(\mathrm{HI}) = [0.1, 1]$ mag. So as to get the best possible correlation between color excess and atomic hydrogen we masked out regions with significant molecular gas, defined as areas with CO emission exceeding $I_{CO} \cong 1$ K km s^{-1}. This value is based on an examination of the Mizuno et al. (2001) CO map, in which they define GMC complexes as regions exceeding 3 K km s^{-1}. The extinction coefficients k_i, which came from the inverse of the best fit slopes, were found to be 20.83 ± 0.52 and 17.30 ± 0.46 for $E(H-K)$ and $E(J-H)$, respectively. Dividing these results gives a ratio of $E(J-H)/E(H-K) = 1.20 \pm 0.04$, which is consistent with the Koornneef (1982) reddening law, which is $E(J-H)/E(H-K) = 1.06$ when converted to the 2MASS photometric system (Carpenter 2001).

In principle, one should be able to determine the NIR reddening law by comparing $E(H-K)$ and $E(J-H)$ directly. And if the color excesses are linearly dependent, the ratio of extinctions in two different bands is constant, a key assumption of the NICE(R) techniques. We found that this direct comparison was not a robust way of measuring the reddening law, in part, because of the lack of a linear relation for low values of $(H-K)$ and $(J-H)$—a result of our data selection (see Figure 4.4). When we examined the reddening

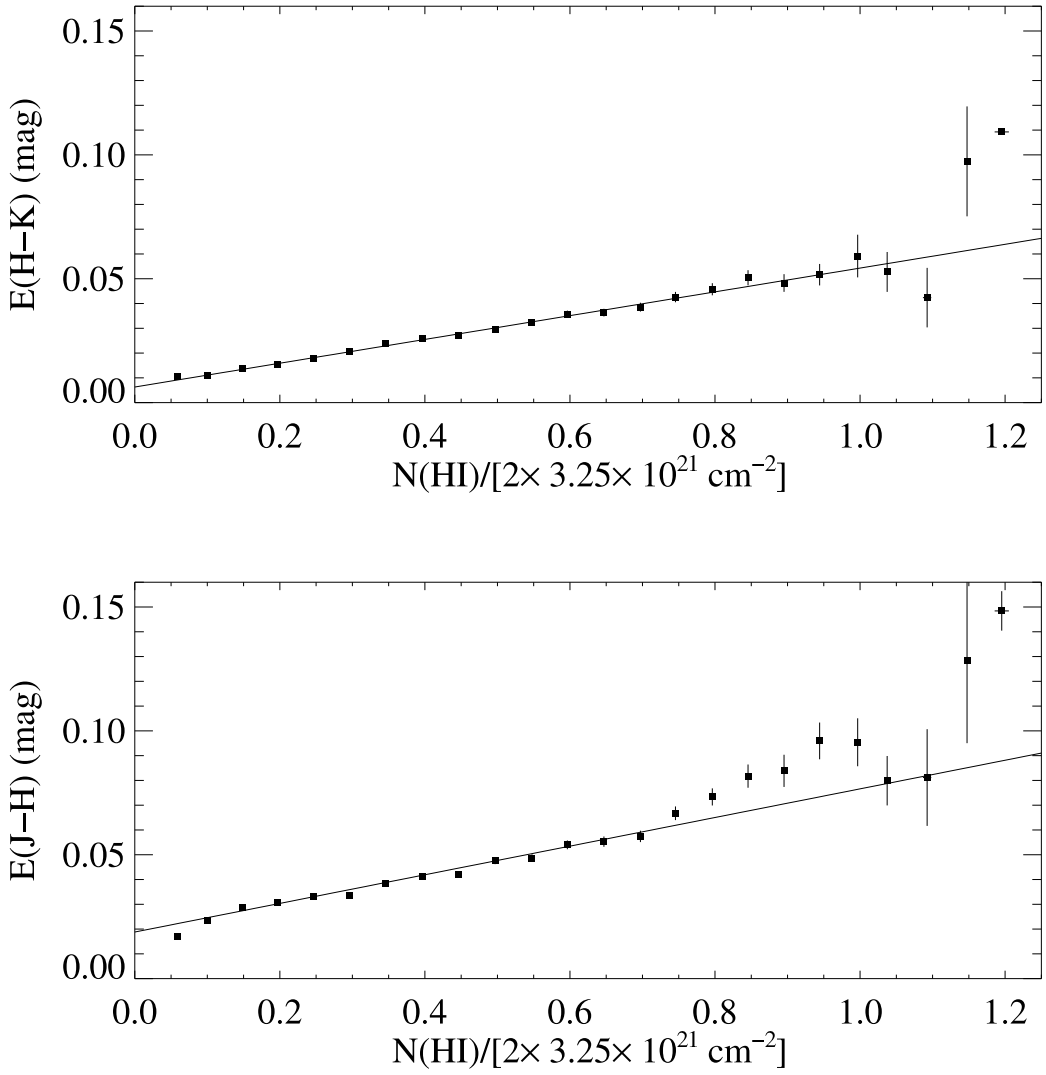

Figure 4.7: LMC reddening as a function of hydrogen column, measured in regions where $I_{\rm CO} < 1$ K km s^{-1}. Error bars represent the deviation around the mean of color excesses inside the bin (ΔN(HI)/[2. $\times$ 3.25 $\times$ 10^{21}cm^{-2}=0.05]).

law in the same regions as the gas-to-dust ratio analysis (i.e., where $I_{\rm CO} < 1$ K km s^{-1}), we found that the data could be fit by two different slopes. Figure 4.8 shows that the majority of stars with little to no reddening are fit by a shallower slope than more highly reddened stars. Below $E(J-H) \approx 0.05$ mag, the data are consistent with a noise population and there is no robust linear fit. Above $E(J-H) \approx 0.1$ mag, however, the data are well approximated by the linear relationship $E(H-K) = (0.84 \pm 0.06)E(J-H) - (0.037 \pm 0.007)$. The reciprocal of the slope, 1.19, is in good agreement with the $E(J-H)/E(H-K)$ ratio of 1.20 we derive via the gas-to-dust ratio measurements and with the Koornneef (1982) reddening law. We also repeated this analysis for the entire reddening maps, i.e., not restricted to regions of low molecular gas. The same result was observed: more highly reddened stars were fit by a linear relationship in agreement with a reddening law with a slope of ≈ 1.20.

Finally, we note that the lack of linearity in the reddening law over the entire range of values is not due to poor photometry. When we repeated the above analysis using stars with increasingly higher S/N ratios, we achieved similar results: stars reddened above $E(J-H) \approx 0.1$ mag were well-fit by a reddening law of ≈ 1.20, while stars with lower reddening were consistent with noise.

4.3.2 NICER Extinction Map

Using the $E(m_{\lambda_1} - m_{\lambda_2})$-$A_{\rm V}$ ratios derived above, an extinction map, shown in Figure 4.9, was constructed using the NICER method (see Lombardi & Alves 2001 for a detailed description). The intrinsic colors and color dispersions, used to calculate the color excess for individual stars, were derived from the control fields (Equations 4.4 and 4.5). Visual extinctions were then calculated for each star, and the data were binned onto $4'$ pixel grids with $2'$ spacing. At this resolution, we can resolve structure down to ≈ 58 pc. Pixels were required to contain at least three stars for subsequent calculations; those with $N < 3$ were given a "not-a-number" value and interpolated over in the extinction map. Out of a total of 44,590 (245×182), there are only 6,089 such pixels, primarily in the periphery of the map where the number density is low.

At our resolution, we found a mean extinction ($A_{\rm V}$) of 0.38 mag and standard deviation of 0.57 mag. The distribution of measured values is displayed by the histogram in Figure 4.10. "Negative" extinction pixels in Figure 4.9 correspond to regions that are bluer than the average intrinsic colors or are due to errors in the measurements. For clarity, a map showing physical extinctions $A_{\rm V} \geq 0$ is shown in Figure 4.11. The most conspicuous feature of the map, which shows extinction due to both the atomic and molecular ISM of the LMC, is 30 Doradus at $\alpha \sim 5^{\rm h}40^{\rm m}$ and $\delta \sim -69^\circ$ to $\delta \sim -71^\circ$ (J2000.0). Other filamentary and arc-like structures are seen, for instance, at $\alpha \sim 5^{\rm h}35^{\rm m}$ and $\delta \sim -68^\circ 20'$ to $-69^\circ 20'$. The "CO arc" identified by Mizuno et al. (2001) is also present in our map, extending southeast of 30 Doradus. Extending southwest from $(\alpha, \delta) \sim (5^{\rm h}, -66^\circ)$ to $(4^{\rm h}40^{\rm m}, -68^\circ 30')$ is a loose "string" of highly extincted clumps, some of which are associated with HI peaks. But there are no peaks in either the HI or CO maps corresponding to the rather large ($\sim 175 \times 90$ pc)

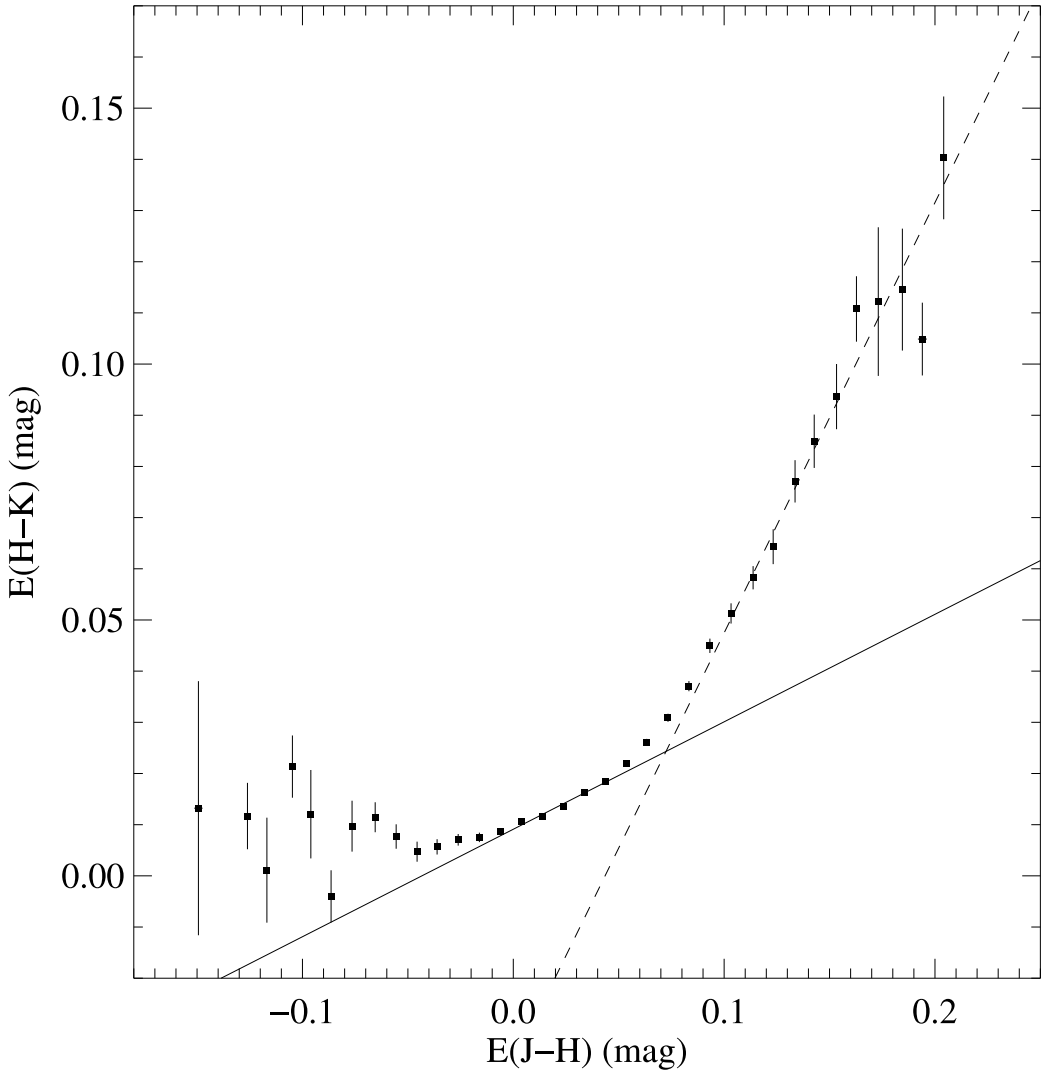

Figure 4.8: The reddening law measured in the same regions as Figure 4.7. The $(H-K)$ color excess is plotted as a function of $(J-H)$ color excess. Error bars represent the deviation around the mean of $E(H-K)$ inside the bin $\Delta E(J-H) = 0.01$ mag. The data are plotted as a function of $E(J-H)$, as opposed to $E(H-K)$ as is often the case, because in this circumstance $E(J-H)$ has a higher overall signal-to-noise.

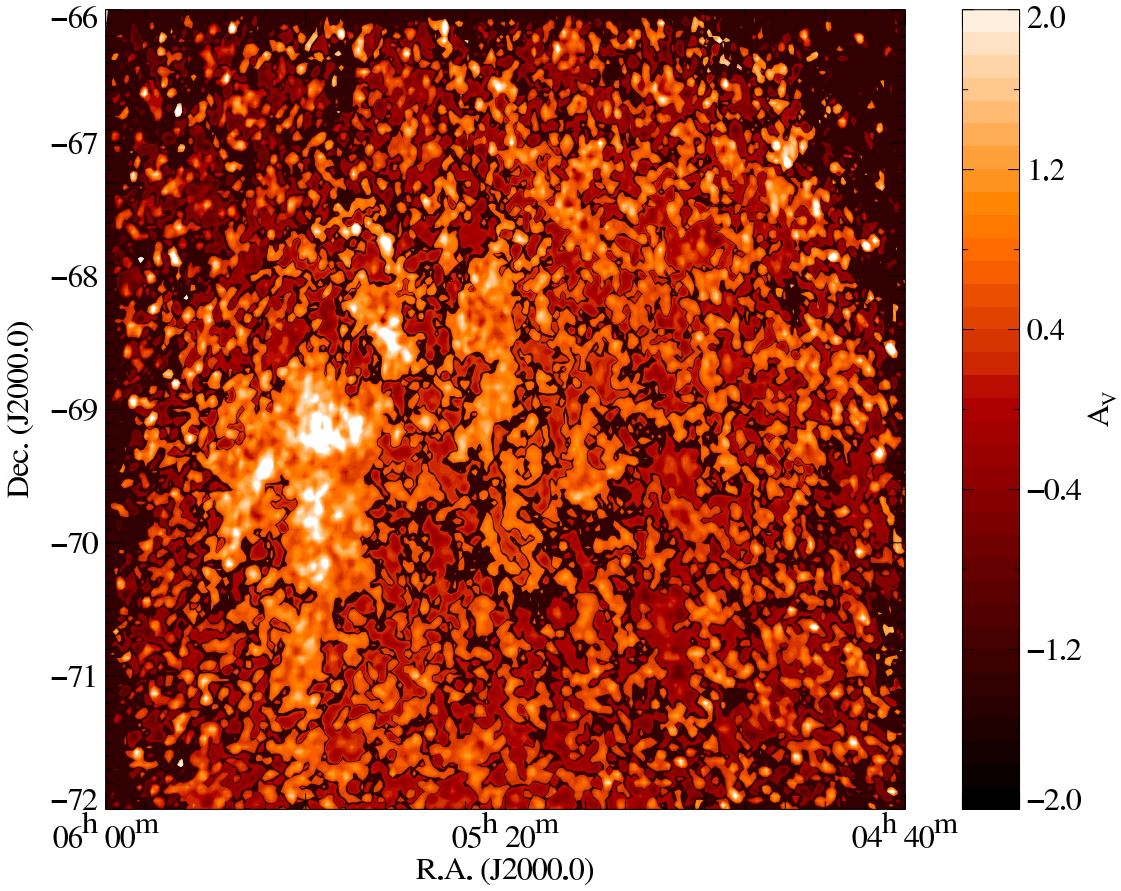

Figure 4.9: Sigma-clipped NICER extinction map of the LMC at a resolution of 4 arcmin.

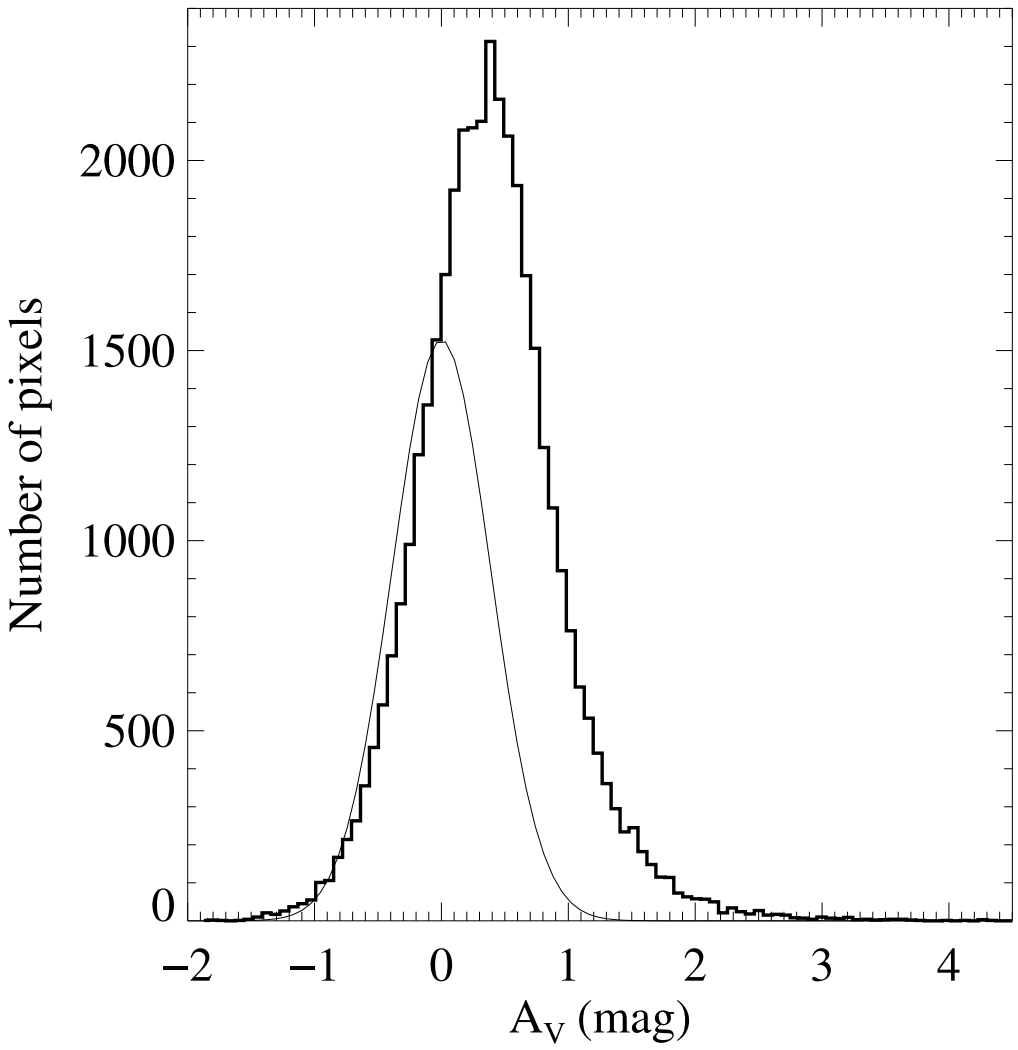

Figure 4.10: The pixel extinction distributions of the the sigma-clipped map (Figure 4.9). Indicating a population of zero-reddening stars is a Gaussian with σ equal to the mean of the propagated measurement errors of the data.

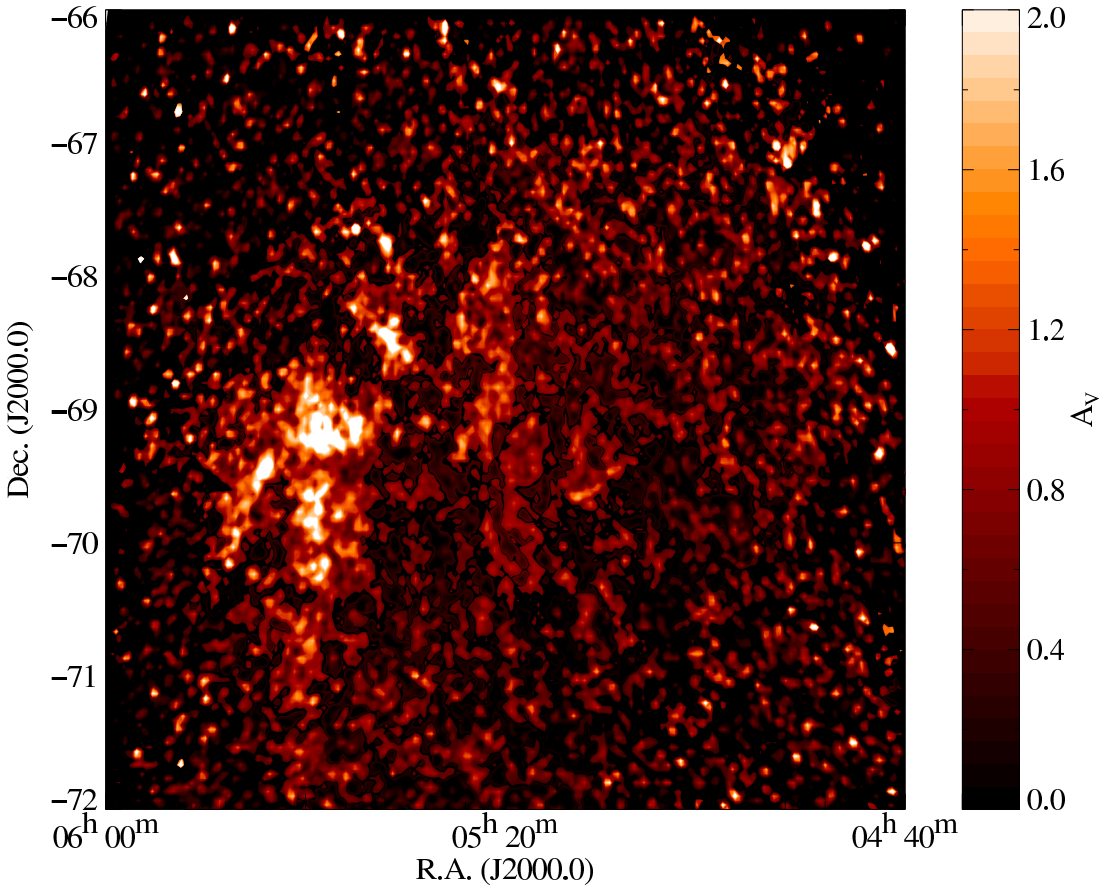

Figure 4.11: Sigma-clipped NICER extinction map of the LMC at a resolution of 4 arcmin. This map shows physically allowable extinctions, i.e., $A_V \geq 0$ mag.

clump at ($4^{\rm h}40^{\rm m}, -68°30'$). We do not find distinct, high-$A_{\rm V}$ features located toward the bar at $(\alpha, \delta) \sim (5^{\rm h}20^{\rm m}, -70°)$.

4.3.3 Uncertainties and noise

The average extinction of a given pixel is estimated by the weighted mean of all stars falling within it:

$$\langle A_{\rm V} \rangle = \frac{\sum_{i=1}^{N} W_i A_{{\rm V},i}}{\sum_{i=1}^{N} W_i}, \tag{4.7}$$

where the weight for the ith star is given by $W_i = 1/\sigma_i^2$, and σ_i^2 is the variance due to the uncertainties in photometry and intrinsic star colors, $\sigma_i^2 = \sigma_{{\rm phot},i}^2 + \sigma_{{\rm color},i}^2$. The error in the mean, or the observed variance, for the pixel is given by

$$\sigma_{\rm mean}^2 = \frac{\sum_{i=1}^{N} W_i \left(\langle A_{\rm V} \rangle - A_{{\rm V},i} \right)^2}{(\sum_{i=1}^{N} W_i)}. \tag{4.8}$$

The signal-to-noise ratio (SNR) of the final map is dependent upon the smoothing technique used. In order to eliminate suspected foreground stars that are expected to increase the uncertainty in $A_{\rm V}$ especially in highly extincted regions, we would have liked to smooth the map using sigma-clipping. In this technique, the local uncertainty in $\langle A_{\rm V} \rangle$, $\sigma_{A_{\rm V}}$, is estimated, and then Equation 4.7 is recalculated using only stars that fall within $\pm n$-$\sigma_{A_{\rm V}}$ of the first estimate of $A_{\rm V}$.

When the distribution of control field colors is sufficiently narrow, or when extinction caused by the clouds is sufficiently high and the fraction of foreground stars low, sigma-clipping is a practical solution to removing foreground stars that contribute to the noise but not the signal. Otherwise, especially when the latter case is untrue, there is the risk of underestimating the extinction. This is because sigma-clipping eliminates outliers with both high and low extinction.

The trend of uncertainty increasing with extinction (see Figure 4.12) results from a number of sources of error, including the uncertainty of the intrinsic colors, small-scale structure within pixels, photometric errors in the individual bands, and foreground stars within the LMC. The latter two uncertainties are expected to increase in highly extincted regions. The stellar number density in high-$A_{\rm V}$ pixels is comparable to low-$A_{\rm V}$ areas of the map (~ 15 stars per pixel and ~ 21 stars per pixel for $A_{\rm V} > 2$ and $A_{\rm V} < 2$ mag, respectively), and so Poisson noise is not the main contributor to the increased dispersion.

In the NICER method, σ_i^2 is calculated for each star from the covariance matrices of the intrinsic scatter in colors and photometric errors. The corresponding measurement error of a pixel is given by $\sigma_{\rm meas}^2 = 1/\sum_{i=1}^{N} W_i^2$. The following analysis of $\sigma_{\rm meas}^2$ and the total dispersion of a pixel, $\sigma_{\rm mean}^2$ (Equation 4.8), can help us determine which types of uncertainties dominate.

As shown in Figure 4.12, in low-extinction regions of our map, measurement (i.e., photometric and intrinsic color) errors contribute to a larger fraction of the overall uncertainty

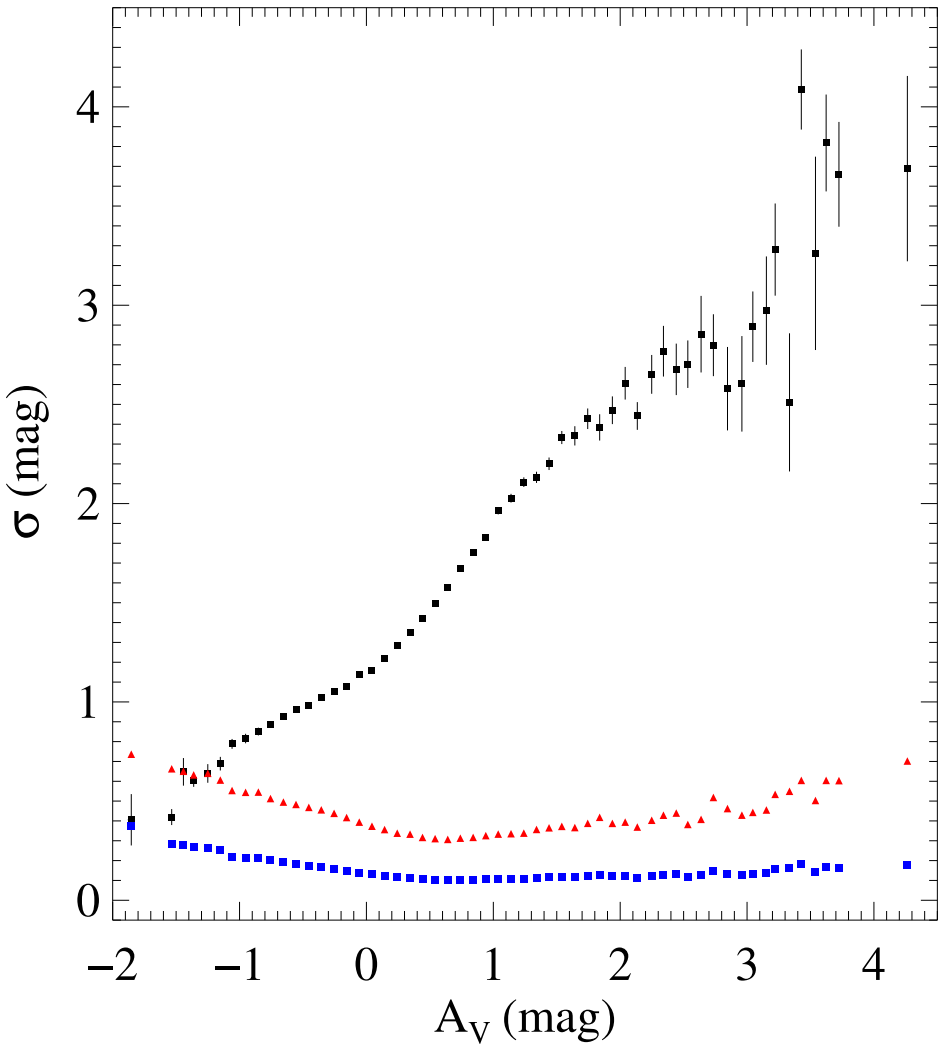

Figure 4.12: Dispersion of measured extinctions as a function of A_V in bins of 0.10 mag. The black squares show $\sigma_{\rm mean}$, as calculated by Equation 4.7, averaged in each bin, with the relative scatters indicated by error bars. For comparison, we plot the mean error due only to scatter in intrinsic color and that due only to photometry, indicated by red and blue triangles, respectively.

than in high-extinction regions. As the extinction increases, the dispersion due to small-scale structure and foreground stars within the LMC increasingly dominate the uncertainty. As discussed in previous studies (e.g. Lada et al. 1994; Alves et al. 1998; Lombardi et al. 2006), these two phenomena are difficult to disentangle since they result in similar statistics. For instance, an un-reddened star appearing through a "hole" in a GMC is indistinguishable from a foreground star in front of the same cloud.

We check the accuracy of our estimated uncertainties by examining the distribution of pixels with $A_V < 0$, The appearance of a significant number ($\sim 1/5$) of such pixels (see Figure 4.10) is consistent with a noise population with a standard deviation characterized by the mean measurement error. That is, stars with $A_V < 0$ are well-fit by a Gaussian with a standard deviation equal to the propagated measurement uncertainties, $\langle \sigma_{\rm meas} \rangle = 0.39$ mag. Recall, the dispersion of the control group colors—the value that determines the significance level of the extinction measurements—is not much less than the dispersion of the field star colors (see Figure 4.6 in § 4.2.2). With deeper observations and better measurements of the intrinsic colors of a well-defined population, these statistics could be improved upon. Meanwhile, as indicated by Figure 4.10, we are unable to distinguish real signal from noise below $A_V \approx 1$ mag. With an overall 1-σ noise level of 0.57, the average SNR of the entire extinction map is 0.66; it is 2.5 for those regions of the map where $A_V > 1$ mag.

We note that the column densities derived in this paper may be systematically lowered if the extinction coefficients derived in § 4.3.1 are too large. This would be the case if we assumed too low of a gas-to-dust-ratio, (see Equation 4.6).

However, the measured columns are more likely to be lower limits, for the following reasons. (1) Foreground contamination results in the dilution of signal, and thus, lower values of A_V. (2) The most highly extincted stars likely went undetected. In § 3.3 we show that our measurements of A_V are relatively insensitive where $I_{CO} > 2$ K km s^{-1}; deeper photometry in these regions would raise the measured extinction.

4.3.4 Comparison with previous studies

The mean internal extinction we derive here is in overall agreement with earlier measurements. Table 4.2 summarizes the mean reddenings given by previous authors, each of whom used some form of the color excess technique—subtracting intrinsic from observed colors—to derive a reddening distribution. All used UBV photometry of early-type stars for their reddening measurements. They were necessarily observing the most luminous stars, which may have additional circumstellar reddening due to heavy mass-loss. This could lead to overestimating the interstellar reddening, as Oestreicher & Schmidt-Kaler (1996) point out.

Other common sources of error and inaccuracy in the results of previous authors included (i) the assumption of Galactic intrinsic colors, (ii) not accounting for the Galactic foreground contribution to reddening, (iii) not addressing selection effects related to completeness, (iv) small data sets, and (v) limited spatial coverage. Adopting Galactic intrinsic colors (e.g., Feast et al. 1960, Isserstedt 1975, Isserstedt & Kohl 1984) leads to an underestimate of

Table 4.2: **Summary of LMC Reddenings.**

$E(B-V)$ (mag) [a]	Reference
0.12 [b]	This paper
0.10	1
0.07 [c]	2
0.02–0.20	3
0.10	4
0.15 (0.01–0.26) [c]	5
0.13 [c]	6
0.16	7
0.13	8
0.13	9

[a] Except for the Isserstedt (1975) value, a maximum detection, values listed are means or ranges of $E(B-V)$.

[b] In converting our derived $\langle A_V \rangle$ to $\langle E(B-V) \rangle$, we used $R = A_V/E(B-V) = 3.1$, as did the authors listed here. The use of Gordon et al.'s more recent value calculated for the LMC, $R = 3.41$, would result in $\langle E(B-V) \rangle = 0.11$ mag.

[c] These authors did not correct for Galactic foreground reddening.

REFERENCES.–(1) Feast et al. (1960); (2) Isserstedt (1975); (3) Isserstedt & Kohl (1984); (4) Grieve & Madore (1986); (5) Hill et al. (1994); (6) Massey et al. (1995); (7) Oestreicher & Schmidt-Kaler (1996); (8) Harris, Zaritsky & Thompson (1997) ; (9) Zaritsky (1999)

the reddening since MW supergiants (the stellar types used by these authors) are intrinsically redder in color than their LMC counterparts, especially in UBV photometry. Not accounting for the completeness limit (e.g., Massey et al. 1995) also biases the measurements toward lower extinction, since highly reddened faint stars are underrepresented (see § 2.2.1). The extinction will be *overestimated*, however, if the Galactic foreground contribution to reddening isn't corrected (e.g., Hill et al., Massey et al. 1995).

Inaccuracies in the overall spatial distribution of reddening may result from items (iv) and (v). Feast et al. (1960) had a small data set (108 supergiants) sampled from across the LMC. Hill et al. (1994) used 7 OB associations, 3 of which are associated with 30 Doradus, one of the most highly reddened regions of the galaxy. Harris et al. (1997) and Zaritsky (1999), as part of connected studies, produced maps of variable spatial resolution which covered areas of $\sim 2^\circ \times 2^\circ$ and $\sim 4^\circ \times 2.7^\circ$, respectively. The most comparable map to ours is that created by Oestreicher & Schmidt-Kaler (1996) from 1,507 O-A stars throughout the LMC. They did not grid their map, but rather analyzed the distribution of reddened stars. Like us, they found reddening throughout the LMC, including in peripheral areas not associated with HI or CO peaks. They also did not find much reddening in the bar.

4.3.5 The X-Factor

The X-factor is defined as

$$X \equiv \frac{N(\mathrm{H_2})\ [\mathrm{cm^{-2}}]}{I_{\mathrm{CO}}\ [\mathrm{K\ km\ s^{-1}}]}. \tag{4.9}$$

To determine X_{LMC}, both the CO data and NICER extinction map were convolved to maps of the same pixel size ($4'$) and grid spacing ($2'$) and then compared on a pixel-by-pixel basis. These maps are displayed in Figure 4.13. For the reasons discussed in the previous section, only pixels in which $A_{\mathrm{V}} \geq 1$ mag (or, SNR$\geq$ 2.5) are used. A linear relationship between A_{V} and I_{CO} would allow us to derive X by fitting the data. However, above about 2 K km s^{-1}, as shown in Figure 4.14, there does not appear to be any linear dependence between I_{CO} and A_{V}. This lack of a linear correlation at high column densities most likely results from insufficient sensitivity in our extinction measurements. The global mean SNR of the A_{V} map (0.66) surpasses that of the I_{CO} map (0.23). But the comparative sensitivities of the two measurements appear to depend on the molecular content in a given area. In high column density regions, above $I_{\mathrm{CO}} = 2$ K km s^{-1}, these SNRs are 1.60 for A_{V} and 6.5 for I_{CO}. In low column density regions, $I_{\mathrm{CO}} < 2$ K km s^{-1}, the trend is reversed and the ratios are 0.82 and 0.18, respectively.

In order to take full advantage of the data in the regions of most concern to us, i.e., regions of highest extinction, we proceed by deriving the X-factor statistically. Of the 4,396 pixels with $A_{\mathrm{V}} \geq 1$ mag, there are 271 remaining corresponding to positions where $I_{\mathrm{CO}} \geq 2$ K km s^{-1}.

The total contribution of hydrogen gas to the column density, $N(\mathrm{H_{tot}}) \equiv N(\mathrm{HI}) + 2N(\mathrm{H_2})$, may be obtained from A_{V}. Statistically, along any given line-of-sight toward the LMC, half the total column contributes to the measured extinction. That is, $N(\mathrm{H}_{\mathrm{tot}}^{(A_{\mathrm{V}})}) = N(\mathrm{H_{tot}})/2$. In terms of the average gas-to-dust ratio calculated by Gordon et al. (63), the column density of molecular hydrogen is

$$N(\mathrm{H_2})[\mathrm{cm^{-2}}] = 3.25 \times 10^{21} A_{\mathrm{V}}[\mathrm{mag}] - \frac{1}{2}\mathrm{N(HI)}[\mathrm{cm^{-2}}]. \tag{4.10}$$

Figure 4.13 displays the map of visual extinction due to $\mathrm{H_2}$, created using this equation. Finally, the mean of Equation 4.9 is calculated for pixels where $A_{\mathrm{V}} \geq 1$ mag and $I_{\mathrm{CO}} \geq 2$ K km s^{-1}. We note that the suitability of this method relies on $2N(\mathrm{H_2})$ being significantly larger than $N(\mathrm{HI})$ since, otherwise, large errors would result from the subtraction in Equation 4.10. For our measurements towards regions of the LMC where $A_{\mathrm{V}} \geq 1$ mag, $2N(\mathrm{H_2})/N(\mathrm{H_{tot}}) = 73\% \pm 17\%$, indicating that it is reasonable to proceed with Equation 4.10.

In units of 10^{20} cm^{-2} (K km s^{-1})$^{-1}$, we found that $X_{\mathrm{LMC}} = 9.3 \pm 0.4$, where the error around the mean (i.e., the random error) was adopted as the uncertainty. Values range from 0.10 to 47.1, and the 1-σ scatter is 6.9. Figure 4.15 displays this distribution. In the same regions, we measure a total $\mathrm{H_2}$ mass of $(4.5 \pm 0.2) \times 10^7 M_{\odot}$ assuming a distance to the LMC of 50 kpc.

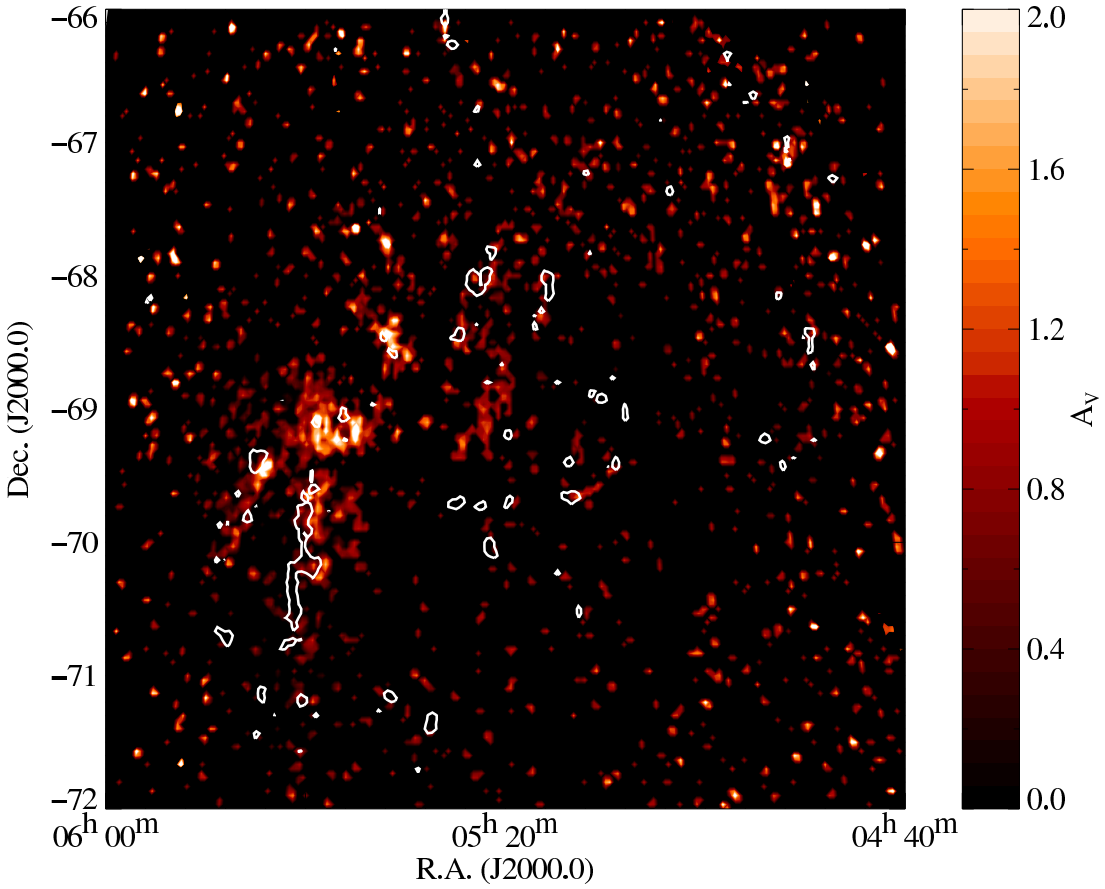

Figure 4.13: This map shows extinction due to H_2. It is created by applying Equation 4.10 to the NICER extinction map (Figure 4.9), using only pixels with total $A_V > 1$ mag. Overlaid are the CO contours of molecular clouds identified by Mizuno et al. (2001).

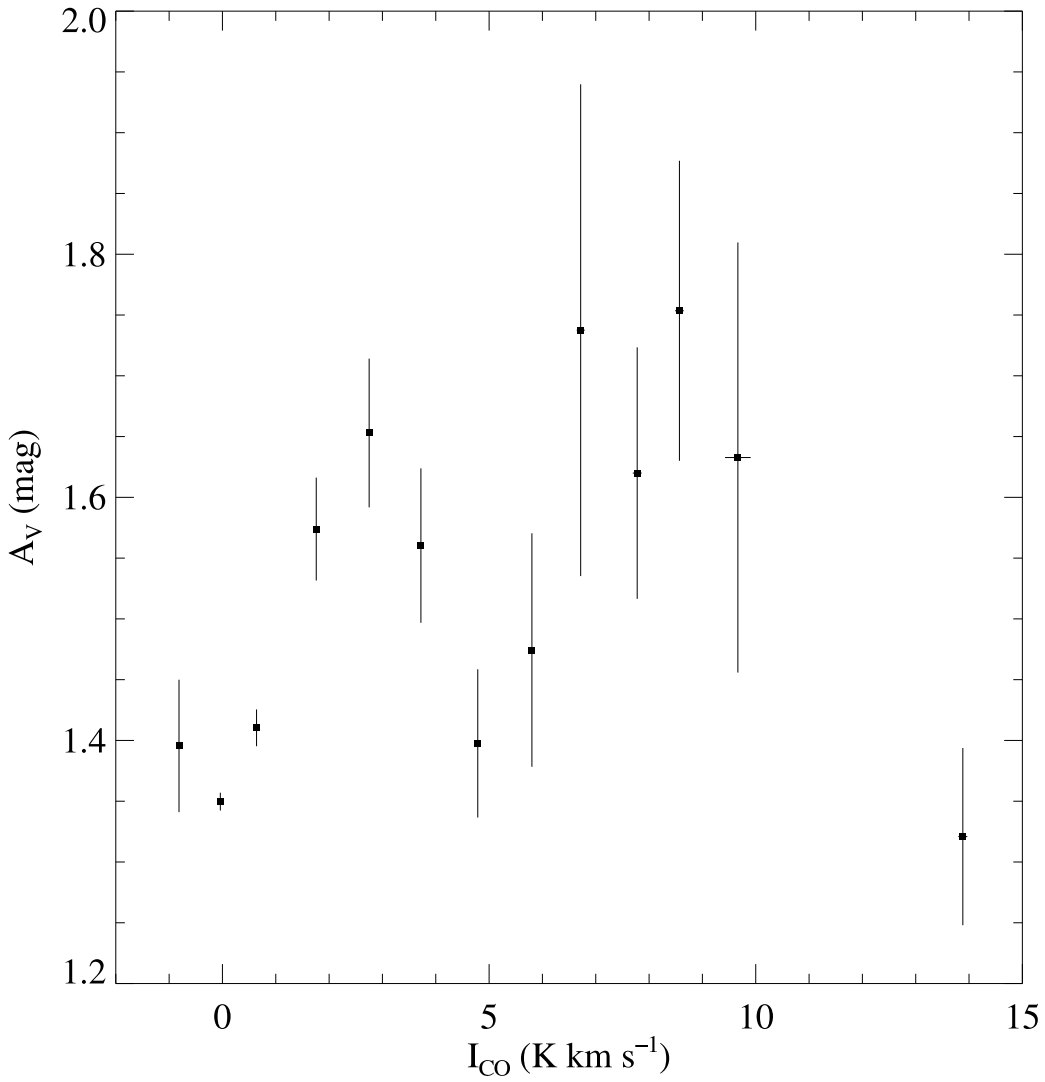

Figure 4.14: Plotted is the $I_{\rm CO}$-$A_{\rm V}$relation for the analyzed regions (see the text for details). Data are binned along the $I_{\rm CO}$ axis in bins of $\Delta I_{\rm CO} = 1.0$ K km s^{-1}.

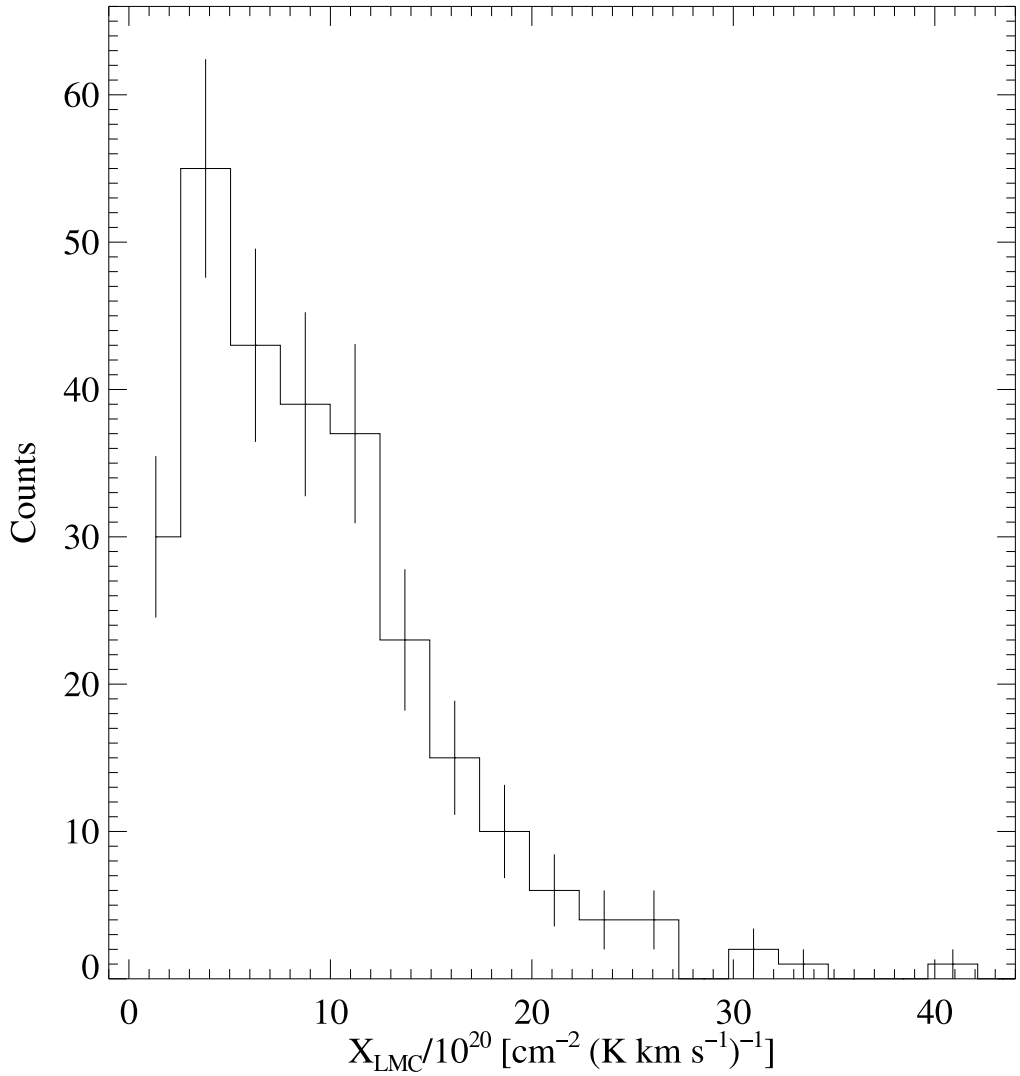

Figure 4.15: The distribution of $X_{\rm LMC}$ for the analyzed regions. The error bars are the deviation in the mean number of counts for each bin.

4.3.6 Comparison with previous studies

Our value of $X_{\rm LMC}$, $\sim 4.7 X_{\rm MW}$, falls in between that of Mizuno et al. (2001; $\sim 4.5 X_{\rm MW}$), who calculated it from high resolution (2.′6) CO observations, and that of Israel (1997; $\sim 6.5 X_{\rm MW}$; see Table 4.3). The former group assumed that CO clouds in the LMC are virialized and calculated the X-factor using $X = M_{\rm vir}/L_{\rm CO}$, where $M_{\rm vir}$ is the virial mass of a cloud and $L_{\rm CO}$ is the CO luminosity. Application of the virial theorem to complex molecular structures, known to exist in the LMC, may be inappropriate. There is no *a priori* reason why the elongated structures associated with 30 Doradus and the supershell regions, for instance, should be virialized. Our value is also significantly larger than the Blitz et al. (2006), who did a revised calculation based on the Mizuno et al. (2001) observations, of $\sim 2.7 X_{\rm MW}$. If the GMCs were not virialized, we would have expected in our calculations a smaller value of $X_{\rm LMC}$ than that obtained by Blitz et al. (2006). Still, their definition of what constitutes a molecular cloud may have led to an underestimate in the total molecular mass.

However, the molecular mass may be overestimated when, at limited resolution, unrelated clouds at different velocities are blended within a beam. At their resolution (8.′8), Cohen et al. (1988) were able to resolve only the largest cloud complexes (~ 140 pc). They derived a value of $X_{\rm LMC}$ nearly 2 times our own, though their results did not assume virialization. Finding that LMC clouds are roughly 6 times fainter in CO than Galactic clouds, Cohen et al. (1988) reasoned that $X_{\rm LMC} \approx 6 X_{\rm MW}$, where they adopted Bloemen et al.'s (1986) value of $X_{\rm MW} = 2.8$. But using the updated value of $X_{\rm MW} = 2.0$ (Bloemen 1989), would result in a value ($X_{\rm LMC} = 12.1$) a bit closer to ours.

Garay et al. (1993), using the same logic and value of $X_{\rm MW}$ as Cohen, found that $X_{\rm LMC} \approx 39$ in the region of 30 Doradus. Israel(1997) found an even greater value (84), while Mizuno et al. (2001) observed no significant difference in the X-factor there compared to other regions. The highest value we measure in this region is 33.7, located at $(\alpha, \delta) = (5^{\rm h}43^{\rm m}51^{\rm s}, -69°26^{\rm m})$. Our relatively low values in this region may result from underestimating $N({\rm H_2})$ (see § 4.3.5). The largest value we find overall, 47.1, is located at $(5^{\rm h}35^{\rm m}05^{\rm s}, -67^{\rm d}38^{\rm m})$ and is associated with a cloud identified by Mizuno et al. (2001) as having an integrated intensity of 4.2 K km s^{-1}.

Deriving the X-factor independently of virialization assumptions by calculating $N({\rm H_2})$ from a comparison of far-IR surface brightness and N(HI), Israel (1997) also measured a larger value ($\sim 6.5 X_{\rm MW}$) than our own. He gives a number of reasons for why his measurements of $N({\rm H_2})$, and therefore $X_{\rm LMC}$, are lower limits. But it appears that his $I_{\rm CO}$ measurements, borrowed from Cohen et al. (1988), are the reason for his comparatively large value of $X_{\rm LMC}$, since $X \propto I_{\rm CO}^{-1}$. The mean integrated intensity of the 22 clouds Israel (1997) uses to determine $X_{\rm LMC}$ is 1.40 K km s^{-1}; the mean $I_{\rm CO}$ detected in corresponding positions by Mizuno et al. (2001) is ~ 8.5 K km s^{-1}. This diminution in measured CO flux by Israel (1997) was likely a result of his convolving Cohen et al.'s (1988) original map to a coarser resolution of 15′.

Previous authors' derivations of $X_{\rm LMC}$, whether over- or underestimated, necessarily tie

Table 4.3: **Summary of LMC X-Factors.**

$X_{\rm LMC}/10^{20}$ cm^{-2} (K km s^{-1})$^{-1}$	Reference
9.3 ± 0.4	This paper
17	1
39 [a]	2
13 ± 2	3
9 ± 4	4
5.4 ± 0.5	5

[a] This value was calculated for the 30 Doradus region. All others are global LMC averages.

REFERENCES.–(1) Cohen et al. (1988); (2) Garay et al. (1993); (3) Israel (1997); (4) Mizuno et al. (2001); (5) Blitz et al. (2007)

to their measurements of total H_2 mass. Cohen et al. (1988), Israel (1997), and Mizuno et al. (2001) derive values of 1.4×10^8 $M_\odot$, $(1.0 \pm 0.3) \times 10^8$ $M_\odot$, and 4–7$\times 10^7$ $M_\odot$, respectively. Our value, $(4.5 \pm 0.2) \times 10^7$ $M_\odot$, as well as our H_2-to-HI mass ratios are consistent with Mizuno et al. (2001). Based on the HI data of Staveley-Smith et al. (2003), we measure a global ratio of $\sim 10\%$. In high-column density regions, where $N({\rm HI}) > 1.5 \times 10^{21}$ cm^{-2} as defined by Mizuno et al. (2001), we find a ratio of $\sim 50\%$. This consistency in mean global measurements is probably due to our relative sensitivities: the CO observations are more sensitive in high-column (i.e., high-mass) regions, whereas our NICER map is more sensitive in the more numerous, low-column regions of the LMC.

Further in keeping with the relative sensitivities of the NICER technique versus CO observations, discussed in § 3.3, is the appearance of our maps. With the exception of the 30 Doradus region, there are few coincidences between the peaks of our H_2 extinction map and GMCs identified by Mizuno et al. (2001), as shown in Figure 4.13. The group cataloged a total of 107 molecular clouds, including 55 "large" molecular clouds. But throughout the LMC, we measure many places where the H_2 is not associated with CO. In a few regions, exemplified by the areas $(\alpha, \delta) \sim (5^{\rm h}40^{\rm m}, -69^\circ)$ and $\sim (5^{\rm h}30^{\rm m}, -68^\circ 30')$, H_2 and CO overlap, with the former extending further than the latter. More commonly, CO and H_2 regions appear adjacent to one another. This suggests that apparently discrete structures are sometimes part of larger complexes that, observed with either method alone, cannot be seen in their entirety. For instance, the three clumps extending from $\sim (5^{\rm h}25^{\rm m}, -66^\circ)$—an H_2 peak bordered by two CO GMCs—may be part of one, elongated structure with varying column density.

4.4 Conclusions

We have used the NICE (Lada et al. 1994) and NICER (Lombardi & Alves 2001) techniques to derive, respectively, the NIR reddening law and $A_{\rm V}$ distribution of the LMC.

Despite the large number of assumptions and uncertainties necessarily introduced in applying these methods to extragalactic sources, results were largely consistent with previous studies. Moreover, with the unprecedentedly large data set from 2MASS, the measured A_V distribution may indeed be an improvement. Our main results are as follows:

1. By comparing the HI and $E(m_{\lambda_1} - m_{\lambda_2})$ distributions (the latter derived with the NICE method) on a pixel-by-pixel basis, we calculated the NIR extinction coefficients for the LMC to be $A_V/E(H-K) = 20.83 \pm 0.52$ and $A_V/E(J-H) = 17.30 \pm 0.46$. Dividing these results $E(J-H)/E(H-K) = 1.20 \pm 0.04$ gives a result consistent with independently measured reddening laws.

2. Using the NICER technique, we created an A_V map whose spatial distribution showed many areas of high column density gas across the face of the LMC that were traced by little CO emission. The mean value of 0.38 mag is consistent with previous results.

3. We created an $A_V(H_2)$ map and compared it to the I_{CO} map provided by Mizuno et al. (107). In regions of significant CO emission we found that X-factor of $(9.3 \pm 0.4) \times 10^{20}$ cm^{-2} (K km s^{-1})$^{-1}$ and $M(H_2) = (4.5 \pm 0.2) \times 10^7\ M_\odot$. Our value of X_{LMC} is less than some authors who, using other methods, probably overestimated it. Since our value is greater than that calculated by both Mizuno et al. (2001) and Blitz et al. (20), this is consistent with their assumption the LMC GMCs are virialized.

We thank Lister Staveley-Smith for providing us with the HI maps of the Galactic foreground and LMC. We also thank Norikazu Mizuno and Yasuo Fukui for providing the CO data.

Chapter 5

Summary and Conclusion

This thesis has provided detailed analyses of the kinematics of individual giant molecular clouds in the Milky Way and M33. The primary goal of this work was to discover what the kinematic properties of GMCs reveal about their formation. A simple question motivated the research presented in Chapters 2 and 3: does the velocity field of a GMC resemble that of the atomic gas with which it is associated and from which it formed? A key result of this work—that the velocity gradient directions of GMCs and of their associated HI are generally unaligned—compels us to reevaluate the view that the linear gradients often observed in GMCs are due to rotation inherited during their formation. In Chapter 4, research was presented on the large-scale properties of molecular clouds in the low-metallicity galaxy the Large Magellanic Cloud. The main goal of this work—to discover the distribution and amount of molecular gas in the LMC that is not detected by CO observations—was achieved and has implications for how GMC and stellar evolution proceed in "primordial" environments. In the remainder of this chapter, I summarize the outcomes of this thesis, put its contributions in a broader context, and I offer recommendations for future work in this field.

5.1 Angular Momentum

In Chapters 2 and 3, I compared the velocity fields of molecular clouds and of the associated atomic gas. I established a set of physically motivated criteria for selecting regions of atomic gas associated with the molecular clouds. In the Milky Way, blending of emission along lines of sight through the Galactic disk toward the GMCs is an unavoidable source of error and can make interpretation of the results difficult. Nevertheless, the main results are consistent with the findings in M33, where source confusion is less of a problem.

Previous studies have reported that the gradient directions of GMCs are occasionally unaligned with the direction of galactic rotation (Kutner et al. 1977; Blitz 1993; Rosolowsky et al. 2003). One of the new outcomes of my research is that local regions of atomic gas also have gradient directions that differ from the sense of galactic rotation (Chapter 3.3.3). This adds to the observational constraints we must take into account when developing theories of

GMC evolution.

In Chapters 2 and 3, alternatives were suggested as the origin for GMC velocity gradients, including expansion driven by HII regions, turbulence, and excess shear in the vicinity of GMCs. To further explore these possibilities, it would be worthwhile to extend the work presented here to more Galactic GMCs. Repeating the analysis established in Chapter 2 on Orion B molecular cloud, which does not have a linear velocity gradient (Kutner et al. 1977), should be especially instructive. Presumably, both clouds in the Orion complex were formed by the same mechanism at about the same time. Bally (2001) proposed that the complex may have originated in the collision of Lindblad's Ring and the Vela supershell discovered by Heiles (1998). These observations are conducive to modeling and, at any rate, a tenable formation theory must be able to explain the properties observed in both Orion A and B.

Two leading theories of GMC formation propose that GMCs originate either from "top-down" gravitational instabilities in which magnetic fields potentially play a vital role (e.g., Mouschovias et al. 1974; Blitz & Shu 1980; Shibata & Matsumoto 1991; Kim et al. 1998), or supersonically converging flows of gas (e.g., Chernin et al. 1995; Vázquez-Semadeni et al. 1995; Ballesteros-Paredes et al. 1999; Hennebelle et al. 2008). Observations such as the GMC mass spectrum and turbulence have traditionally been used as constraints for GMC formation theories. The results presented in this thesis provide additional tests. For instance, formation models can be checked by seeing how well they reproduce the velocity gradient properties observed in the atomic gas surrounding GMCs. Secondly, any theory proposing that the rotation rate of GMCs is slowed by external forces during the course of their evolution should be able to quantify *how much* angular momentum is redistributed and how this affects the dynamical state of the atomic gas in the vicinity of GMCs. Another simple parameter for comparing observation and theory is $\beta_{\rm rot}$, the ratio of an HI region's rotational energy to its self-gravitational energy. Observations in M33 indicate that HI regions associated with GMCs tend to have higher values of $\beta_{\rm rot}$ (~ 0.4) than do regions in which GMCs have not been detected (~ 0.1; Chapter 3.4). Is a relatively high value of $\beta_{\rm rot}$ a condition necessary for GMC formation, or is it a consequence of GMC evolution? Further work in theory and numerical simulations may be able to provide a physically motivated answer to this question.

High-resolution data will soon exist for a comparable analysis of the velocity fields of GMCs and HI in the Large Magellanic Cloud (see §5.4). Such a study would contribute to our understanding of how GMCs form in different environments. Questions that could be addressed include: *How do the properties of GMC and* HI *velocity gradients in the LMC compare to those in M33 and the Milky Way; and what are physically motivated explanations of the similarities or differences*? *How is molecular material collected into GMCs in galaxies that have relatively low molecular fractions or low metalicities (compared to spiral galaxies)*? *What is the dominant mechanism of GMC formation in "primordial" galaxies that lack prominent spiral arms, where GMCs are thought to form in spiral galaxies like the Milky Way*?

5.2 GMCs in Primordial Environments

Though the primary goal of the research presented in Chapter 4 was to calculate the CO-to-H_2 conversion factor in the Large Magellanic Cloud independent of assumptions regarding the virialization or morphology of GMCs, there were a number of other useful results. Using JHK photometry of over 200,000 point sources from the 2MASS catalog, the Near Infrared Color Excess Revised (NICER) method of Lombardi & Alves (2010) was used to create a $6^\circ \times 6^\circ$ reddening map of the LMC, from which an average visual extinction of $A_V = 0.38$ mag was measured. The map in Figure 4.13 demonstrates that there is extensive extinction due to molecular hydrogen across the LMC that does not correspond to peaks in CO emission. This extinction map was compared to the ^{12}CO observations of Mizuno et al. (2001), and an X-factor of 9.3 cm^{-2} (K km s^{-1})$^{-1}$, nearly 5 times X in the Milky Way, was derived. These results are consistent with the expectation that CO is more susceptible to photodissociation in the low-metallicity environment of the LMC. Thus, this map can be used to detect nascent molecular clouds in regions where CO has yet to form, as well as GMCs that have all but dispersed and in which the CO is mostly destroyed.

I used the method outlined in Chapter 4 to create an extinction map of the Small Magellanic Cloud, which has an even lower average metallicity (0.1 $Z_\odot$; Lequeux et al. 1979) than the LMC. But low signal-to-noise proved to be a major obstacle. In fact, this was the biggest challenge to overcome with the LMC work presented in Chapter 4, as well. Recall, the color excess technique, originally applied to nearby molecular and dark clouds in the Galaxy, assumes that stars observed along the line-of-sight to a cloud are background stars (Chapter 4.2.2). Extinction measurements are diluted when foreground contamination is not or cannot be taken into account. The color excess method also assumes that the background stars and control group are homogeneous. If the control group is not homogenous and has a large dispersion of intrinsic colors, this increases the noise in the extinction measurements. With the LMC, these problems were mitigated due to the effectiveness of sigma-clipping and because the large number of sources available made it possible to make reasonable conclusions on a probabilistic basis.

Compared to the LMC, the SMC has a larger stellar scale height, which means that foreground contamination within the galaxy is exacerbated. And because the SMC is at a larger distance ($\sim$ 60 kpc) than the LMC ($\sim$ 50 kpc), photometry from the 2MASS catalog does not penetrate as deeply into it. The combination of these two factors prevented me from creating an extinction map of the SMC, using the 2MASS catalog, in which signal could be distinguished from noise. There are, however, a few solutions to this problem: First, deeper photometry would increase the signal-to-noise ratio. Obtaining more sensitive near-infrared observations would also lead to an improvement in the LMC extinction map, especially in regions of high extinction. Secondly, methods for identifying different stellar populations based on their photometry can be exploited to minimize intragalactic foreground contamination. In Chapter 4.2.2, I used the Nikolaev & Weinberg (2000) study of the LMC color-magnitude diagram to eliminate point sources unlikely to have undergone interstellar reddening. This general idea can be applied in even greater detail: by modeling or by cross-

correlating the 2MASS catalog with other data sets, it is possible to identify distinct stellar populations to an even greater degree of precision (e.g., Egan & van Dyk 2000; Demers et al. 2002).

5.3 High-Resolution Observations

In recent years, much of the state-of-the-art research on GMCs has been driven by the goal to study GMCs at increased resolution. Though much of the evidence to date seems to point towards GMCs in different galaxies having uniform properties (e.g., Blitz et al. 2007; Bolatto et al. 2008), as Hughes et al. (2010) discuss, this does not rule out the possibility that individual GMC properties are regulated by their local environment. The Magellanic Cloud Mopra Assessment (MAGMA) project, a high angular resolution follow-up to the NANTEN survey of LMC molecular clouds, is scheduled to have a data release in 2011 (Hughes et al. 2010). With a spatial resolution of ~ 10 pc—5 times higher than the NANTEN survey—MAGMA will be able to quantify the basic properties of GMCs in the LMC to an even greater degree of accuracy and precision than previous surveys.

Numerical simulations, which have increased in particle resolution and complexity over the years, provide another promising avenue for helping us to understand the key factors that determine GMC properties. But in spite of advancements in computation and the great wealth of data that are available for testing various numerical models, consensus on the dominant mechanism(s) of GMC formation does not appear much closer to being achieved than it was decades ago. Favored theories of GMC formation range from self gravity (e.g., Kim & Ostriker 2002, 2006; Glover & Mac Low 2007) to thermal instabilities (e.g., Kosiński & Hanasz 2007) to colliding flows (e.g., Vázquez-Semadeni et al. 2006; Hennebelle et al. 2008). And recently, research teams led by Dobbs have revived the idea of GMC growth by agglomeration (Dobbs et al. 2006; Dobbs 2008). Among other things, their work challenges the notion that self gravity must play a dominant role at some stage in GMC evolution.

Far from feeling dismayed or overwhelmed by the many, at times conflicting, theories and various interpretations of observations, I find it encouraging that there are scientists who continue to think outside the box and challenge long standing hypotheses. Once the problem of GMC formation is solved—if the priorities and interests of the scientific community continue to evolve—an equally compelling mystery will undoubtedly take its place.

Bibliography

[1] Alves, J., Lada, C. J., Lada, E. A., Kenyon, S. J., & Phelps, R. 1998, ApJ, 506, 292
[2] Andersson, B.-G., Wannier, Peter G., & Morris, Mark 1991, ApJ, 366, 464
[3] Arimoto, N., Sofue, Y., & Tsujimoto, T. 1996, PASJ, 48, 275
[4] Ballesteros-Paredes, J., Vázquez-Semadeni, E., & Scalo, J. 1999, ApJ, 515, 286
[5] Bally, J., Stark, A. A., Wilson, R. W., & Langer, W. D. 1987, ApJ, 312, 45
[6] Bally, J. 2001, in ASP Conf. Ser. 231, Tetons 4: Galactic Structure, Stars, and the Interstellar Medium, ed. C. E. Woodward, M. D. Bicay, & J. M. Shull (San Francisco: ASP), 204
[7] Bash, F. N., Green, E., & Peters, W. L., III 1977, ApJ, 217, 464B
[8] Beck, R. 2000, in The Interstellar Medium in M31 and M33, Proc. 232nd WE-Heraeus Seminar, ed. E. M. Berkhuijsen, R. Beck, & R. A. M. Walterbos (Aachen: Shaker), 171
[9] Bigiel, F., Leroy, A., Walter, F., Brinks, E., de Blok, W. J. G., Madore, B., & Thornley, M. D. 2008, AJ, 136, 2846
[10] Blitz, L. 1978, Ph.D. dissertation, Columbia Univ.
[11] Blitz, L. 1979, Giant Molecular Clouds in the Galaxy, ed. P. M. Solomon & Edmunds (Oxford: Pergamon Press)
[12] Blitz, L., & Shu, F. H. 1980, ApJ, 238, 148
[20] Blitz, L., & Thaddeus, P. 1980, ApJ, 241, 676
[14] Blitz, L., Cohen, R. S., Dame, T. M., Grabelsky, D. A., Thaddeus, P., Hermsen, W., & Lebrun, F. 1986, A&A, 154, 25
[15] Blitz, L., & Stark, A. A. 1986, ApJ, 300, 89
[16] Blitz, L. 1990, ASPC, 12, 273
[17] Blitz, L. 1993, Protostars and Planets III, ed. E. H. Levy, J. I. Lunine, (Tucson, AZ: Univ. Arizona Press), 125
[18] Blitz, L., & Rosolowsky, E. 2004, ApJ, 612, 29
[19] Blitz, L., & Rosolowsky, E. 2006, ApJ, 650, 933
[20] Blitz, L., Fukui, Y., Kawamura, A., Leroy, A., Mizuno, N., & Rosolowsky, E. 2007, Protostars and Planets V, ed. B. Reipurth, D. Jewitt, & K. Keil (Tucson, AZ: Univ. Arizona Press), 81
[21] Bloemen, J. B. G. M., Strong, A. W., Mayer-Hasselwander, H. A.,
[22] Bloemen, J. B. G. M. 1989, Physics and Chemistry of Interstellar Molecular Clouds, ed. G. Winnewisser & J. T. Armstrong (Berlin: Springer), p. 22

[23] Bohlin, R. C., Savage, B. D., & Drake, J. F. 1978, ApJ, 224, 132
[25] Burkert, A., & Bodenheimer P. 2000, ApJ, 543, 822
[25] Burkert, A., & Hartmann, L. 2004, ApJ, 616, 288
[27] Carpenter, J. M. 2000, ApJ, 120, 3139
[27] Carpenter, J. M. 2001, AJ, 121, 2851
[28] Carr, J. S. 1987, ApJ, 323, 170
[29] Castets, A., Duvert, G., Dutrey, A., Bally., J., Langer, W. D. , & Wilson, R. W. 1990, A&A, 234, 469
[30] Celnik, W. E. 1983, A&A, 53, 403
[31] Chernin, A. D., Efremov, Y. N., & Voinovich, P. A. 1995, MNRAS, 275, 313
[32] Cohen, R. S., & Thaddeus, P. 1977,ApJ, 217, 155
[33] Cohen, R. S., Dame, T. M. Garay, G., Montani, J., Rubio, M., & Thaddeus, P. 1988, ApJ, 331, L95
[35] Corbelli, E., & Schneider, S. E. 1997, ApJ, 479, 244
[35] Corbelli, E., & Salucci, P. 2000, MNRAS, 331, 441
[36] Crutcher, R. M., Hartkopf, W. I., & Giguere, P. T. 1978, ApJ, 226, 839
[37] Crutcher, R. M. 1999, ApJ, 520, 706
[39] Dame, T. M., Elmegreen, B. G., Cohen, R. S., & Thaddeus, P. 1986, ApJ, 305, 892
[39] Dame, T. M., Hartmann, Dap, & Thaddeus, P. 2001, ApJ 547 792
[40] Demers, S., Dallaire, M., Battinelli, P. 2002, AJ, 123, 3428
[41] de Zeeuw, P. T., Hoogerwerf, R. de Bruijne, J. H. J., Brown, A. G. A., & Blaauw, A. 1999 ApJS, 117, 354
[43] Dobbs, C. L., & Bonnell I. A., 2006, MNRAS, 367, 873
[43] Dobbs, C. L., 2008, MNRAS, 391, 844
[44] Dufour, R. J. 1984, in Structure and Evolution of the Magellanic Clouds, ed. S. van den Bergh & K. S. de Boer (Dordrecht: Reidel), 353
[45] Egan, M. P., & van Dyk, S. D. 2000, AAS, 197, 7803
[47] Elmegreen, B. G. 1993, ApJ, 411, 170
[47] Elmegreen, B. G. 1994 Protostars and Planets III, ed. E. H. Levy, J. I. Lunine, (Tucson, AZ: Univ. Arizona Press), 97
[48] Elmegreen, B. G. 2007, ApJ, 668, 1064
[49] Engargiola, G., Plambeck, R., Rosolowsky, E., & Blitz, L. 2003, ApJS, 149, 343
[50] Falgarone, E., & Lequeux, J. 1973, A&A, 25, 253
[51] Feast, M. W., Thackeray, A. D., & Wesselink, A. J. 1960, MNRAS, 121, 337
[52] Flaccomio, E., Micela, G., Sciortino, S., Damiani, F., Favata, F., Harnden, F. R., Jr., & Schachter, J. 2000, A&A, 355, 651
[53] Fleck, R. C., Jr., & Clark, F. O. 1981, ApJ, 245, 898F
[54] Frerking, M. A., Langer, W. D., & Wilson, R. W. 1982, ApJ, 262, 590
[55] Fukui, Y., Mizuno, N., Yamaguchi, R., Mizuno, A., Onishi, T., Ogawa, H., Yonekura, Y., Kawamura, A., Tachihara, K., Xiao, K., et al. 1999, PASJ, 51, 745
[56] Furész, G., et al. 2006, ApJ, 648, 1090
[57] Garay, G., Rubio, M., Ramirez, S., Johansson, L. E. B., & Thaddeus, P. 1993, A&A,

274, 743
[58] Genzel, R., Reid, M. J., Moran, J. M., & Downes, D. 1981, ApJ 224, 884
[59] Glover S. C. O., & Mac Low M.-M., 2007, ApJS, 169, 239
[60] Goldreich, P., & Lynden-Bell, D. 1965, MNRAS, 130, 97
[61] Goodman, A. A., Benson, P. J., Fuller, G. A., & Myers, P. C. 1993, ApJ, 406, 528
[62] Gordon, M. A., & Burton, W. B. 1976, ApJ, 208, 346
[63] Gordon, K. D., Clayton, G. C., Misselt, K. A., Landolt, A. U., & Wolff, M. J. 2003, ApJ, 594, 279
[64] Grieve, G. R., & Madore, B. F. 1986, ApJS, 62, 427
[65] Harris, J., Zaritsky, D., & Thompson, I. 1997, AJ, 114, 1933
[66] Heiles, C. 1998, ApJ, 498, 689
[97] Heiles, C., & Troland, T. H. 2005, ApJ, 624, 773
[68] Henderson, A. P., Jackson, P. D., & Kerr, F. J. 1982, ApJ, 263, 116
[97] Hennebelle, P., Banerjee, R., Vázquez-Semadeni, E., Klessen, R. S., & Audit, E. 2008, A&A 486, 43
[70] Heyer, M. H., Morgan, J., Schloerb, F. P., Snell, R. L., & Goldsmith, P. F. 1992, AppJ, 395, 99
[71] Heyer, M. H., Williams, J. P., & Brunt, C. M. 2006, ApJ, 643, 956
[72] Hill, R. J., Madore, B. F., & Freedman, W. L. 1994, ApJ, 429, 192
[73] Israel, F. P. 1997, A&A, 328, 482
[74] Isserstedt, J. 1975, A&A, 41, 175
[97] Isserstedt, J., & Kohl, W. 1984, A&A, 138, 115
[76] Kalberla, P. M. W., Burton, W. B., Hartmann, Dap, Arnal, E.M., Bajaja, E., Morras, R., & Poppel, W. G. L. 2005, A&A, 440, 775
[77] Kennicutt, R. C., Jr. 1998, ApJ, 498, 541
[97] Kharchenko, N. V. Piskunov, A. E., Roesler S., Schilbach, E., & Scholz, R. D. 2005, A&A, 438, 1163
[97] Kim, J., Hong, S. S., Ryu, D., & Jones, T. W. 1998, ApJ, 506, 139
[97] Kim W.-T., & Ostriker E. C., 2002, ApJ, 570, 132
[81] Kim, W.-T., Ostriker, E. C., Stone, J. M. 2003, ApJ, 599, 1157
[97] Kim W.-T., Ostriker E. C., 2006, ApJ, 646, 213
[83] Koornneef, J. 1982, A&A, 107, 247
[84] Koornneef, J. 1983, A&A, 128, 84
[97] Kosiński R., & Hanasz M., 2007, MNRAS, 376, 861
[86] Kuchar, T. A., & Bania, T. M. 1993, ApJ, 414, 664
[87] Kuchar, T. A., Bania, T. M., Blitz, L., & Stark, A. A. 1991, ASPC, 13, 151
[88] Kutner, M. L., Tucker, K. D., Chin, G., & Thaddeaus, P. 1977, ApJ, 215, 521
[97] Kwan, J. 1979, ApJ, 229, 567
[97] Lada, E. A., Bally, J.. Stark, A. A. 1991, ApJ, 368, 432
[91] Lada, C. J., Lada, E. A., Clemens, D. P., & Bally, J. 1994, ApJ, 429, 694
[105] Lada, C., Alves, J., & Lombardi, M. 2007, Protostars and Planets V, ed. B. Reipurth, D. Jewitt, & K. Keil (Tucson, AZ: Univ. of Arizona Press), 3

Protostars and Planets V, , University of Arizona Press, Tucson, 951 pp., 2007., p.3-15
[93] Lombardi, M., & Alves, J. 2001, A&A, 377, 1023
[97] Larson, R. B. 1981, MNRAS, 194, 809
[97] Larson, R. B. 1985, MNRAS, 214, 379
[97] Leisawitz, D., Bash, F. N., & Thaddeus, P. 1989, ApJS, 70, 731
[97] Lequeux, J., Peimbert, M., Rayo, J. F., Serrano, A., & Torres-Peimbert, S. 1979, A&A, 80, 155
[98] Maddalena, R. J., Morris, M., Moscowitz, J., & Thaddeus, P. 1986 ApJ, 303, 375
[99] Martin, C. L., & Kennicutt, R. C., Jr. 2001, ApJ, 555, 301
[100] Massey, P., Lang, C. C., DeGioia-Eastwood K., & Garmany, C. D., 1995, ApJ, 438, 188
[101] McCray, R. & Kafatos, M. C. 1987 ApJ, 375, 177
[103] McKee, C. F. 1989, ApJ, 345, 782
[103] McKee, C. F., & Ostriker, E. C. 2007, ARA&A, 45, 565
[104] Menten, K. M., Reid, M. J., Forbrich, J., & Brunthaler, A. 2007, A&A, 474, 515
[105] Mestel, L., & Spitzer, L., Jr. 1956, MNRAS, 116, 503
[106] Mestel, L., & Paris, R. B. 1984, A&A, 136, 98
[107] Mizuno, N., Yamaguchi, R., Mizuno, A., Rubio, M., Abe, R., Saito, H., Onishi, T., Yonekura, Y., Yamaguchi, N. Ogawa, H., & Fukui, Y. 2001, PASJ, 53, 971
[108] Mouschovias, T. C., Shu, F. H., & Woodward, P. R. 1974, A&A, 33, 73
[109] Mouschovias, T. 1977, ApJ, 211, 147
[110] Mouschovias, T. C., & Paleologou, E. V. 1979, ApJ, 230, 204
[111] Nagahama, T., Mizuno, A., Ogawa, H., & Fukui, Y. 1998, AJ, 116, 336
[112] Nikolaev, S., & Weinberg, M. D. 2000, ApJ, 542, 804
[148] Norman, C., & Silk, J. 1980, ApJ, 238, 158
[114] Oestreicher, M. O., & Schmidt-Kaler, T. 1996, A&AS, 117, 303
[115] Parker, E. N. 1966, ApJ, 145, 811
[116] Phillips, J. P. 1999, A&AS, 134, 241
[117] Racine, R. 1968, AJ, 73, 233
[148] Ramírez, S. V., et al. 2004, AJ, 128, 787
[120] Rosolowsky, E., Engargiola, G., Plambeck, R., & Blitz, L. 2003, ApJ, 599, 258
[120] Rosolowsky, E. 2005, PASP, 117, 1403
[148] Rosolowsky, E., & Leroy, A. 2006, PASP, 118, 590
[148] Sagar, R., & Joshi, U. C. 1983, MNRAS, 205, 747
[148] Sancisi, R. 1974, IAUS, 60, 115
[148] Sanders, D. B., Scoville, N. Z., & Solomon, P. M. 1985, ApJ, 289, 373
[148] Santillán, A., Kim, J., Franco, J., Martos, M., Hong, S. S., & Ryu, D. 2000, ApJ, 545 353
[126] Sargent, A. I., ApJ, 233, 163
[127] Savage, B. D., Bohlin, R. C., Drake, J. F., & Budich, W. 1977, ApJ, 216, 291
[128] Scalo, J. M. 1986, Fund. Cosmic Phys., 11, 1
[129] Schlegel, D. J., Finkbeiner, D. P., & Davis, M. 1998, ApJ, 500, 525

[148] Scoville, N. Z., & Solomon, P. M. 1975, ApJ, 199, 105
[131] Scoville, N. Z., & Hersh, K. 1979, 229, 578
[132] Shibata, K., & Matsumoto, R. 1991, Nature, 353, 633
[148] Solomon, P. M., & Sanders, D. B. 1979, Giant Molecular Clouds in the Galaxy, ed. P. M. Solomon & M. G. Edmunds (Oxford: Pergamon Press)
[148] Solomon, P. M., Rivolo, A. R., Barrett, J., & Yahil, A., 1987, ApJ, 319, 730
[148] Spergel, D. N., & Blitz, L. 1992, Nature, 357, 665
[136] Staveley-Smith, L., Kim, S., Calabretta, M. R., Haynes, R. F., & Kesteven, M. J. 2003, MNRAS, 339, 87
[148] Strong, A. W., & Mattox, J. R. 1996, A&A, 308, 21
[148] Stutzki, J., & Güsten, R. 1990, ApJ, 356, 513
[139] Thilker, D. A., Braun, R., & Walterbos, R. A. M. 2002, in Seeing Through the Dust, ASP Conf., ed. A. R. Taylor, T. L. Landecher, & A. G. Willis, 276
[148] Vázquez-Semadeni, E., Passot, T., & Pouquet, A. 1995, ApJ, 441, 702
[148] Vázquez-Semadeni E., Ryu D., Passot T., González R. F., & Gazol A., 2006, ApJ, 643, 245
[148] Wada, K., Spaans, M., & Kim, S. 2000, ApJ, 540, 797
[148] Wannier, P. G., Lichten, S. M., & Morris, M. 1983, ApJ, 268, 727
[144] Welch, W. J., et al. 1996, PASP, 108, 93
[145] Williams, J. P., de Geus, E. J., & Blitz, L. 1994, ApJ, 428, 693
[146] Williams, J. P., Blitz, L., & Stark, A. A. 1995, ApJ, 451, 252
[147] Williams, J. P., & McKee C. F. 1997, ApJ 476 166
[148] Wilson, C. D. 1995, ApJ, 448, 97
[149] Wong, T., & Blitz, L. 2002, ApJ, 569, 157
[150] Zaritsky, D. 1999, AJ, 118, 2824

Appendix A

HI Regions in M33

The following figures display the velocity maps, position-velocity plots, surface density maps, and spectra of the HI regions associated with the remaining molecular clouds not displayed in Chapter 3. If for a given region the GMC was resolved in the Rosolosky et al. (2003) catalog, a circle proportional to the size of the GMC is overlaid on the surface density map.

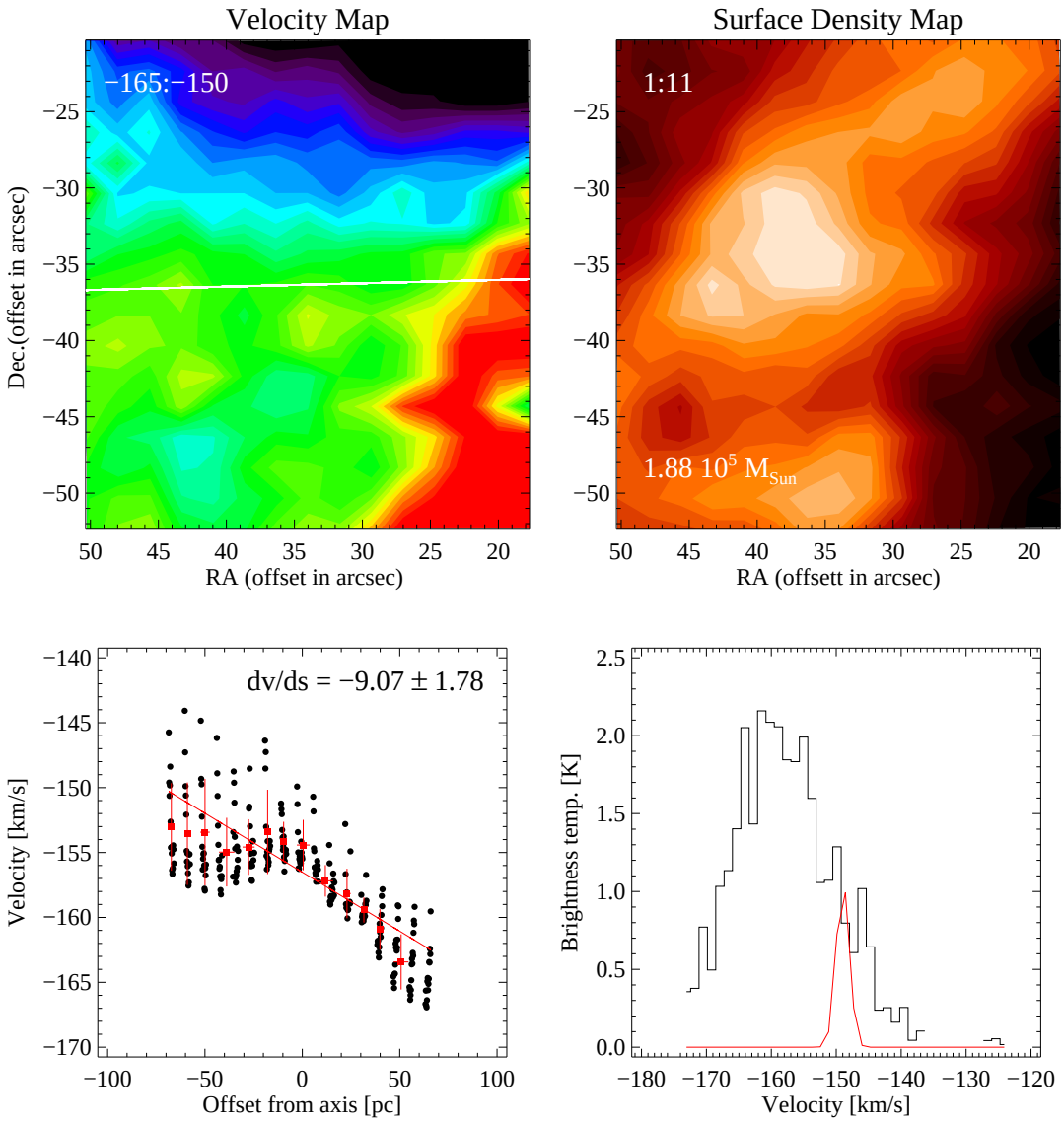

Figure A.1: Cloud 2: The top left figure shows the intensity-weighted first moment map of the HI with the gradient axis overlaid. The velocity range of the map is indicated in the top left corner in units of km s^{-1}; red represents the maximum speed. Below this figure is a plot of the central velocity at a given location in the first-moment map versus perpendicular offset from the gradient axis; the linearity of the plot indicates that a plane is a good fit to the first-moment map. The top right figure is a surface density map of the HI. The range of HI surface densities displayed in the map are in the top right corner in units of $M_\odot$ pc^{-2}, and the total HI mass in the region is written in the bottom left corner. Below is a plot of the average spectra of HI emission (black) and CO emission (red) toward the region.

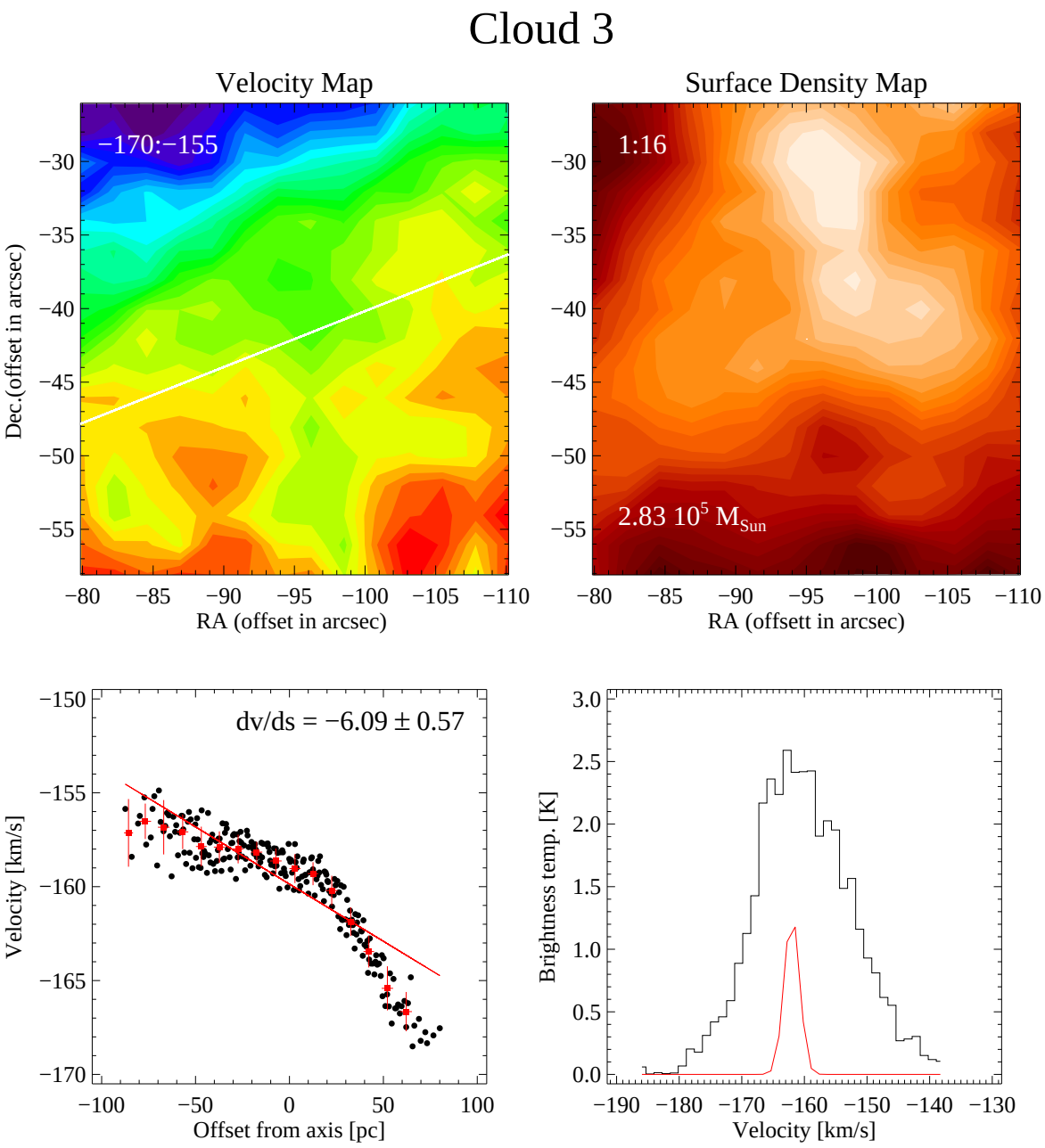

Figure A.2: Cloud 3: Same as Figure A.1.

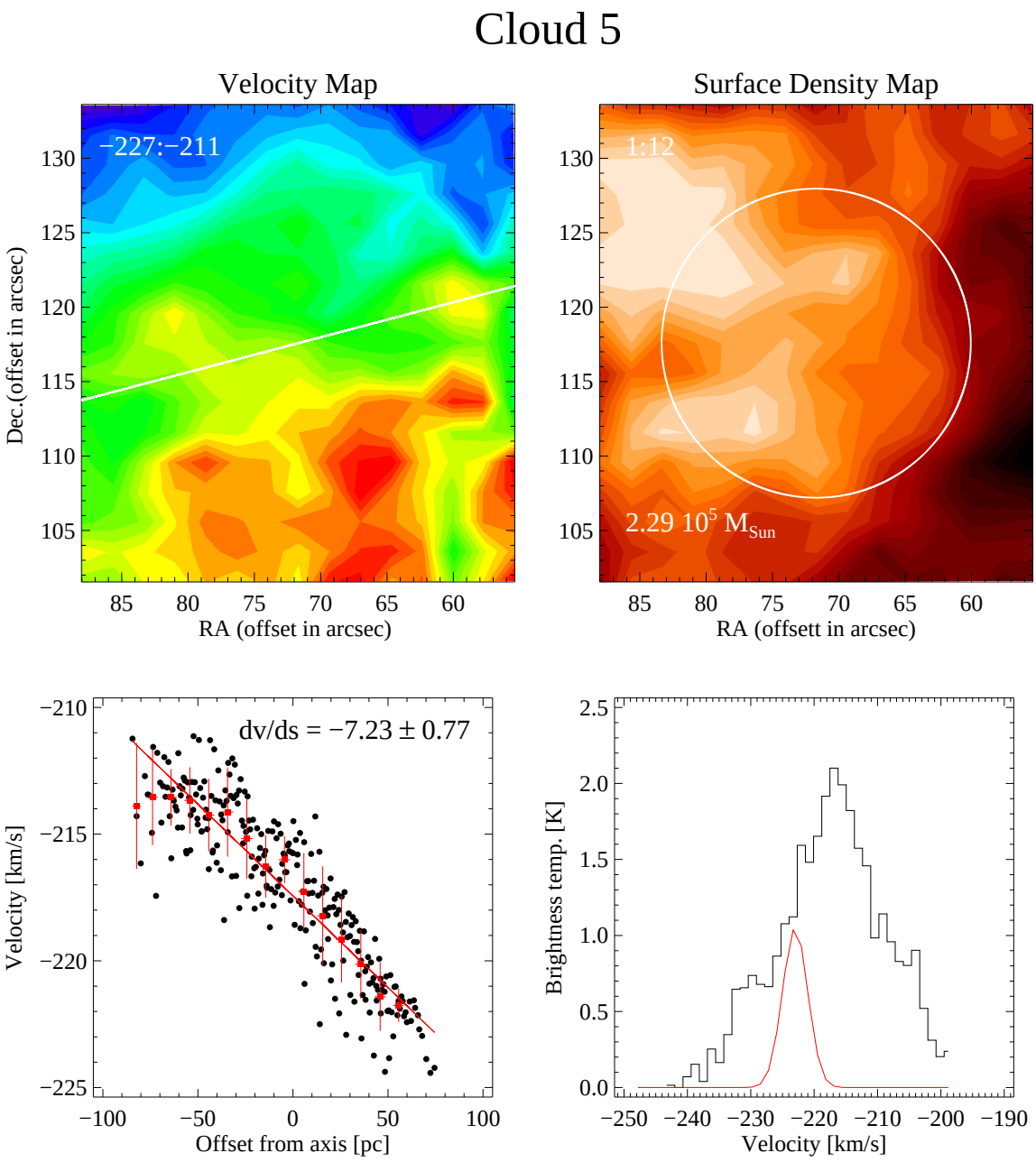

Figure A.3: Cloud 5: Same as Figure A.1.

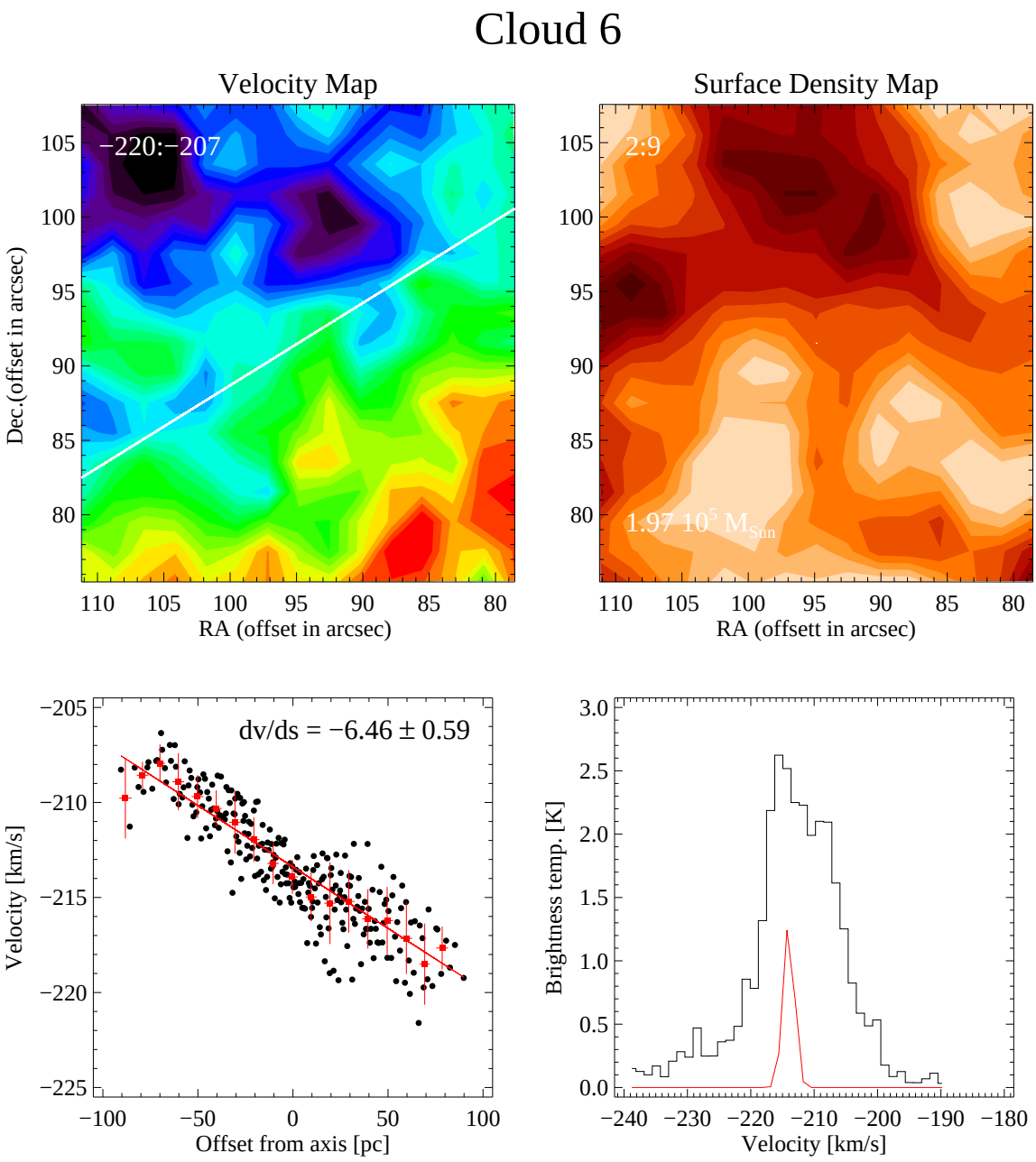

Figure A.4: Cloud 6: Same as Figure A.1.

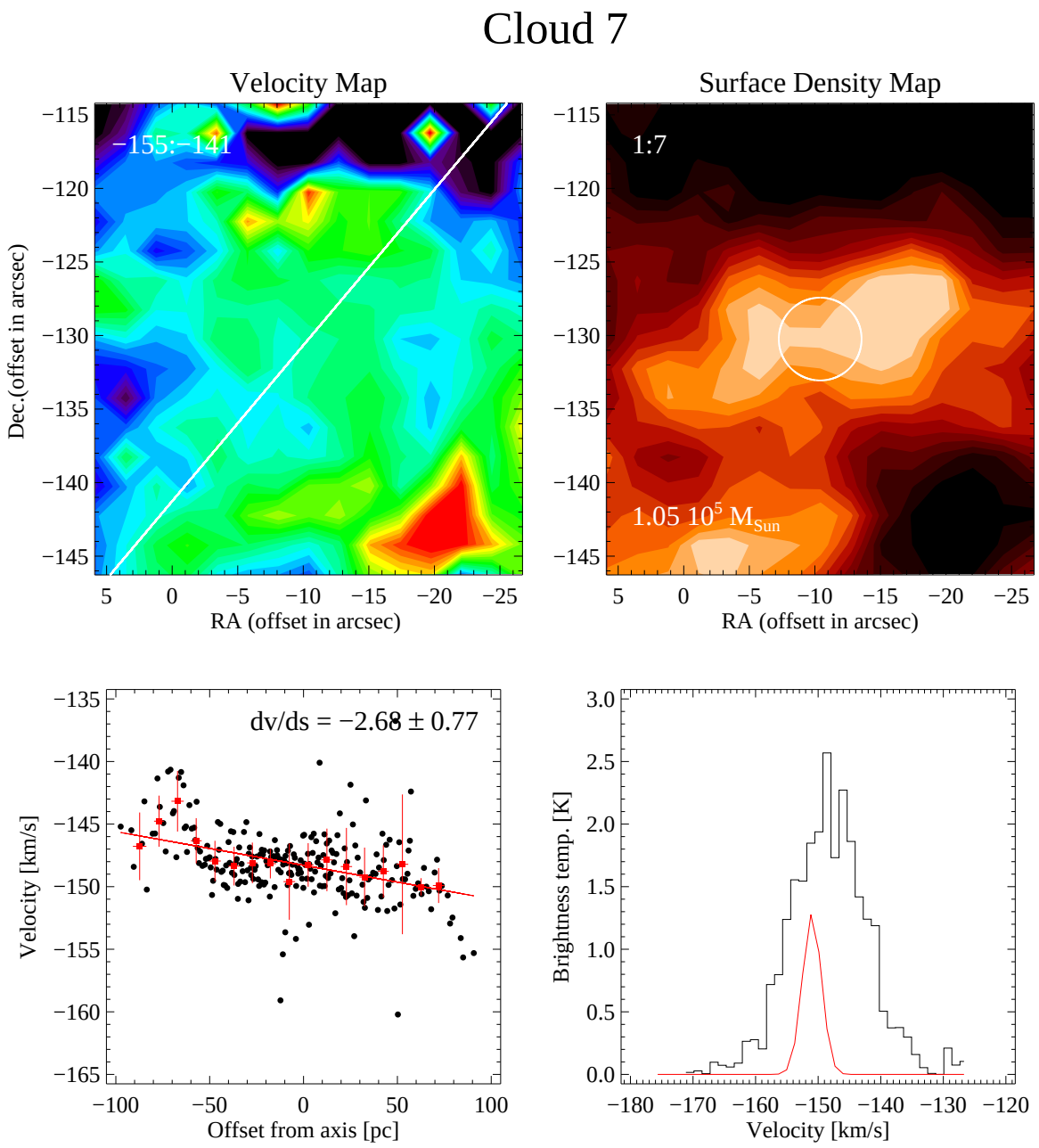

Figure A.5: Cloud 7: Same as Figure A.1.

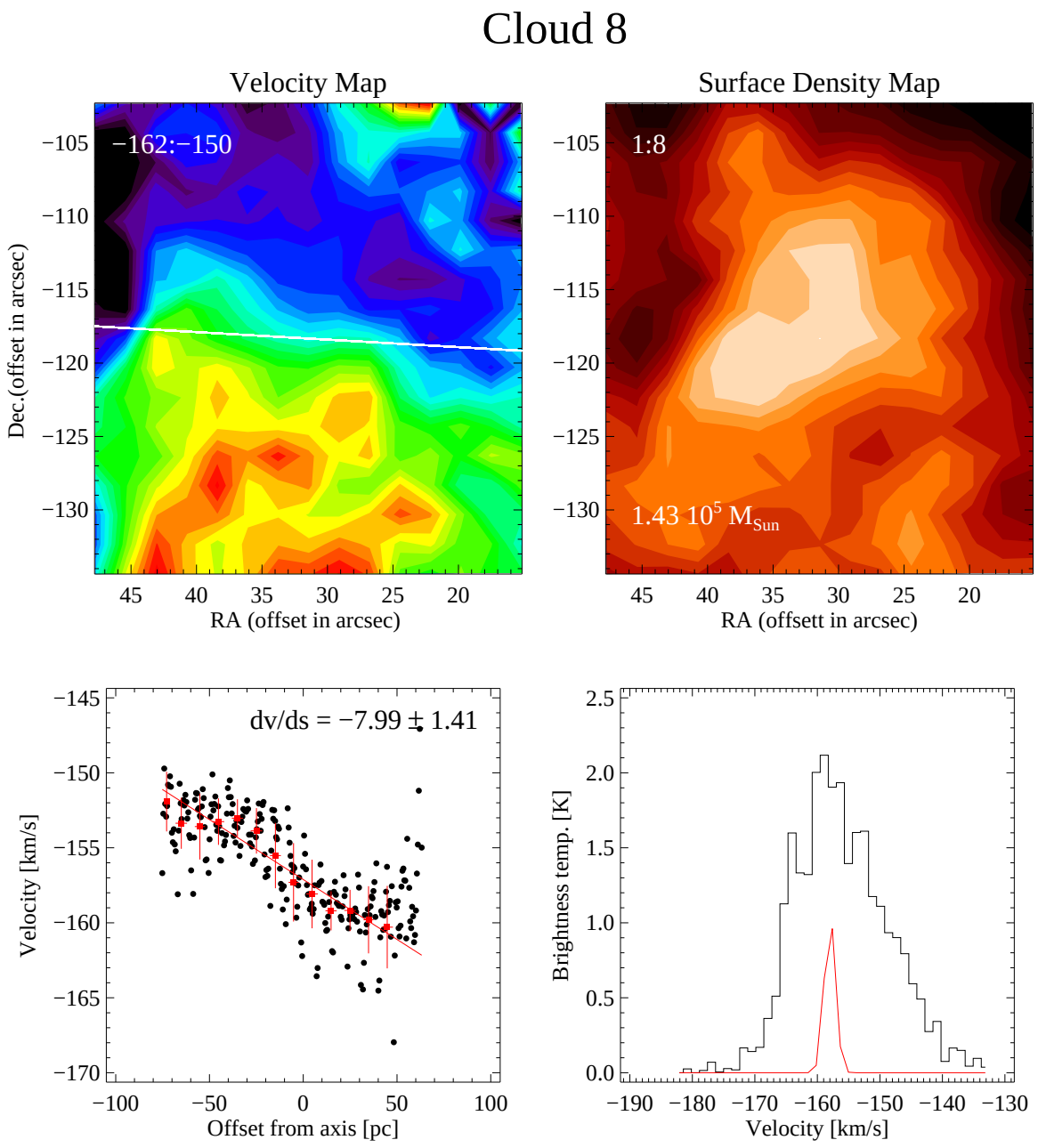

Figure A.6: Cloud 8: Same as Figure A.1.

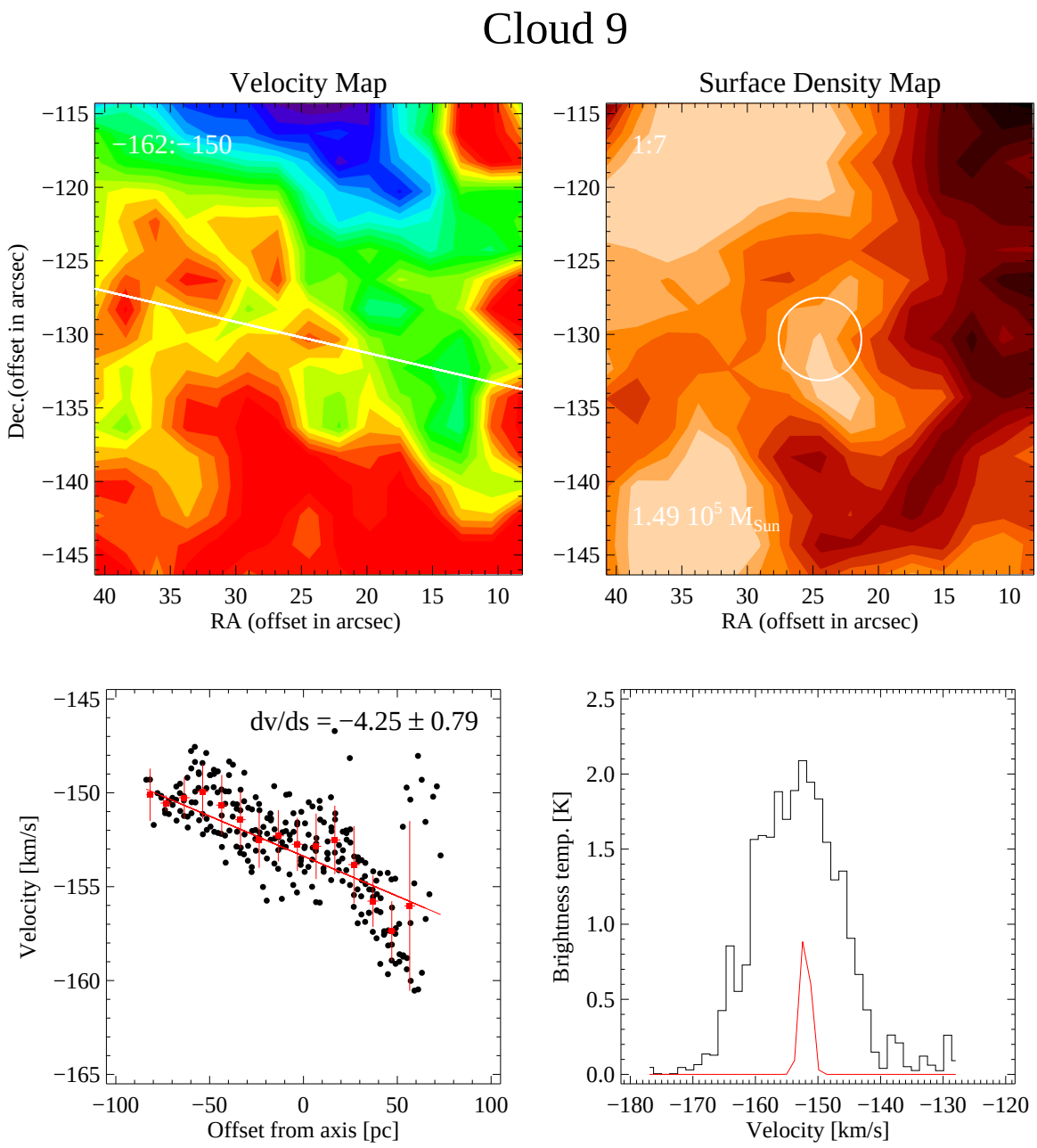

Figure A.7: Cloud 9: Same as Figure A.1.

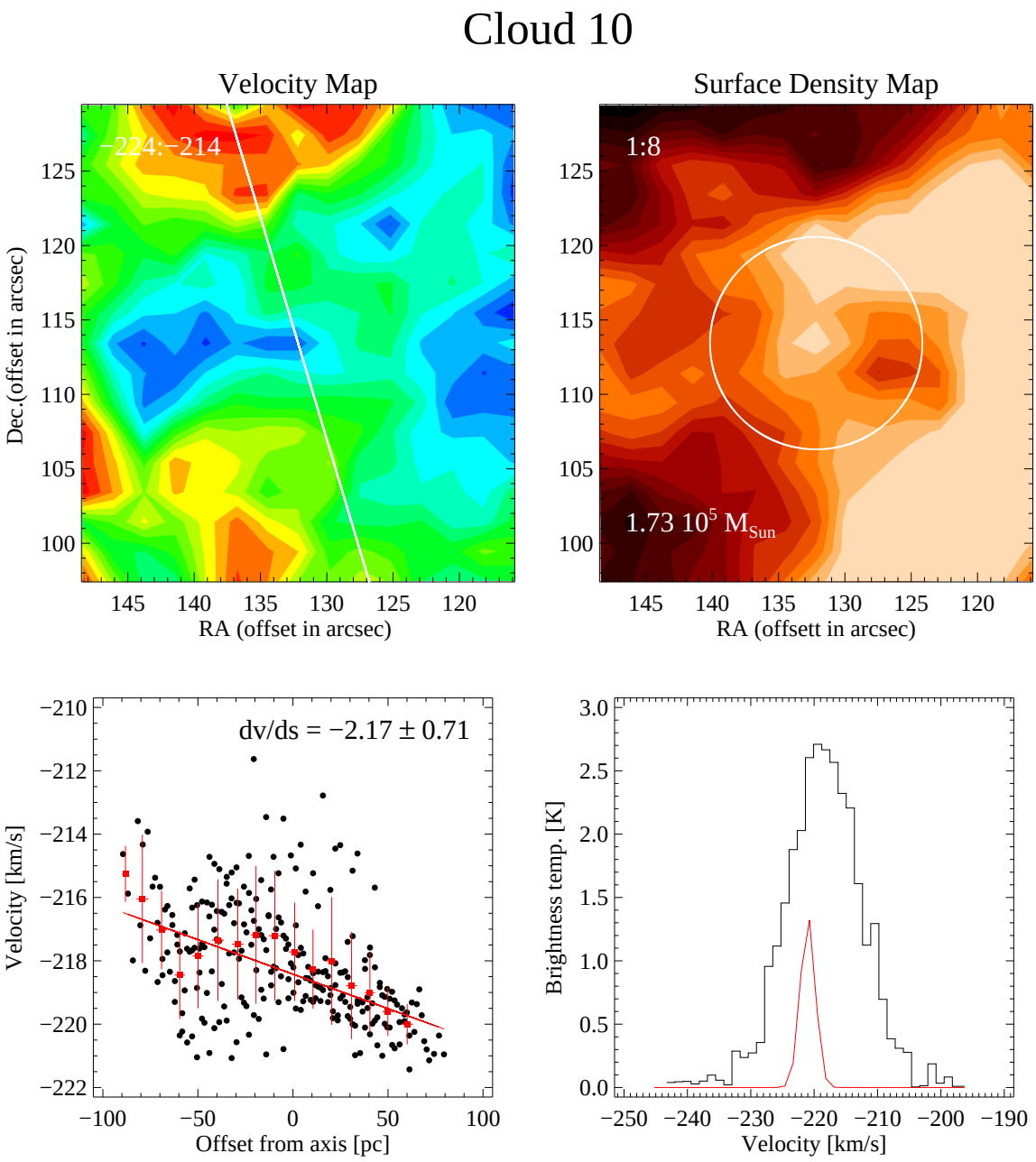

Figure A.8: Cloud 10: Same as Figure A.1.

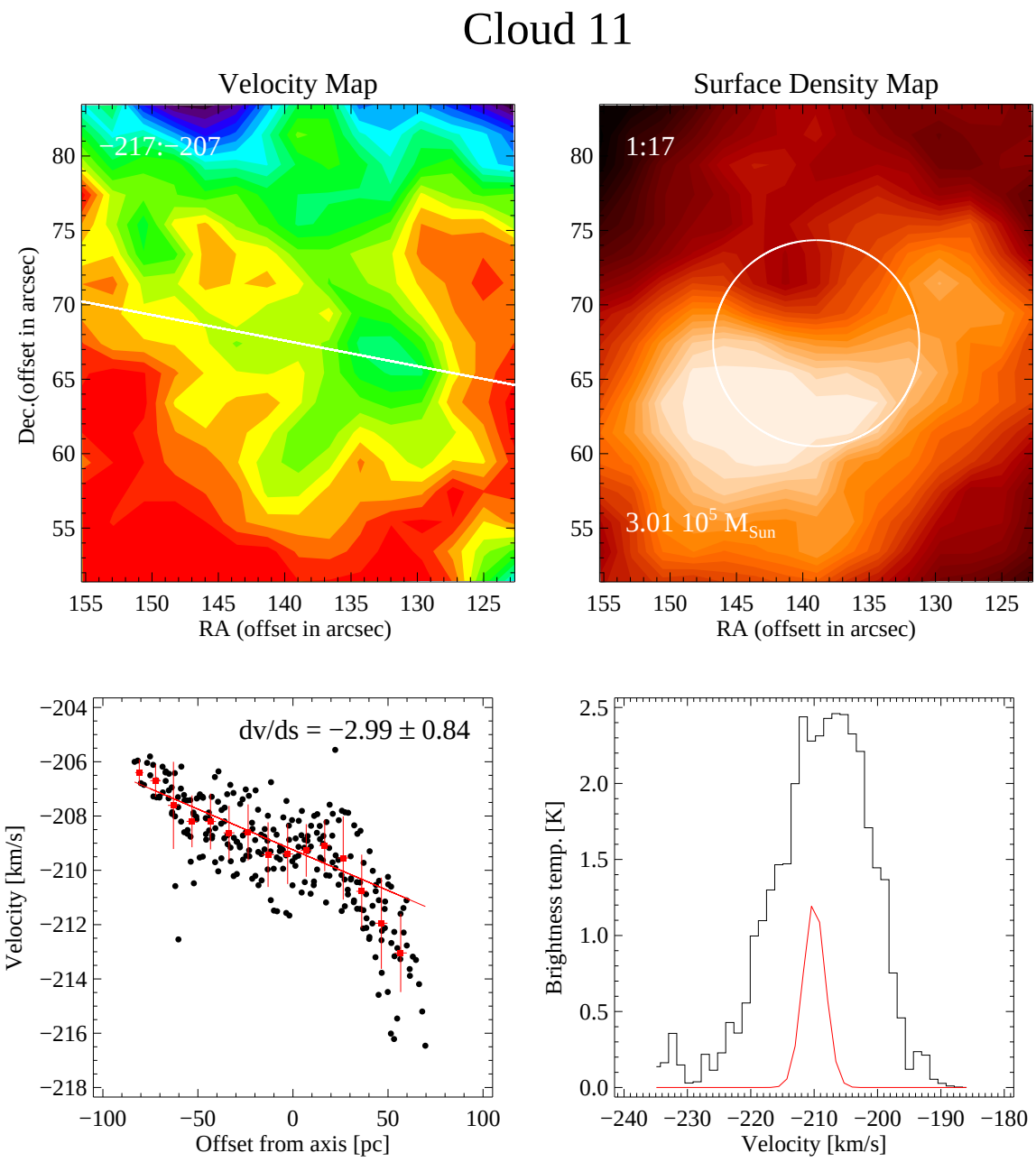

Figure A.9: Cloud 11: Same as Figure A.1.

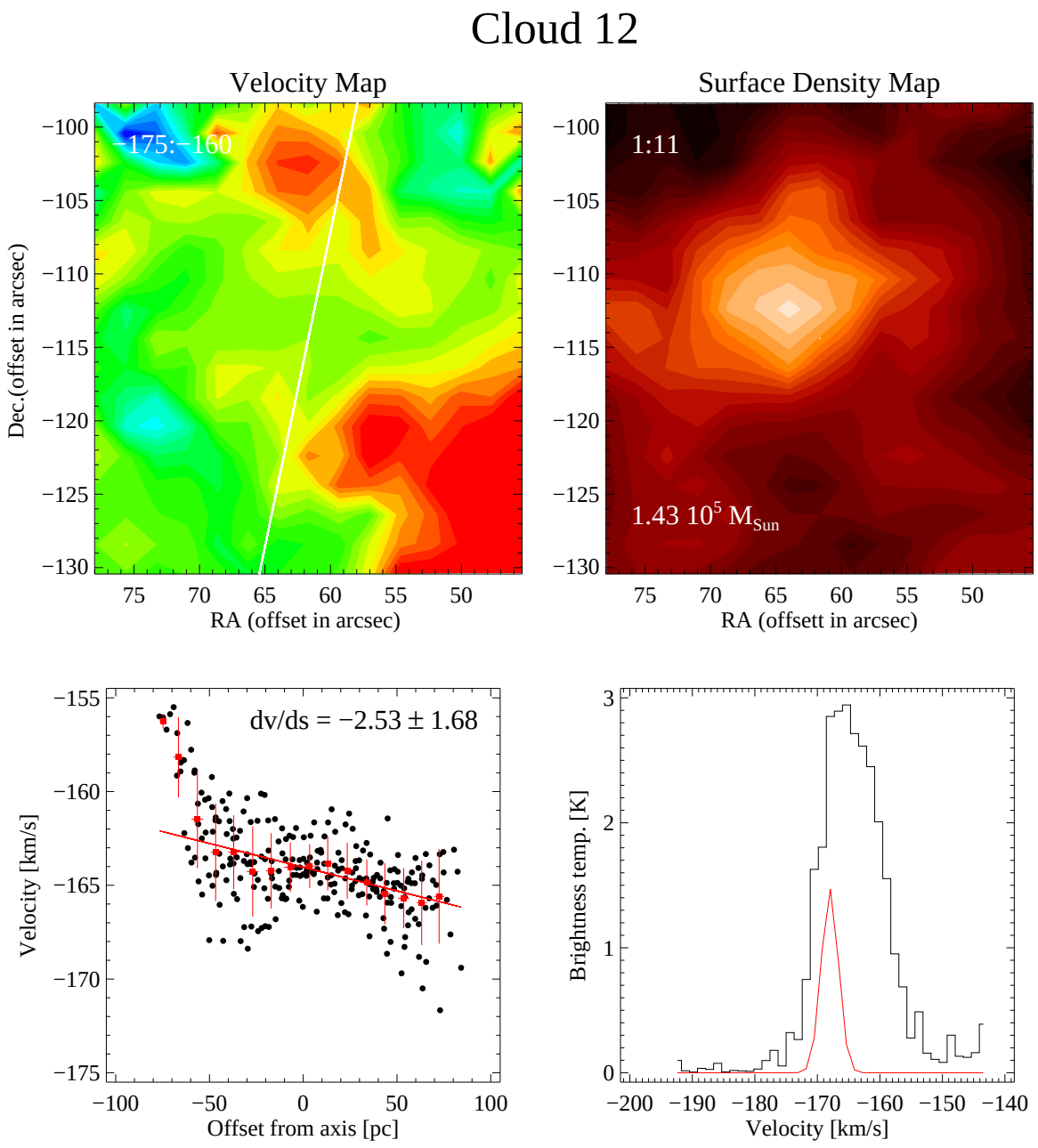

Figure A.10: Cloud 12: Same as Figure A.1.

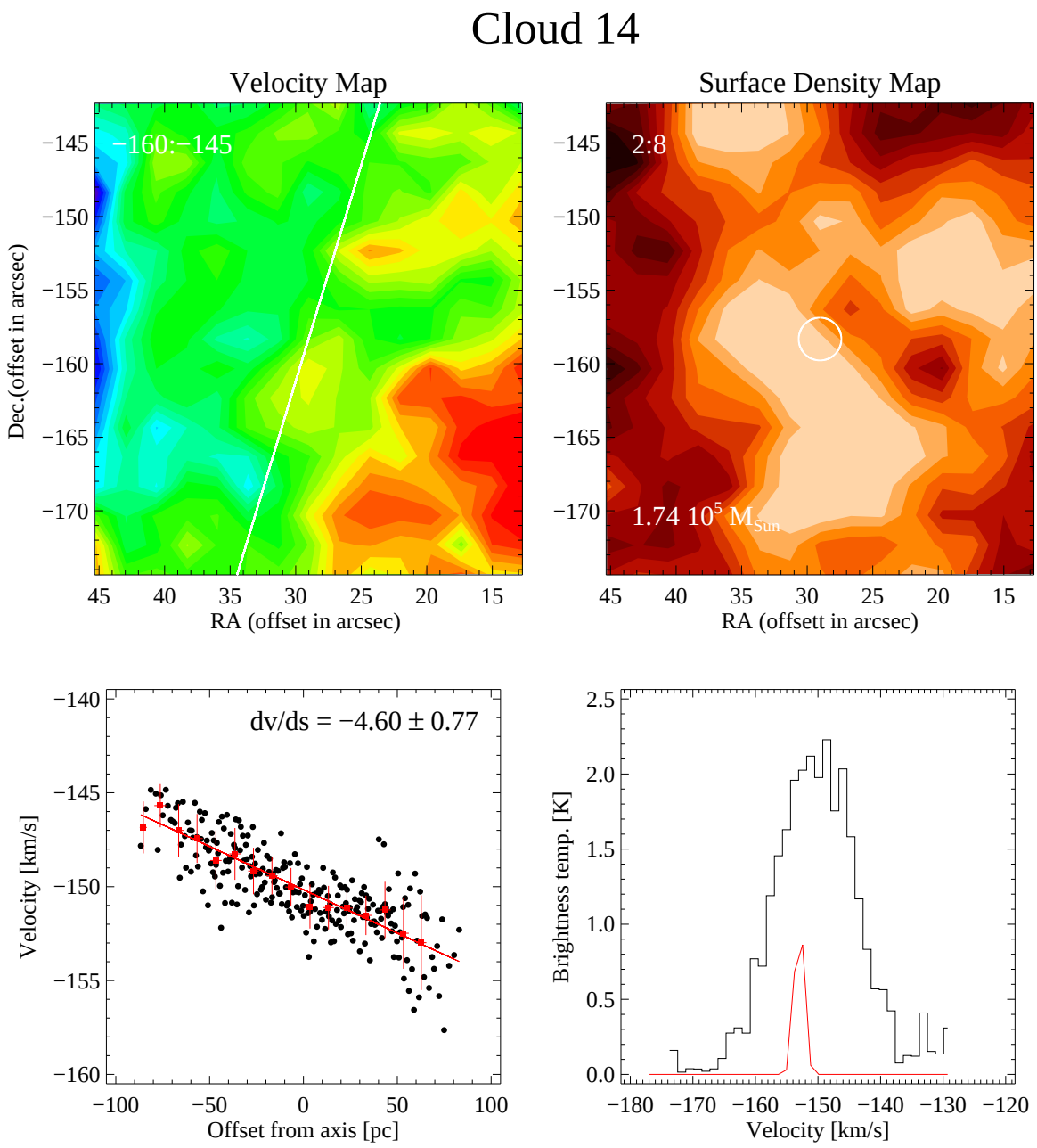

Figure A.11: Cloud 14: Same as Figure A.1.

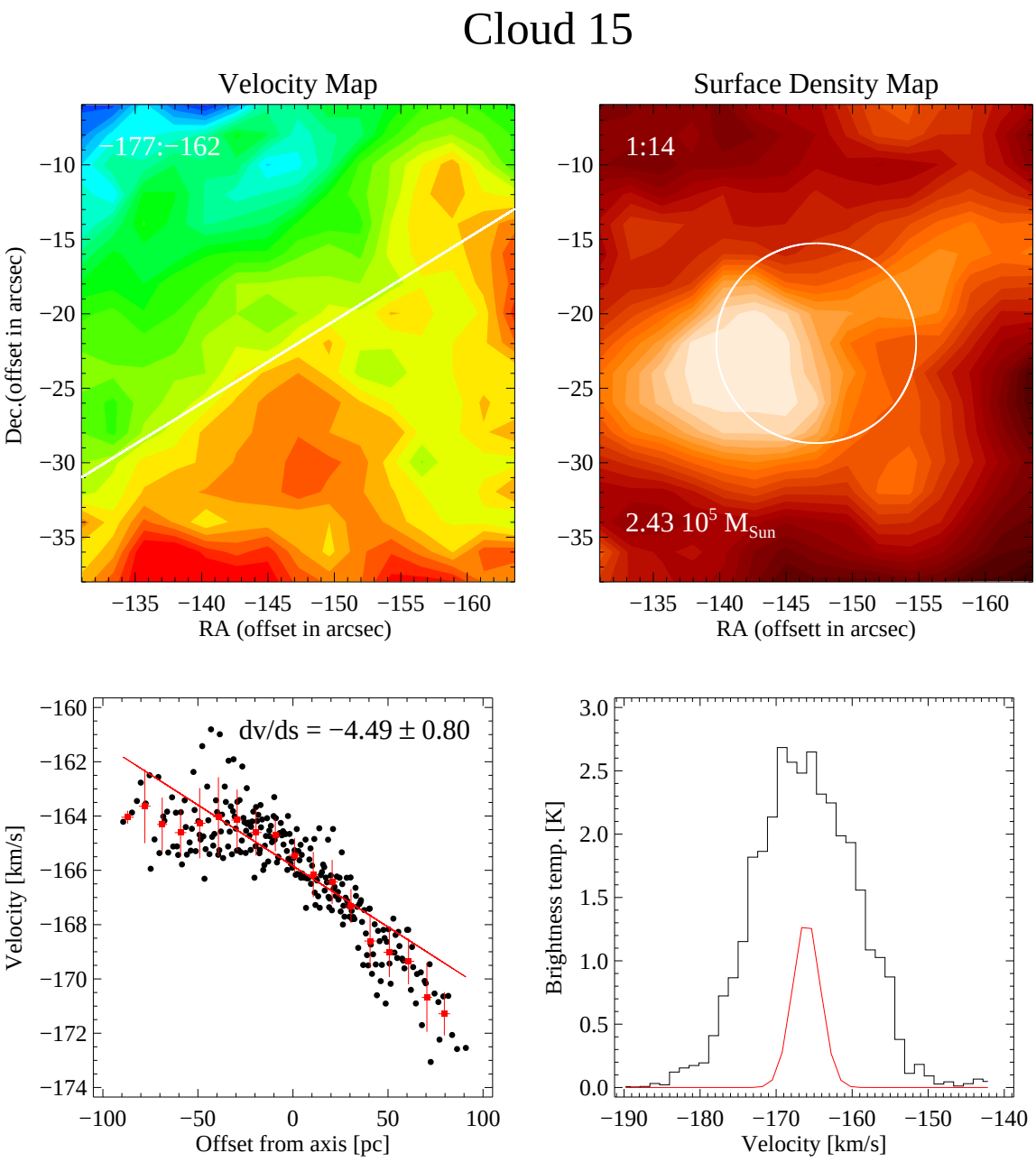

Figure A.12: Cloud 15: Same as Figure A.1.

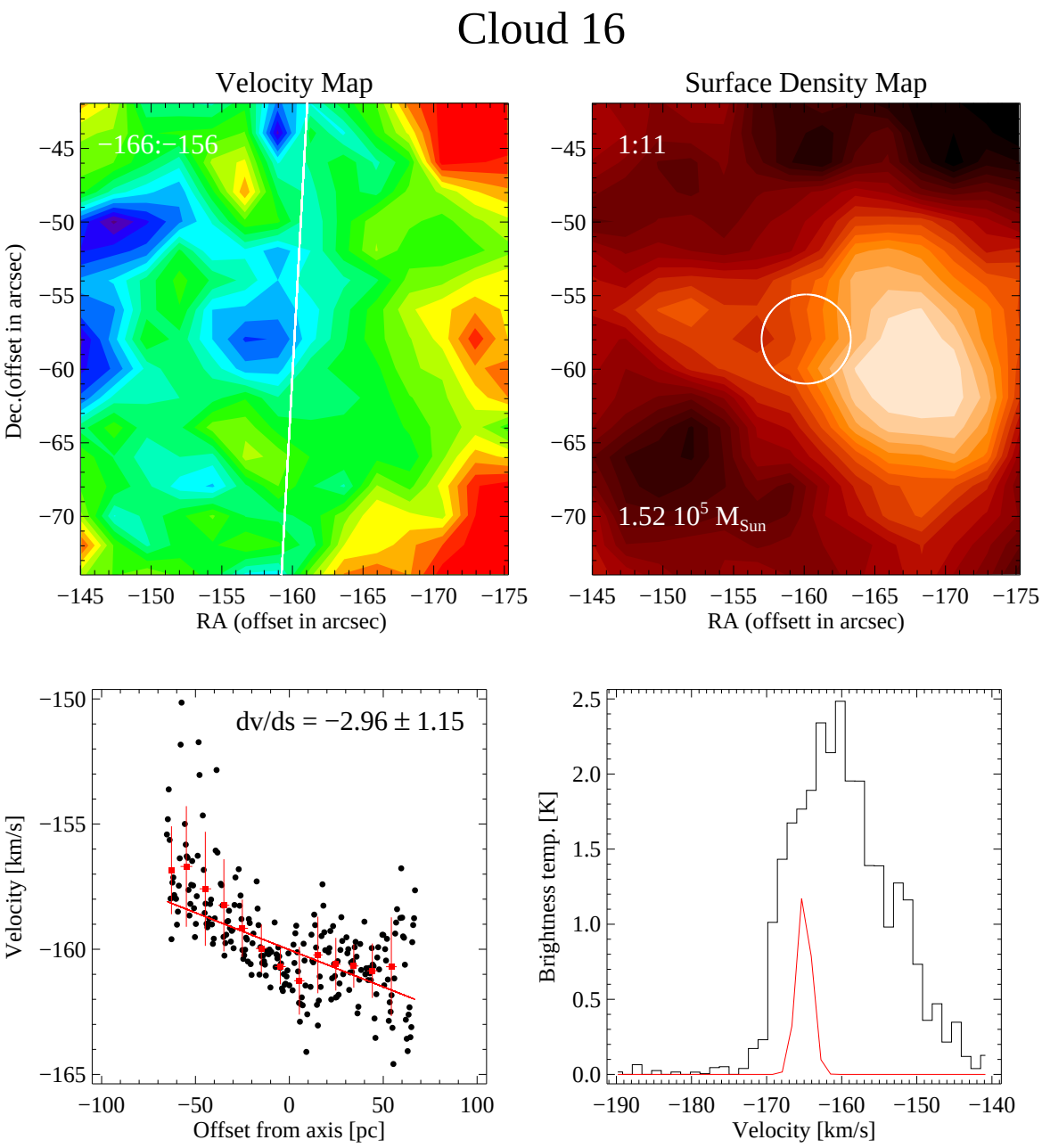

Figure A.13: Cloud 16: Same as Figure A.1.

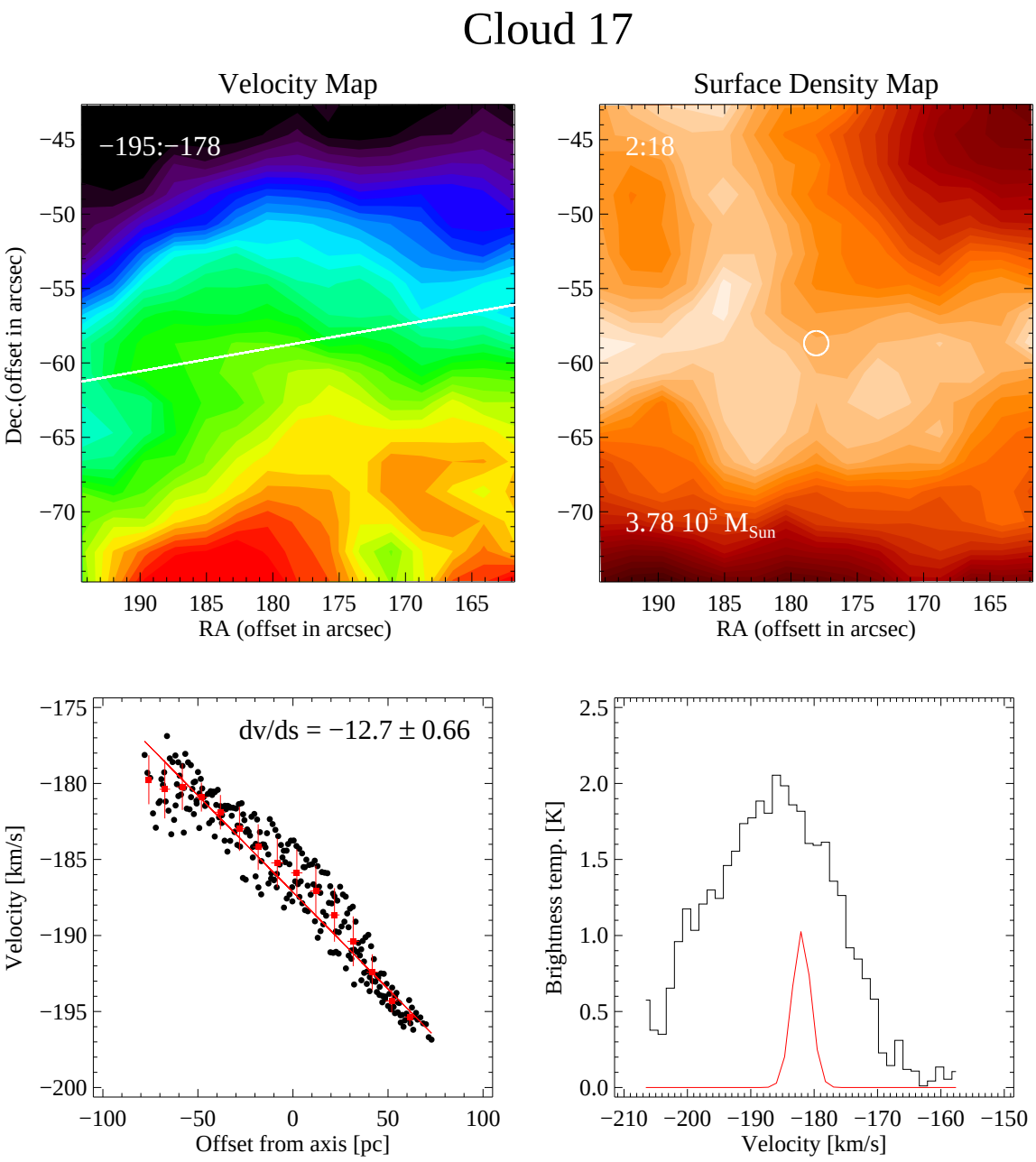

Figure A.14: Cloud 17: Same as Figure A.1.

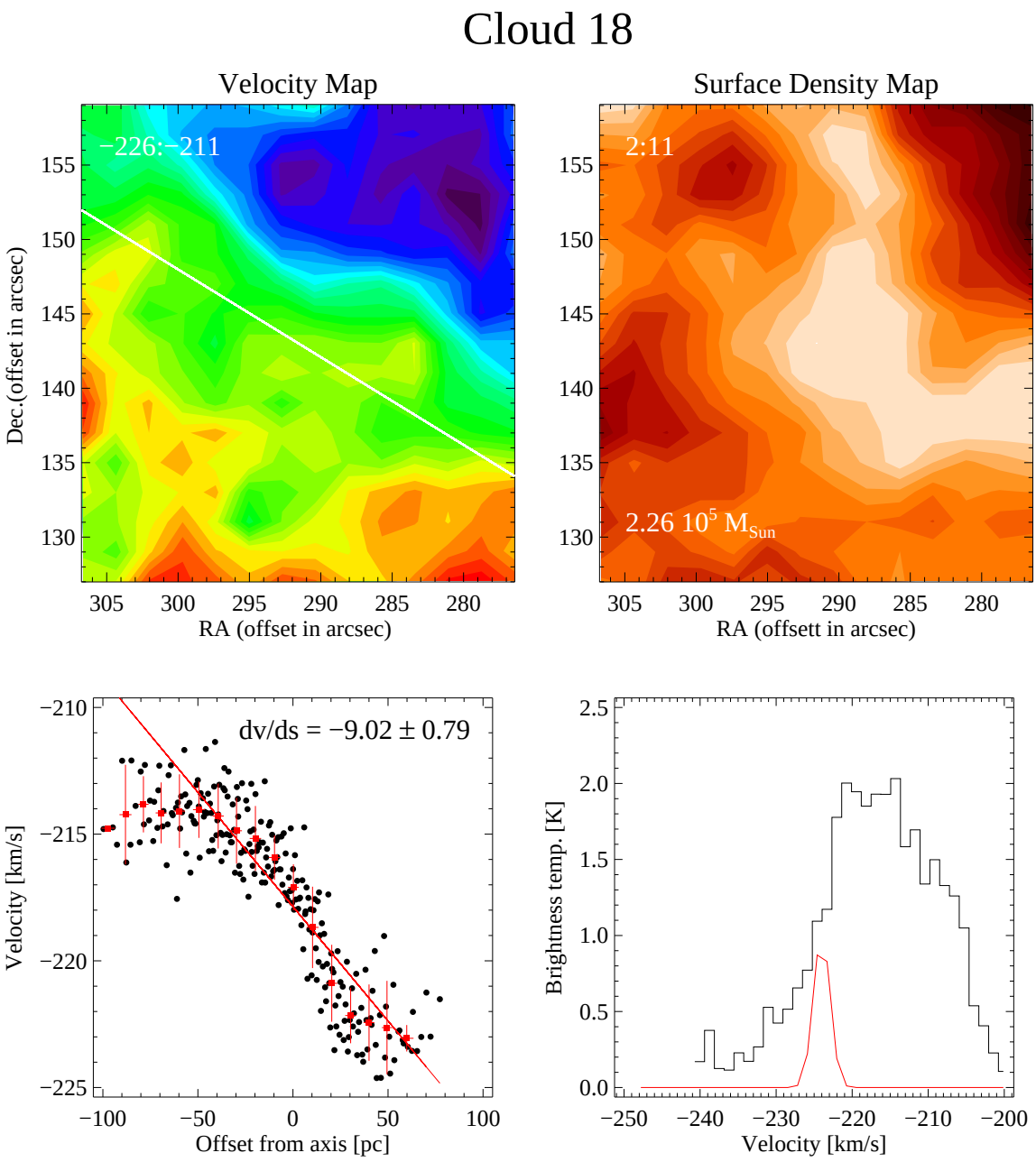

Figure A.15: Cloud 18: Same as Figure A.1.

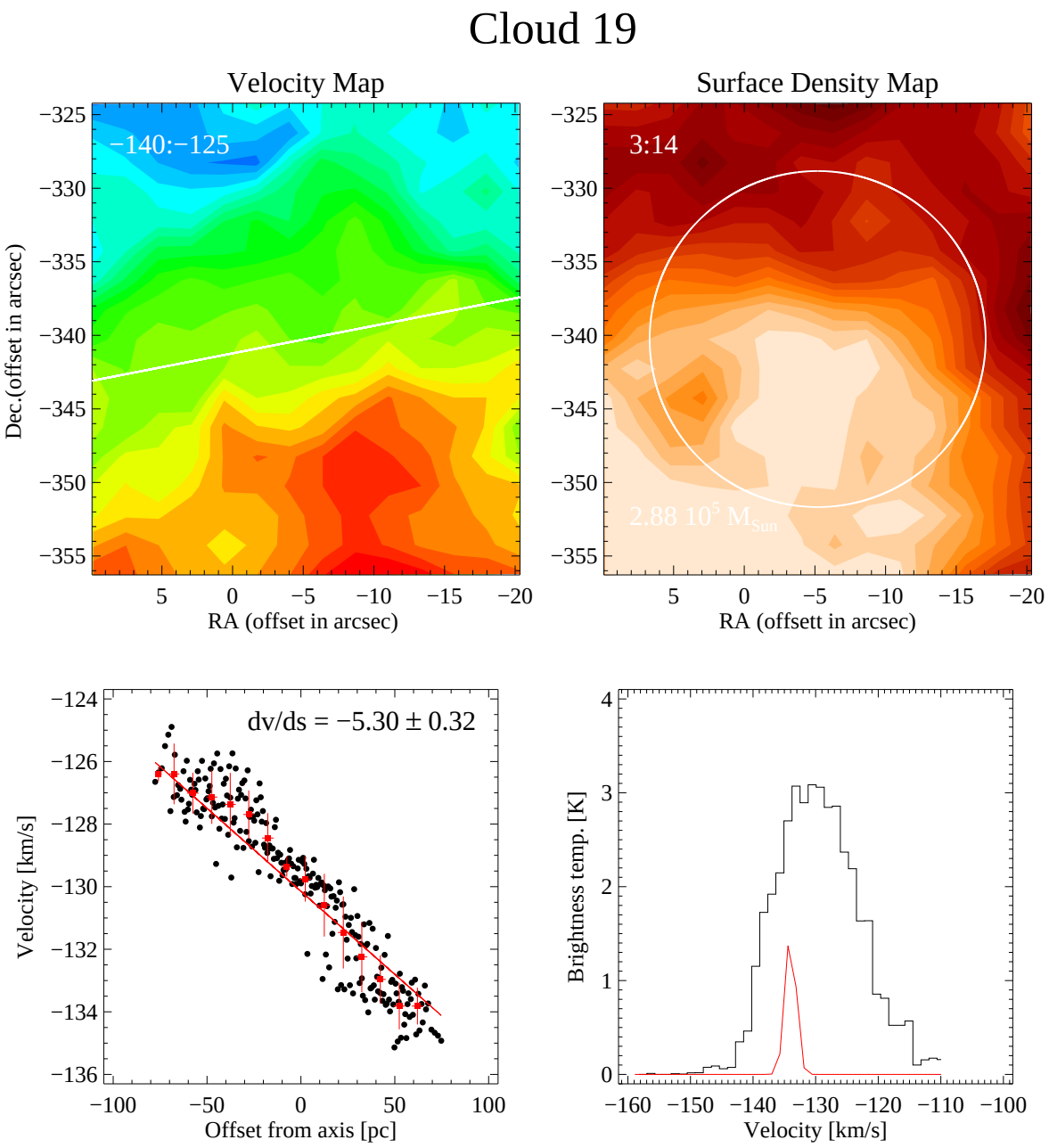

Figure A.16: Cloud 19: Same as Figure A.1.

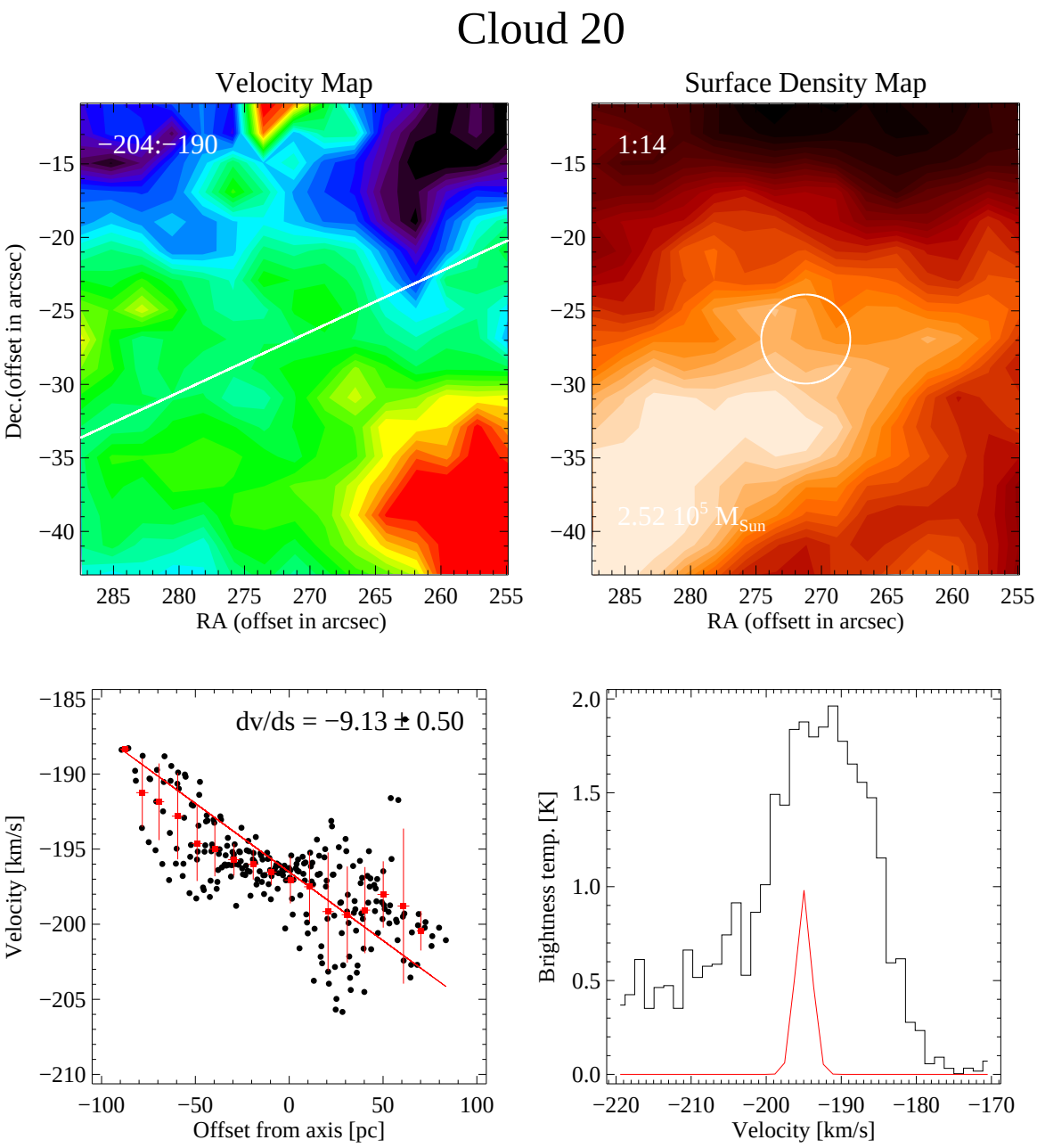

Figure A.17: Cloud 20: Same as Figure A.1.

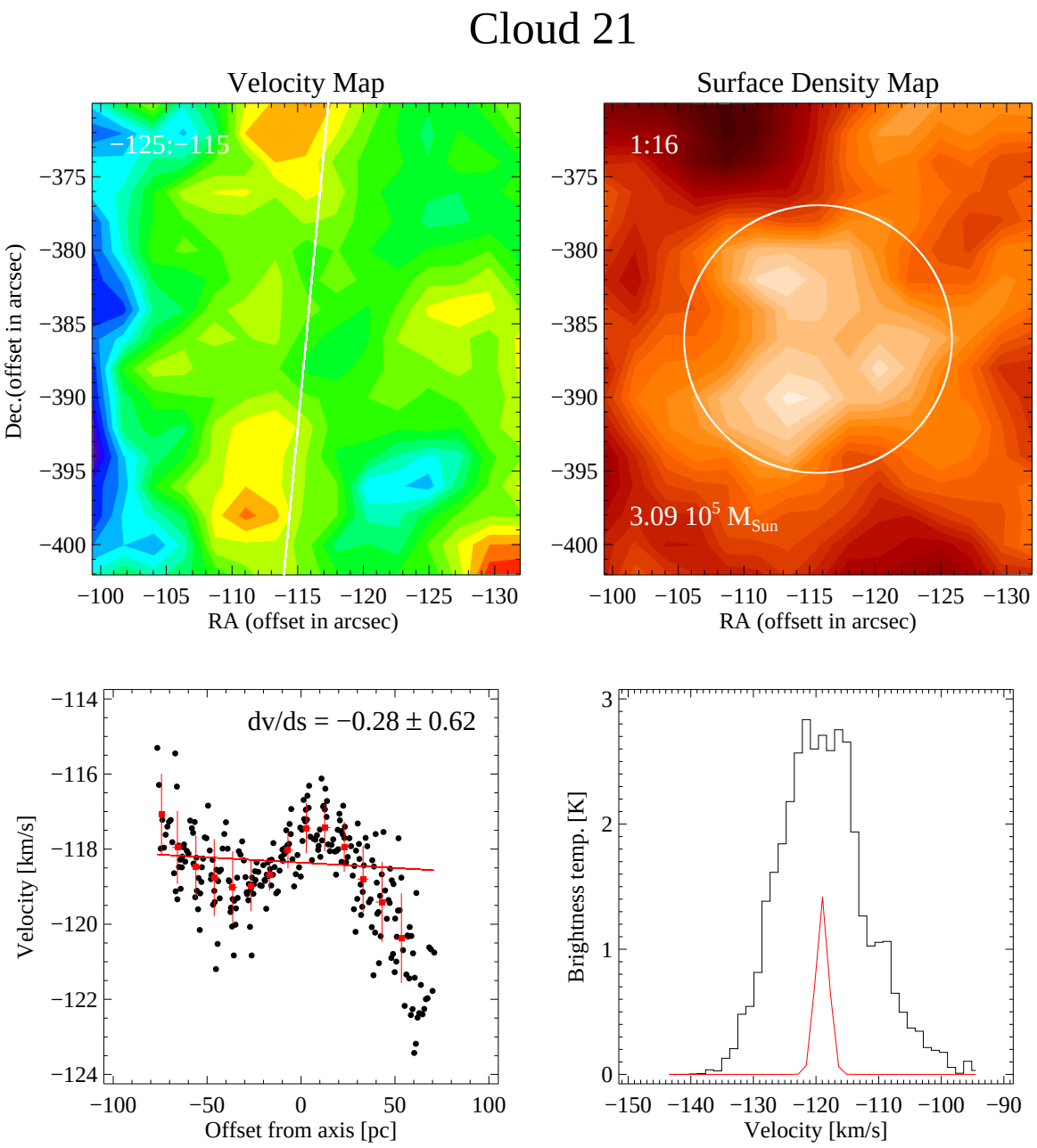

Figure A.18: Cloud 21: Same as Figure A.1.

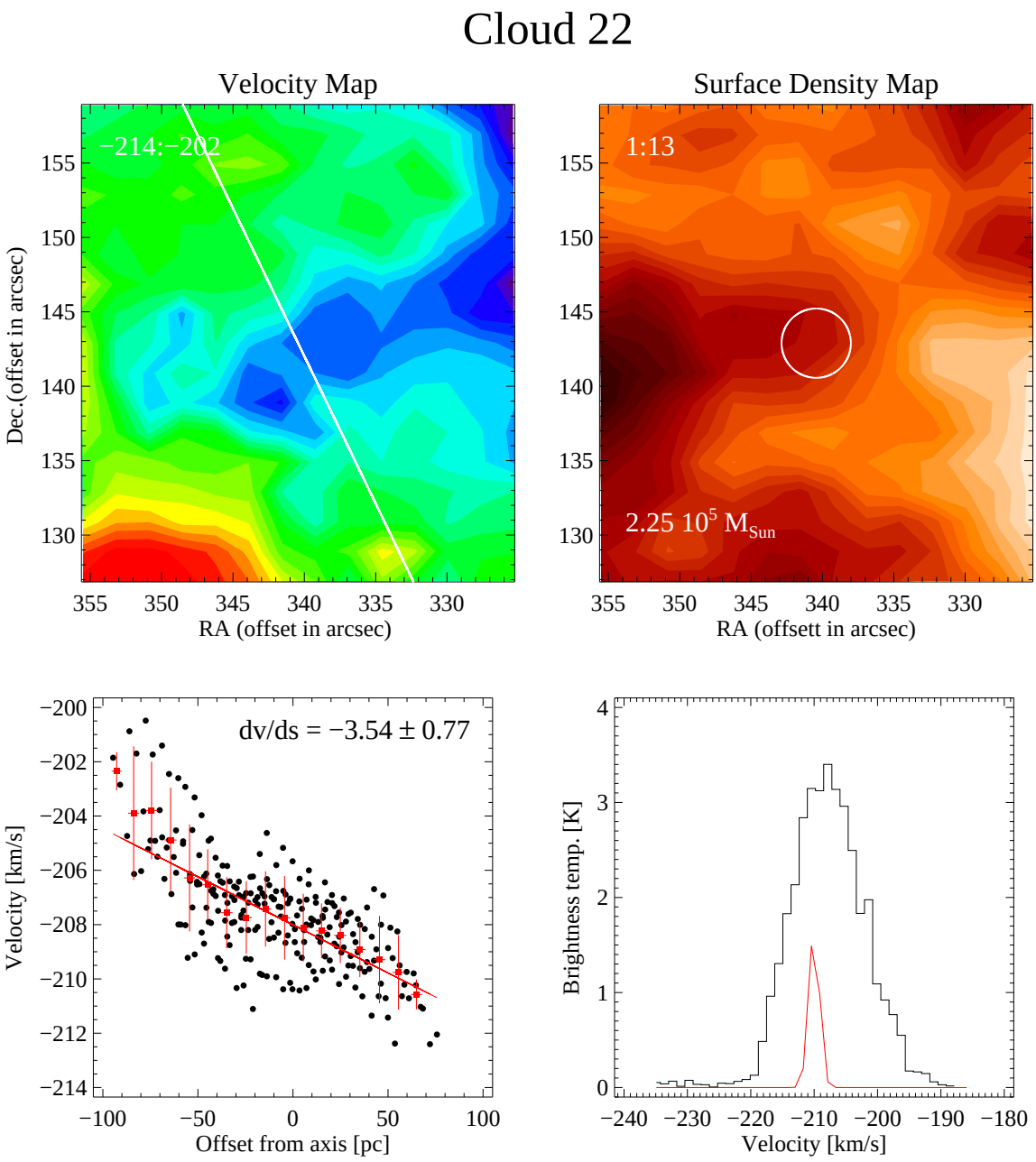

Figure A.19: Cloud 22: Same as Figure A.1.

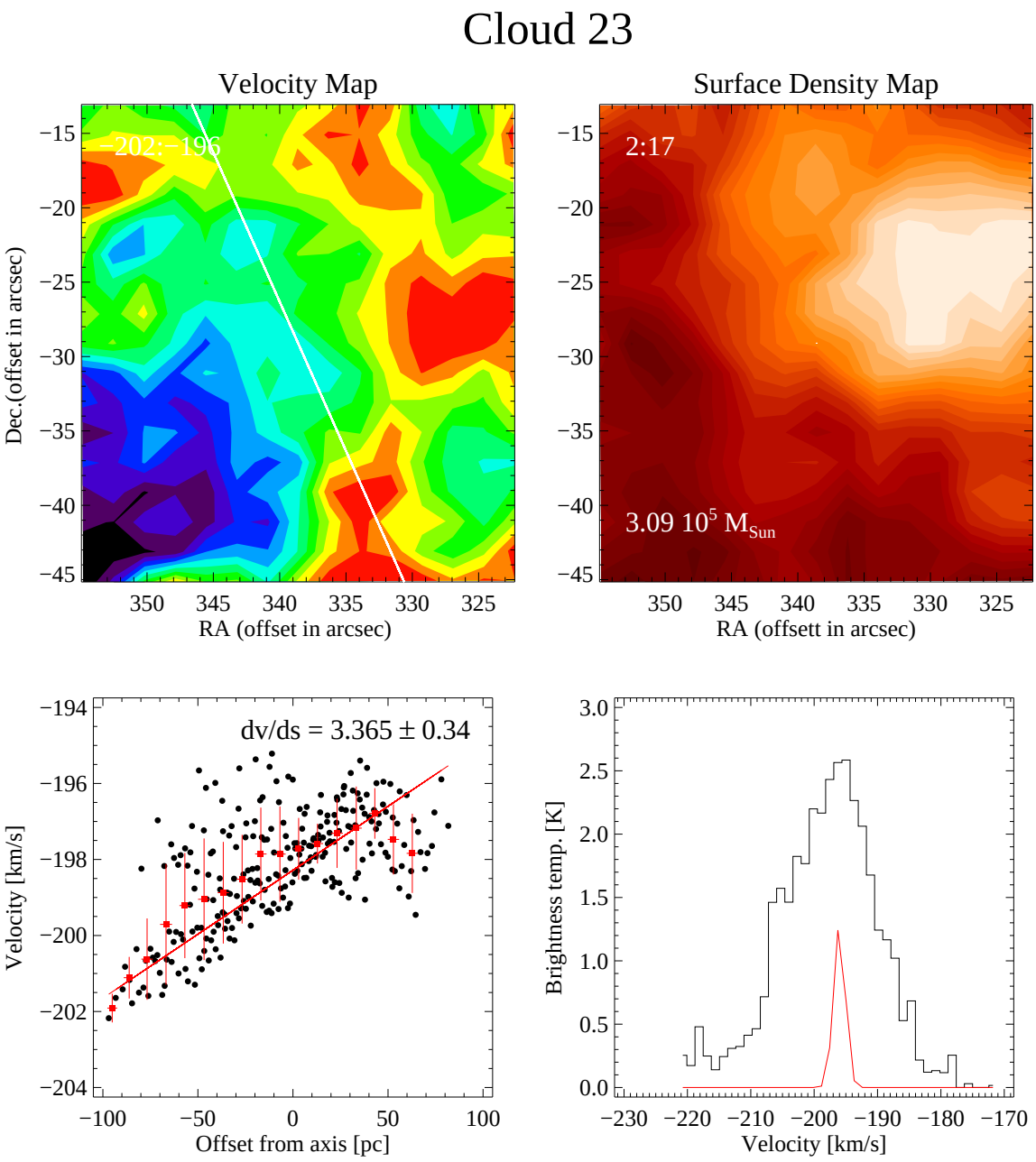

Figure A.20: Cloud 23: Same as Figure A.1.

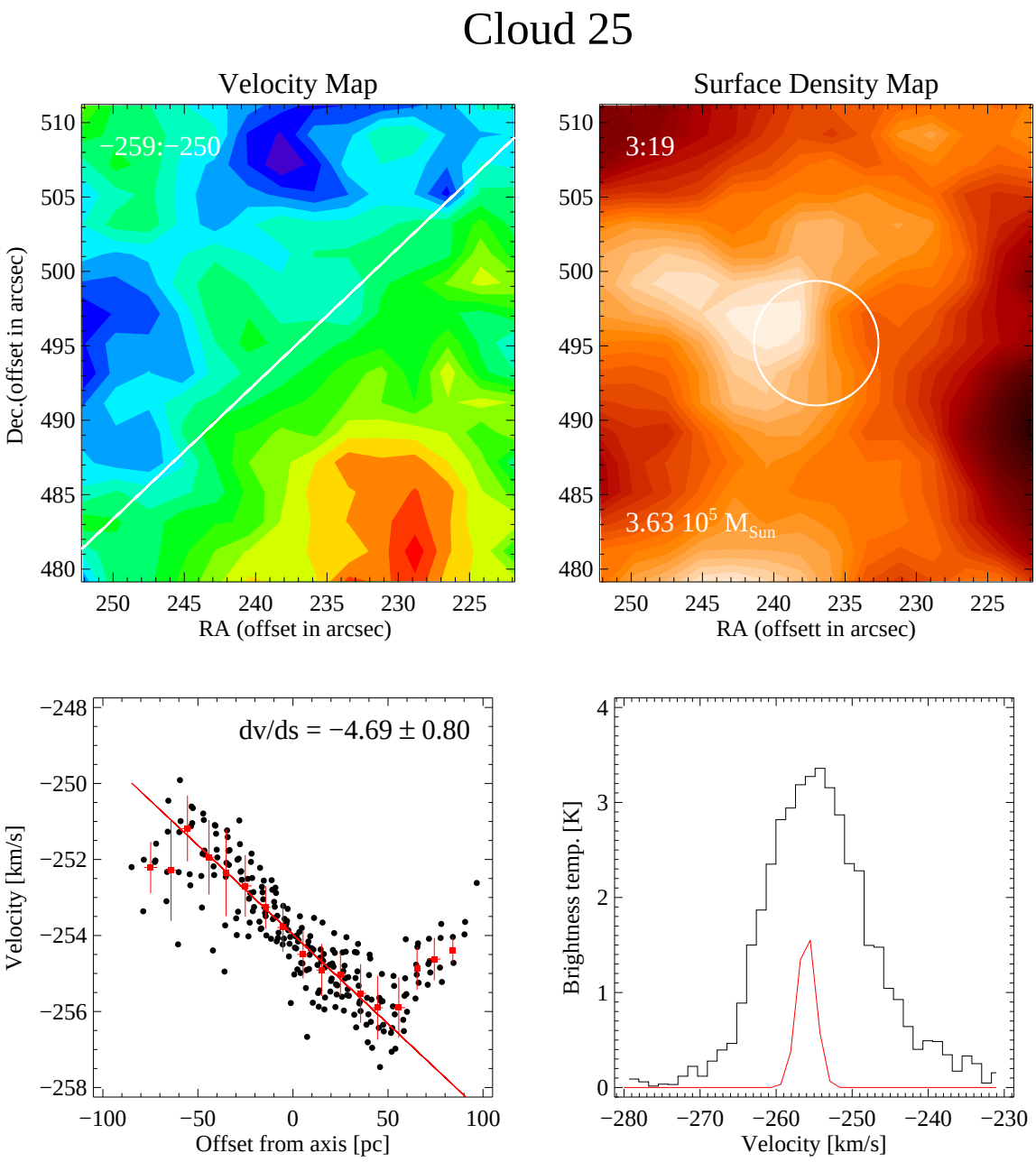

Figure A.21: Cloud 25: Same as Figure A.1.

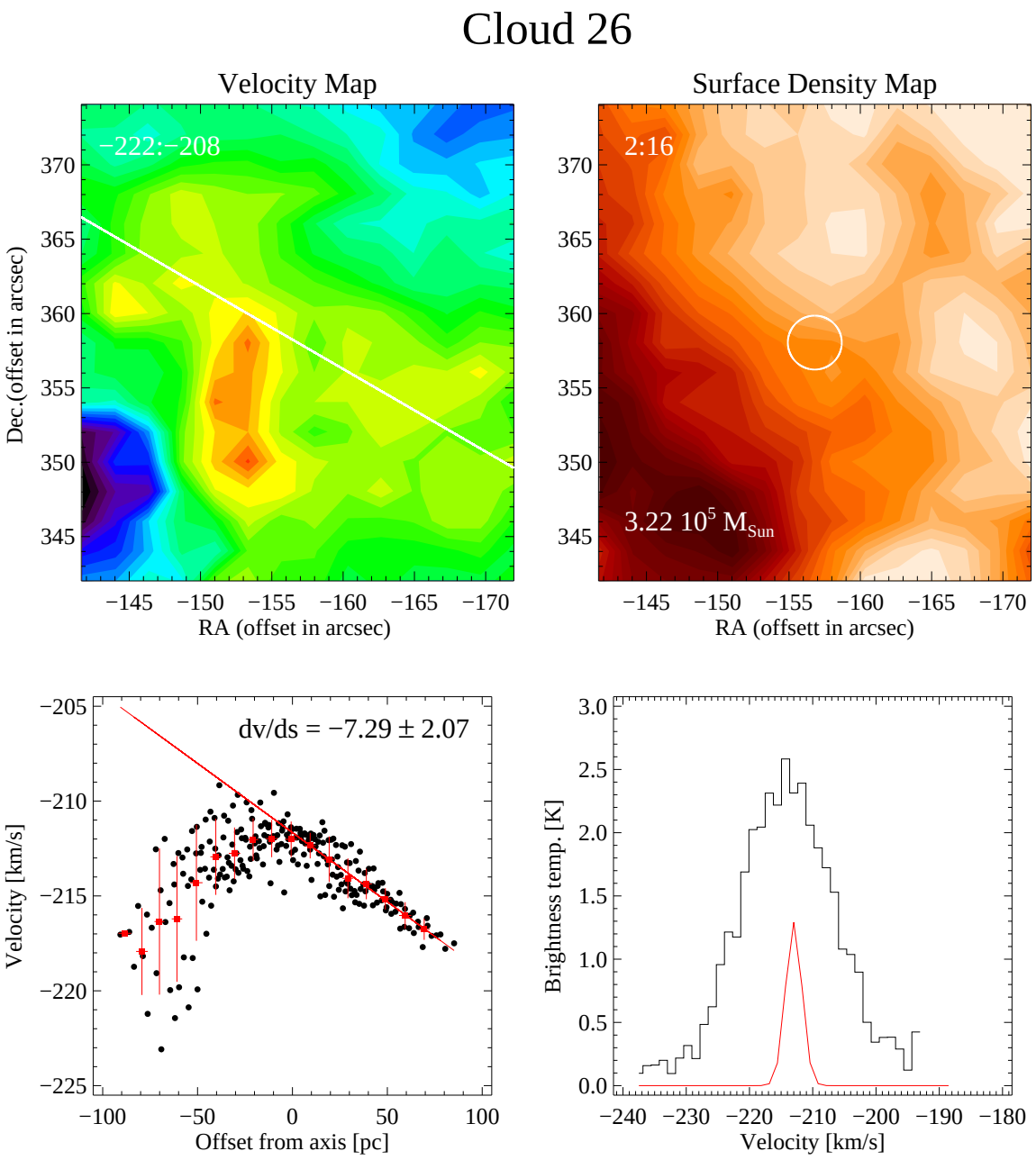

Figure A.22: Cloud 26: Same as Figure A.1.

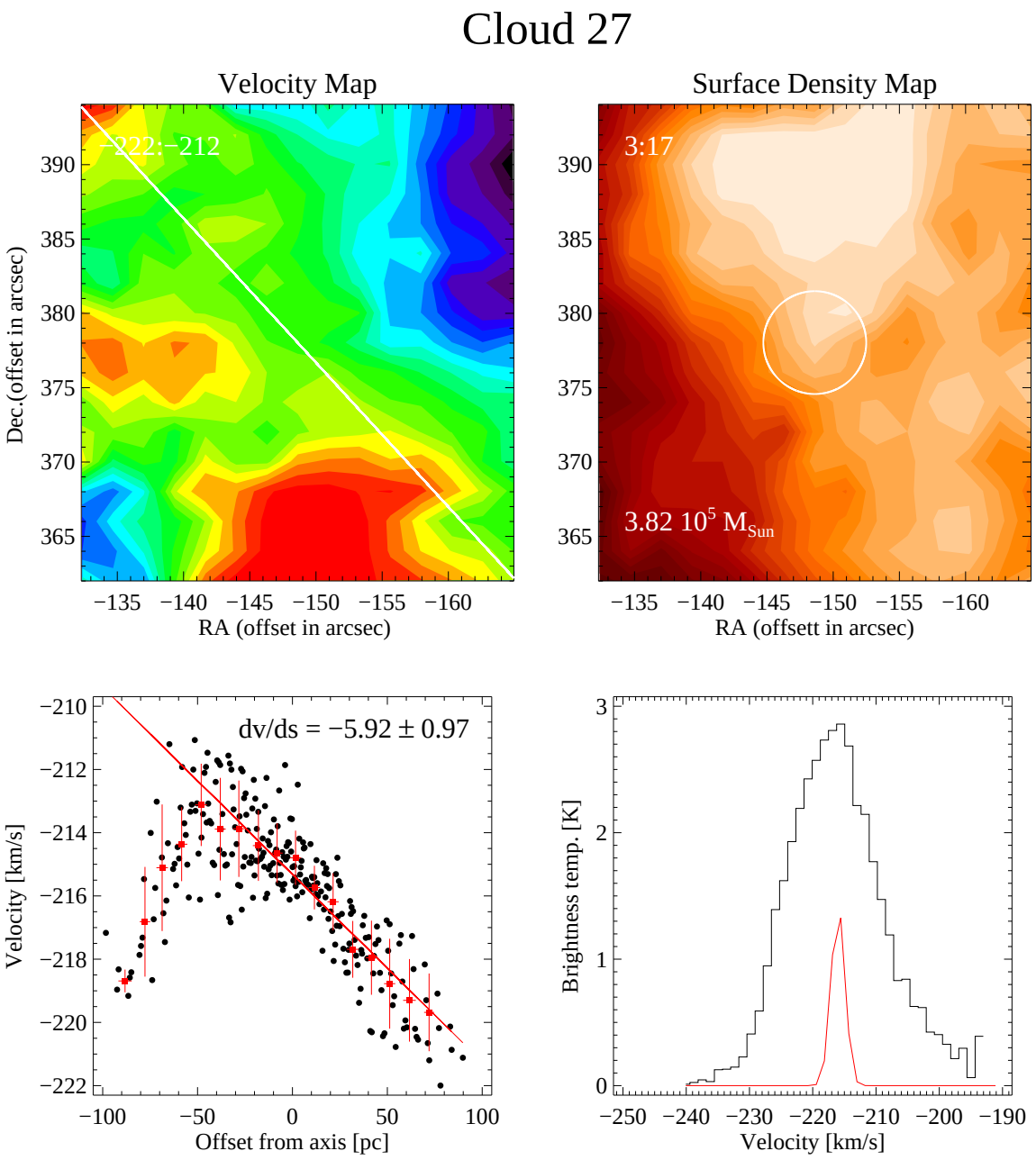

Figure A.23: Cloud 27: Same as Figure A.1.

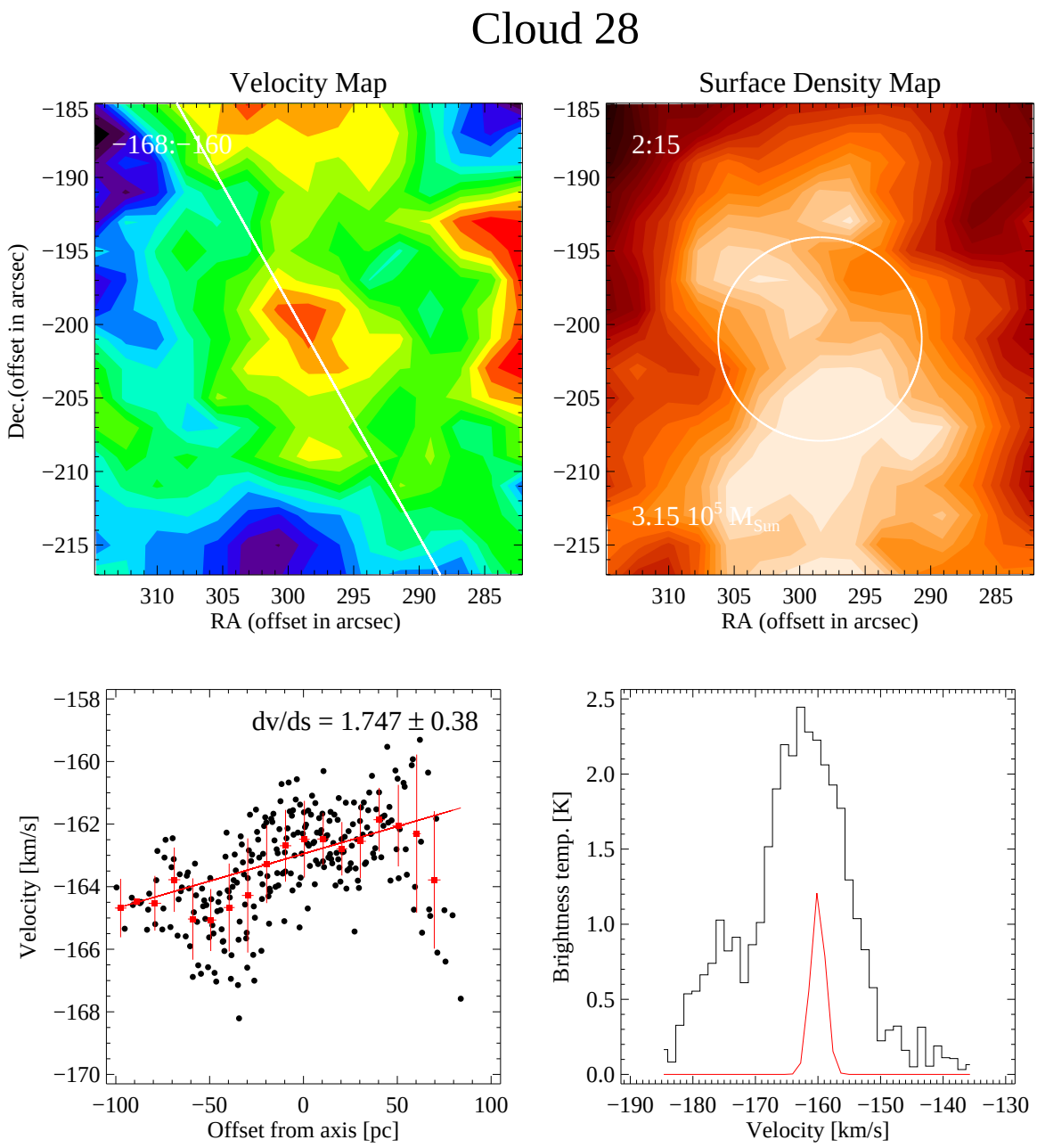

Figure A.24: Cloud 28: Same as Figure A.1.

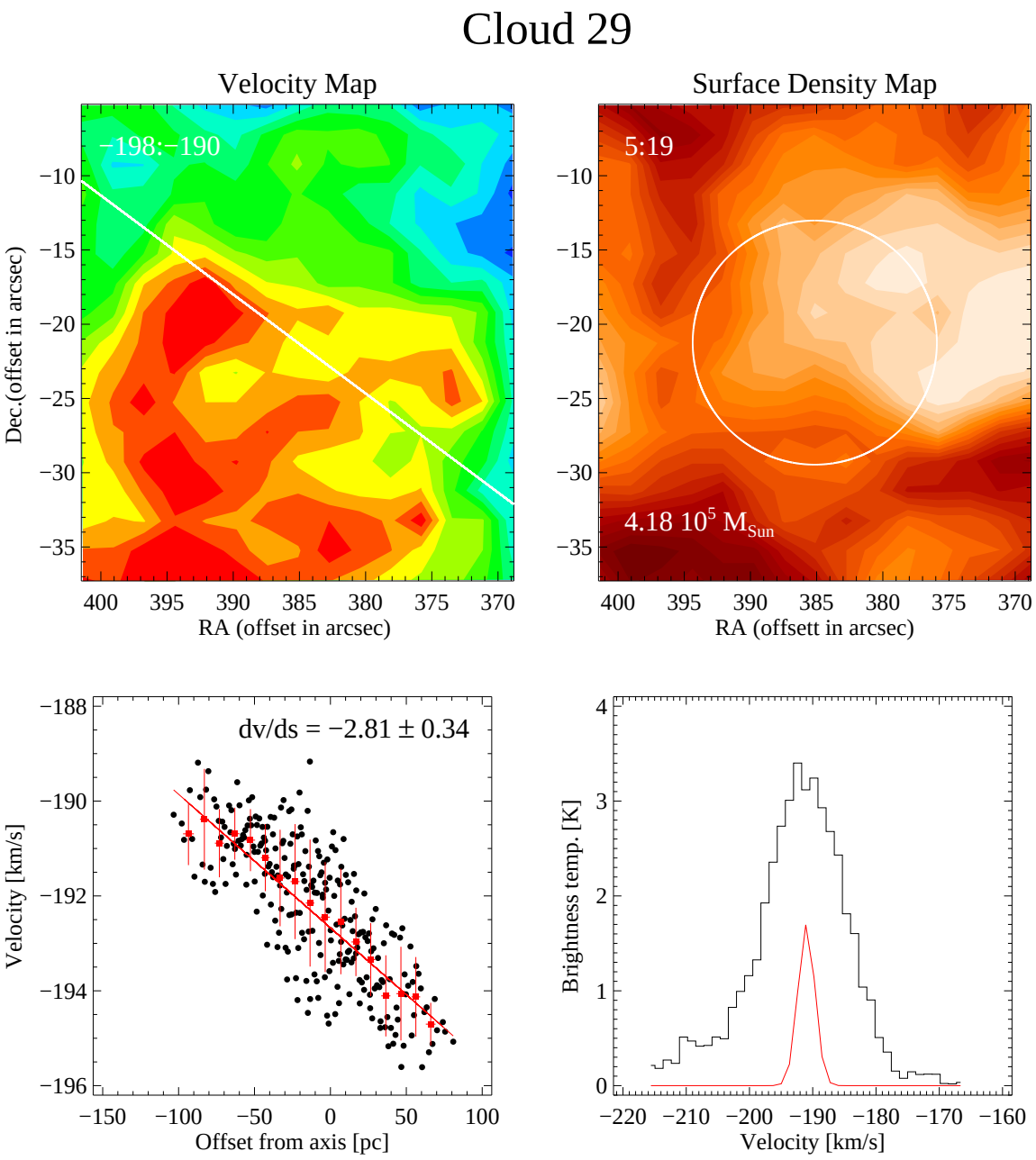

Figure A.25: Cloud 29: Same as Figure A.1.

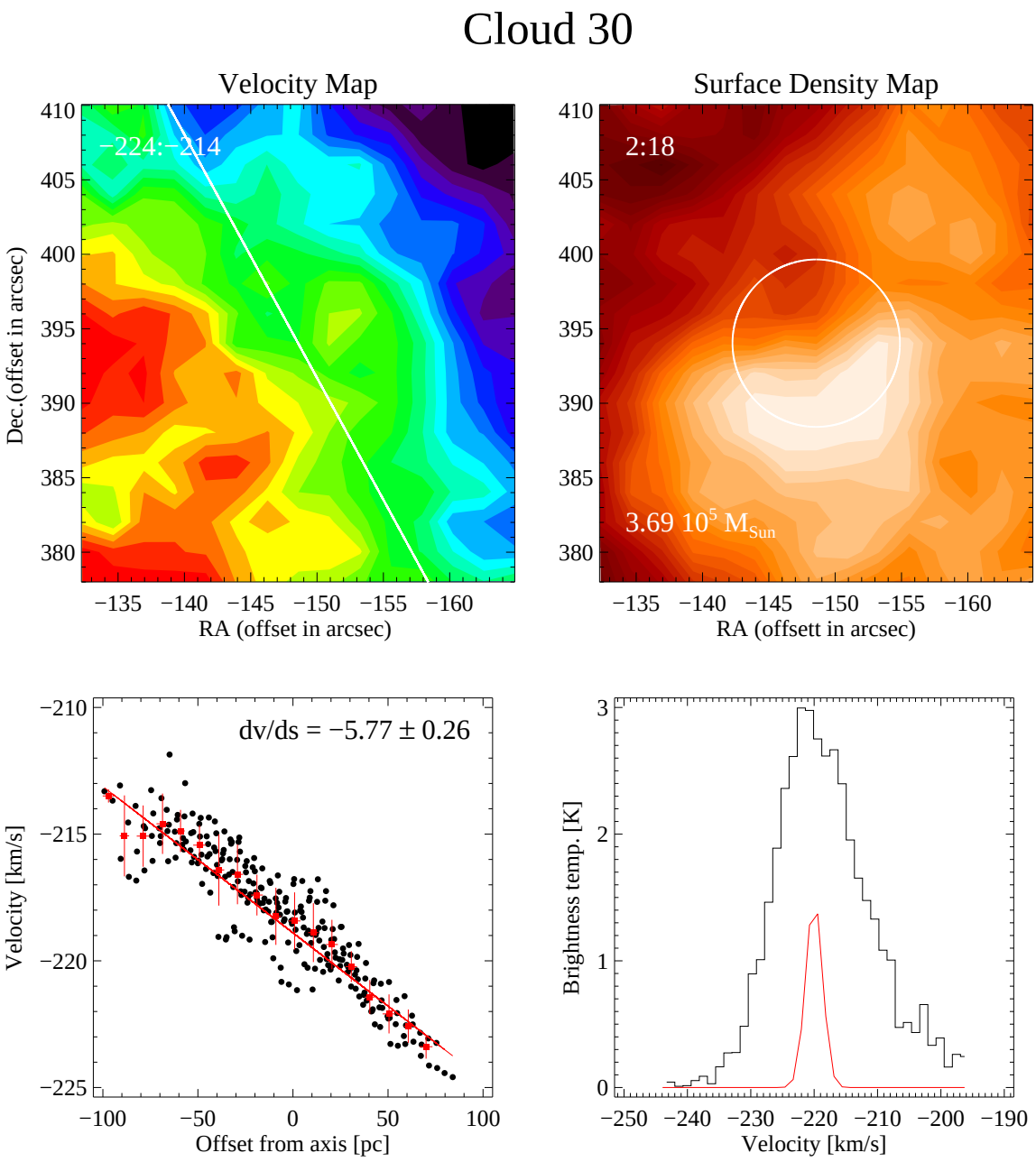

Figure A.26: Cloud 30: Same as Figure A.1.

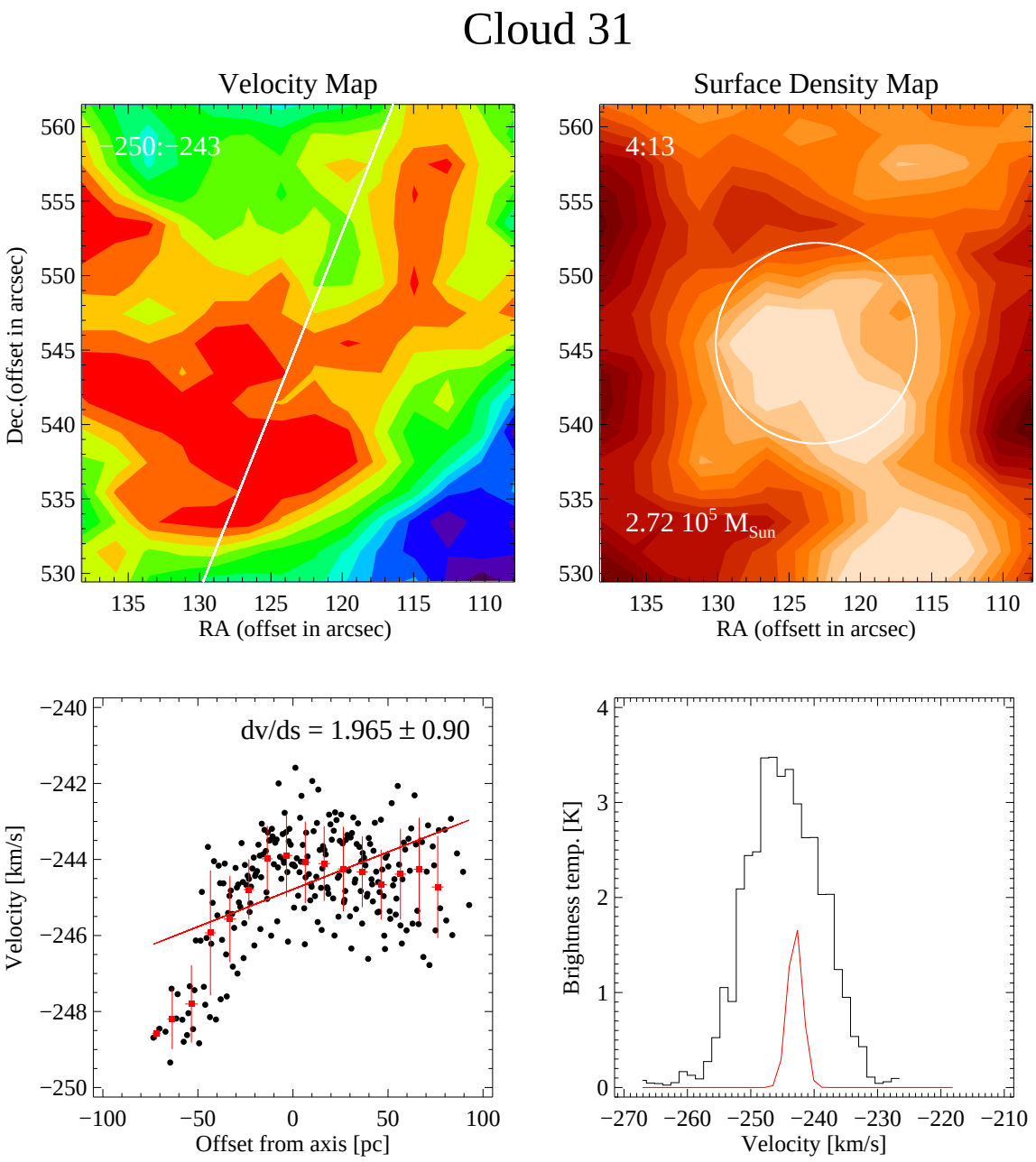

Figure A.27: Cloud 31: Same as Figure A.1.

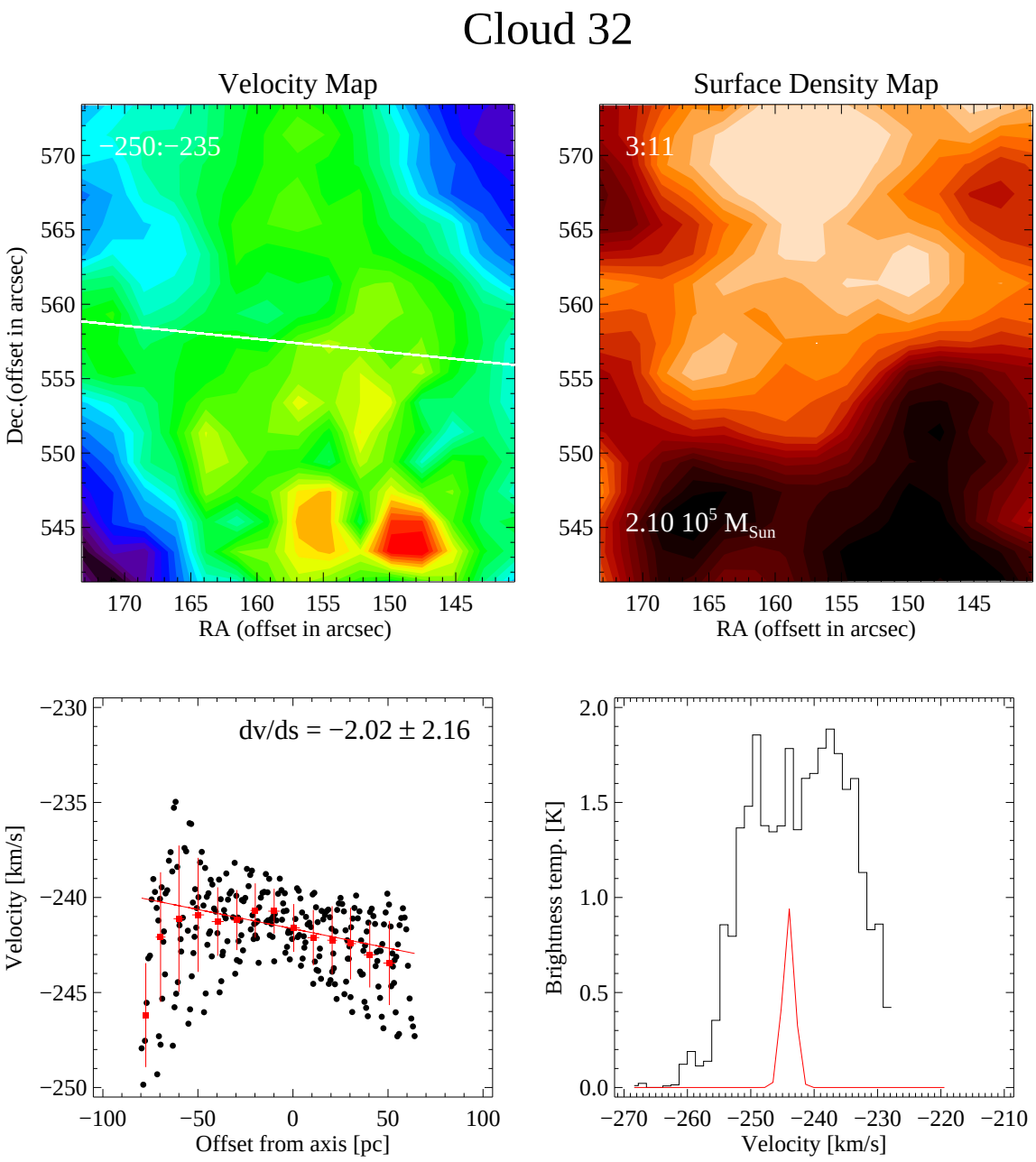

Figure A.28: Cloud 32: Same as Figure A.1.

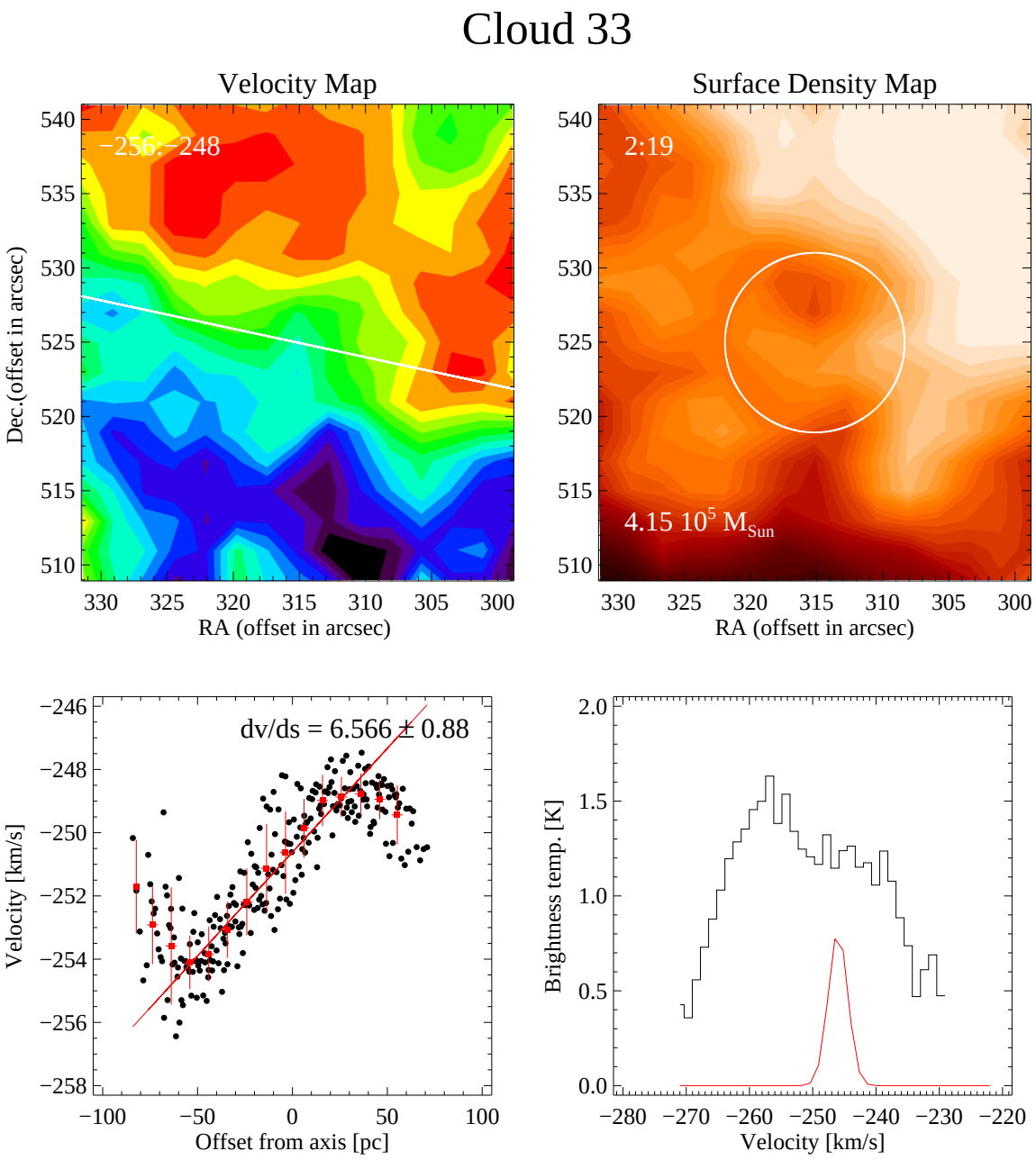

Figure A.29: Cloud 33: Same as Figure A.1.

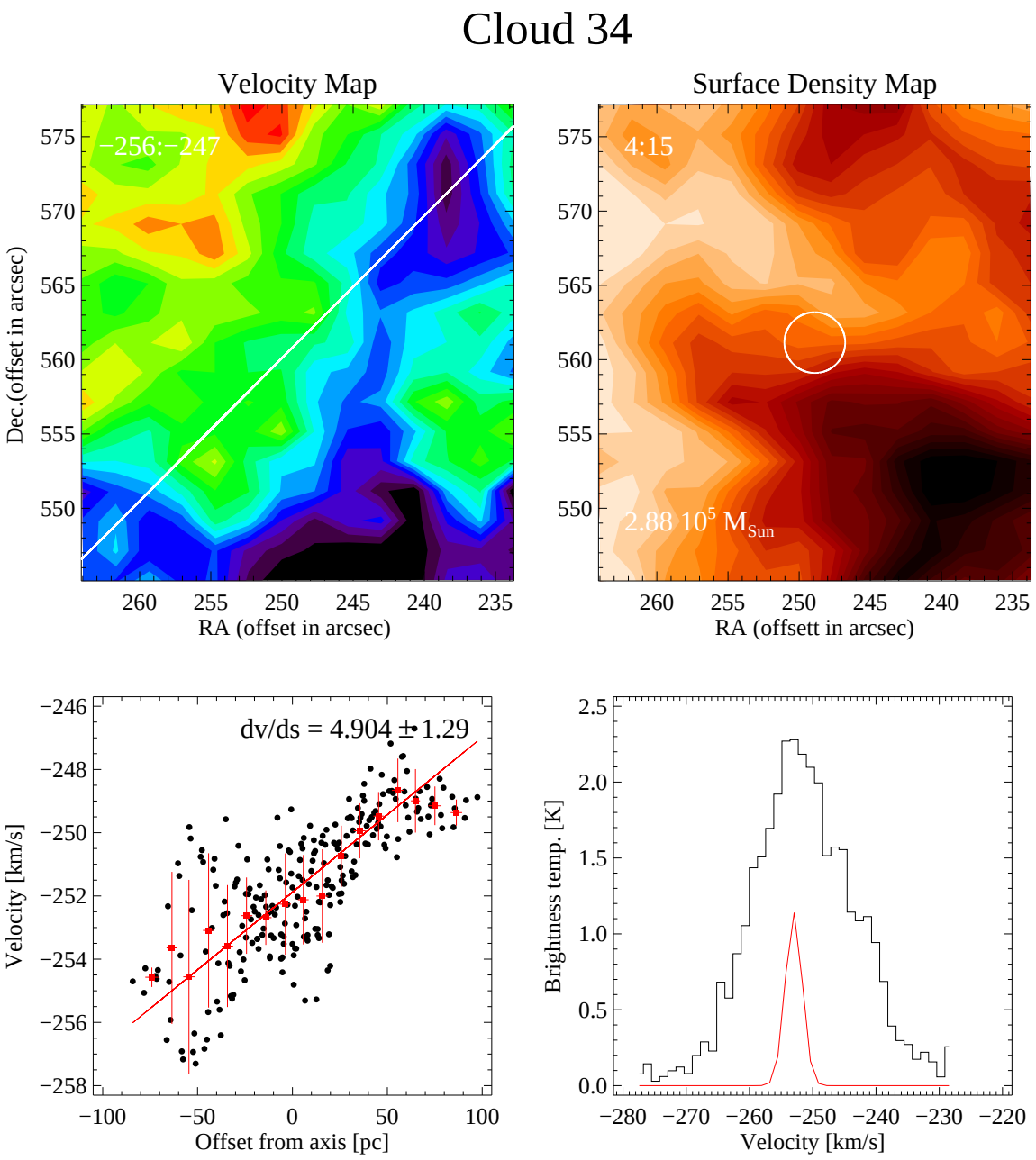

Figure A.30: Cloud 34: Same as Figure A.1.

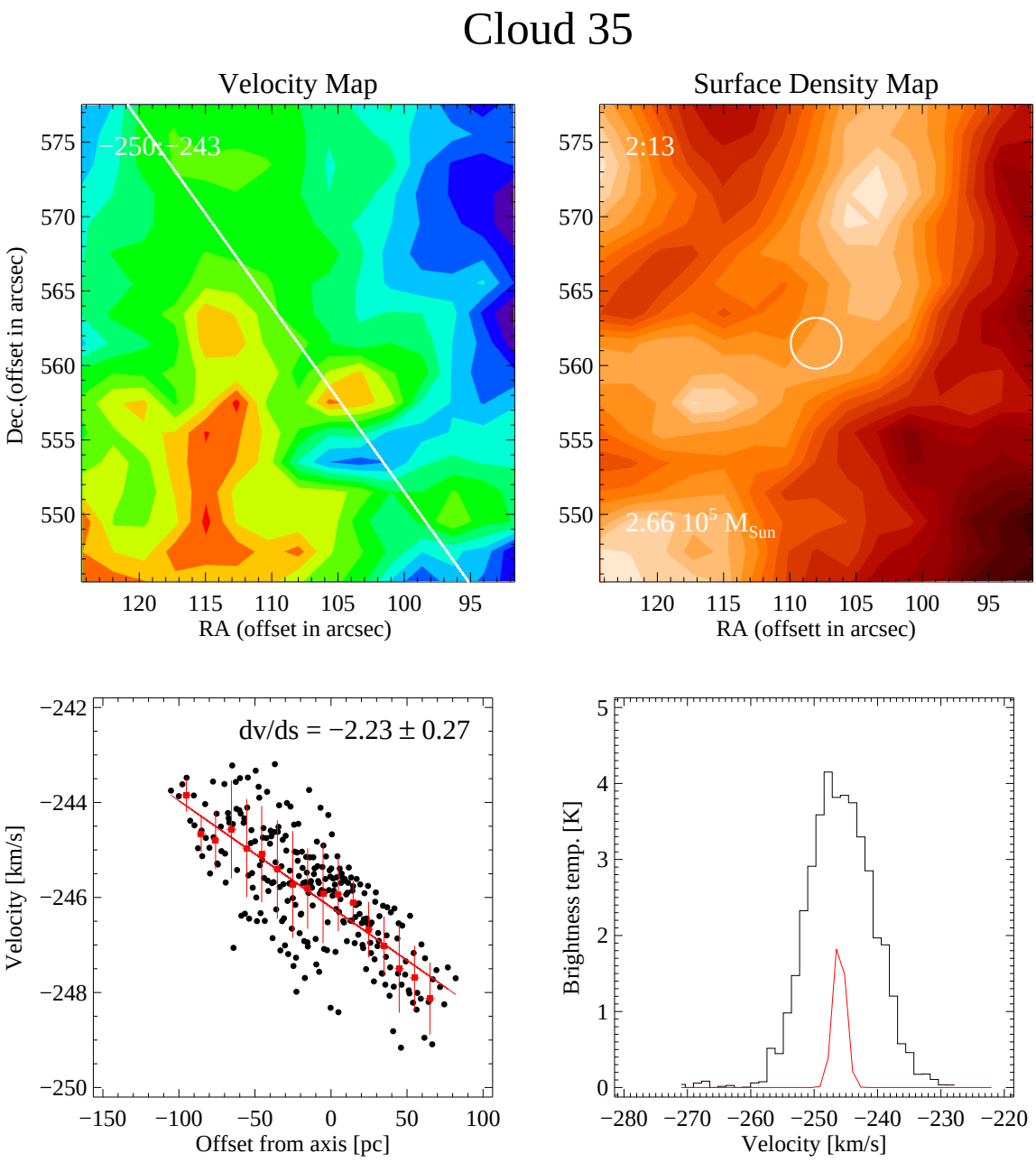

Figure A.31: Cloud 35: Same as Figure A.1.

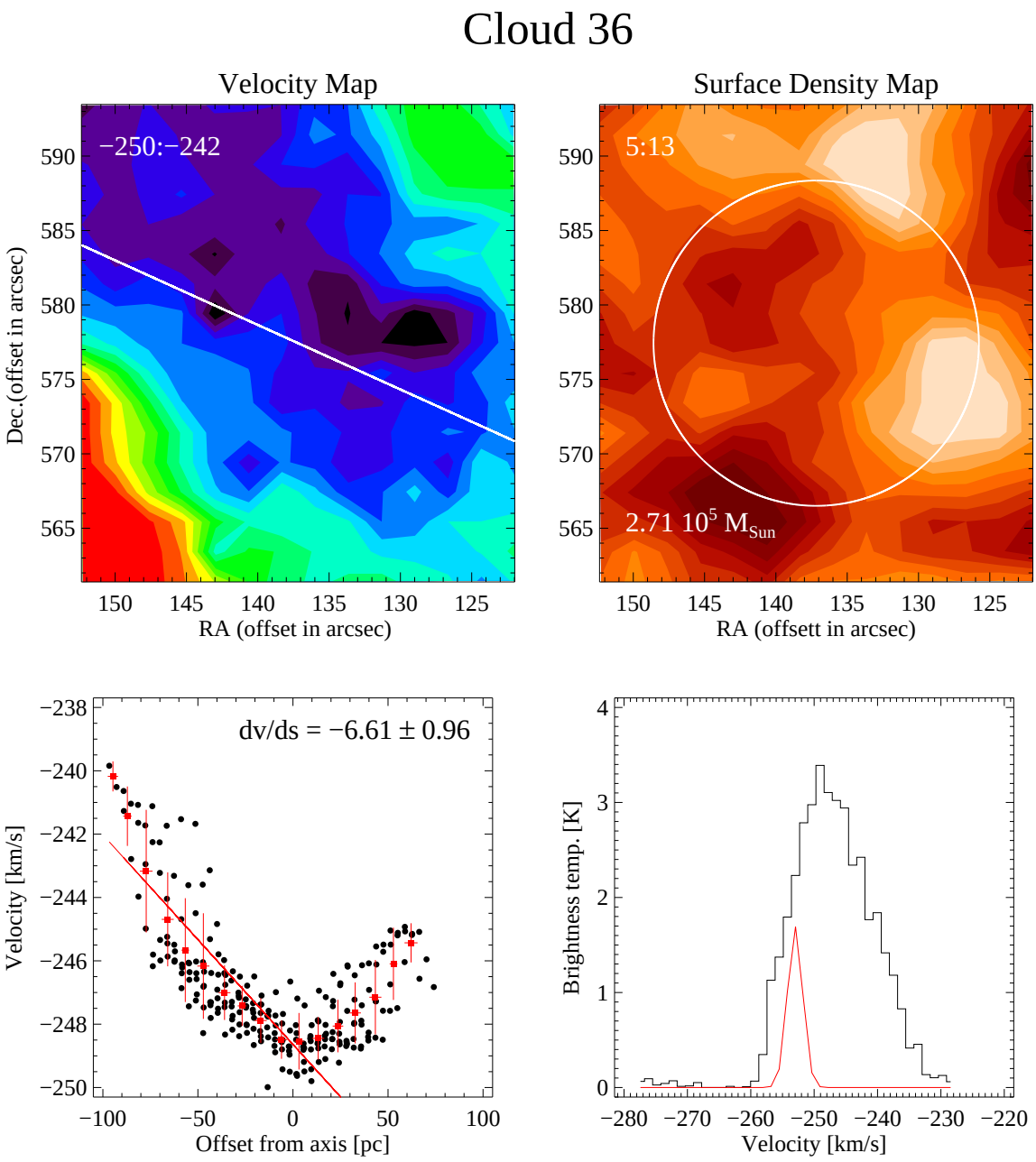

Figure A.32: Cloud 36: Same as Figure A.1.

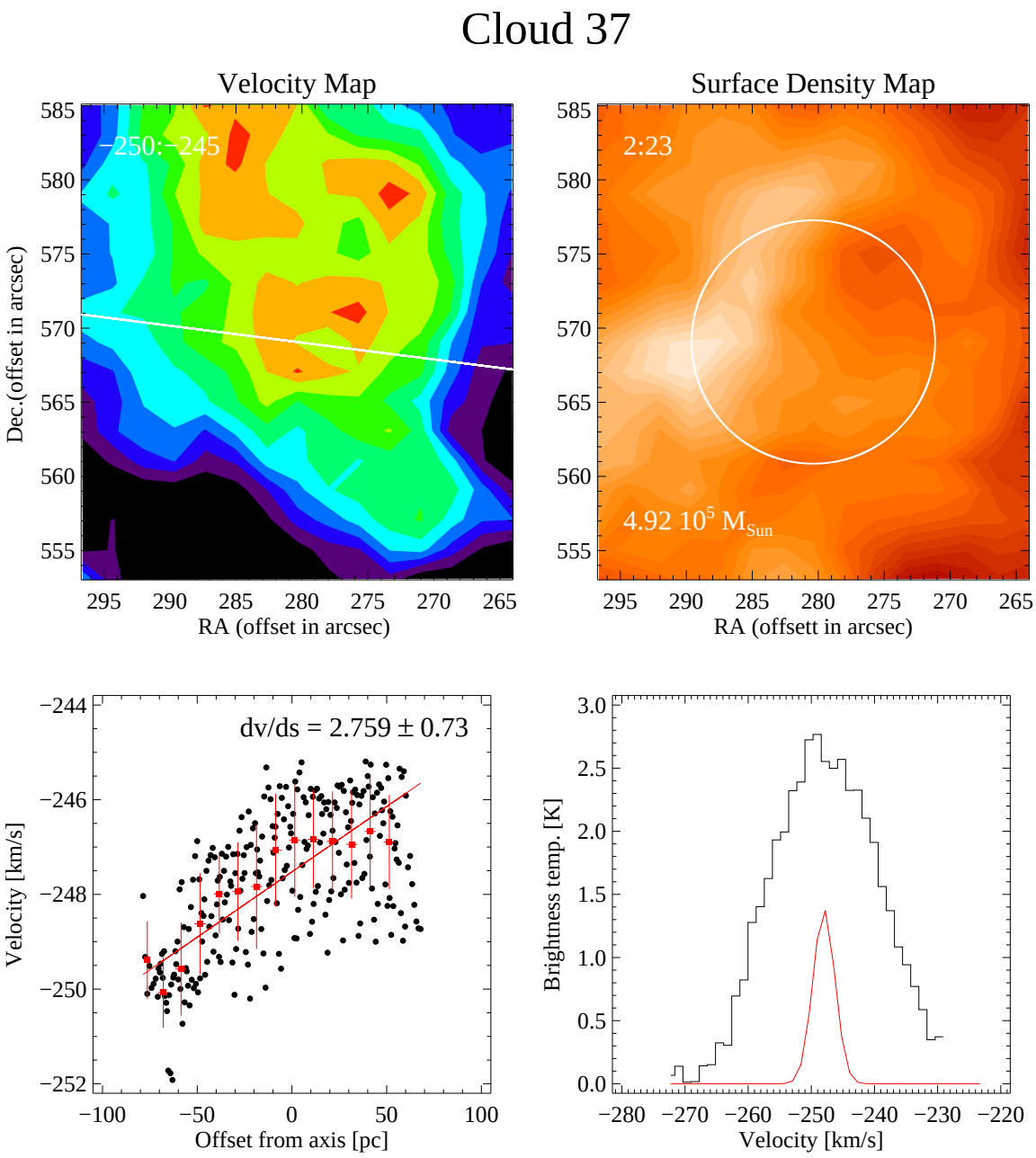

Figure A.33: Cloud 37: Same as Figure A.1.

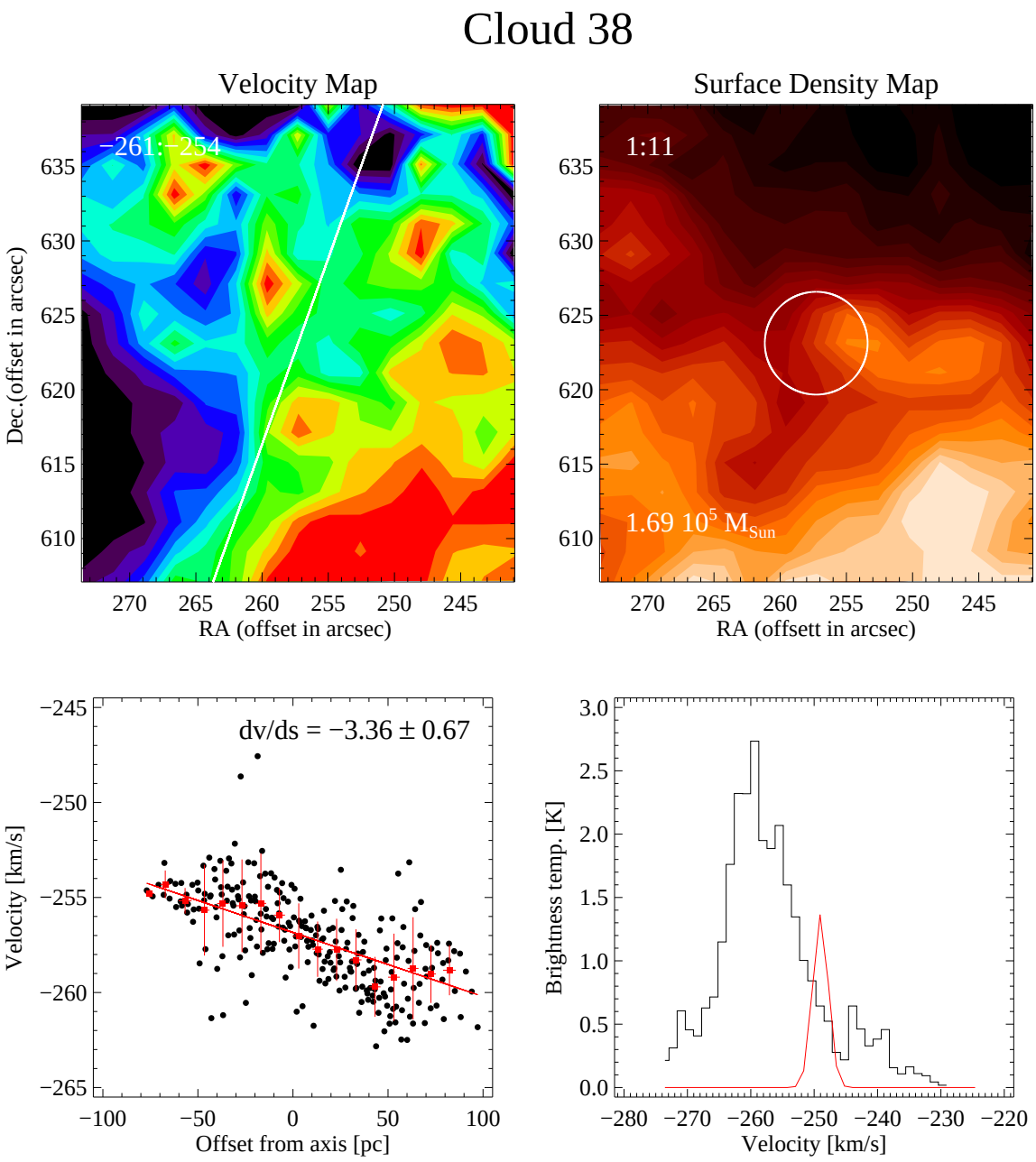

Figure A.34: Cloud 38: Same as Figure A.1.

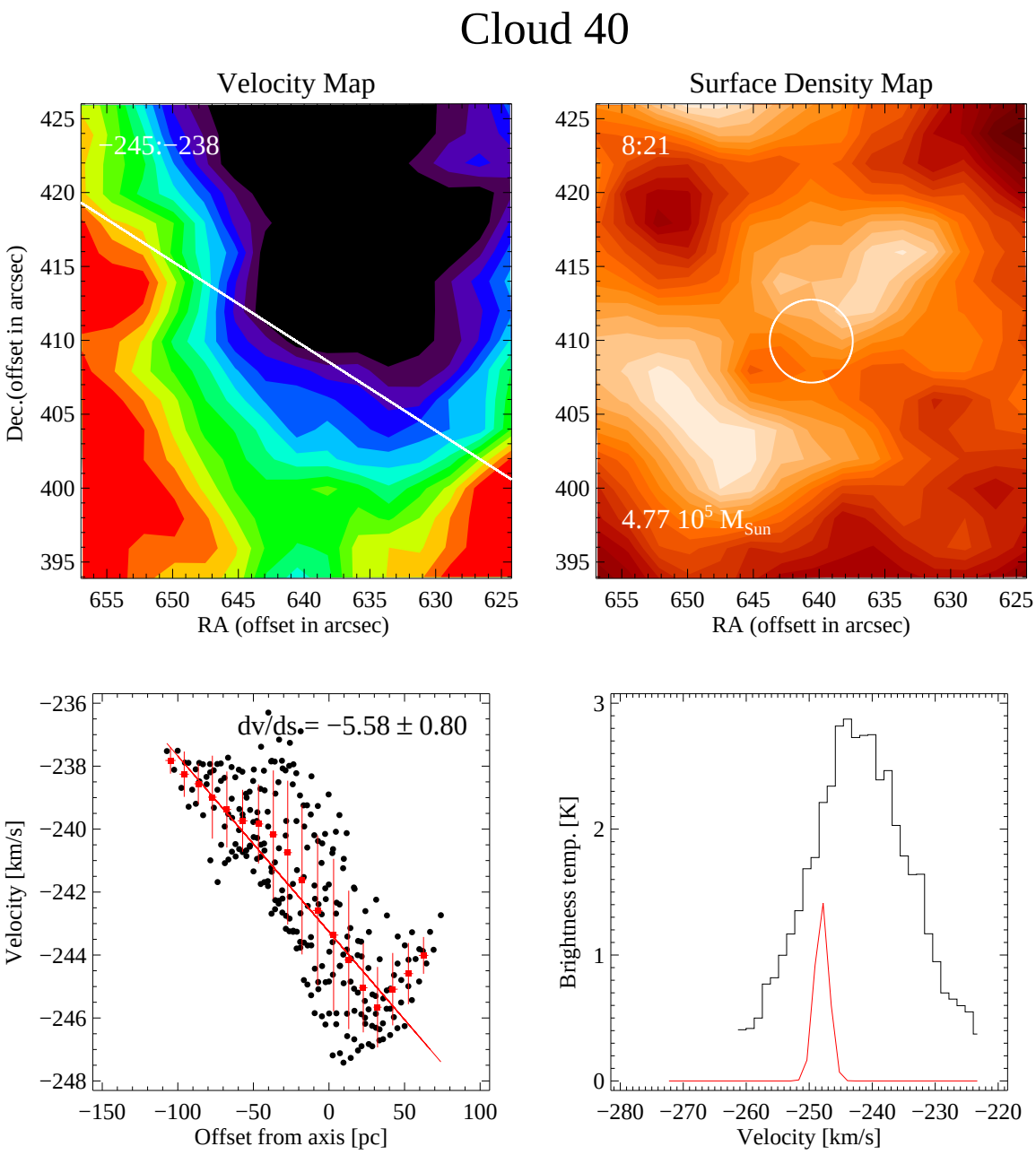

Figure A.35: Cloud 40: Same as Figure A.1.

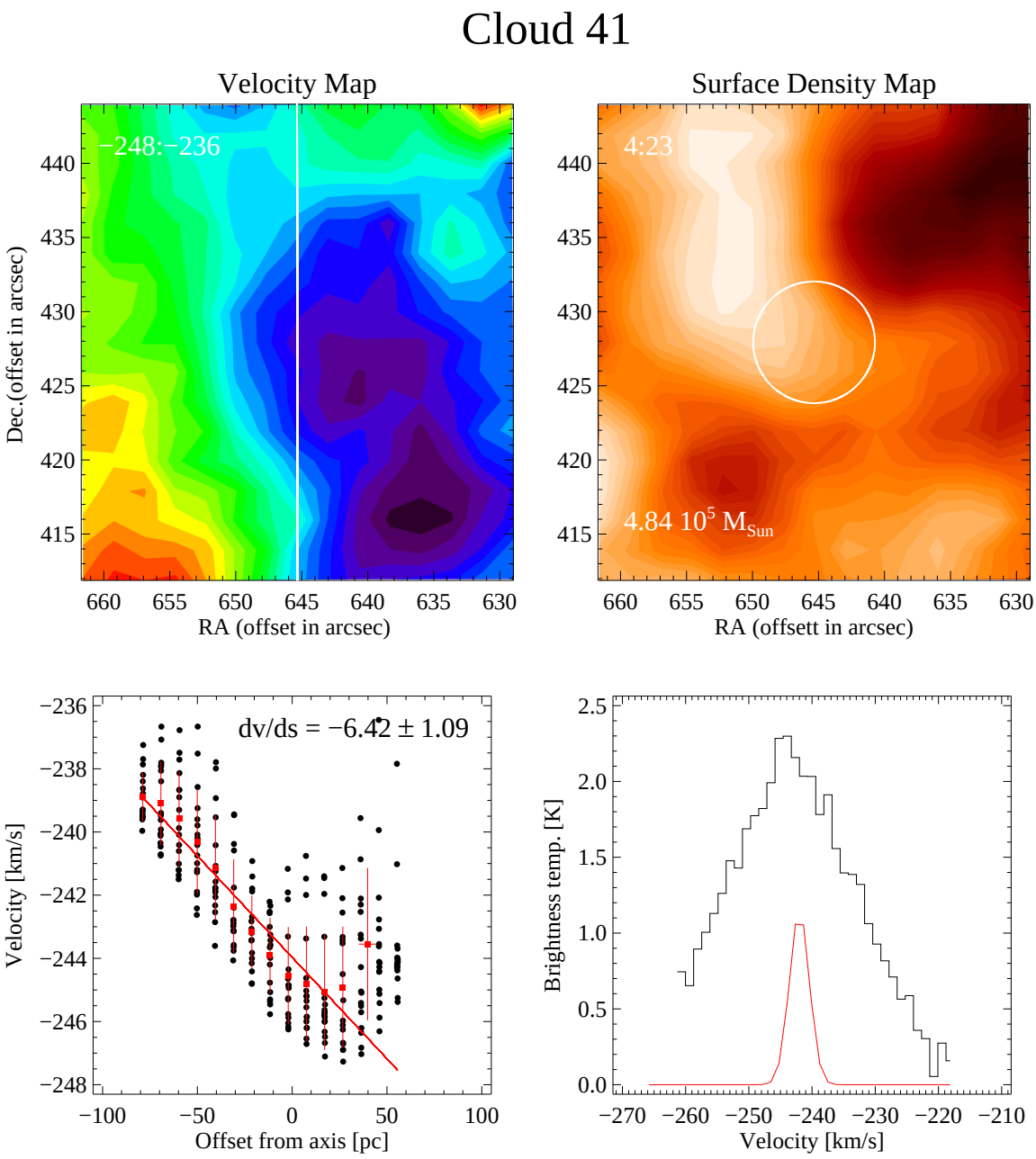

Figure A.36: Cloud 41: Same as Figure A.1.

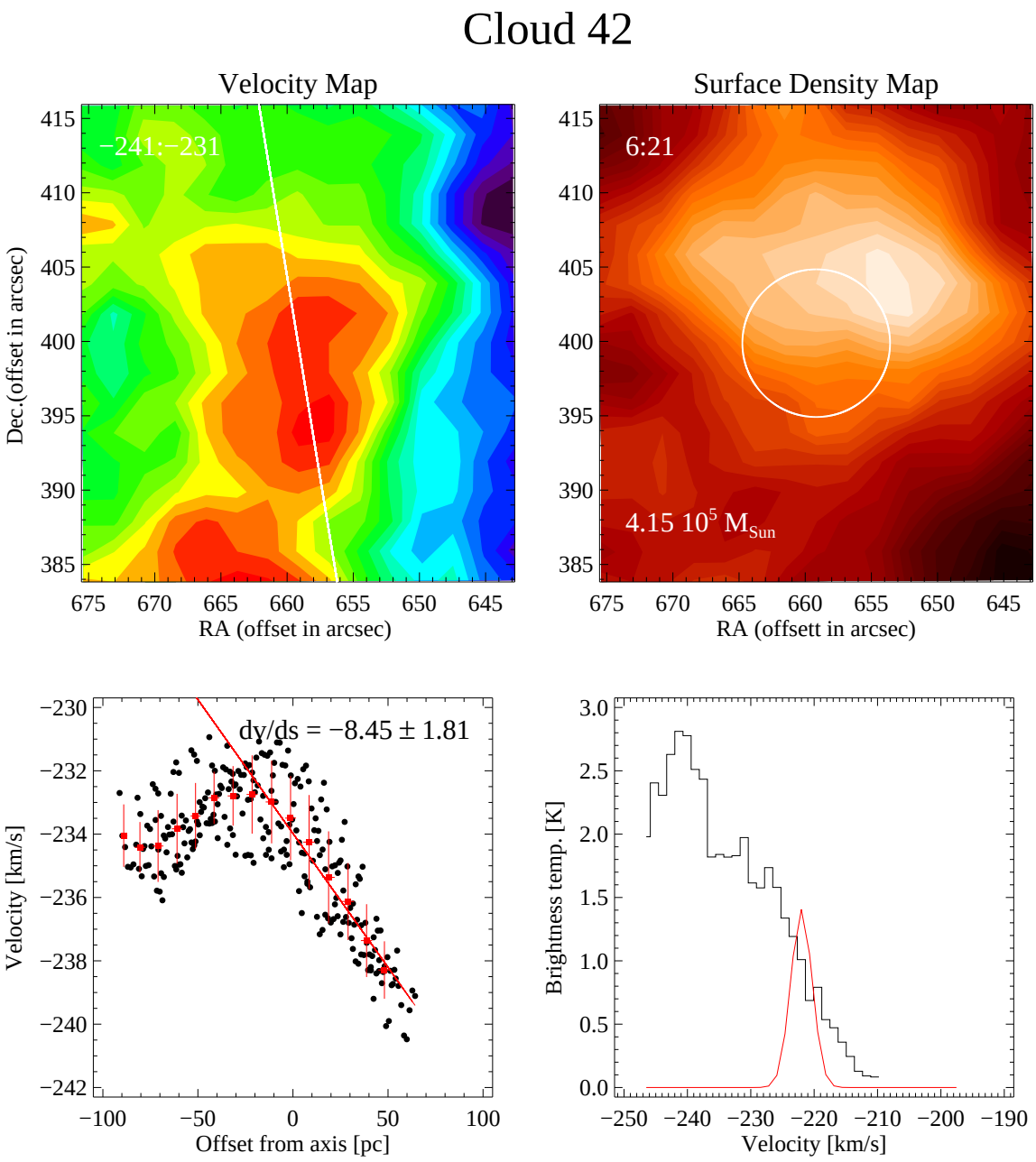

Figure A.37: Cloud 42: Same as Figure A.1.

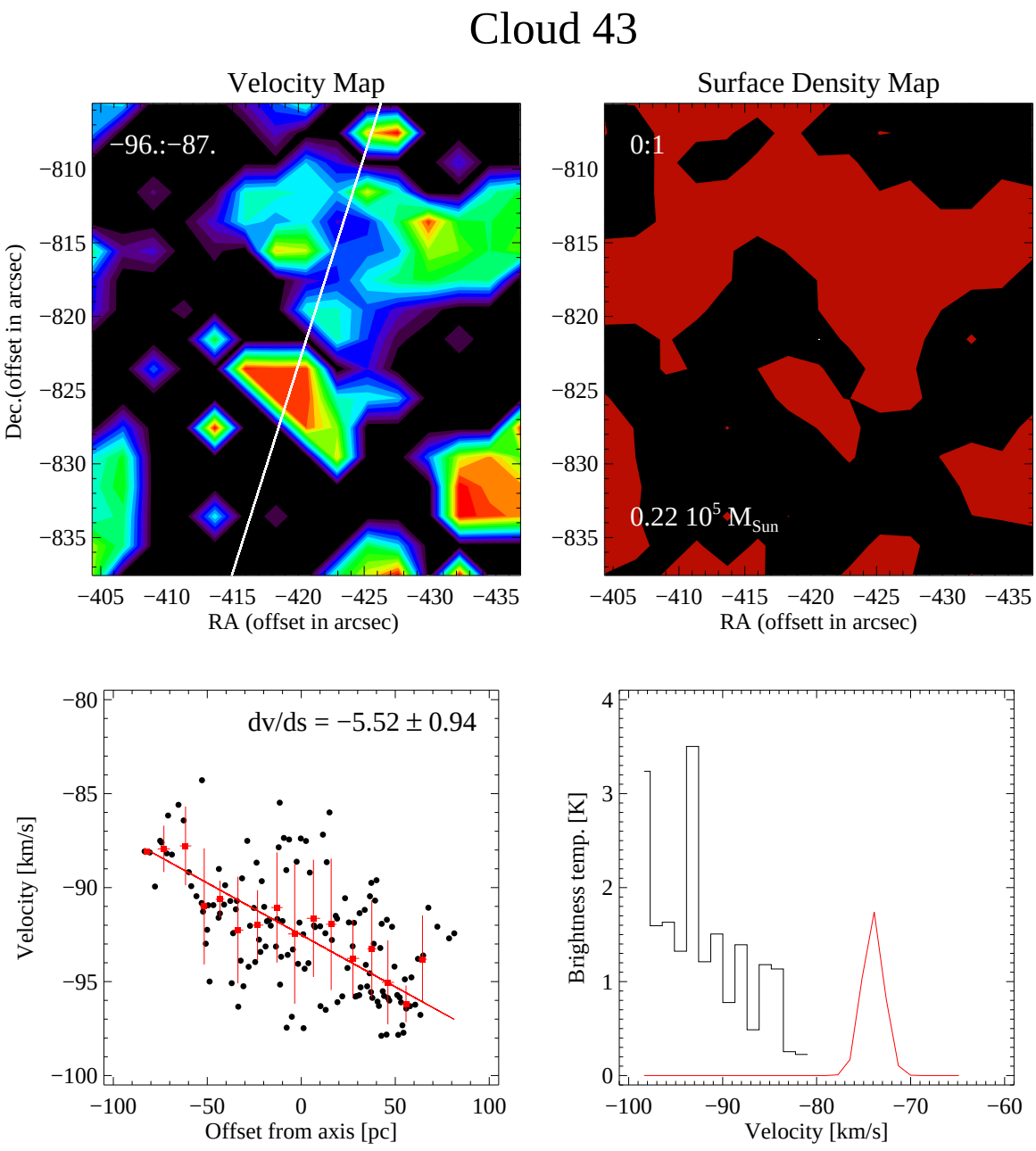

Figure A.38: Cloud 43: Same as Figure A.1.

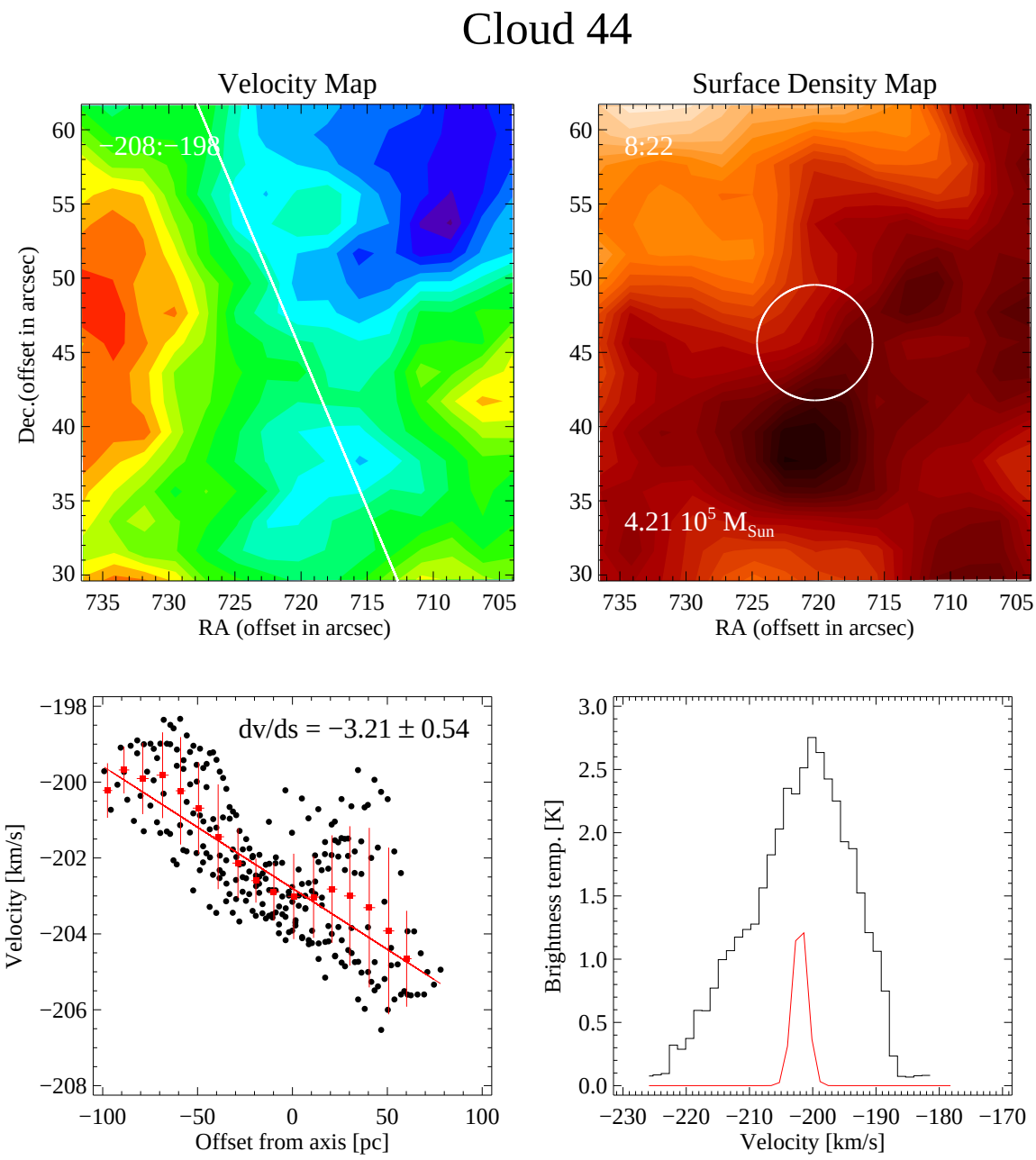

Figure A.39: Cloud 44: Same as Figure A.1.